DOCTORAL COURSE IN

CHEMICAL SCIENCES

CICLO XXXIII

DIRECTOR Prof. Alberto Cavazzini

DESIGN STRATEGIES AND TECHNICAL ASPECTS OF NANOSCALE DRUG CARRIERS

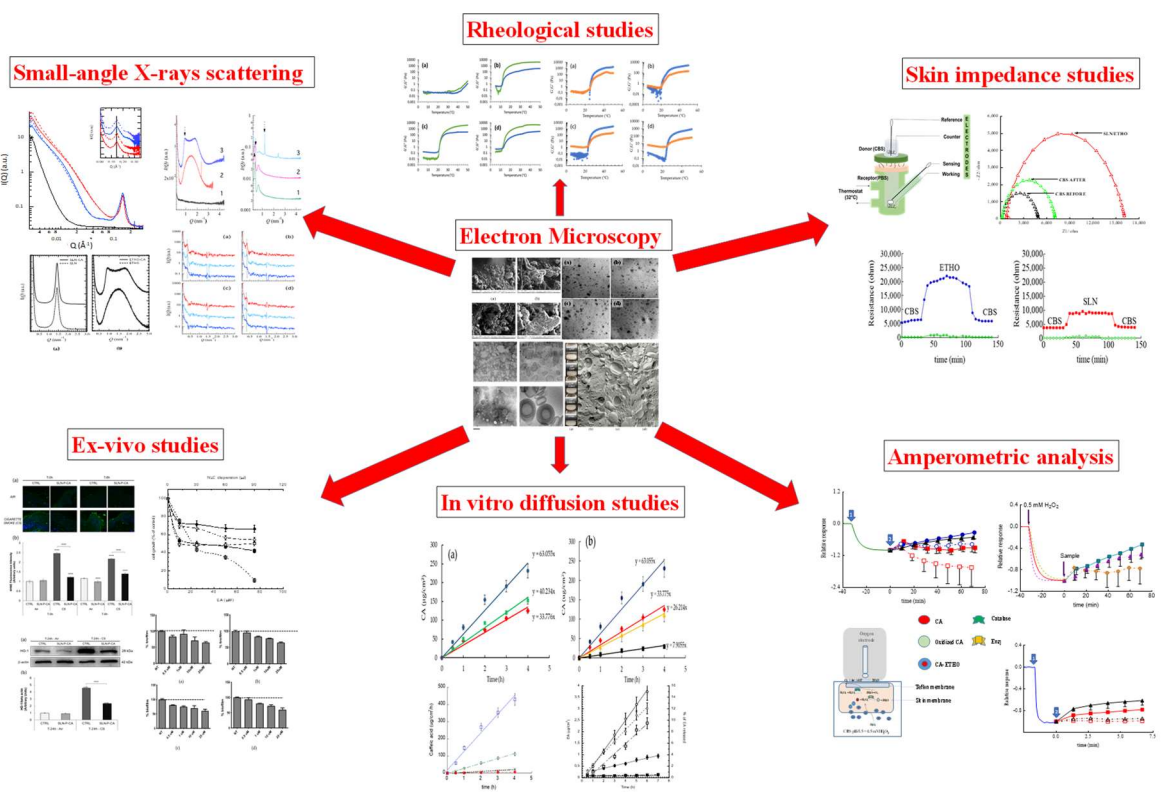Scientific/Disciplinary Sector (SDS) CHIM/09

Candidate	**Supervisor**
Dott. Hallan Supandeep Singh	Prof. Cortesi Rita

_____   _____

(firma)   *(firma)*

Years 2017/2020

GRAPHICAL ABSTRACT

CONTENTS

LIST OF ACRONYMS

CA	Caffeic acid
CA- ETHO-pol	Caffeic acid containing ethosomes gel
CA-ETHO	Caffeic acid containing ethosomes
CA-SLN	Solid lipid nanoparticles contain caffeic acid
CA-SOL	Caffeic acid solution
CAT	Catalase
CBS	Citrate buffer saline
Cryo- TEM	Cryo-Transmission Electron Microscopy
CS	Cigarette smoking
CUR	Curcumin
D	Diffusion coefficient
Dapp	Apparent diffusion coefficient
DMSO	Dimethyl sulfoxide
DPPH	2, 2-diphenyl-1-picrylhydrazyl
EA	Ellagic acid
EE	Encapsulation efficiency
ETHO	Ethosomes
ETHO T80-MG	Ethosomes modifies with polysorbate80 containing mangiferin
ETHO-MG	Ethosomes containing mangiferin
ETOH	Ethanol
F	Flux
G'	Elastic modulus
G''	Viscous modulus
H_2O_2	Hydrogen peroxide
HA	Hyaluronic Acid
HO-1	heme-oxygenase
HPLC	High performance liquid chromatography
LC	Loading capacity
LP-DCP	Liposomes with dicetyl phosphate
LP-DDAC	Liposomes with didecyldimethylammonium chloride

LP-DEBDA	Liposomes with di isobutyl phenoxy ethyl dimethyl benzyl ammonium chloride
LP-P	Plain liposomes
MG	Mangiferin
MNP	Magnetic nanoparticles
MRI	Magnetic resonance imaging
M-SLN	Magnetic solid lipid nanoparticles
NLC	Nanostructured lipid carriers
NLC- EA	Ellagic acid containing Nanostructured lipid carriers
OE	Oxygen electrode
P188	Poloxamer 188
P407/ P	PEO_{98}-POP_{67}-PEO_{98} Poloxamer 407
PC	Phosphatidylcholine
P-CA	Poloxamer- caffeic acid gel
PCS	Photon correlation spectroscopy
PER	Peroxidase
P-HA	Poloxamer - Hyaluronic Acid gel
P-HA-CA	Poloxamer - Hyaluronic Acid gel contain caffeic acid
PI	Polydispersity index
P-P188-CA	Poloxamer 407- poloxamer 188 gel contain caffeic acid
QS	Quorum Sensing
QSi	Quorum Sensing inhibitors
ROS	Reactive oxygen species
SA	Stearyl amine
SAXS	Small angle X-rays scattering
SC	Stratum corneum
SCOE	Skin covered oxygen electrode
SEM	Scanning electron microscope
SLN	Solid lipid nanoparticles
SLN-P	Solid lipid nanoparticles- poloxamer 407 gel
SLN-P-CA	Solid lipid nanoparticles- poloxamer gel contain caffeic acid
TEM	Transmission Electron Microscopy

t_{lag}	Lag time
TS	Tape stripped
Tsol-gel	Sol-gel transition temperature
UVB	Ultraviolet B

x

1   INTRODUCTION

1.1   AIM AND PLANNING

The overall aim of this research is based on the development and characterization of lipid-based formulations namely lipid-coated magnetic nanoparticles (MNP) for theranostic applications, Solid lipid nanoparticles (SLN), Nanostructured lipid carriers (NLC), ethosomes (ETHO), transethosomes, gels for dermal and transdermal drug delivery, and liposomes to target biofilm inhibitors.

The first chapter entitled 'introduction' based on the design, characteristics, and biomedical applications of various lipid-based novel drug delivery systems have been used in this research.

The second chapter deals with the materials used and the third chapter describe various research methodologies adopted in the design and characterization of nano-carriers for innumerable purposes.

The fourth chapter is based on the principle of magnetism, where iron oxide nanoparticles (manufactured in the laboratory or commercial products) have been coated with biocompatible lipids exploring various possible strategies. These lipid- MNP can be the source of dual functioning (magnetically driven targeted drug delivery), and contrast agents for diagnostic imaging by minimizing toxicity which is generally considered a great obstacle in their clinical applications.

Chapters number five to ten describe improvements in drug delivery for various active agents.

In chapter fifth, the study aimed to develop NLC able to encapsulate ellagic acid (EA) for dermal delivery. The EA-loaded nanoparticles were prepared using two different lipid compositions, namely tristearin/tricaprylin and tristearin/labrasol. The influence of formulations on size, entrapment efficiency, and stability of EA-loaded nanoparticles was investigated. Further, developed nanoparticles were tested for cytotoxicity and anti-oxidant activity.

In chapter sixth, caffeic acid (CA) has been encapsulated in SLN by hot homogenization and ultra-sonication. To improve the consistency of the aqueous nanodispersion, different types of polymers have been considered. Particularly, poloxamer 407 (P) and hyaluronic acid (HA) gels containing CA have been produced and characterized. Finally, the antioxidant effect of CA loaded in the nanoparticulate gel has been demonstrated by ex-vivo evaluation on human skin explants exposed to cigarette smoke (CS), suggesting a protective effect provided by the nanoparticles.

In chapter seventh, an investigation describes a formulative study aimed at designing ETHO for CA transdermal administration. Size distribution and morphology of ETHO were investigated by photon correlation spectroscopy (PCS), small-angle X-ray spectroscopy (SAXS), and cryogenic transmission electron microscopy (cryo-TEM). CA stability in ETHO was compared to the stability of the molecule in water, determined by mass spectrometry. ETHO dispersion was thickened by poloxamer 407, obtaining an ethosomal gel that was characterized for rheological behavior and deformability.

Chapter eighth describes a comparative study between SLN and ETHO for CA delivery through the skin. The effect of lipid matrix has been evaluated on morphology and size distribution of SLN and ETHO loaded with CA. Particularly morphology has been investigated by cryo-TEM and SAXS, while mean diameters have been evaluated by PCS. The antioxidant power has been evaluated by the 2,2-diphenyl-1-picrylhydrazyl (DPPH) methodology. The influence of the type of nanosystems on CA diffusion has been evaluated by Franz cell-associated to a nylon membrane, while to evaluate CA permeation through the skin, an amperometric study has been conducted, based on porcine SCOE. Finally, an irritation patch test was conducted on 20 human volunteers to test the efficacy of both systems.

In chapter ninth, the use of liposomes to deliver two novel synthetic biofilm inhibitors is presented, focusing on a preformulatory study to select the best liposome composition for in vitro test. Five different liposome formulations, composed of phosphatidylcholine, cholesterol, and charged surfactant (2:1:1, molar ratio) have been prepared by direct hydration and extrusion method. As charged surfactants dicetyl phosphate (DCP), didecyldimethylammonium chloride (DDAC), di isobutyl phenoxy ethyl dimethyl benzyl ammonium chloride (DEBDA), and stearyl amine (SA) have been used. Liposome charge,

size, and morphology were investigated by zeta potential, PCS, SAXS, and electron microscopy. The optimized liposomes with QSI (Quorum sensing inhibitors) were tested for in vitro biofilm inhibition assays and toxicity.

In the tenth chapter, basic optimization has been done for ETHO and ETHO modified with surface activators such as T80 and DDAB to choose the best carrier for transdermal delivery of mangiferin (MG). Moreover, a modified oxygen electrode (OE) is employed to assess the anti-oxidant potential of developed vesicles. Finally, the three formulations have been tested for cell viability studies.

Chapter eleventh contains the conclusions of the above-mentioned research work considering the obtained results and discussions.

1.2 DESCRIPTION OF NANO-SIZED DRUG DELIVERY SYSTEMS

The worldwide researchers are working to protect the entire population from numerous diseases by designing novel strategies or by improving the existing medicine systems to enrich patient safety and compliance. A drug carrier plays a very essential role to accomplish good therapy. Substantial development has taken place to combat the number of diseases using different drug cargos, which maintain the concentration, time, and releasing rate of therapeutic moieties in the body. The main motive of drug delivery systems is to distribute the active to a targeted site within a suitable time window along with a higher concentration in the infected sites and as low as possible in the healthy tissues (Hallan et al., 2016).

The established and commercially available conventional drug transport systems can increase plasma drug concentration to maintain a therapeutic window for a definite time, and then start declining to an ineffective level followed by the same event on the second administration. However, the achievement of adequate drug concentration for a consistent time during disease state is the major failure in drug therapy. Moreover, conventional drug delivery systems can not meet certain requirements such as targeted drug delivery, biodistribution, controlled release, enhanced bioavailability, and mean residence time (Pankhurst et al., 2016).

The design of perfect drug transporter with the capability of maintaining drug concentration efficiently for a required duration at the desired site without affecting normal cell and body

organs is much needed. Nanosized transporters hold the potential of precise drug delivery through various administration routes providing benefits including cargo protection, accumulation at the target site, improved pharmacokinetics bio-distribution, reduced dose frequency, enriched drug transport across biological membranes, and prolonged or controlled drug release. Nanocarriers excellently drive the drug to its target by balancing safety and efficacy (Abdel-Mottaleb et al., 2014).

During the last three decades, nanotechnology for biomedical applications has been explored a lot by researchers worldwide. Nanomedicine is not only limited to drug delivery employing different administration routes such as intravenous, oral, transdermal, nasal, pulmonary, and more, but also a multitude of areas such as vaccination, antibacterial, diagnostic and imaging, and gene delivery.

Based on composition and properties, nano-carriers can be divided into two major categories- namely organic nanoparticles including polymer-based micelles, liposomes, ETHO, SLN, NLC, dendrimers, and inorganic nanoparticles such as carbon nanotubes, graphene nanomaterials, gold nanoparticles, MNP, quantum dots (Lombardo et al., 2019). Some well-known nanomaterials will be discussed in this introduction part.

1.2.1   Diagnostic applications

Nanotechnology has gained considerable interest in the diagnosis and treatment of various life-threatening diseases mainly cancer. The imaging procedures are categorized based on morphological, functional, and molecular levels, which provide the biological detail of a disease with a non-invasive approach have been proposed. Particularly, spherical nano-sized particles made of inert silica, metals, or crystals. MNP are a wonderful tool with numerous biomedical applications, including magnetic hyperthermia, cell separations, magnetic resonance imaging (MRI) to track tumor cells or lesion by comparing the overall magnetic response of MNP between pathological and normal tissues, tissue engineering, and drug delivery to very specific areas. MNP can be categorized as pure metals, metal oxides, and magnetic nanocomposites. However, MNP have gained the highest attention in the biomedical field composed of Co, Fe, Ni, Ti, iron oxide, and some ferrites ($BaFe_{12}O_{19}$ and $CoFe_2O_4$) (Li et al., 2016).

In general, magnetic materials are considered as multi magnetic arrangements within one structure. However, After conversion to the nano-scale with diameters around 10-15 nm, these magnetic materials act as a single magnetic domain structure. They are responsive only in the presence of a magnetic field which means are associated with para magnetism. Therefore, can be controlled very precisely via an external magnetic field (Avval et al., 2020).

The MNP are available in three major forms named as magnetite (Fe_3O_4), maghemite (γ-Fe_2O_3), and hematite (α-Fe_2O_3). Magnetite (Fe^{2+} and Fe^{3+} ions in the 1:2 ratio) is primarily preferred among the three forms of iron oxides. If ferromagnetic material is exposed to an external magnetic field and later turns it off, still holds the magnetization for a short period which gives the possibility to control heat and magnetic effect in-vivo (Dulińska-Litewka et al., 2019).

Hyperthermia is a well-established phenomenon, whereby applying high-frequency alternating magnetic field results in heat production by MNP. This transformation of the electromagnetic energy into heat due to MNPs oscillation is very useful in cancer therapy, as tissues exposed to conditions of high temperature (41-47°C) may undergo apoptosis of the tumor cells. However, precise control of magnetic heating can be accomplished by controlling some nano-magnetic parameters (Figure 1) such as size (V), anisotropy (K), saturation magnetization (MS), and coercivity (HC) during the entire process, otherwise could damage neighboring cells too. The principle of heat diffusion should cause maximum destruction or killing of tumor cells deprived of damaging the normal cells (Hervault and Thanh, 2014). It is worth noting that, surface engineered MNP can be utilized for various purposes, including linking of antibodies, specific peptides, drug molecules, fluorescent dye, and CT contrast agents.
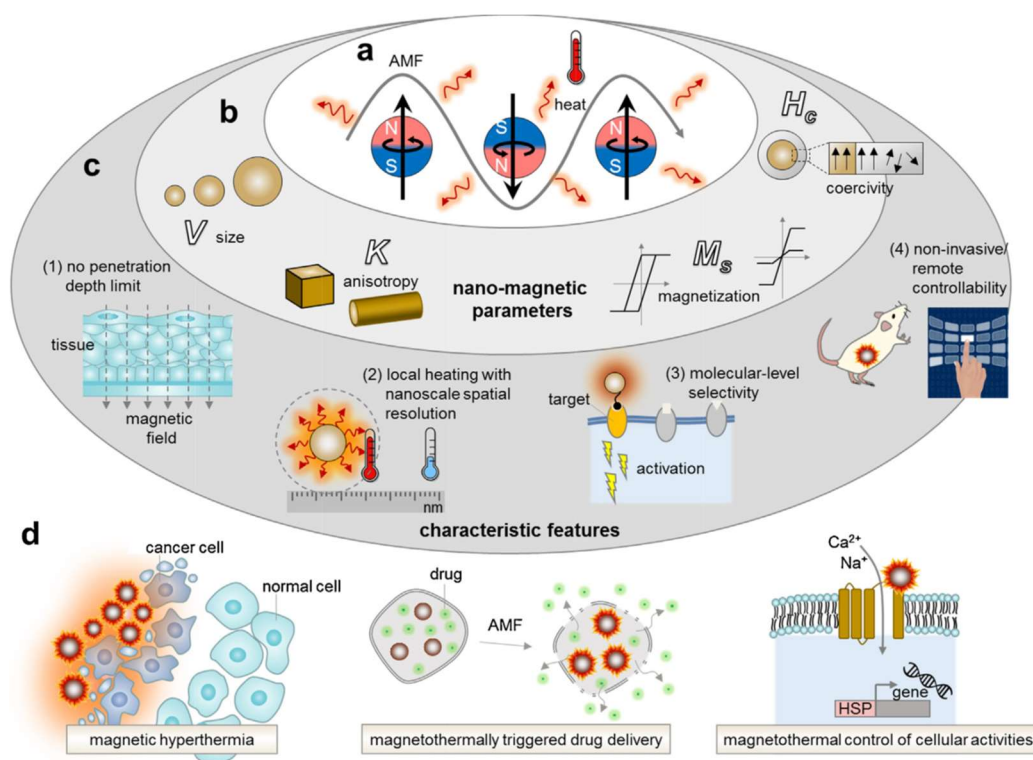
Figure 1. Development phases and applications of MNP (Noh et al., 2017).

More than one target can be achieved simultaneously on a single delivery run of MNP in the body as mentioned in Figure 2 (Montiel Schneider and Lassalle, 2017). In addition, the pivotal concept of artificial engineering has been explored based on the iron oxide nanoparticles as an ultra-sensitive nanoprobe, where antibodies can be linked to MNP. The proposed biomarkers could enhance the real-time visualization of certain biological events including cell trafficking, cancer metastasis, cellular signaling at the molecular and cellular levels (Lee et al., 2007). Apart from various advantages, MNP also experienced certain challenges, including rapid agglomeration due to large surface-to-volume ratio, chemical reactivity, and high surface energy, consequently cause loss of magnetism. By applying a suitable coating around MNP can make them more biocompatible with improved functioning (Zhu et al., 2018). For instance, Byoun et al. have modified MNP by incorporating them into the silica matrix, functionalize them with a fluorescent dye. The multi-Fe_3O_4@SiO_2 NPs have outstandingly retained dual functioning namely fluorescence and magnetism.
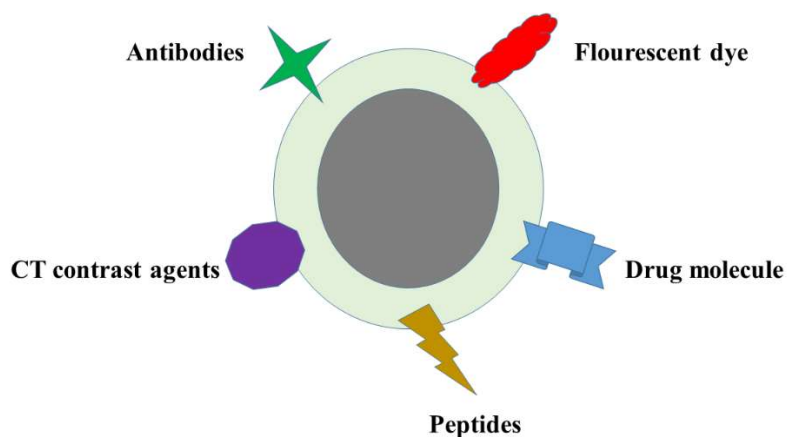
Figure 2. Functionalization strategies of MNP.

Moreover, MNP below 10 nm with paramagnetic behavior is susceptible to rapid clearance from the kidney because of a smaller size. This increased dimensions with the application of polymer or lipid as a coating material have been proved to be supportive to maintain a longer shelf life in the blood circulation (Byoun et al., 2019). Some most explored coating material for MNP is Dextran and PEG (Ling et al., 2019), dextran-spermine biopolymer (Ghadiri et al., 2017), b-cyclodextrin, and chitosan (Chen et al., 2017), poly (lactide-co-glycolide) as a magnetic core, with folate-chitosan conjugate shell (Shanavas et al., 2017).

1.2.2   Drug delivery

Some of the widely investigated lipid-based drug delivery systems along with their physicochemical properties, characterization, and applications have been discussed below.

1.2.2.1   Lipid nanoparticles- Solid lipid nanoparticles (SLN) and nanostructured lipid carriers (NLC)

SLN with a diameter of 10 and 1000 nm have emerged as an alternative to colloidal drug delivery systems comparable to liposomes, lipid emulsions, and polymeric nanoparticles. They contain physiologically tolerated lipids dispersed in an aqueous phase containing stabilizers. Due to their ability to embed both hydrophilic and lipophilic molecules, they

became outstanding prototypes for controlled and targeted drug delivery (Mishra et al., 2018).

The biomimetic property of SLN is valuable for penetration through various biological barriers. Owing to these characteristics, lipids nanoparticles have been put forward as an effective drug carrier, particularly for lipophilic active moieties that also offer distinctive properties such as small diameter, large surface area, high drug loading (Mukherjee et al., 2009).

SLN are nano-dispersions, in which lipid nanoparticles are dispersed as a heterogeneous system with an inner lipid phase and an outer aqueous phase, stabilized by one or two stabilizers (Garcês et al., 2018).

Combination therapy is a much-appreciated approach to establish synergism in resulted response. The concept of co-delivery is also feasible in the case of lipid-based nanoparticles. Recently, clotrimazole and alphalipolic acid have been entrapped into cationic lipid-containing SLN. A prolonged-release was recorded without any burst effect. In-vitro testing on 25 strains of Candida albicans demonstrates that the anti-microbial capacity was well maintained on loading into SLN. Thus, the findings of studies are well agreed that topical dual drug delivery through SLN as cargo is an effective approach against microbial infections related to C. albicans (Carbone et al., 2020).

During storage, the solid lipids constituting SLN are subjected to crystallization. The formation of a rigid core takes place that limits the movement of active molecules within the core results in the expulsion of the drug into dispersion media. This serious problem of instability affects the entrapment efficiency of the system (Salvi and Pawar, 2019).

For further understanding, the theoretical models of SLN and NLC have been established using sophisticated analytical techniques including differential scanning calorimetry (DSC) and SAXS, these techniques are capable to identify the polymorphic forms of lipid matrix, which are dependent on the specific ratio and composition of lipid and surfactant used. Moreover, Cryo-TEM describes the morphology of nanoscale objects (Pardeike et al., 2009). The diagrammatical illustration (Figure 3) and characteristics (Table 1) of these theoretical models for both SLN and NLC have been discussed.
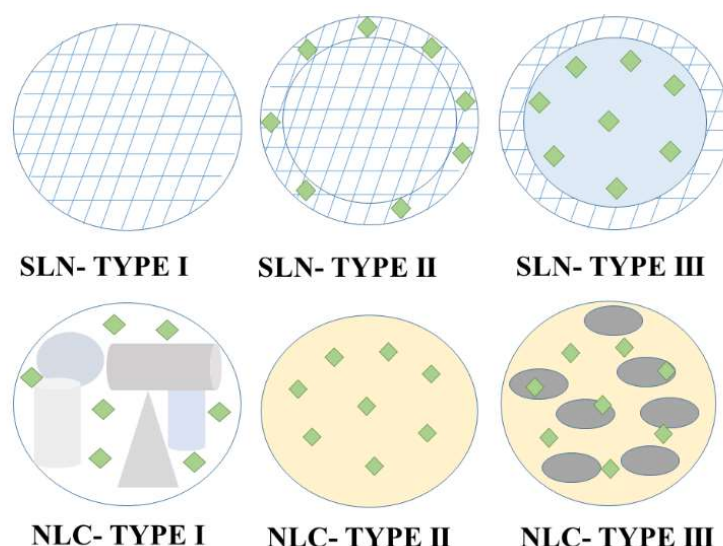
Figure 3. The theoretical models for the inner structure of Solid lipid nanoparticles (SLN) and Nanostructured lipid carriers (NLC).

The polymorphic state of the lipid depends upon its compatibility with other oils and stabilizers. Crystallinity throughout the manufacturing process of lipid nanoparticles and their storage determines the drug incorporation and its release pattern (Tetyczka et al., 2019). The crystallization pattern of the lipid inside the nanoparticles is different compared to that in bulk. Crystallization is highly dependent upon the critical crystallization temperature required to obtain rigid nanoparticles after the homogenization step, liquid state particles (supercooled emulsion) will be produced if a specific temperature is not reached. Further, the choice of surfactant is another crucial factor that influences the kinetics of the polymorphic transition of lipids (Üner, 2016).

Table 1: Basic characteristics of various theoretical models for the inner structure of Solid lipid nanoparticles (SLN) and Nanostructured lipid carriers (NLC).

Type	Name	Characteristics
SLN Type I	Homogeneous matrix model	On the production of SLN by the cold homogenization technique, the drug is molecularly dispersed in the matrix of lipid. In this case, neither surfactant nor drug-solubilizing agent is utilized, core resulted as amorphous clusters can show controlled release properties (Müller, 2000).
SLN Type II	Drug enriched shell model	Re-partitioning of the drug to the lipid phase results in lower drug concentration in the melted lipid. Hence, lipids present in the core with reduced concentration will be in the molten state, while the shell with drug and lipid will be solidified. This is the best-fit model to obtain a burst release of the drug.
SLN Type III	Drug enriched core model	Drug precipitation followed by recrystallization takes place where drug concentration is relatively close to or at its saturated solubility in the lipid phase. Under the cooling of nanoemulsion, the solubility of drugs will decrease, when the saturation solubility ultimately leads to drug crystallization before lipid crystallization will further result in recrystallization of the lipid around the drug core as a membrane.
NLC Type I	The imperfect crystal model	Composed of disordered structure with a mixture of different chain lengths of the fatty acids and the mixture of mono-, di- and triacylglycerols, create many voids and imperfections, makes them able to accommodate the drug molecules. Therefore, increasing drug penetration capacity through the lipid layer (Müller et al., 2002).
NLC Type II	The amorphous model	When lipids with a special composition (e.g., Hydroxyl octacosanylhydroxystearate, isopropyl myristate, dibutyl adipate) mixed, they prevent crystal formation during cool down. Lack of crystallinity is responsible for the reduction in the leakage of the loaded drug. Hence particles are amorphous.
NLC Type III	The multiple model	For drugs with higher solubility in liquid lipid than in solid lipids, phase separation occurs, where very peculiar oil compartments within the solid lipid matrix of the nanoparticles formed.

The inappropriate concentration of lipid and surfactant can affect the overall internal structure of lipid nanoparticles. Recrystallization of lipid in nanoparticles is less than in bulk where b'-modification transforming rapidly into the b-form to reduce imperfections, this transition could be responsible for drug expulsion. A smart way is adopted in designing the SLN (by controlling temperature and water loss) with the initiation of transformation from a- to b-forms (Pardeshi et al., 2012). Thus, it has been drawn as a conclusion that drug incorporation decreases in the following order:

Supercooled melt < a-form < b'-form < b-form

The cutaneous utility of lipid nanoparticles holds several benefits, such as the prevention of chemical degradation of active, increasing the deposition in the stratum corneum, and reduce flux, attributes to some very interesting outputs such as prolonged contact with the skin surface, film-forming properties to prevent water loss. The mechanism of mixing of lipid nanoparticles and lipids of SC promotes penetration of active into deeper tissues. Lipid nanotransporters can establish adjacent contact with the superficial junctions of SC and furrows between corneocyte islands, allowing uniform distribution of the drug. They also offer a widening of inter-corneocyte gaps (Wissing and Müller, 2003). Further, four different models described in Figure 4 can explain the interaction of lipid nanoparticles with skin.
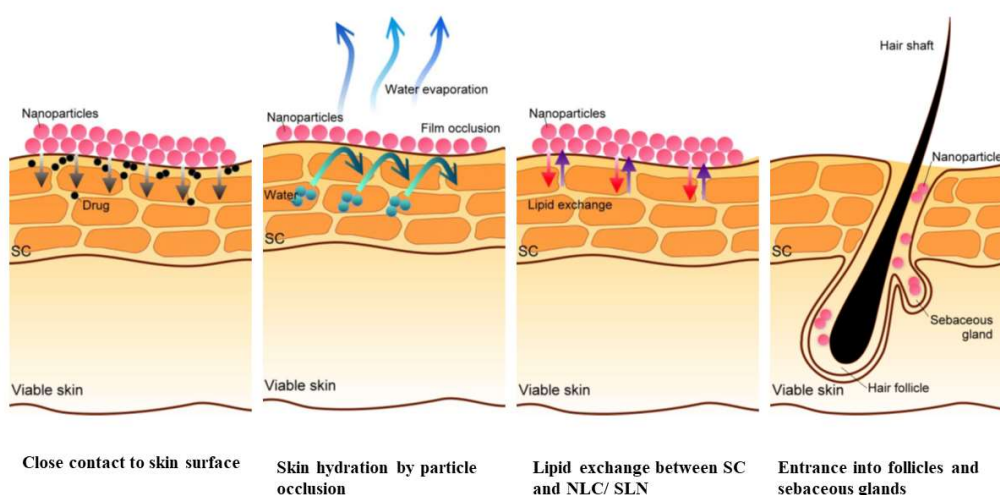
Figure 4. Possible mechanisms for skin permeation improvement with lipid nanoparticles (Fang et al., 2013).

Because of physiological lipid composition, SLN/ NLC offer an easy attachment to the SC on forming its lipid rearrangement, allowing embedded drug molecule reaching to the deeper skin layers. Furthermore, their nanoscale diameter also contributes to the enhancement of the influx through the skin. Nonetheless, the adequate selection of lipid composition concerning the molecule's physicochemical properties also affects skin penetration largely. The film-formation/ an occlusive film property of SLN/ NLC on the SC surface avoids evaporation of water and also fills the defects in the skin (Garcês et al., 2018).

Furthermore, Lademann and co-workers have concluded in one study that the hair follicles (particularly, scalp, calf, and forehead regions) are better drug depots than the stratum corneum. They have considered nanoparticles are well suited for driving the drugs into deeper functional structures and accumulate even for some days (Lademann et al., 2007).

1.2.2.2 Liposomes

Liposomes are one of the most successful products of nanotechnology have been launched in the market for clinical applications. Liposomes are phospholipid and cholesterol(resembles biomembrane) containing round vesicles along with amphiphilic character widely accepted for various biomedical applications. Liposomes can be of many types depending upon the lipid composition, charge on the surface, diameter, and fabrication process. Phospholipid composition makes them free moving entities across the biological barriers within the body, are biocompatible (Lamichhane et al., 2018). Liposomes have been introduced to research along with various advantages as a successful biomimetic approach. They can be modified to achieve certain objectives such as drug loading and the target-specific precise release by avoiding rapid clearance (Allen and Cullis, 2013; Chandrawati and Caruso, 2012).

Being foreign bodies, liposomes are usually cleared out immediately, therefore a suitable coating material (such as synthetic phospholipids, polyethylene glycol (PEG), chitin derivatives) is required. The much-explored PEGylation to escape liposomes against their uptake by macrophages to enhance circulation time. Further, the biodistribution of PEGylated vs non-PEGylated liposomes has been explained in Figure 5. This technique has been adopted successfully to produce doxorubicin-loaded liposomes commercially available as Doxil (Janssen Biotech, Inc., Horsham, USA) or Caelyx (Schering- Plough Corporation, Kenilworth, USA) for the treatment of solid tumors (Akbarzadeh et al., 2013).
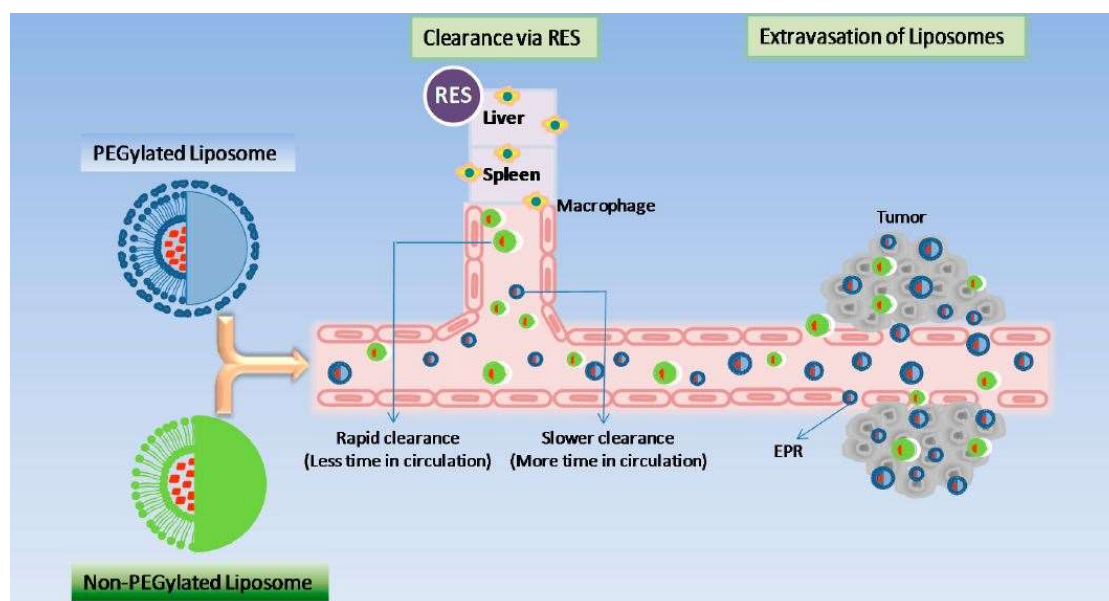
Figure 5. Pharmacokinetics of stealth and non-stealth liposomes (Bulbake et al., 2017).

Liposomes being a commercial product, present a rationale for unloading the anti-cancer agent specifically in tumor tissues, sparing the non-cancerous tissues by employing passive targeting (exhibit enhanced permeability and retention (EPR) effect). After administration, liposomes head towards the extravasation into tumor interstitium followed by the uptake via TAM. Finally, intracellular trafficking of liposomes either with endosomes or lysosomes results in the release of drugs in the cytosol and infiltration to the nucleo-cytoplasmic membrane with possible DNA destruction (Gabizon et al., 2020).

Tumor-associated macrophages (TAM) is a contributing factor for tumor growth that alters the tumor microenvironment to diminish growth barriers to protect cancer cells from targeted immune responses. Liposomes can intrude these biological interactions within tumors by altering TAM phenotypes via polarization. This "macrophage polarization" can switch this growth-promoting phenotype to the cancer cell killing phenotype (Reichel et al., 2019).

Additionally, functional liposomes can be developed which are responsive to external stimuli such as temperature and pH. Unlike MNP, where an alternating magnetic field as a source of heat production applies to kill tumor cells. Here, liposomes can also kill cancerous cells when the lipid phase of liposomes undergoes gel to liquid phase transitions at temperatures above the physiological temperature. A clinically approved synergistic effect

of radiation and chemotherapy is possible with liposomes. Because in terms of mild hyperthermia, vascular permeability of cancer cells will increase significantly the mean residence time of liposomes. Hence, the triggered release of anti-cancer agents on the target site has assured the effectiveness of this approach (Ta and Porter, 2013).

Gadodiamide is a paramagnetic, gadolinium-based contrast agent that has been entrapped in pH-responsive liposomes (Dipalmitoyl phosphatidylethanolamine (DPPE)/ dipalmitoyl glycerosuccinate (DPSG), to monitor acidic pH in cancer cells. As previously mentioned in hyperthermia, after spending persistent time in blood, these liposomes can be reached at the target site in large numbers because of increased vascular permeability. The gadolinium-based contrast agent was released in this study due to increased T_1-relaxivity at pH lowered than the physiological value (Løkling et al., 2004).

Concerning the biodistribution of liposomes, an approach has been established (Pollock et al., 2010), where liposomes can unload drugs, peptides, nucleic acids, or markers directly in the ER membrane in 30 minutes after entering into cells, this technique is efficient for both lipophilic and hydrophilic moieties. In this, the composition of liposomes is very important, because the lipid used should resemble the ER membrane and perform endocytosis into target cells.

The membrane fusibility of liposomes is quite challenging because of the complexity of the natural biomembrane and glycoproteins. However, Chen-Yen Wang described in their study that liposomal fusion with the membrane could be obtained in the presence of polyhistidine under acidic conditions only. Thus, negatively charged liposomes (with anionic lipid-phosphatidylserine) have shown the highest fusion (Wang and Huang, 1984). Besides, a study has been conducted to assess electrostatic adhesiveness of charged liposomes to healthy and colitis induced intestinal epithelium. Anionic liposomes over cationic and neutral liposomes have presented better results.

Additionally, triggered drug release by disease-associated enzymes is another approach to activate prodrugs. For instance, the retinoid phospholipid derivative has been incorporated into liposomes which could be hydrolyzed and degraded by phospholipase A2 IIA for site-specific delivery in colon cancer (Pedersen et al., 2010).

1.2.2.3   Ethosomes

In the 90s, modification in the production of liposomes with ethanol fraction has emerged as the most preferable approach towards effective transdermal delivery. This second generation of liposomes along with flexible phospholipid vesicles are known as ETHO. The intactness of organized vesicles with 50% of ethanol and the fluidic state of a phospholipid membrane (elastic nature) due to the lowering of transition temperature by ethanol has been verified by 31P NMR and differential scanning calorimetry analysis (Lai et al., 2020; Touitou et al., 2000).

For comparison, both the ETHO and elastic liposomes have been loaded with hepatitis B surface antigen for transcutaneous delivery. Both these formulations have shown the ability to stimulate T helper response after uptake by dendritic cells recorded as a protective response against an immune response. However, among both types of carrier systems, ETHO have been reported for higher internalization and immunogenicity (Mishra et al., 2010). A simple production method eliminates all the possible sources (thermal or light) of drug degradation during processing. Consequently, 100% of drug encapsulation can be achieved. The recently reported study regarding the development of ETHO for percutaneous delivery of Coenzyme Q10, where 90% drug was remained associated with multi-lamellar ETHO possibly because of high interaction of a drug with ethanol and phospholipids. All results from this study reflect that ETHO loaded with Coenzyme Q10 are very promising in the treatment of oxidative stress (Sguizzato et al., 2020b).

As described in Figure 6, ETHO are associated with the combined functioning of ethanol, vesicle, and skin lipids. The ethanol effect generates the interaction between ethanol and the polar head region of SC lipids that reduce their transition temperature, ultimately leads to the state of fluidity and decreased density of lipid multilayer. Secondly, the ETHO effect includes the fusion of ETHO with skin lipids resulting in opening new pathways facilitating drug release more deeply into the skin (Verma and Pathak, 2010). Furthermore, the presence of intact elastic vesicles within the SC has been demonstrated, but claims that intact elastic vesicles can permeate through the viable epidermis to the blood circulation are more contentious (Benson, 2016).

Transethosomes has developed as a combination of deformable liposomes (designed with edge activators also named as transferosomes) and ETHO (Figure 7). The edge activators in

transferosomes such as span 60, span 25, span 80, tween 60, tween 80, sodium deoxycholate, and sodium cholate can be helpful to make vesicles more flexible, but still are unable to deliver drugs more deeply, so synergism along with ethanol can solve this issue (Kumar et al., 2016).
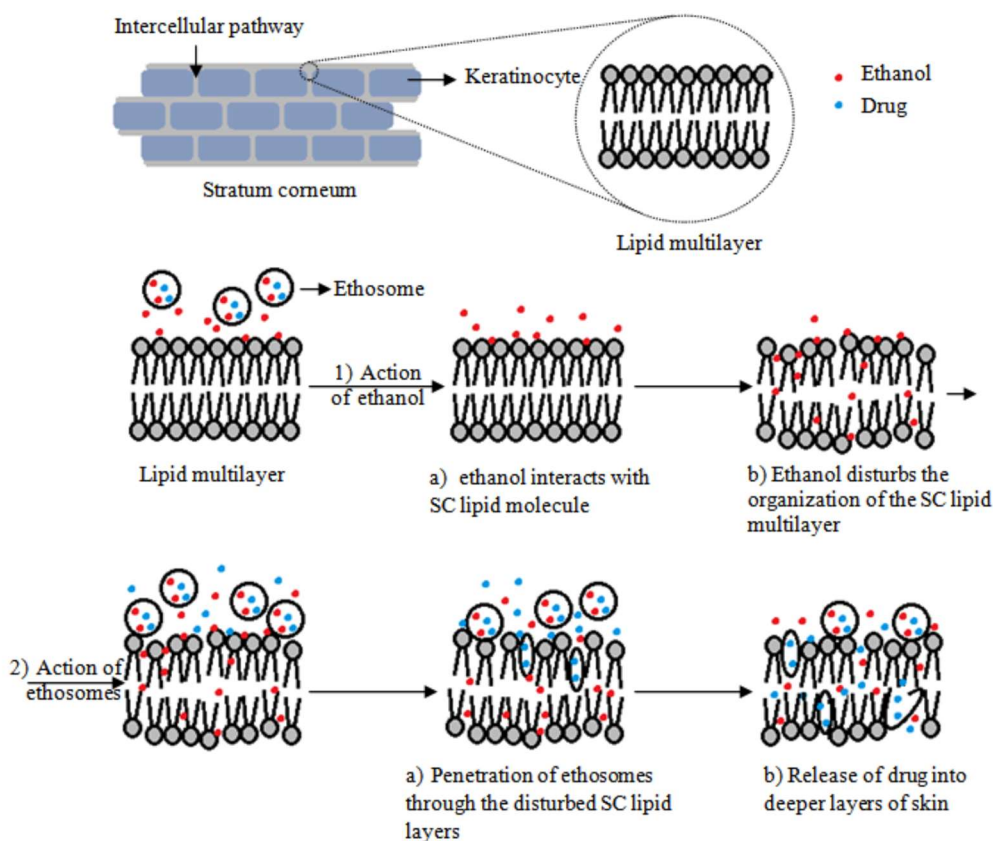
Figure 6. Proposed model for the mechanism of skin delivery from ETHO containing phospholipids, ethanol, and the drug (Kesharwani et al., 2015)**.**

The skin permeation of nano-sized formulations has always remained conflicting. To make ETHO a realistic approach, microneedle driven delivery of different ETHO has investigated. Where authors have claimed that all nano-carriers are not able to cross SC barriers. Therefore, the utilization of microneedles of appropriate sizes is helpful to cross the SC and release the drug into the probable deepest layers of the dermis. It is very important here to underline that even after crossing SC, the role of edge activators (Tween®80 and the Nachol) and ethanol cannot be denied which makes the transethosomes more preferable among other

nanotransportors. More precisely, cationic nano-carriers with ethanol and edge activators have been chosen as the most promising transdermal drug delivery system (Bellefroid et al., 2019).
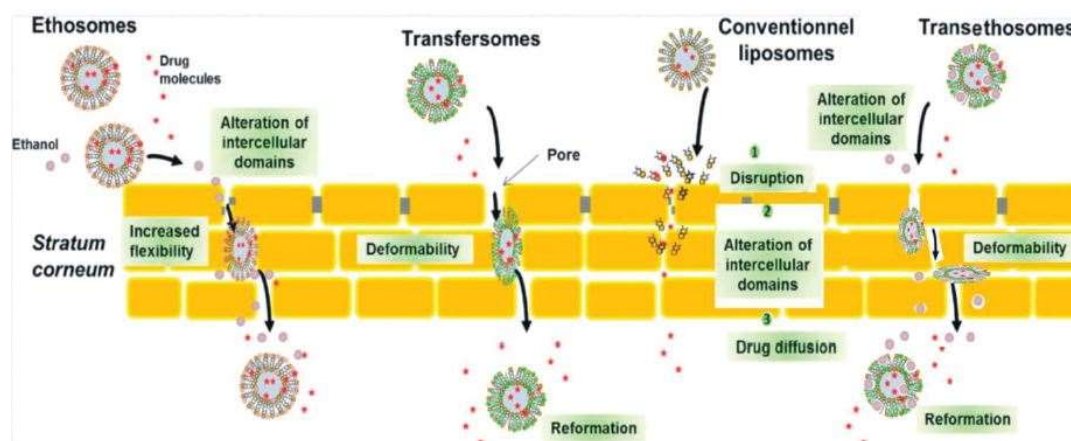
Figure 7. Schematic representation of the main permeation mechanisms of ETHO, transferosomes, conventional liposomes, and transethosomes (Kumar Mishra et al., 2019).

1.2.2.4 Gels

During the entire development of skin therapy, semi-solid drug delivery systems have gained tremendous success at commercial levels. For example, thermo-sensitive gels along with swelling behavior on exposure to liquids without undergoing dissolution. The polymeric gels composing biocompatible polymer matrices have drawn significant attention. The crucial objectives while designing topical formulations such as controlled drug delivery, sustained and prolonged release, tissue-engineering, reducing dose frequency with the least side effects can be achieved with the thermo-gelling property of such polymers (Buwalda et al., 2014). Gels mainly constitute a gelling agent (natural, semi-synthetic, or synthetic polymer) that improves their structural strength and adhesiveness ultimately gives rise to a three-dimensional matrix (loosely cross-linked) with increased residence time. Physical cross-linking (with hydrogen bonding, ionic interactions) is reversible, while chemical crosslinking (covalently Bonded) is irreversible (un Nabi et al., 2016). Some external factors make the gels stimuli-responsive within a living body by changing in temperature, pH, presence of the analyte, and ion responsiveness (Chaterji et al., 2007).
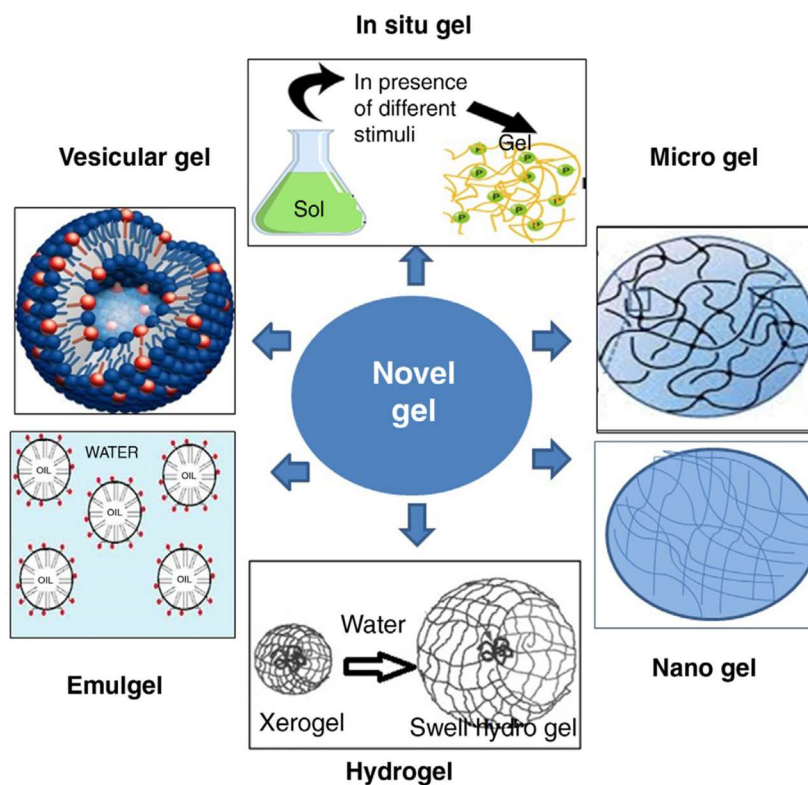
Figure 8. Various types of novel gels (Paul et al., 2017).

There are various types of nanogels (Figure 8) are available. Thermo-responsive gels are more considerable, composed of polymers (Poly (N isopropyl acrylamide), methylcellulose, pluronics, tetronics, and N-vinyl caprolactam) undergone sol-gel transitions associated with lower critical solution temperature (LCST) and upper critical solution temperature (UCST) (Jagur-Grodzinski, 2010).

Poloxamers have been listed in the US and European Pharmacopoeia after FDA approval for human use as a biocompatible solubilizer or surfactant (Johnston and Palmer, 1993). Recently, poloxamer gel containing gallic acid to treat skin melanoma has been studied (Sguizzato et al., 2020c). Where gallic acid- poloxamer gel is found very effective in scratch wound healing and migration assays performed on human keratinocytes and melanoma cells. The combination of gels such as Pluronic®127 and with hydroxypropyl methylcellulose can be associated with anti-bacterial activity in burn-infections. To attain targeted drug delivery efficiently, this combinational gel is linked to gold nanoparticles using tunable surface plasmon resonance (SPR). In this proposed mechanism, gold nanoparticles exert their

antibacterial activity by creating holes in the bacterial cell wall resulted in cell death due to the release of cell content (Arafa et al., 2018).

1.2.3   GENE DELIVERY

Gene delivery involves the delivery of nucleic acids such as plasmid DNA, RNA interference, Small interfering RNA, antisense oligonucleotides. The gene therapy mechanism is based on the incorporation of a gene that encodes a functioning protein significantly involves in the cure or prevention of any disease progression. However, gene modulation seems a very promising method; still, it has some obstacles regarding its delivery to the desired site. The main limitations are rapid clearance, site-specific targeting, degradation by nucleases, which affect the serum half-life of siRNA to 5-60 minutes, unmodified DNA to 10 minutes. However, ligand approach or hydrodynamic injection can minimize these shortcomings, well-designed biocompatible cargo with the capability to escape from the removal by the immune system, enhanced transgene expression still required (Prabu et al., 2017). Obstructions in non-viral gene delivery are linked DNA can be lost due to lack of strong complexation with cationic lipid, DNA-Cationic lipid complex can be eliminated from the circulation before binding to the cell surface. Moreover, the internalization of the complete complex is uncertain after invading the cell membrane. Following endocytosis, a fraction of delivering DNA may be degraded because of acidic pH or cytoplasmic DNAse. Improvement in transfection efficiency can be attained with modification in particle chemistry, size control, surface charge, shape ligand modification (Adler and Leong, 2010). Advancements in nanocarriers offer plentiful possibilities and flexibility to choose a target. Due to biodegradability, ease in synthesis/ functionalization, scale-up production, Polymers can suppose to be an alternative. Moreover, the use of PEGylation to promote polymeric nanoparticle interactions at the cellular level is a well-defined mechanism. However, certain limitations are also associated with the use of polymers that cannot be avoided including, the high cost of manufacturing add on biological analyses and process development, lack of understanding of the mechanism of degradation leads to a generation of toxic metabolites. Further, the toxicity and stability of polymers in a protein-rich biological medium are still conflicting (Rai et al., 2019).

Notably, some conducted investigations on lipid nanocarriers for gene delivery eliminate all these problems. For instance, a Cationic surfactant composing liposomes conjugated with

lambda DNA exposed to endo and exo-nucleases present in serum remained intact and stable without causing any toxicity. Transfection by liposomes is a well-established technique (Cortesi et al., 1996).

2   MATERIALS

Fe_3O_4- 14-29 nm with purity 99.55 % kind gift sample by Nano Teknoloji bilişim Imalat Ve Danişmanlik Ltd. Şti., Turkey.

Miglyol 812N (tricaprylin; C8/C10 fatty acid triglycerides; caprylic/capric triglycerides; 1,2,3-propanetriyl ester caprylic acid; caprylic acid, 1,2,3-propanetriyl ester; glycerol trioctanoate; glyceryl tricaprylate; octanoic acid, 1,2,3propanetriyl ester) was a gift of Cremer Oleo Division (Witten, Germany). Labrasol® (caprylocaproyl macrogol-8 glyceride; PEG-8 caprylic/capric glycerides) was purchased form Gattefossé (France). The copolymers poly(ethylene glycol)-block-poly(propylene glycol)-block-poly(ethylene glycol) Pluronic F127 (poloxamer 407, p407) (PEO98-POP67-PEO98) was obtained from BASF (Ludwigshafen, Germany). Hyaluronic acid (HA) with molecular weight 300 kDa, was a kind gift of Soliance (Paris, France).

Clark-type oxygen electrode was purchased from UAB "OPTRONIKA", (Vilnius, Lithuania).

Nylon membranes (pore size 200 nm) and dialysis tubing cellulose membrane (size-100 feet, mol wt 12 kDa) were purchased from Millipore Sigma (St Louis, MO, USA). Soybean lecithin (PC) (90% phosphatidylcholine) used for liposome/ ETHO preparation was Epikuron 200 from Lucas Meyer, Hamburg, Germany.

Iron (II) chloride, Iron (III) chloride, Curcumin (CUR), Tween 80, stearic acid, EA, Tritearin, poloxamer 188 (methyl-oxirane polymer, 75:30), Cholesterol (CH), dicetyl phosphate (DCP), didecyldimethylammonium chloride (DDAC), di isobutyl phenoxy ethyl dimethyl benzyl ammonium chloride (DEBDA) and stearylamine (SA), sodium citrate dihydrate, citric acid monohydrate, sodium chloride, 2,2-Diphenyl-1-picrylhydrazyl (DPPH), dimethyl sulfoxide (DMSO) and ascorbic acid. Nylon and polycarbonate membranes (pore size 200 and 50 nm respectively). catalase (CAT) from bovine liver (H_2O_2:H_2O_2 oxidoreductase, mol wt 250 kDa) (CAT) and PER from horseradish (mol wt 44 kDa) (PER) and all other solvents and materials were provided by Merck (Milano, Italy).

3   METHODS

3.1   PRODUCTION OF NANOSYSTEMS

3.1.1   Preparation of MNP

The MNP were synthesized with slight modifications as described by Toledo et al (de Alcântara Sica de Toledo et al., 2018). In detail, the iron (II) chloride and iron (III) chloride (see chapter 4, Table 5) were dissolved into water and the mixture was subjected to magnetic stirring for 30 minutes. The sodium hydroxide was added gradually until the color changes from deep orange to non-uniform black. Then the mixture was centrifuged (Thermo scientific CL31R multispeed centrifuge) at 4000 rpm with a radius 112 for 10 minutes. After removing the supernatant, MNP were congealed at -20°C for 7-8 hours. Finally, the resulting MNP were lyophilized overnight using an Edwards modulyo freeze dryer.

3.1.2   Preparation of lipid nanoparticles

3.1.2.1   Solid lipid nanoparticles by emulsion-dilution technique

Briefly, a mixture of stearic acid and Polysorbate 80 was melted at 80 °C and bidistilled water was heated at the same temperature. Bidistilled water was dispersed into the fused lipid phase to form O/W hot emulsion under sonication for 5 minutes (Branson® ultrasonic cleaner, Opto-lab, MO, Italy). The hot emulsion was diluted with cold bidistilled water under high-speed homogenizer (Ultra Turrax T25, IKA-Werke GmbH & Co. KG, Staufen, Germany) at 11,000 rpm for 10 min. The dilution of the system leads to precipitation of the lipid phase forming fine particles those were stored at room temperature. The composition is reported in chapter 4, Table 6.

In the case of loaded SLN (chapter 4, section 4.2.2), MNP and CUR were added to the lipid phase before the emulsion formation (Sguizzato et al., 2017).

3.1.2.2   Solid lipid nanoparticles by homogenization and ultra-sonication technique

SLN were prepared by a hot homogenization technique based on ultrasound treatment (Esposito et al., 2008). The dispersing phase was an aqueous solution of poloxamer F68 or p188 (2.5% w/w) while the disperse phase was constituted of tristearin (5% w/w, with

respect to the whole weight of the dispersion). Briefly, the p188 aqueous phase (4.75 mL) heated at 80 °C has been added to the molten lipid phase (250 mg) and mixed at 15000 rpm, at 80 °C for 1 min (IKA T25 digital ultraturrax). The obtained emulsion has been submitted to ultrasound homogenization at 6.75 kHz for 15 min (Microson ultrasonic Cell Disruptor-XL Minisonix) and let cooling at 25 °C. SLN dispersions were stored at room temperature.

In the case of CA loaded SLN (see chapter 6 and 8, section 6.2.1 and 8.2.1 respectively), CA (0.1% w/w with respect to the whole dispersion; 2% w/w with respect to the lipid phase) was added to the fused lipid phase before the emulsification step.

3.1.2.3 NLC preparation

NLC were prepared by hot homogenization and ultra-sonication (Esposito et al., 2019b). Shortly, a lipid mixture composed as reported in chapter 5 (Table 11) constituting the 5% by weight as compared to the total weight of dispersions, was melted at 70°C. Then poloxamer 188 aqueous solution (2.5% w/w) was added at the same temperature under 15,000 rpm homogenization for 1 min (Ultra Turrax T25, IKA-Werke GmbH & Co. KG, Staufen, Germany). Afterward, the obtained emulsion was ultrasonicated (MicrosonTM, Ultrasonic cell Disruptor) at 7 kHz for 15 min and cooled down to room temperature.

EA-containing NLC (NLC-EA) were prepared (see chapter 5, section 5.2.1) by adding a DMSO solution of the drug to the molten lipid mixture at 70°C. Afterward, the production protocol proceeded with the addition of the poloxamer aqueous phase as above described. NLC dispersions were stored at room temperature.

3.1.2.4 Miscellaneous techniques

Some other strategies (chapter 4, section 4.2.7) also have been adopted to encapsulate MNP along with slight modifications including as follows and remarks have been given in Table 9.

SLN containing surface-modified MNP (Abidi et al., 2018), Emulsion-diffusion method (Oliveira et al., 2018), hot homogenization technique (Grillone et al., 2015), solvent diffusion method (Ying et al., 2011), microemulsion technique (Peira et al., 2003), air spray technique (Rasekh et al., 2017) and, NLC (de Almeida et al., 2017).

3.1.3 Preparation of liposomes

Plain (phosphatidylcholine, cholesterol, 2:1 molar ratio) and charged (phosphatidylcholine, cholesterol, charged surfactant, 2:1:1 molar ratio) liposomes have been obtained (chapter 9, section 9.2.2) using direct hydration method with slight modifications (Puglia et al., 2010). In detail, liposome dispersions were produced by solubilizing 25 mg/ml lipid phase in methylene chloride/methanol mixture (1:1, v/v). The organic solvent residue was removed using a rotary evaporator under vacuum to attain a thin lipid film, which was subsequently hydrated with 2 ml of sterile water followed by 10 minutes of swirling. Liposomes were then subjected to extrusion to obtain possibly uni-lamellar vesicles with a homogeneous size distribution (Cortesi et al., 2007). For this, the liposomal suspension was subjected to five extrusion cycles through two stacked standard 25 μm diameter polycarbonate filters with 0.2 μm pore size (Nucleopore Corp.) supported by a 25 μm polyester drain disk. 10–20 bars nitrogen pressure has been maintained within an extruder (Lipex Biomembranes, Vancouver, Canada) during the entire process. Finally, liposomes were collected and stored for further studies.

QSi loaded liposomes were prepared (chapter 9, section 9.2.4) using a similar scheme. However, QSi dissolved in the aforementioned organic solvents along with other components to achieve a final concentration of 10 mM in the system.

3.1.4 Preparation of Ethosomes

ETHO preparation was obtained by dropping bidistilled water into an ethanolic solution of PC (30 % w/v) (Sguizzato et al., 2020b). Briefly, water was slowly added to the ethanol phase up to a final 70:30 (v/v) ratio, magnetically stirring the system at 750 rpm (IKA RCT basic, IKA®-Werke GmbH & Co. KG, Staufen, Germany) for 30 min at room temperature in the dark.

In the case of CA (chapter 7 and 8) and MG (chapter 10) containing ETHO (CA-ETHO and ETHO-MG respectively), CA/ MG was added to PC ethanol solution before the addition of water.

Transethosomes loaded with MG have been prepared by incorporating surface activators such as DDAB and Tween 80 (see chapter 10, section 10.2.1).

3.1.5   Preparation of gels

3.1.5.1   Poloxamer (P407) gel

P407 gel was prepared according to the "cold technique"(Esposito et al., 2018). Briefly, a weighed amount of p407 was gradually added to cold water (5-10 °C) under magnetic stirring up to a final concentration of 15 (P15) or 30 (P30) % w/w Poloxamers. The container was sealed and left in a refrigerator overnight at 5 °C. CA-gel, CA loaded nanoparticulate and ethosomal gel were prepared as described in chapter 6 and chapter 7, section 6.2.2 and 7.2.6 respectively).

3.1.5.2   Hyaluronic Acid (HA) gel

Two different methods were used to prepare gels containing HA: a "direct method" and a "dilution method". The "direct method" involved the addition of HA (2% w/v) powder to P15 at 4 °C under stirring as described in chapter 6, section 6.2.2.

The "dilution method" involved preliminary solubilization of HA (300 kDa) in water (4% w/v). The HA solution was then diluted with P30 (1:1, v/v) and maintained at 4 °C on an orbital shaker for 24 hours. CA loaded nanoparticulate gel was prepared as described in chapter 6, section 6.2.2.

3.2   PHYSICAL CHARACTERIZATION

3.2.1   Particle size and Polydispersion Index

Submicron particle size and Polydispersion Index (PI) analyses were performed using a Zetasizer Nano S90 (Malvern Instr., Malvern, England) equipped with a 5 mW helium neon laser with a wavelength output of 633 nm. Plastic-ware was cleaned with detergent washing and rinsed twice with Milli-Q water. Measurements were made at 25 °C at an angle of 90°. Data were analyzed using the "CONTIN" method (Pecora, 2000). The measurements were performed in triplicate.

3.2.2   Zeta potential measurements

Zeta potential values were determined by Zeta sizer ultra (Malvern panalytical Ltd., United Kingdom). For all measurements, water was used as the dispersant with the index of refraction 1.33 and temperature 25° C. Samples were characterized in the disposable folded

capillary cell (DTS 1080, Malvern) and diluted using deionized water. Values were obtained from three independent experiments and performed in triplicates.

These measurements have been performed at Biofilms – Research Center for Biointerfaces, Faculty of Health and Society, Malmö University, Sweden during long-term research mobility (January 2020 to July 2020).

3.2.3 Electron Microscopy
3.2.3.1 Scanning Electron Microscopy

The morphology of MNP and SLN was evaluated by variable-pressure scanning electron microscopy (VPSEM) (Zeiss Evo 40XPV, Carl Zeiss AG, Oberkochen, Germany). A small quantity of various lyophilized SLN and MNP has been taken on the butter paper and a uniform sample layer has been applied on stab by tapping them on the powder for 3-4 times and observed under variable pressure. Elemental analysis of MNP and SLN was done using a scanning electron microscope (SEM) equipped with a microanalytical system energy-dispersive (EDS). The two areas have been selected randomly to investigate the presence of iron inside the lipid core of SLN.

The group of the Electron Microscopy Center of the University of Ferrara (Italy) conducted the analyses.

3.2.3.2 Freeze-fracture electron microscopy

Aliquots of liposome preparations were sandwiched between copper plates and frozen using liquid propane ($-180°C$). Afterward, the holders containing the frozen samples were transferred to a Balzers BAF 400 freeze replica apparatus (Balzers, Liechtenstein) and subjected to fracture at $-150°C$. The samples were immediately replicated with Pt/C (2 nm) at an angle of 45 ° followed by C (20 nm) at an angle of 90 °. After cleaning stripped replicas with 30% sodium hypochloric and potassium dichromate-H_2SO_4 solution followed by distilled water, they were mounted on 300-mesh Ni grids, and visualized after drying by mean of a transmission electron microscope (JEM200 CX, JEOL, Tokyo, Japan). Micrographs were taken randomly within replica regions representative of the sample.

Dr. Markus Drechsler of the University of Bayreuth (Germany) has conducted the analyses.

3.2.3.3 Cryo-Transmission Electron Microscopy (Cryo-TEM)

To vitrify samples for Cryo- TEM, sample droplets (2 µl) were put for some seconds on a lacey carbon filmed copper grid (Science Services, München) (Esposito et al., 2012). Afterward, most of the liquid has been removed by a blotting paper, obtaining a thin film stretched over the lace holes. The rapid immersion of specimen into liquid ethane cooled to approximately 90 K (-180 °C) by liquid nitrogen in a temperature-controlled freezing unit (Leica EMGP, Leica, Germany) instantly allowed their vitrification. All sample preparation steps have been conducted at controlled constant temperature in the Leica EMGP chamber. The vitrified specimen was transferred to a Zeiss/Leo EM922 Omega EFTEM (Zeiss Microscopy GmbH, Jena, Germany) transmission electron microscope using a cryoholder (CT3500, Gatan, Munich, Germany). During the microscopy observations, sample temperature was kept below 100K. Specimens were examined with reduced doses $\approx$1000-2000 e/nm^2 at 200 kV. Zero-loss filtered images have been recorded by a CCD digital camera (Ultrascan 1000, Gatan, Munich, Germany) and analysed using a GMS 1.9 software (Gatan, Munich, Germany).

Dr. Markus Drechsler of the University of Bayreuth (Germany) has conducted the analyses.

3.2.3.4 Transmission Electron Microscopy (TEM)

For TEM analyses, CA-SLN and CA-ETHO were negatively stained by depositing a drop of sample on a TEM screen covered with a Formvar film (Media System Lab S.r.l. Macherio, MB, Italy). After 1 min, the excess drop was removed from the screen with filter paper, in order to keep a very light veil of sample on the supporting substrate. A drop of 2% phosphotungstic acid was placed on the screen for 1 min and then removed with filter paper, to surround the particles of the preparation deposited on the screen and adhere to their surface. The screen prepared in this way was observed with a ZEISS EM 910 transmission electron microscope (Carl Zeiss Microscopy, GmbH, Munich, Germany).

Paola Boldrini has done the TEM analysis and imaging at the Electron Microscopy Center of the University of Ferrara, Italy.

3.2.4   Small-angle X-rays scattering (SAXS)

Samples were placed into PCR tubes in an automated sample changer and then transferred to a temperature-controlled quartz capillary and exposed for 1s, acquiring 30 frames at 35 °C to check equilibrium conditions and to eventually monitor radiation damage. Data collection was performed using a Pilatus Dectris 2 M detector. The X-ray wavelength λ was 0.10 nm and the explored Q-range (Q is the modulus of the scattering vector, defined as $4\pi \sin \theta/\lambda$, where 2θ is the scattering angle) was 0.1 to 4.4 nm^{-1}. 2D data were corrected for background, detector efficiency, and sample transmission and then radially averaged to derive I(Q) vs. Q curves (Barbosa et al., 2010).

SAXS experiments were conducted by the group of Prof. Mariani of Università Politecnica delle Marche (Italy) and Nikul Khunti at the bioSAXS beamline B21 of Diamond Light Source (Harwell, United Kingdom).

3.2.5   Rheological studies

Rheological measurements were performed with an AR-G2 controlled-stress rotational rheometer (TA Instruments, New Castle, DE, USA) (Sguizzato et al., 2020a). The geometry used was an aluminum cone-plate with a diameter of 40 mm, an angle of 1° and a truncation of 28 μm, equipped with a solvent trap to prevent solvent evaporation during the experiments. The viscoelastic properties of the gels (elastic modulus G' and viscous modulus G'') were assessed in oscillation mode. The oscillation frequency was set at 1 Hz and the deformations applied were all in the linear regime. Temperature ramps from 5 °C to 50 °were obtained at a temperature rate of 1 °C/min and were controlled by a Peltier plate. Before starting the experiments, a 2-min conditioning time at 5 °C was applied. Measurements were performed thrice at least for each sample, to ensure reproducibility.

The experiments were conducted by the group of Prof. Nicolas Huang of the Institut Galien Paris-Sud (University of Paris-Sud) (France).

3.2.6   Lyophilisation and reconstitution of solid lipid nanoparticles

For lyophilization of the SLN, a 10% w/w trehalose has been selected concerning the total weight of the final preparation. To check the stability of lyophilized SLN, they have

undergone reconstitution with MilliQ water as the same weight of preparation before lyophilization. All vials were kept undisturbed for 5 minutes to ensure proper wetting of the cake and the reconstitution time for each formulation has been recorded. Finally, the physical stability of reconstituted SLN has been analyzed for 30 days with diameter measurements.

3.2.7 Deformability

Deformability measurement of ethosomal vesicles was done by an extrusion method (Jain et al., 2007). Ethosomal dispersions (ETHO, CA-ETHO) and ethosome gels (ETHO-pol and CA-ETHO-pol) were extruded through polycarbonate filter membrane (pore diameter 50 nm) using stainless steel, 25-mm diameter filter holder (extruder, Lipex Biomembranes, Vancouver, BC, Canada), applying 2.5 bars of pressure at 25 °C. The volume of ETHO formulation extruded in 1 (ethosome dispersions) or 25 (ethosome gels) min was measured. Vesicle size has been measured by PCS before and after the extrusion. The deformability of the vesicles membrane was calculated according to the following equation:

$$Def = J \times (rv/rp) \qquad (1)$$

Where, Def is the vesicle deformability; J is the ratio between the volume of extruded formulation (mL) and the time of extrusion (min); rv is the vesicle size (after extrusion); and rp is the pore size of the filter membrane.

3.2.8 Spreadability studies

The spreading capacity of P, P-CA, P-HA and P-H-CA was evaluated at ambient temperature (25 °C) 48 h from gel preparation (Esposito et al., 2015). Precisely, 100 mg of gel were placed on a Petri dish (3 cm diameter) then subjected to pressure by a glass dish carrying a 50-g mass. The time taken by the gel to fill the entire dish was measured. The spreadability test was performed three times and the mean values ± standard deviations were calculated using the following equation:

$$S = m \times l / t \qquad (2)$$

where S is the spreadability of the gel formulation, m is the weight (g) tied on the upper plate, l is the diameter (cm) of the glass plates, and t is the time (s) taken for the gel to fill the entire diameter (Esposito et al., 2015).

3.3   DRUG CONTENT

3.3.1   Encapsulation efficiency and loading capacity

The encapsulation efficiency (EE) of CUR in SLN, EA in NLC, CA in SLN or ETHO, QSI (CDC & PF) in liposomes, MG in ETHO were determined as described (Esposito et al., 2019b). A 0.5 mL aliquot of each type of dispersion was poured into a centrifugal filter (Microcon centrifugal filter unit YM-10membrane, NMWCO 10 kDa, Sigma-Aldrich, St. Louis, MO, USA) and centrifuged (Spectrafuge™ 24D Digital Microcentrifuge, Woodbridge, NJ, USA) at 8,000 rpm for 20 min. The amount of entrapped drug was determined after solubilizing the lipid phase with a known amount of methanol in case of SLN, NLC and ethanol in case of ETHO, liposomes (1:10 v/v) and kept under stirring for 3 or 0.5 hours. Whereas the amount of free drug was determined in the filtered aqueous phase. The samples were then filtered through 0.45/ 0.22 μm membrane pore size and analyzed by HPLC. All data were the mean of 6 determinations on different batches of the same type of dispersion.

Firstly, the EE was calculated as:

$$= \text{amount of drug detected in lipid phase} \times 100/\text{Total amount of drug employed} \qquad (3)$$

Secondly, the amount of free drug was calculated as:

$$= \text{Total amount of drug employed- amount of free drug detected / total amount of drug employed} \times 100 \qquad (4)$$

Thirdly, loading capacity was calculated as:

$$= \text{amount of drug detected/ amount of lipid phase} \times 100 \qquad (5)$$

3.3.2   Shelf-life studies

Shelf-life stability studies in case of EA-NLC were conducted in triplicate by analyzing at predetermined times, the physical aspect, the drug entrapment and the size of NLC dispersions up to 2 months from production.

Particularly, physical stability studies were performed analyzing macroscopic aspect (phase separation, turbidity and macroscopic viscosity) under visual inspection; the drug entrapment was analyzed by HPLC as above described while the size was by PCS analyses as above indicated.

Chemical stability was evaluated determining EA content by HPLC analyses (see above), thus shelf-life values were calculated as described by and summarized below.

Log (EA residual content, %) was plotted against time allowing the calculation of the slopes (m) by linear regression. Afterwards, the slopes (m) values were used for the determination of k values applying the equation.

$$K = m \times 2.303 \qquad (6)$$

Shelf life values (the time for 10% loss, t_{90}) and half-life (the time for 50% loss, $t_{1/2}$) were then calculated by mean of equations, respectively.

$$t_{90} = 0.105/ K \qquad (7)$$

$$t_{1/2} = 0.693/ K \qquad (8)$$

3.3.3 Solubility and stability evaluation

The solubility of CA was determined by saturating water, or ethanol/water 30:70 solution, with an excess of drug in sealed glass vials, at 22 °C. The obtained saturated solutions were horizontally shaken at 300 rpm for 8 h, in the dark and centrifuged at 3000 g for 15 min. The supernatant was withdrawn and filtered through a regenerate cellulose filter membrane, 0.22 μm pore size, 25 mm diameter (Millipore-Sigma-Aldrich Merck, Darmstadt, Germany). CA concentration was determined by mass spectrometry analysis as below reported. In order to detect CA chemical stability, 1 ml samples of CA-SOL were stored in different conditions, namely at 4, 22 and 40 °C for 30 days.

Stability profiles were evaluated by mathematical modelling, particularly the following mathematic models were applied to the percentage of a residual drug as follows (Permana et al., 2020):

$$\text{Zero order: Qt = Q0 + K t} \tag{9}$$

$$\text{First order: lnQt = lnQ0 - K t} \tag{10}$$

where Qt (%) is the percentage of residual drug at time t, Q0 is the initial value of Qt, t is the time, and K is the coefficient corresponding to zero or first-order kinetic models.

Further, the physical-chemical stability of Nano systems stored at 22 °C for 6 months was investigated. Particularly size stability was determined by PCS periodically, evaluating Z-average diameter and dispersity index of SLN, CA-SLN, ETHO and CA-ETHO. To evaluate CA chemical stability, its content was quantified by disaggregation of CA-SLN with methanol (1:10 v/v), or dilution of CA-ETHO with ethanol, (1:10 v/v), and kept under stirring for 2 or 0.5 h, respectively. A CA-SOL (0.5 mg/ml) (CA-water) was taken as control. After sample filtration by nylon syringe filters (0.22 μm pores), the amount of CA has been analyzed by HPLC, as below reported.

3.4 ANTI-OXIDANT ACTIVITY

3.4.1 DPPH (2, 2-diphenyl-1-picrylhydrazyl) assay

DPPH radical-scavenging assay is widely used to rapidly evaluate antioxidant capacity (Blois, 1958) and in particular, it is ideal for phenolic compounds. This assay allows measuring the hydrogen donation ability of an antioxidant to convert the stable DPPH free radical into 1, 1-diphenyl-2-picrylhydrazyl, which is accompanied by a colorimetric reaction from deep-violet to light-yellow, which can be evaluated by measuring the percentage reduction of the absorbance of the solution at 517 nm after the radical reaction with the products to be tested. The percentage of radical scavenging capacity was calculated using an equation.

$$\text{DPPH radical-scavenging capacity (\%) = [1- (A1 – A2/A0] × 100} \tag{11}$$

Where, A0 is the absorbance of the control (without EA), A1 is the absorbance in the presence of the EA, and A2 is the absorbance without DPPH. To a methanol solution of DPPH (1.5 mL) 0.750 mL of EA (solution or NLC in DMSO) at different concentration were added. The absorbance at 517 nm was measured with a UV-VIS spectrophotometer (Jenway

7305 Spectrophotometer) according to a described procedure (Wang et al., 1998) Results were expressed as μmol Trolox equivalent/g of compounds.

In the case of CA, the absorbance of the sample (DPPH solution plus CA-SLN or CA-ETHO or CA-SOL). The ability to scavenge the DPPH• was evaluated using different sample concentrations. Particularly, the IC50 values (i.e. the sample concentration required to scavenge 50% of the DPPH-free radicals) were obtained, expressing values as ascorbic acid equivalents, by linear regression analysis. The absorbance values have been measured with Safire plate reader (Tecan Trading AG, Switzerland), the IC50 for ascorbic acid was roughly 6.1 μg/ml (Hallan et al., 2020)

Also, the total antioxidant value of CA-ETHO and CA ethanol solution has been measured by photo chemiluminescence assay using Photochem, ACL kit (Analytica Jena AG, Germany). The antioxidant values of the samples were determined following the manufacturer's instructions, the results have been expressed in terms of trolox equivalents (TE) (Dhavamani et al., 2014).

3.4.2 FRAP assay

The FRAP method is a quantitative assay for measuring the ferric ion reducing the ability of plasma and is based on the reduction of ferric ions (Fe^{3+}) to ferrous ions (Fe^{2+}) under acidic conditions in the presence of 2,4,6-tripyridyl-s-triazine (TPTZ) (Benzie and Strain, 1996). In the presence of an antioxidant, the Fe^{3+}–TPTZ complex is reduced to the ferrous form, corresponding to an intense blue coloration that is read to a fixed wavelength of the absorption maximum (593 nm). The antioxidant activity has given as μmol Trolox equivalent/g of compounds, as this standard was used to perform the calibration curves.

3.5   ANALYTICAL TECHNIQUES
3.5.1   Ultra-violet spectrophotometric method

The UV-Spectrophotometer (Perkin Elmer, UV/ VIS/ NIR spectrophotometer, lambda19) has been used for the analysis of MG. The absorption values (n=5) have been taken for each analysis, which were corresponding to the maximum absorption of MG (255 nm).

3.5.2 High-performance liquid chromatography (HPLC) analysis

HPLC determinations were performed using a HPLC system (1200 Series, Agilent Technologies, USA) equipped with an isocratic pump, an UV-detector and a 7125 Rheodyne injection valve with a 50 µl loop. Each injection was performed in triplicate (n=3) and compared with standards of known concentration.

Details of HPLC conditions for each drug studied are below reported in Tables 2 to 4.

3.5.2.1 Curcumin

Table 2. HPLC analysis method for curcumin.

Specifications	Details
Column	C18 RP-column (Kinetex® (5 µm) 4.6 × 150 mm)
Mobile phase	Acetonitrile, acetic acid, methanol 65:30:5 v/v/v
Flow	0.5 ml/ min
Injection	50 µl
Wave length	425 nm
Retention time	3 min

3.5.2.2 Ellagic acid

Table 3. HPLC analysis method for ellagic acid.

Specifications	Details
Column	C_{18} RP-column (Kinetex® (5 µm) 4.6 × 150 mm)
Mobile phase	Methanol, water and phosphoric acid 55:45:0.1 v/v/v
Flow	0.6 ml/min
Injection	40 µl
Wave length	254 nm
Retention time	5.9 min

3.5.2.3 Caffeic acid

Table 4. HPLC analysis method for caffeic acid.

Specifications	Details
Column	C_{18} RP-column (Grace® - Platinum (5 µm) 4.6 x 150 mm)
Mobile phase	Water, acetonitrile, 80:20 v/v, pH 2.5
Flow	0.7 ml/ min
Injection	50 µl
Wave length	325 nm
Retention time	4.5 min

3.5.2.4 Quorum sensing inhibitors (CDC & PF)

Reverse-phase high-performance liquid chromatography (RP-HPLC) analyses of QS inhibitors containing LP-SA have been performed on a Beckman HPLC System Gold equipped with a 126 Solvent Module and a UV detector Module 168. In the case of CDC, samples have been loaded on a stainless steel Zorbax® C_{18} (4.6 x 150 mm,) packed with 3.5 µm particles (Agilent, Santa Clara CA, USA), while for PF, samples on a stainless steel Kinetex C_{18} (4.6 x 150 mm,) packed with 5 µm particles has been used (Phenomenex Inc., Torrance CA, USA). The compounds have been monitored at 220 nm using a linear gradient from 0% of solvent A (water containing 0.1% TFA) to 100% solvent B (acetonitrile containing 0.1% TFA) over 25 min at a flow rate of 0.7 ml/min in the case of CDC (retention time 5.7 min) and at 0.5 ml/min flow rate in the case of PF (retention time 16.89 min). Data acquisition and processing were performed using 32Karat 8.0 software. The method was validated for linearity ($R2 = 0.995$), repeatability (relative standard deviation 0.02%, n=6 injections) and limit of quantification (0.04 µg/ml). Analyses were conducted in triplicate, mean and standard deviation values were calculated.

3.5.3 Mass spectrometry

The CA concentration was determined weekly by a LC-MS/MS system (Thermo Scientific, Waltham, MA, USA) composed of a micro HPLC Surveyor Plus (pump, column, thermostated compartment, autosampler, and solvent delivery system) and a LTQ XL mass spectrometer according to a previously developed method (Bergantin et al., 2017).

CA was separated by HPLC under gradient elution condition with H_2O + 0.1% v/v formic acid and acetonitrile + 0.1% v/v formic acid as mobile phases. Flow rate was 150 μl/min and gradient was 5-30% acetonitrile in 20 min. Chromatographic column was a Symmetry (Waters) 100 x 2.1 mm, packed with 3 μm fully porous particles and thermostated at 25 °C. Main MS conditions were as following: capillary temperature 275 °C; sheat gas 40 au; source voltage – 4.00 kV; capillary voltage – 6.00 V; tube lens – 47.20 V. Detection of CA was performed by selected reaction monitoring (SRM) mode. The SRM detection was operated in the negative electrospray ionization mode using the transitions m/z 179 ([M - H] –) → 135.

3.5.4 Gas chromatographic analysis

After ETHO preparation, the ethanol presence was checked by gas-chromatographic analysis (Agilent G4407) equipped with a thermal conductivity detector and a Restek Porapak Q porous polymers packed column (80/100 mesh, 20 m): carrier gas flow rate was set at 200 kPa; injector temperature was 200 °C; column temperature was 150 °C; detector temperature was 180 °C. One microliter of 1:10 diluted ETHO sample (n = 3) was injected and ethanol (retention time around 3.3 min) was determined by external calibration (Weatherly et al., 2014).

The mass spectrometry and gas chromatographic analysis were conducted with the help of Prof. Nicola Marchetti, Department of Chemical and Pharmaceutical Sciences, University of Ferrara, Italy.

3.6 IN VITRO ANALYSIS
3.6.1 In vitro diffusion studies

CA diffusion from SLN /ETHO or their respective gels, while EA diffusion from NLC was studied using Franz diffusion cells supplied by Vetrotecnica (Padua, Italy) and associated to nylon membranes (pore diameter 0.2/0.45 μm). The membrane, previously hydrated for 1 h, was mounted on the lower receiving section of the cell previously filled with 5 ml of bidistilled water in case of CA and ethanol and phosphate buffer 60 mM (30:70, v/v) alternatively at pH 7.4 or pH 5.5 in case of EA . This solution was stirred at 500 rpm by a magnetic bar and thermostated at 32 ± 1°C (Puglia et al., 2010). After mounting the upper donor section on the lower by mean of a clamp, 1 ml of each formulation was poured on the

membrane surface. The donor compartment was then sealed to avoid evaporation. Two hundred microliters samples of receiving phase were withdrawn at predetermined time intervals (1-8 h) and analyzed for CA/ EA content using HPLC. Each removed sample was replaced with an equal volume of receiving phase. The CA/ EA concentrations were determined six times in independent experiments and the mean values ± standard deviations were calculated. The mean values were then plotted as a function of time. Flux values were computed from the slope of the linear portion of the accumulation curves, while D were calculated dividing fluxes by the CA/ EA concentration (mg/ml) in the analyzed form.

3.6.2 In vitro release studies

In vitro release studies were performed by dialysis using dialysis membranes (Merck Millipore, Milan, Italy) with 15000 Da cut-off. Sink conditions and QSi solubilization were established adding 30% methanol by volume to the aqueous receiving phase (Siewert et al., 2003). 20 ml of receiving phase was poured in the external compartment and continuously stirred at 500 rpm with a magnetic bar (see chapter 9, section 9.2.5.). 2 ml of each QSi loaded LP-SA were placed in the dialysis bag then at predetermined time intervals 0.15 ml of receiving phase were withdrawn and QSi content was evaluated by HPLC as above reported. Each removed sample volume was replaced with the same amount of fresh receiving phase.

3.6.3 Skin Resistance measurements

Skin resistance measurements (see chapter 8, section 8.2.9) have been conducted using electrochemical impedance spectroscopy (EIS). The measurements have been made with the skin membrane mounted in Franz diffusion cell (PermeGear Inc. Hellertown, PA, USA) equipped with 4 electrodes (Björklund et al., 2013). Briefly, impedance measurements were carried out using potentiostat from Ivium Technologies (Eindhoven, Netherlands) within a frequency range 0.1 Hz-1M Hz and 10 mV voltage amplitude. The temperature 32 ± 1 °C has been maintained throughout the measurements. The interactions of SLN and ETHO with skin membrane were evaluated measuring skin membrane resistance. The donor chamber was filled with citrate buffer saline (CBS, 10 mM sodium citrate dihydrate, citric acid monohydrate, and 150 mM sodium chloride, pH 5.5) (SC site of skin), while phosphate buffer saline (PBS, sodium chloride-disodium hydrogen phosphate-potassium chloride-potassium dihydrogen phosphate (1:1:1:1), pH 7.4) was poured in the receptor chamber

(dermal part of the skin) to mimic physiological conditions. The impedance spectra of skin membrane were recorded for 30 min (5 min interval); afterward CBS was replaced by SLN or ETHO. The impedance measurements were then carried on for 70 min in the presence of the nanosystems. Lastly, SLN or ETHO were again replaced by CBS, followed by a recording of impedance data for 20 min. Alterations in skin and solution resistance were evaluated using a data analysis program included in Ivium Potentiostat software. Specifically, skin resistance was determined by fitting impedance vs frequency data to an equivalent circuit considering the solution resistance, (Rsol), connected in series with skin membrane impedance. The skin membrane impedance was represented as a parallel combination of a resistor (for skin membrane resistor, Rmem) and a constant phase element (CPE). The change in skin membrane resistance (Ohm) was plotted vs time (min).

These measurements have been obtained from Biofilms – Research Center for Biointerfaces, Faculty of Health and Society, Malmö University, Sweden during long-term research mobility (January 2020 to July 2020)

3.6.4 In vitro assessment of CA-hydrogen peroxide reactions in the skin using SCOE

A SCOE apparatus was employed as previously described with some modification (Hallan et al., 2020; Nocchi et al., 2017). Briefly, an oxygen electrode was covered with excised porcine skin membrane (500 μm thickness, 16 mm diameter) and fixed by rubber o-ring. Amperometric measurements were performed under immersion of the assembled SCOE into an electrochemical measurement glass cell containing 10 ml of CBS (10 mM sodium citrate dihydrate, citric acid monohydrate, and 150 mM sodium chloride, pH 5.5) under constant agitation with magnetic stirrer. The current of the electrode was recorded using AMEL model 2059 potentiostat/galvanostat (AMEL, Milano, Italy) by applying -0.7 V (vs Ag/AgCl) on the Pt electrode of the oxygen electrode. After achieving the stable baseline, the response to 0.5 mM H_2O_2 was recorded, and CA (0.5 mM) in ethanol:CBS (30/70 v/v) solution (CA-SOL), SLN, CA-SLN, ETHO and CA-ETHO were measured. All measurements were conducted at 32 °C. From the current response of the SCOE, the lag time, t_{lag} (i.e., the period required to establish a linear concentration gradient across the membrane) was calculated. The time zero was assigned to the moment of CA addition into the measurement cell and the delta current values were integrated over the experimental time. The integral vs time curve became linearly dependent on the time when approaching a

steady-state of the current response. This linear part of the integral vs time dependence was fitted to a linear equation and extrapolated towards time-axis. The intercept was taken as a t_{lag} value. The Dapp was calculated according to the following equation:

$$Dapp = d^2/ 6\ t_{lag} \qquad\qquad (12)$$

Where d is the thickness of the stratum corneum, assumed to be 10 μm.

Moreover, SCOE model was modified by replacing skin with dialysis membrane entrapping relevant enzymes to model skin response to the antioxidants in the presence of H_2O_2. The possibility to model skin response with two enzymes, namely CAT and PER, was explored by drop-casting a CAT/PER mixture (1:1, v/v, comprised of 1 mg/mL of each enzyme) onto the tip of oxygen electrode and covered with dialysis membrane (this set-up is referred to as OE). The enzyme-modified oxygen electrode (OE) was then used in measurements in a similar way as SCOE. Compared to SCOE experiments, a lower H_2O_2 concentration, specifically 0.1 mM, was added to CBS pH 5.5, followed by the addition of 0.03 mM of CA-SOL, SLN, CA-SLN and MG-SOL, MG-ETHO. The response of OE was evaluated for each type of nanosystem.

These measurements have been obtained from Biofilms – Research Center for Biointerfaces, Faculty of Health and Society, Malmö University, Sweden during long-term research mobility (January 2020 to July 2020).

3.7 CELL LINE STUDIES

3.7.1 In vitro MTT test

3.7.1.1 Nanostructured lipid carriers with EA and ETHO with MG

HaCaT cells were grown in Dulbecco's modified Eagle's medium High Glucose (DMEM), (Lonza, Milan, Italy), supplemented with 10% FBS (foetal bovine serum), 100 U/ml penicillin, 100 μg/mL streptomycin and 2 mM L-glutamine. Cells were incubated at 37 °C for 24 h in 95% air/5% CO2 until 80% confluence.

The different formulations, namely EA DMSO solution, both types of empty NLC, NLC-EA1 and NLC-EA2, were dispersed in cell culture medium and diluted to reach EA concentrations ranging from 10 to 75 μM. Concerning empty-NLC, they were added

following the same dilution step used for NLC-EA to reach their same content in lipid nanoparticles within the wells.

Similarly, in case of MG, different formulations, namely ETHO/ MG-ETHO, ETHO T80/ MG-ETHO T80, ETHO DDAB/ MG-ETHO DDAB and MG-SOL (MG in ethanol and water) were dispersed in cell culture medium and diluted to reach MG concentrations ranging from 5 to 50 µM.

Seeded cells were exposed to the selected formulations for 24 h, afterward, the treatment was completely removed and 110 µl of MTT (0.5 mg/ml) were added and incubated for 4 h. To convert the MTT solution into a violet-colored formazane, 100 µl of DMSO was subsequently added and incubated for 15 minutes. After shaking, the solution absorbance, proportional to the number of living cells, was measured using a spectrophotometer at 590 nm and, after subtracting background at 670 nm, thus converted into a percentage of viability.

3.7.1.2 Cell culture and cytotoxicity studies on liposomes for QSI

The effect of plain, cationic or anionic liposomes on cell proliferation was determined on in vitro cultured human lung carcinoma A549 cells(ATCC® CCL-185™) (Fahr et al., 2005). Standard conditions for cell growth were D-MEM/F-12 (1:1) (1X), liquid - with L-Glutamine (Invitrogen), medium supplemented with 10% fetal calf serum (Irvine Scientific, Santa Ana, CA) and Pen-Strep 1x (Omega Scientific Inc., Tarzana, CA) in 5% CO2 at 90% humidity. Cell viability was determined by MTT test (3-(4,5-dimethilthiazol-2yl)-2,5-diphenyl tetrazolium bromide) colorimetric assay (Roche Diagnostics Corporation, Indianapolis, IN) following the manufacturer's instructions as previously described (Bortolotti et al., 2015). Cell viability was determined by treating A549 cells with different concentrations of cationic nanocarriers in terms of cationic detergent, from 0 to 25 µM, for 24 h. Afterward absorbance was read at 590 nm.

3.7.2 P. aeruginosa culture and biofilm formation assay

Pseudomonas aeruginosa PAO1 strain was grown at 37 °C in aerobic condition in M9 Minimal Salts medium (Sigma-Aldrich, St Louis, MO, USA). Biofilm studies were performed on planktonic P. aeruginosa PAO1 culture by microtiter plate colorimetric assay

(Chugani et al., 2012). After overnight growth, optical density at 600 nm was assessed to determine bacterial growth. After appropriate dilution in M9 medium, 100 µl of P. aeruginosa suspension was added in each well of a microtiter plate. The optical density (OD600) at inoculation was 0.04. Bacteria were then treated with different concentration (0.1-25 µM) of QS inhibitors, empty liposomes and drug-encapsulated liposomes in triplicates for 24 h or 48 h at 37 °C. Broth without bacteria was used as negative control. Extent of biofilm formation was measured using crystal violet dye. Briefly, after incubation, the wells were washed three times with phosphate-buffered saline (PBS; Sigma-Aldrich) and plate was 60 °C-dried for 90 min. Samples were then stained with 200 µl of crystal violet solution (1%) for 15 min. After incubation, wells were washed several times with tap water to eliminate the excess of dye and the plate air-dried. Then, 100 µl of acetic acid 33% was added to each well to solubilize crystal violet and the absorbance read at 570 nm.

The biofilm formation assay were performed by Dr. Daria Bortolotti and Prof. Roberta Rizzo. Department of Chemical and Pharmaceutical Sciences, University of Ferrara, Italy.

3.7.3   Immunohistochemistry

Paraffin sections of human skin biopsies (4 µm) were deparaffinized in xylene and rehydrated in decreasing alcohol gradients. Antigen retrieval was achieved using heat-based epitope retrieval with 10 mM sodium citrate buffer (AP-9003-500, Thermo Fisher Scientific, USA) (pH 6.0) at a sub-boiling temperature in a 500 W microwave for 10 min. After cooling for 20 min, sections were washed 2 times for 5 min in PBS, blocked with 5% BSA in PBS at RT for 45 min, and incubated overnight at 4 °C with primary antibodies for 4HNE (AB5605 Millipore Corp., USA) at 1:400 dilution in 2% BSA in PBS. The next day, sections were washed 3 times in PBS for 5 min, followed by a 1 h incubation with fluorochrome-conjugated secondary antibodies (A11008 Alexa Fluor 488) at 1:500 dilutions in 2% BSA in PBS at RT, and then washed with PBS 3 times for 5 min. Nuclei were stained with DAPI (D1306, Invitrogen) for 1 min in PBS at RT, and sections were then washed with PBS. The sections were mounted onto glass slides using PermaFluor mounting media (ThermoFisher Scientific) and imaged via epifluorescence on a Leica light microscope equipped at 40x magnification. Images were quantified using ImageJ (Pecorelli et al., 2011).

Dr. Maddalena Sguizzato has performed Immunohistochemistry at the Plants for Human Health Institute of the North Carolina State University (USA).

3.8   IN VIVO TESTS

3.8.1   Patch test

An in vivo irritation test was performed to evaluate the effect of SLN and ETHO applied in single dose on the intact human skin. The occlusive patch test was conducted at the Cosmetology Center of the University of Ferrara, following the basic criteria of the protocols for the skin compatibility testing of potentially cutaneous irritant cosmetic products on human volunteers (SCCNFP/0245/99) (Nohynek et al., 2010; Robinson et al., 2002). The protocol was approved by the Ethics Committee of the University of Ferrara, Italy (study number: 170583). The test was run on 20 healthy volunteers of both sexes, under their written consent to the experimentation, in accordance with The Code of Ethics of the World Medical Association (Helsinki Declaration 1964) and its later amendments for experiments involving humans. Subjects affected by dermatitis, with history of allergic skin reaction or under anti-inflammatory drug therapy (either steroidal or non-steroidal) were excluded. Ten microliters of SLN, CA-SLN, ETHO or CA-ETHO were posed into aluminum Finn chambers (Bracco, Milan, Italy), and applied onto the skin of the forearm or the back protected by self–sticking tape. The samples were directly applied into the Finn chamber by an insulin syringe without a needle and left in contact with the skin surface for 48 hours. Skin irritant reactions (erythematous and/or edematous) were evaluated 15 min and 24 hours after removing the patch and cleaning the skin from sample residual. Erythematous reactions have been sorted out into three groups, according to the erythema degree: light, clearly visible and moderate/serious. The average irritation index was calculated as the sum of erythema and edema scores and expressed according to a scale, considering 0.5 as the threshold above which the formulation is to be classified as slightly irritant, 2.5-5.0 as moderately irritant and 5.0-8.0 as highly irritant.

3.9   EX VIVO TESTS

3.9.1   Human skin explant culture

Human skin explants (HSE) were prepared from the superfluous skin of healthy adult donors (18–60 years old). Breast or abdominal tissue specimens were obtained from patients

undergoing plastic surgery. Skin biopsies (12 mm punches) were cultured into standard 6-well plates in contact with culture medium at 37 °C in 5% CO_2 humidified air. The culture medium was Dulbecco's Modified Eagle Medium (DMEM) with 1% antibiotic-antimycotic solution (10,000 units penicillin, 10 mg streptomycin and 25 μg amphotericin B – Sigma-Aldrich, Germany) and 1% L-glutamine (Sigma-Aldrich, Germany) (Esposito et al., 2015). After 1 day in culture, the medium was changed and HSEs were topically treated with 20 μL of SLN-P-CA for 24 h.

3.9.2   Cigarette smoke exposure

After 24 h of treatment, the HSEs were exposed for 30 minutes to CS generated by burning one research cigarette (12 mg tar, 1.1 mg nicotine) using a vacuum pump, as previously described (Ximena Maria Muresan et al., 2018). Control HSEs were exposed to filtered air. After exposure, the explants were incubated in fresh media at 37 °C in a humidified 5% CO_2 atmosphere for 24 h.

3.9.3   Protein extraction

Samples for Western blot analysis were washed in PBS and frozen in liquid nitrogen. The biopsies were extracted in ice-cold conditions using a tissue protein extraction reagent (T-PER buffer, Thermo Fisher Scientific, MA, USA) added consisting of protease and phosphatase inhibitor cocktails (Sigma, Milan, Italy), using a bead-based homogenizer at 12400 rpm at 4 °C for 15 min. The protein concentration was measured by the Bradford method (BioRad, CA, USA) (Kulkarni, 2012).

3.9.4   Western blot analysis

The samples (20 μg protein) were loaded onto 12% sodium dodecyl sulfate polyacrylamide gel (SDS-PAGE) and then transferred onto nitrocellulose membranes. Blots were blocked in PBS containing 0.5% Tween 20 and 5% not-fat milk (BioRad). The membranes were incubated overnight at 4 °C with the appropriate primary antibody HO-1 (Abcam, Cambridge, UK). The membranes were then incubated with horseradish PER conjugated secondary antibody for 90 min at RT, and the bound antibodies were detected in a chemiluminescent reaction (ECL, BioRad). Chemiluminescence was detected on a ChemiDoc imager (BioRad) (Ximena M. Muresan et al., 2018). The blots were reprobed

with β-actin as the loading control. Images of the bands were digitized, and the densitometry of the bands was performed using ImageJ software (Valacchi et al., 2017).

Dr. Maddalena Sguizzato has performed ex-vivo studies at the Plants for Human Health Institute of the North Carolina State University (USA).

3.10 DATA ANALYSIS AND STATISTICS

For each of the variables tested, two-way analysis of variance (ANOVA) was used. A significant result was indicated by a p value <0.05. All the results are expressed as mean ± SD of 6 determinations for nanoparticle characterization experiments and 3 determinations obtained in 3 independent experiments for in vitro cultured cells tests.

4 DEVELOPMENT AND CHARACTERIZATION OF LIPID COATED MAGNETIC NANOPARTICLES

4.1 INTRODUCTION

The utilization of functionalized superoxide paramagnetic iron oxide nanoparticles (SPION) with magnetic properties offers a new promising direction towards theranostic aids (the combination of both diagnostic and therapeutic applications). They work under influence of the external magnetic field. To attain Para-magnetism, the diameter of such MNP should be below 20 nm. It has long been a scientific and technological challenge to synthesize these systems by avoiding particle aggregation, achieving the desired particle shape and uniform size distribution. The toxicity associated with these particles is the main concern and the extent of biocompatibility highly depends on the nature of the magnetic content, final NP size and the nature of the coating. Therefore, non-toxic surface coatings should be required for the MNP to improve their in-vivo effectiveness (Akbaba et al., 2017). The surface modification of these particles will be helpful not only to stabilize the colloidal system; but will also solve the shortcomings with their biocompatibility by enhancing the circulation time. Additionally, the ligand approach can provide improved site-specificity with minimal drug load in cancer management (Luchini and Vitiello, 2019).

MNP coated with polyarabic acid and functionalized with doxorubicin presented excellent membrane permeation properties. The remarkable drug loading and release behavior, insignificant in-vivo toxicity, and favorable therapeutic potential concerning commercially available clinical MRI contrast agents (Patitsa et al., 2017). MNP were chosen to fabricate the markers and modified to enhance the lipophilicity by incorporating them into the lipid phase. Under Magnetic Resonance Imaging (MRI), the bio-distribution pattern of these lipid nanoparticles has been studied. Owing to their soft surfactant and lipid shell, adequate stability resulted in satisfying magnetite release across an injured Brain–Blood Barrier (Igartua et al., 2002).

Another study has been conducted where the self-assembled lipid nanotubes (LNTs)with glycolipid composing of glucose and oleic acid, have been used as a coating material. The LNTs were also able to maintain their morphology in warm water because they form crystals

below the gel-to-liquid crystalline transition temperature. The proposed coating has avoided the strong aggregation tendency of the MNP. This strategy has presented tremendous dispersibility and biocompatibility (Han et al., 2012).

Further, the loading of MNP and drug molecule together into SLN could also be a possible solution to the above-mentioned problem. This synergism will accomplish the theranostic effectiveness as shown in Figure 9, where the drug can release under the influence of the alternating magnetic field.

● Lipid-coated MNPs   Drug release

(a)   **(b)**
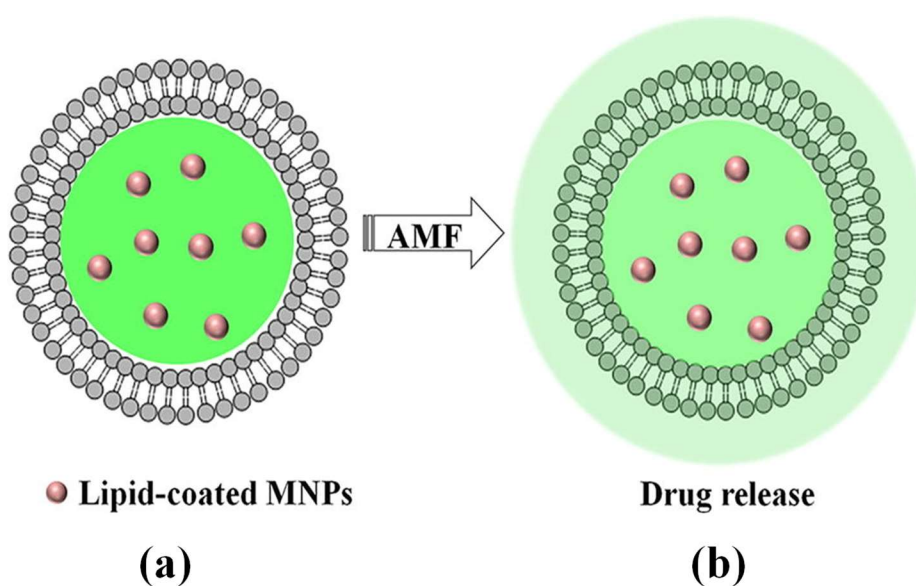
Figure 9. Release of drug from magnetic-lipid nanoparticles under magnetic field.

The magnetic solid lipid nanoparticles (M-SLN) loaded with ibuprofen were successfully fabricated using the emulsification dispersion-ultrasonic technique. This particulate system have shown 80% drug encapsulation. Further, the loaded MNP inside the core have been verified with TEM analysis. This study indicates the possibility to achieve a controlled drug release with MNP (Pang et al., 2009).

This investigation aimed at exploring the possibility of combining the advantages of both SLN and MNP for better drug targeting. MNP and SLN have been fabricated using the co-

precipitation method and emulsion followed by the dilution technique respectively. After optimizing blank SLN, successful loading of MNP have been achieved and the presence of MNP inside the core of SLN have been assured by elemental analysis. Separately, schemed SLN also have been optimized for CUR and evaluated for various parameters.

4.2   RESULTS AND DISCUSSIONS

4.2.1   Preparation of MNP

The MNP have been produced along with composition (Table 5) and their macroscopic and microscopic aspects have been characterized. The MNP were dark brown in appearance (Figure 10 (a)) and no alteration in color has been observed during the entire storage time. The SEM images of MNP has been shown in Figure 10 (b).

Table 5. Composition of MNP.

Sample no.	Components	% W/W
1	$FeCl_3$ (Fe^{2+})	1.97
2	$FeCl_2$ (Fe^{3+})	3.2
3	NaOH	Traces
4	H_2O	95

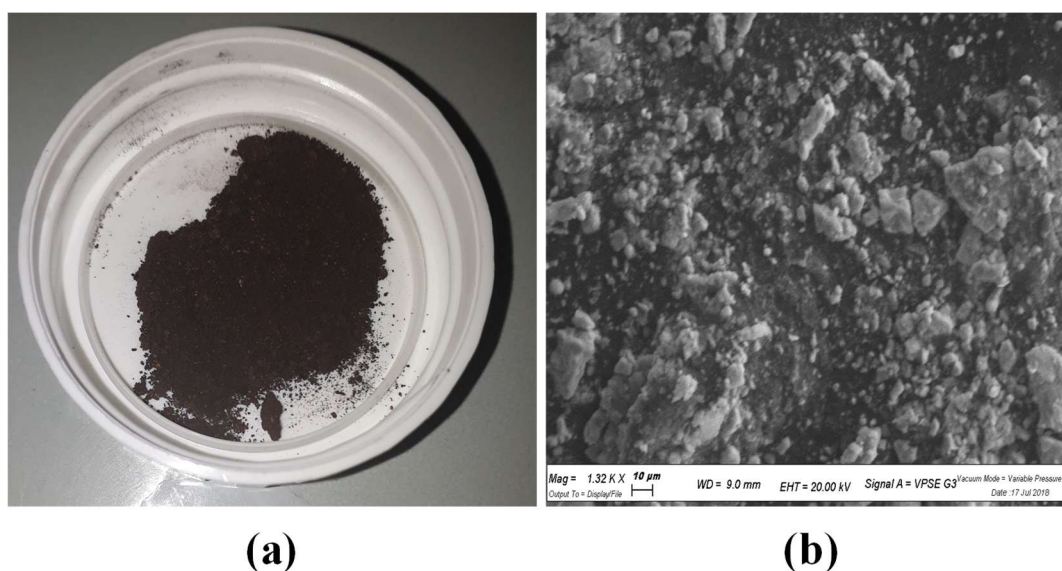**(a)**   **(b)**

Figure 10. (a) Physical appearance and **(b)** SEM image of MNP.

4.2.2 Preparation of solid lipid nanoparticles

The empty SLN (F-SLN) have been produced by the emulsion-dilution technique as per composition (Table 6) and were found physically stable in terms of dimensions during storage. Further, the loading of MNP into SLN have been accomplished after optimizing the empty SLN system. However, the settlement of MNP have been observed at bottom of vials during storage time. The possible reason for this settlement could be an inadequate ratio of lipid to MNP. It must be underlined that the brown color of M-SLN (Figure 11, b-d) unlike the empty SLN (Figure 11, a), indicates that MNP have been loaded into the SLN up to some extent.

Table 6. Percentage (% w/w) composition of SLN.

	SA[1]	P80[2]	Aqueous Phase		CUR	MNP
			80°C	4°C		
F30M-SLN	0.86	1.43	21.94	75.76	-	0.08
F70M-SLN	2	3.34	21.26	73.40	-	0.08
F100M-SLN	2.85	4.77	20.74	71.63	-	0.08
CUR-SLN	2	3.34	21.26	73.40	0.05	-

[1]Stearic acid, [2] Polysorbate 80.

To verify this point, three different ratios of lipid phase to MNP were selected namely F30M-SLN, F70M-SLN, F100M-SLN for 30:1, 70:1, and 100:1 w/w receptively. On the other hand, CUR loaded SLN were produced and were macroscopically stable (Figure 11, e) without undergoing phase separation or aggregation. The CUR-SLN gave the yellowish appearance verifying the presence of CUR distributed uniformly throughout the system.
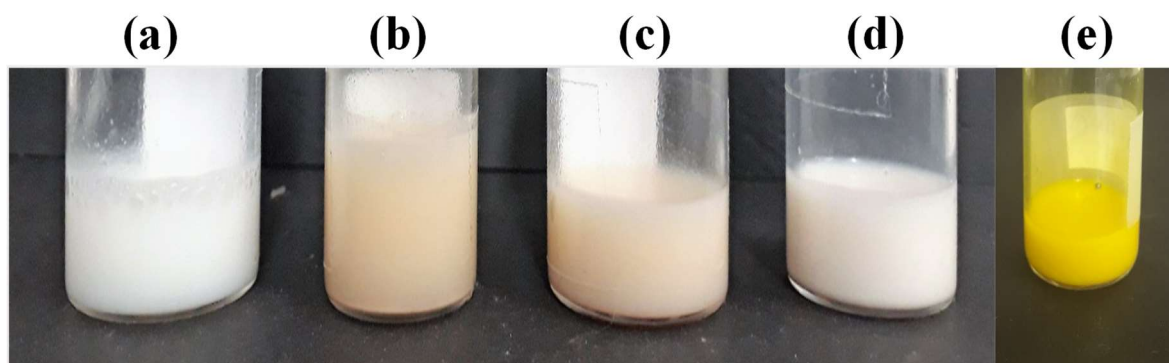
Figure 11. Macroscopic aspects of **(a)** F-SLN, **(b)** F30M-SLN, **(c)** F70M-SLN, **(d)** F100M-SLN, and **(e)** CUR-SLN.

4.2.3 Particle size and Polydispersion Index

The diameter of all SLN was measured using PCS from day 1 to day 90 reported in Table 7. No drastic change in diameter has been noticed during the entire storage period. Moreover, PCS analysis evidenced a monomodal size distribution, indicated by dispersity indexes below 0.3 in all cases.

Table 7. Dimensional distribution parameters of SLN, M-SLN, and CUR-SLN.

Day	F-SLN Z ave (nm) *P.I.*	F30 M-SLN Z ave (nm) *P.I.*	F70 M-SLN Z ave (nm) *P.I.*	F100 M-SLN Z ave (nm) *P.I.*	CUR-SLN Z ave (nm) *P.I.*
1	537.9 ± 38.9 *0.20*	702.9 ± 222.6 *0.10*	597.17 ± 118.7 *0.14*	546.3 ± 37.5 *0.13*	480.3 ± 59.9 *0.18*
30	583.3 ± 84.7 *0.21*	760.5 ± 30.62 *0.14*	598.33 ± 212.5 *0.10*	590.3 ± 65.1 *0.18*	477.5 ± 47 *0.12*
60	547 ± 84.1 *0.15*	724.4 ± 141.6 *0.21*	413.9 ± 179.9 *0.16*	522.1 ± 67.3 *0.28*	413.8 ± 68.0 *0.17*
90	513.8 ± 109.1 *0.19*	674.8 ± 32.6 *0.34*	344.63 ± 79.6 *0.13*	459.3 ± 41.5 *0.12*	413.7 ± 63.6 *0.21*

4.2.4 Morphology and elemental analysis of nanoparticles

The morphology of SLN and MNP has been investigated with the VPSEM technique. Initially, liquid and lyophilized samples of SLN have been tested under VPSEM. However, it was not feasible to analyze the samples. For better visualization, all the samples have been

lyophilized with 10% Trehalose (cryo-protectant). The lyophilization along with cryo-protectant has given better result quality. The 100:1 (lipid phase: MNP w/w) has represented better particle morphology (Figure 12).

Additionally, the elemental analysis has been performed by VPSEM equipped with microanalytical energy dispersive system in Figure 13. Wherein, the empty SLN shows the presence of carbon $64.2 \pm 0.2\%$ and oxygen $35.8 \pm 0.2\%$ by weight, while M-SLN evidenced by 51.6 ± 0.3 %, oxygen 48.2 ± 0.3, and 0.2 % iron. This analysis assured the successful entrapment of iron inside the lipid core.

(a)   **(b)**

(c)   **(d)**
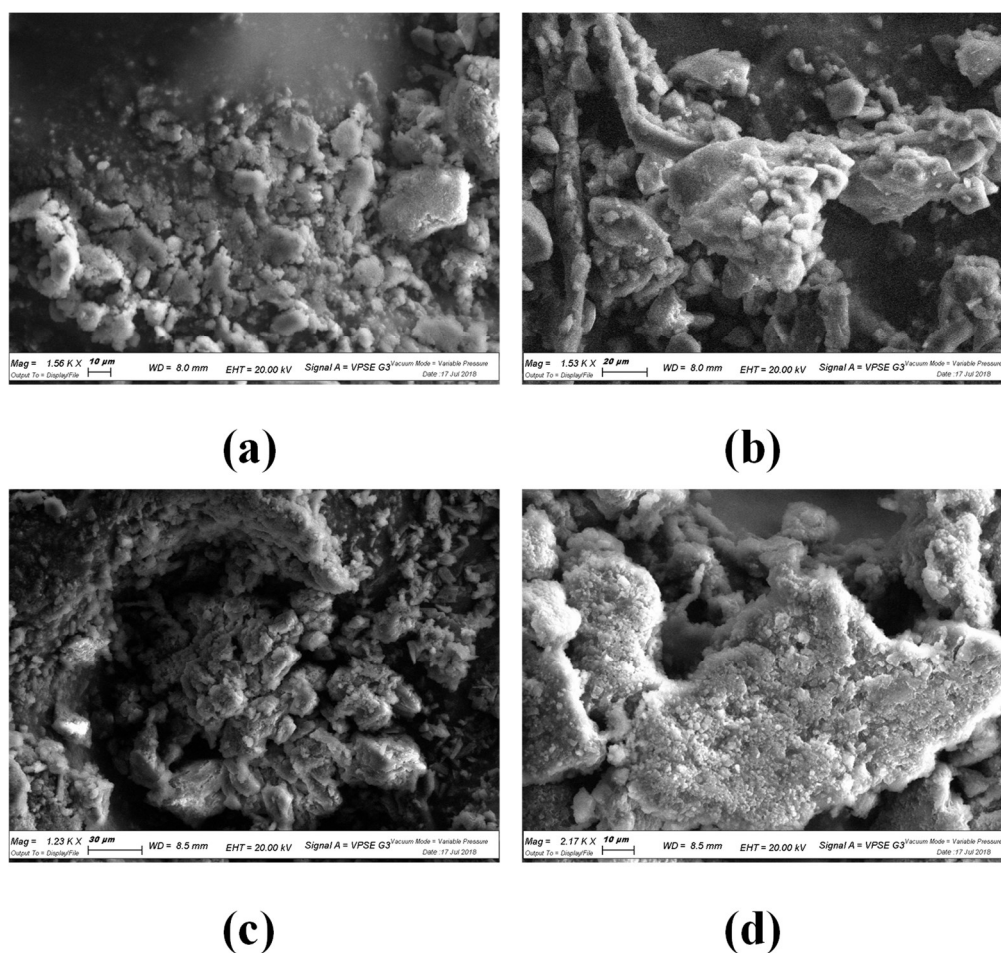
Figure 12. SEM images of **(a)** F-SLN, **(b)** F30M-SLN, **(c)** F70M-SLN, **d)** F100M-SLN.

4.2.5   Characterization of Lyophilised SLN

The SLN were lyophilized in the presence of 10% trehalose, followed by sample reconstitution with MilliQ water at defined conditions. All the lyophilized cakes were brittle, easy and rapid to reconstitute. The higher reconstitution time was recorded in the case of the lowest lipid content that is F30M-SLN. The redispersed SLN have shown better physical stability in terms of mean diameter up to 30 days (Table 8).
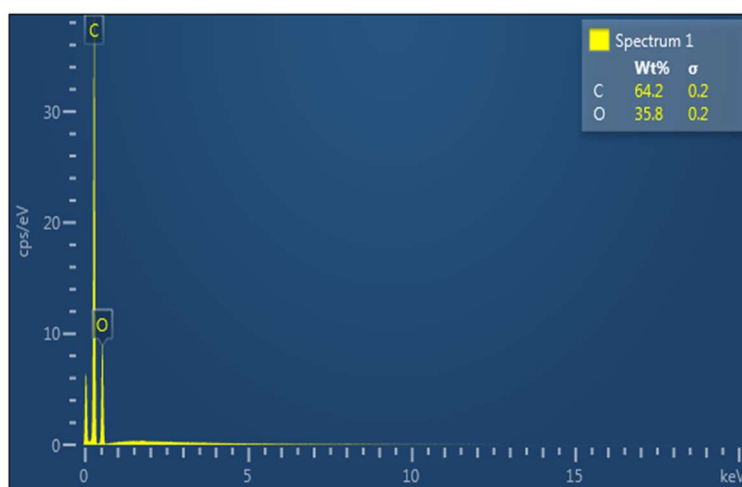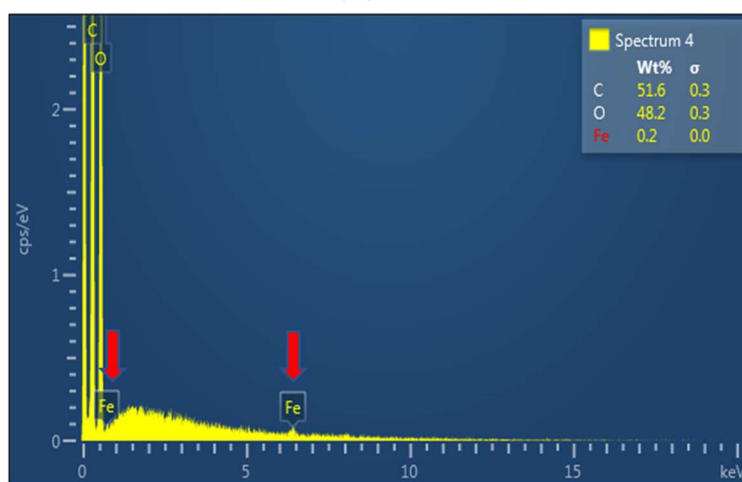
Figure 13. Elemental analysis of (**a**) F-SLN, and (b**)** F70M-SLN.

Table 8. Dimensions and reconstitution time of reconstituted SLN.

Day	F-SLN Z ave (nm) *P.I.*	F30M-SLN Z ave (nm) *P.I.*	F70M-SLN Z ave (nm) *P.I.*	F100M-SLN Z ave (nm) *P.I.*
1	492.4 ± 59.6 *0.15*	596.6 ± 43 *0.23*	582.7 ± 21.7 *0.15*	539.1 ± 35.86 *0.11*
30	568.13 ± 31.1 *0.16*	528.8 ± 9.9 *0.21*	508.5 ± 22 *0.15*	540.77 ± 74.3 *0.09*
[1]R. T. (min)	3.30 ± 0.3	5.49 ± 0.9	3.5 ± 0.7	2.5 ± 0.4

[1] Reconstitution time.

4.2.6 Encapsulation efficiency

The amount of CUR encapsulated into SLN with respect to the total amount used initially for the preparation of SLN was evaluated using ultracentrifugation and HPLC method. After centrifugation, the two separated phases (aqueous phase and lipid phase) have been tested via HPLC separately. The results indicate that 84.28 ± 4.25 % CUR was associated with the lipid phase of SLN.

4.2.7 Miscellaneous techniques used to load MNP

Some other strategies by changing the type of lipids and techniques have been explored. The remarks of all the techniques have been discussed in Table 9.

Experiments are still in progress to design the best strategy to accomplish the successful loading of MNP to the lipid nanoparticles.

Table 9. Various methodologies adopted to load MNP.
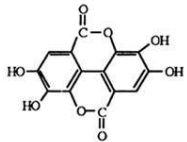
Technique	Remarks
SLN containing surface-modified MNP	The high surface to volume ratio can be responsible for the settlement of MNP in SLN. The stearic acid coating was done to stabilize the MNP followed by incorporation into SLN.
Emulsion-diffusion method	The mixture of phosphatidylcholine and glyceryl monostearate employed and stabilized by pluronic F-68.
Hot homogenization technique	The o/w type emulsion obtained by cetyl palmitate and MNP as oil phase and aqueous dispersion was stabilized by tween-80.
Solvent diffusion method	In this ultrasonic technique, MNP first dispersed in 2.5% w/w poloxamer 188 aqueous solution and stabilized by oleic acid. Finally, the resulting mixture added to monostearin.
Microemulsion technique	The combination of MNP, stearic acid, and phosphatidylcholine was employed. To achieve a clear microemulsion, sodium taurocholate and butanol have been used.
Air spray technique	The lipid phase composing tristearin, polyethylene glycol, and MNP was sprayed into the aqueous phase containing 2.5 % w/w poloxamer.
NLC	Three different triglycerides namely tristearin, suppocire, and tripalmitin have been used along with capric triglycerides in 1:1 w/w, stabilized by tween 20.

5 ELLAGIC ACID CONTAINING NANOSTRUCTURED LIPID CARRIERS FOR TOPICAL APPLICATION: A PRELIMINARY STUDY

5.1 INTRODUCTION

Phyto-pharmaceuticals are pharmaceuticals derived from botanicals. These natural ingredients are more easily and readily metabolized by the body, thus after administration they may provide increased absorption in the bloodstream. EA is a phyto-pharmaceutical substance found in many fruits and plants such as raspberries, strawberries, pomegranates, blackberries and many other plants food. EA (2,3,7,8-tetrahydroxy-chromeno [5,4,3-cde]chromene-5,10-dione) (Table 10) is the dimeric derivative of gallic acid and has a significant attractiveness in food supplements because of its potentially beneficial effects against a wide range of diseases (Malik et al., 2011).

Table 10. Chemical structure and some physicochemical characteristics of EA.

chemical structure	MW	λ_{max} (nm)	Log P	Melting point (°C)
	302.20	254	1.59 (2.32)	>360

Various studies indicate that EA possesses antimutagenic, antiagenic, antioxidant and anti-inflammatory activity in bacterial and mammalian systems (Khanduja et al., 1999; Loarca-Piña et al., 1998). In addition, EA has been proved to be an efficient skin whitener and suppressor of pigmentation. Besides anti-oxidant activities, EA also is cytotoxic towards different types of cancer cells, such as osteogenic sarcoma, tongue, pancreatic, leukemic, neuroblastoma, breast, prostate gland and colon cells (Edderkaoui et al., 2008; Fjaeraa and Nånberg, 2009; Seeram et al., 2005). It also possesses anti-inflammatory, anti-bacterial, anti angiogenesis, anti-atherosclerosis, anti-hyperglycemic, antihypertensive and cardio- effects (Landete, 2011; Larrosa et al., 2010; Malik et al., 2011; Rosillo et al., 2011).

However, EA has found limited use in therapeutic applications due to its low water solubility (around 9.7 µg/mL) and permeability (class IV of the BCS) (Bala et al., 2006; Chavda et al., 2010). When orally administered EA is poorly absorbed due to low aqueous solubility, metabolism in gastrointestinal tract (Seeram et al., 2004), first pass effect and irreversible binding to cellular DNA and proteins problems.

The incorporation of drugs in lipid nanoparticles is a smart approach to overcome bioavailability (Lim et al., 2004). Among lipid-based colloids, SLN and NLC can be mentioned. SLN are generally produced using solid lipids stabilized by the presence of surfactants dispersed in the aqueous phase. As a drawback during the time the lipid crystallization of the solid lipid core of these particles may lead to the leakage of the included active compound, thus influencing the EE. NLC were developed to overcome these drawbacks by mean of a partial replacement of the solid lipid with a fluid lipid. In this way, the lipid core matrix becomes less ordered as compared to SLN and can accommodate high amounts of active compound reducing loss problems.

For our studies, we analyzed two different blends of solid and liquid lipids. The first one based on the use of a mixture of the liquid caprylic/capric triglycerides (Miglyol) and the solid tristearin. In the second case, a mixture of caprylocaproyl macrogol-8 glyceride (Labrasol) and tristearin was used to produce NLC. In the hot state the two lipids form one phase and during the cooling process, a phase separation occurs in which small oily droplets are included in the solid matrix. Taken into the account these assumptions, the present paper will describe the preparation, characterization and preliminary in vitro studies of EA-containing NLC for dermatologic purposes.

5.2   RESULTS AND DISCUSSION

5.2.1   Production and characterization of NLC-EA dispersions

The NLC-EA composed as reported in Table 11, were obtained by dispersing the lipid phase in the aqueous phase under sonication (Esposito et al., 2019b) achieving stable and homogenous dispersions. The corresponding empty NLC, namely e-NLC1 and e-NLC2, were obtained using the same procedure apart for the addition of EA. As already known, a fluid lipid (i.e. tricaprylin or labrasol) when mixed to solid lipids allows to the formation of solid particles homogenously embedded of fluid compartments. However, during the

preparation almost the 4% by weight of total used lipid phase was lost on the vessel and less than 1% gave rise to the formation of agglomerates.

After production, nanoparticles were characterized in terms of dimensions and morphology. Dimensions and size distribution of the produced NLC were determined by mean of PCS. The analyses were made immediately after preparation and periodically at regular intervals in order to investigate the stability of nanoparticles by time. Table 12 summarizes the obtained values of mean diameters and polydispersity.

Table 11. Composition of the produced NLC-EA.

	NLC-EA1	NLC-EA2
	(% of total dispersion's weight)	
Tristearin	3.35	4
Miglyol	1.65	-
Labrasol	-	1
Poloxamer 188 (2.5% w/v)	95	95
Ellagic Acid (EA)	0.025	0.025

Analyzing the obtained values, it should be noted that in general no variations of the diameters occur during time. Some differences in size are appreciable between empty and drug-containing nanoparticles only in the case of NLC1, which shows an increase from 116.5 nm to 195.7 nm in the presence of EA. However, concerning the polydispersity indexes, empty NLC showed a reduction during time while EA-loaded NLC showed no great variations, indicating that NLC has maintained up to 2 months their monomodal dimensional distribution.

Cryo- TEM allows the study of the morphology of the produced NLC. Figure 14 depicts the cryo-TEM images of e-NLC1, e-NLC2, NLC-EA1 and NLC-EA2. It is evident that no morphological differences are evident among the considered types of NLC. Notably, some large and flat particles are detectable together with deformed, elongated and circular platelet-like or elliptical shaped nanoparticles depending to their position with respect to the site of observation, namely from the top to edge-on view or intermediate positions (Esposito et al., 2017; Sguizzato et al., 2017).

Table 12. Mean diameters of NLC as determined by PCS.

Day	e-NLC1 Z ave (nm) *P.I.*	e-NLC2 Z ave (nm) *P.I.*	NLC-EA1 Z ave (nm) *P.I.*	NLC-EA2 Z ave (nm) *P.I.*
1	116.5 ± 0.6 *0.37*	188.3 ± 1.2 *0.31*	195.7 ± 2.1 *0.36*	189.6 ± 3.9 *0.33*
20	118.9 ± 5.6 *0.40*	183.1 ± 6.2 *0.31*	192.0 ± 0.8 *0.52*	181.3 ± 5.1 *0.29*
30	117.2 ± 7.6 *0.43*	182.0 ± 1.5 *0.28*	190.4 ± 2.9 *0.40*	195.8 ± 6.4 *0.37*
60	118.7 ± 2.3 *0.39*	176.6 ± 3.2 *0.33*	189.8 ± 2.3 *0.30*	189.2 ± 2.6 *0.31*

s.d. = standard deviation calculated after 5 determinations on different batches of the same type of dispersion. P.I.= polydispersity index.
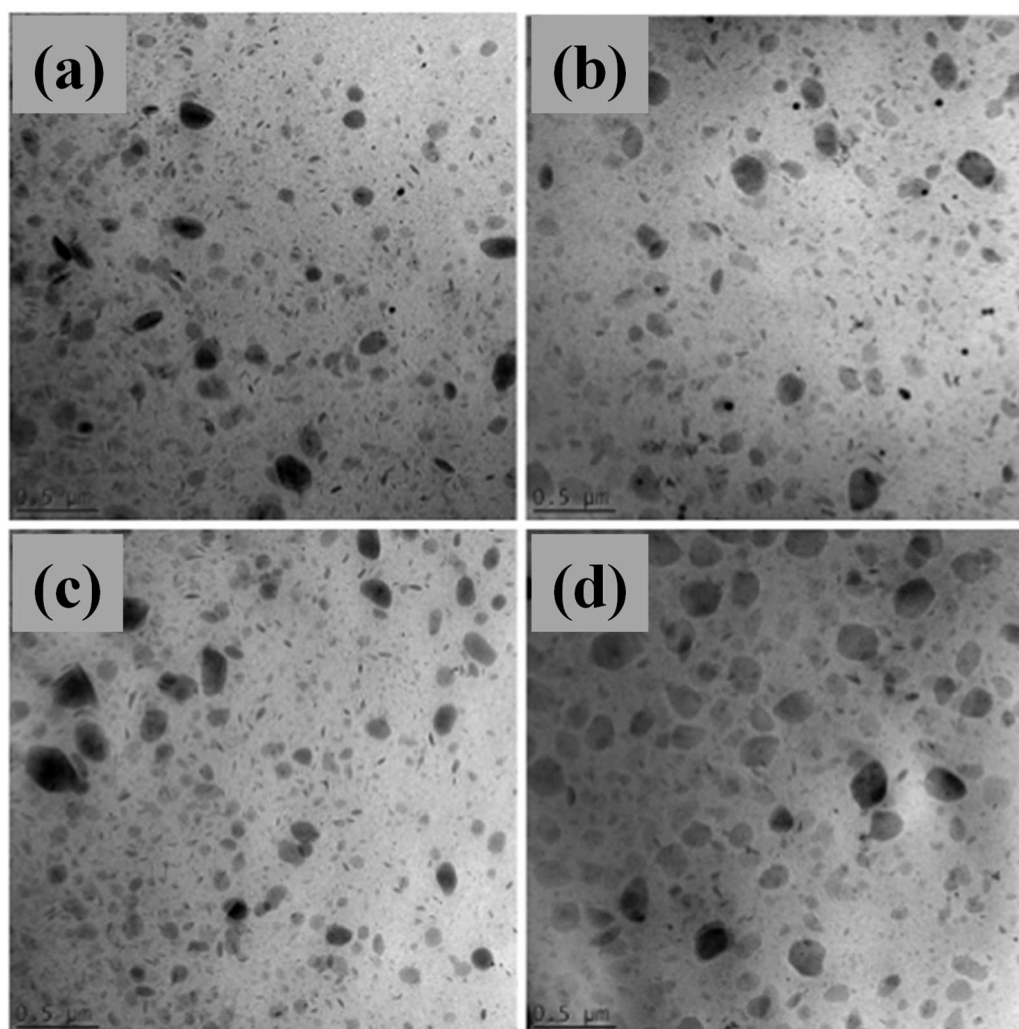

Figure 14. Cryo- TEM images of e-NLC1 (panel A), NLC-EA1 (panel B), e-NLC2 (panel C) and NLC-EA2 (panel D).

The inner structural features of NLC, NLC-EA1 and NLC-EA2 were investigated by SAXS. Results are reported in Figure 15 and clearly indicate that NLC-EA1 and NLC-EA2 nanoparticles are characterized by a lamellar organization of the inner matrix, both in the presence or absence of EA. Particularly, SAXS profiles show a Bragg peak at Q=0.143 Å-1, which corresponds to a lamellar structure with a repeat distance (which measures the sum of the bilayer thickness and the thickness of the water layer separating two adjacent bilayers) of 43.9 Å. Indeed, the four preparations are very similar, therefore it can be asserted that neither the different lipid composition nor the presence of EA modifies the structural organization of lipid nanoparticles. Note that considering the very low solubility of EA in water, data suggests solubilization of the drug inside the paraffinic region of the lipid layer.
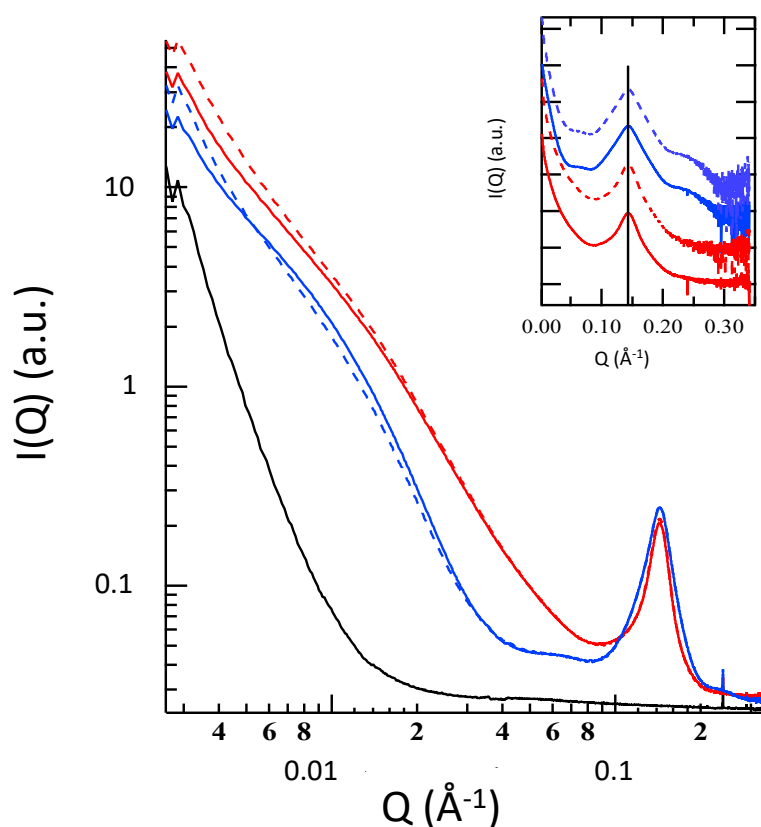

Figure 15. SAXS profiles of e-NLC1 (full blue line), e-NLC2 (full red line), NLC-EA1 (dotted blue line), NLC-EA2 (dotted red line). The signal of sole water is indicated with a black line. The inset shows the SAXS profiles after the subtraction of the water contribution. Here, the curves are scaled for clarity. The vertical black line indicates the constant position of the Bragg peaks.

5.2.2 Drug encapsulation efficiency and shelf life

The amount of drug encapsulated in NLC concerning the total amount used for the preparation was evaluated by high-performance liquid chromatography (HPLC) using a reversed-phase column. The amount of entrapped EA was determined after centrifugation by dissolving in a known amount of ethanol the lipid phase, while the amount of free EA was determined in the filtrated aqueous phase. The content of EA in both fractions was calculated by comparison with a standard solution. Particularly, EA content in the produced NLC was calculated as a function of time and expressed as a percentage of the total amount used for the preparation.

As reported in Table 13, drug recovery after NLC production was almost quantitative as compared to the total amount used for the preparation. In the aqueous fraction, the amount of EA was always below the detection limit of the analytical method employed, indicating a high EE of loaded-NLC. Indeed, the drug encapsulation was 91.50 ± 2.42 % in the case of NLC-EA1 and 96.61 ± 3.67 % in the case of NLC-EA2 dispersions.

Shelf life stability was calculated plotting Log (EA residual content, % with respect to drug content at time 0) against time, obtaining first-order kinetics (data not shown). From the slopes (m) obtained by linear regression, the time at which the drug concentration has lost 10% and 50%, namely shelf life (t_{90}) and half-life ($t_{1/2}$) respectively, were calculated and reported in Table 13. All data were statistically significant ($p<0.0001$).

It was found that EA in solution decomposes quickly ($t_{1/2}$ being 56 days), while NLC are able to increase the protection of EA as compared to the solution with different efficiency. Indeed NLC-EA1 maintain 90% of EA stability for almost 2 months (57 days), whilst for NLC-EA2, t_{90} is around 40 days. The $t_{1/2}$ values reach more than one year for NLC-EA1 (378 days) and 8.5 months for NLC-EA2, increasing the stability of EA of 6.72 and 4.59 fold as compared to the solution.

The macroscopic aspect of both NLC-EA1 and NLC-EA2 did not change over time. Notably, no phase separation phenomena, settling of particles, and absence of aggregate formation were evident after three months from production.

Table 13. EA content in NLC as a function of time and shelf-life values.

Time (days)	EA recovery (%)[a]		
	EA (ethanol solution)	NLC-EA1	NLC-EA2
1	100.00 ± 1.41	91.50 ± 2.42	96.61 ± 3.67
10	96.58 ± 2.22	91.06 ± 3.91	92.69 ± 0.93
20	84.31 ± 2.81	90.37 ± 2.50	91.15 ± 2.27
30	74.29 ± 2.63	89.66 ± 2.51	90.86 ± 1.85
60	48.24 ± 6.14	87.57 ± 2.40	88.63 ± 3.67
Shelf life values			
K	0.012325	0.001832	0.002682
t_{90} (days)[b]	8.52	57.30	39.14
$t_{1/2}$ (days)[c]	56.23	378.18	258.33

[a] percentage as a function of initial EA content by weight. [b] time at which the drug concentration has lost 10%. [c] time at which the drug concentration has lost 50%. The results are the average of 3 independent experiments $\pm$ s.d.

5.2.3 In vitro experiments

5.2.3.1 Antioxidant activity

It is well known that various pathophysiological processes are due to the presence of free radicals, thus the antioxidant intervention is of pivotal importance. Indeed, the beneficial effects of polyphenols on human skin are largely described, such as antioxidant, anti-aging, anti-inflammatory and anti-cancer activities (Badhani et al., 2015; Lo et al., 2011; Yang et al., 2016). In this view, both EA-containing NLC formulations were subjected to two different tests to evaluate their antioxidant capacity as compared to the active solution and the empty NLC. The chosen tests were DPPH and FRAP.

It has to be underlined that in both cases it was impossible to test the activity of empty NLC because the addition of their DMSO solution to the radical or FRAP mixture gave rise to the formation of a certain opalescence or precipitation, respectively. As for the NLCs containing EA, the data summarized in Table 14 relate to extremely diluted solutions that did not give great opalescence or precipitation problems in the test media. However, unlike EA in the chosen solvent (DMSO) is perfectly soluble, the two NLCs in the same solvent appeared as suspensions.

Table 14. Antioxidant activity of NLC-EA as determined by FRAP and DPPH assays.

Compound	DPPH		FRAP	
	μmolTE/g[a] ± SD	% of activity[b]	μmolTE/g[a] ± SD	% of activity[b]
EA-solution	25834.90 ± 0.00	100	34052.21 ± 1902.66	100
NLC-EA1	9545.16 ± 0.00	37	19852.21 ± 1419.89	58
NLC-EA2	4786.36 ± 112.17	18	20879.52 ± 1981.78	61

*all the compounds were test at the same concentration (0,005 mg/ml) [a]: μmol Trolox equivalents/g [b]:% of activity = percentage of antioxidant activity as compared to EA in DMSO solution.

In light of these observations, the antioxidant activity data reported in Table 14 indicate for both types of NLC-EA a lower activity with respect to EA solution. In particular, regarding the FRAP assay, the antioxidant activity of both the loaded NLC is around 60% as compared to the solution. This behavior could be possibly ascribed to a combination of events. Firstly (a) the recovered amount of EA within the formulation which is lower as compared to the solution being comprised between 91 to 96 % (Table 13) and (b) the amount of solubilized EA in the could possibly influence also a lasting antioxidant activity during time. On the other hand, the values obtained with the DPPH assay are quite far from those expected, certainly due to the incompatibility of the DMSO solvent with the test methodology (Cao et al., 1993; Soare et al., 1997).

The profile that emerged from these tests underlines how the two new formulations preserve the excellent antioxidant capacity of the active.

5.2.3.2 EA diffusion from NLC

To evaluate the release of EA from NLC-EA1 and NLC-EA2 formulations, Franz-cells associated with nylon membrane were used. Particularly, two different pH values were considered for the receiving phase constituted of phosphate buffer, namely pH 7.4 and 5.5. Furthermore to establish the sink conditions and to promote EA solubilization, 30% ethanol by volume was added to the receiving phase (Santos et al., 2013; Siewert et al., 2003). Moreover, it has to be underlined that due to the poor water-solubility of EA, the comparative EA solution used for diffusion release experiments was made in DMSO.

Figure 16 reported the diffusion release profiles of EA from solution and both types of NLC. The amount of EA that penetrated through the membrane per unit area was plotted against time and the slopes, which represent the steady-state fluxes, were calculated by linear regression. The calculated regression coefficients squared were higher than 0.96. The normalized fluxes (Jn) calculated and the results of these calculations are reported in Table 15.
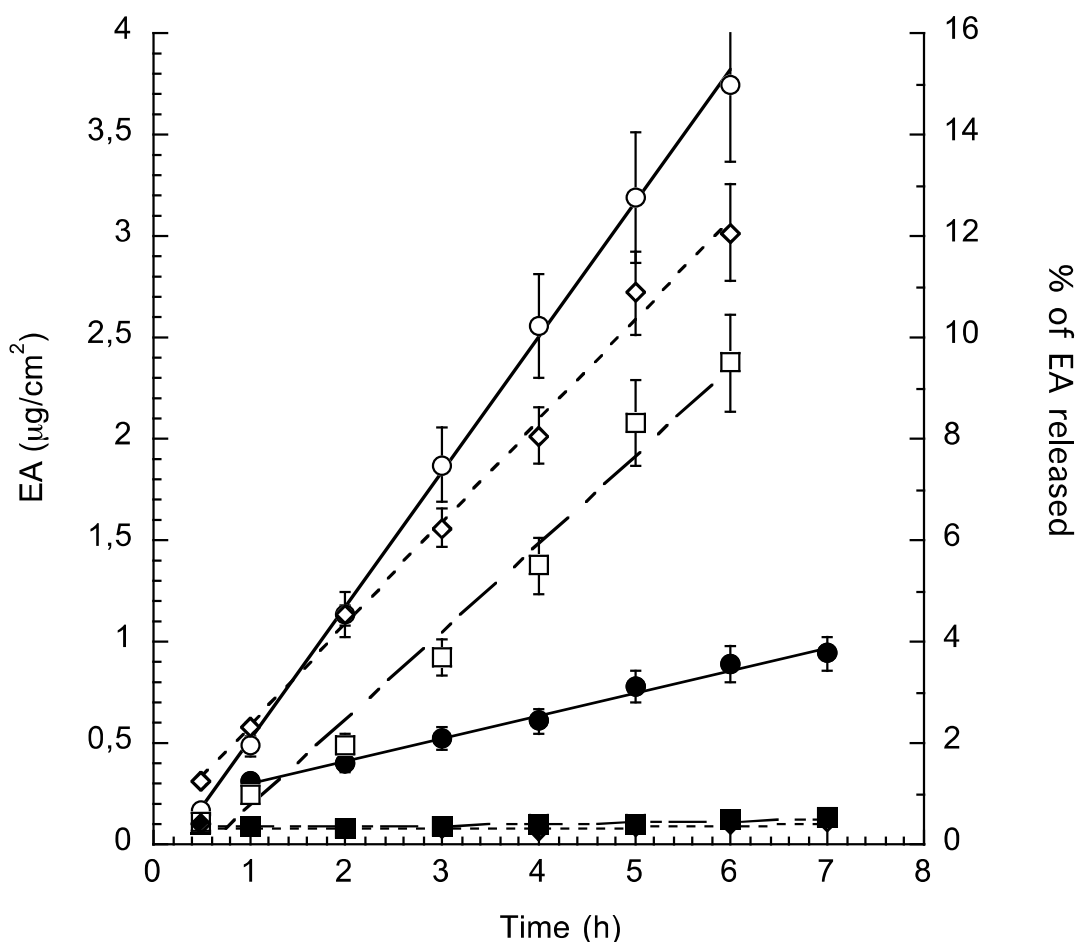

Figure 16. In vitro diffusion kinetics of EA from DMSO solution (circles) or NLC-EA1 (squares) and NLC-EA2 (diamonds) as determined by Franz cell associated to nylon membranes. Experiments were conducted in phosphate buffer at different pH, namely 7.4 (closed symbols) and 5.5 (open symbols). Data are the mean of 4 independent experiments ± s.d.

Particularly, in agreement with the scarce water solubility of EA, the Jn values were in general very low being comprised 0.003 and 0.663. Notwithstanding these results, from the obtained profiles it is evident that the two NLC systems displayed similar behavior in controlling EA release. Moreover, as expected the influence of the pH of the receiving phase is appreciable. Indeed as indicated by literature, pH influences the release, solubility and permeation of acidic drugs (Akula and P.K., 2018; Lambers et al., 2006; Salamanca et al., 2018; Spagnol et al., 2018).

It is interesting to see that at pH typical of the skin surface, which ideally should be slightly acidic being comprised in the acidic range from pH 4.0 to 7.0 (Lambers et al., 2006) the release of EA is higher as compared to the same formulation tested at neutral pH (i.e. pH 7.4) (see Figure 16 and Table 15). This result could be noteworthy for a potential topical application of NLC-EA onto the skin.

Table 15. In vitro diffusion coefficients of EA.

	Jn ($\mu g/cm^2/h$)	log Jn	R^2
NLC-EA1 pH 7.4	0.005	- 2.30	0.969
NLC-EA2 pH 7.4	0.003	- 2.52	0.984
EA-solution pH 7.4	0.112	- 0.95	0.990
NLC-EA1 pH 5.5	0.430	- 0.36	0.979
NLC-EA2 pH 5.5	0.500	- 0.30	0.995
EA-solution pH 5.5	0.663	- 0.17	0.999

5.2.3.3   Cytotoxicity studies

It is well known that lipid nanocarriers can improve solubilization and stabilization of drug molecules thus influencing the pharmacokinetics of drugs in reason of the different distribution after systemic administration (Hristo Svilenov, and Christo Tzachev, 2014). Moreover, lipids are physiological safe compounds being components of many natural food sources and therefore presenting metabolic pathways for their degradation. In addition, due to the promising results concerning EA diffusion and antioxidant activity, the in vitro activity of the produced formulation was further investigated. Particularly, cytotoxicity was assessed by MTT assay on HaCaT cells comparing the activity of EA-loaded NLC to that of EA in DMSO solution. The obtained results are graphically shown in Figure 17.

It should be underlined that, although both types of NLC are characterized by some toxicity, NLC1 are less cytotoxic than NLC2. Furthermore, the presence of EA does not heavily influence the cytotoxicity of these formulations. On the other hand, a result that confirms our initial hypothesis is that both these formulations have a reduced cytotoxicity as compared to that of the DMSO solution allowing us to propose them as a possible vehicle for the EA.
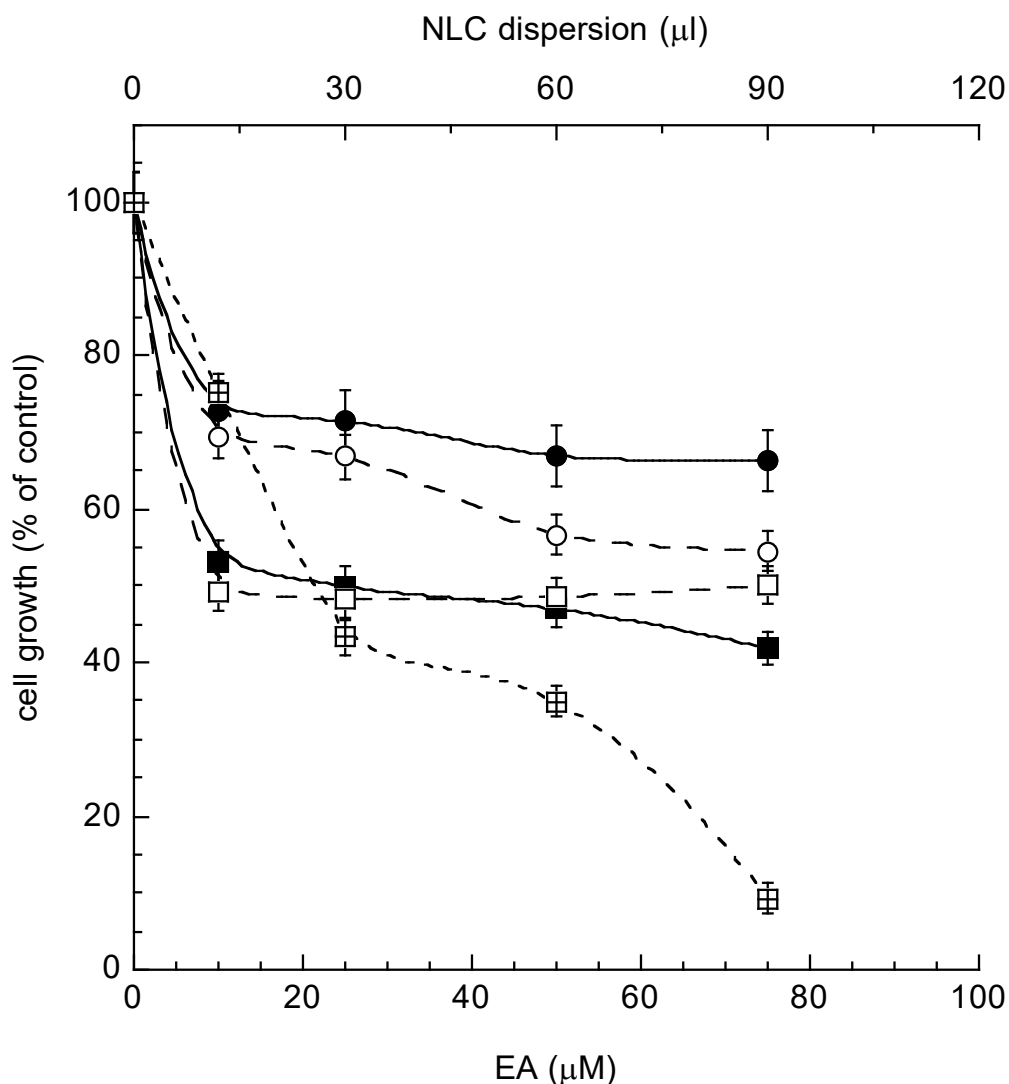

Figure 17. In vitro antiproliferative effect on HaCat cells of EA in DMSO solution (crossed squares), e-NLC1 (closed circles), e-NLC2 (closed squares), NLC-EA1 (open circles) and NLC-EA2 (open squares). Data are the mean of three independent experiments ± s.d. conducted in triplicate. *P* values are always <0.01.

6 NANOPARTICULATE GELS FOR TOPICAL ADMINISTRATION OF CAFFEIC ACID

6.1 INTRODUCTION

CA is a naturally occurring hydroxycinnamic acid amply present in coffee, fruits, vegetables, oils, grapes, and tea (Janbaz et al., 2004; Khan et al., 2016). CA (Figure 18) and its derivatives can be considered as strong antioxidants due to different mechanisms, such as radical scavenging activity and inhibition of lipid peroxidation (Gulcin, 2006; Valko et al., 2007). The capability to inhibit or retard oxidation reactions makes CA suitable to counteract inflammatory diseases, aging and some type of tumors (Kang et al., 2008; Nichols and Katiyar, 2010; Prasad et al., 2009). Indeed CA has a photoprotective effect against UVB-induced cellular changes and can prevent DNA damage induced by free radicals, thus it has been proposed as a chemo-preventive agent against cutaneous malignant melanoma (Kang et al., 2008; Nichols and Katiyar, 2010).
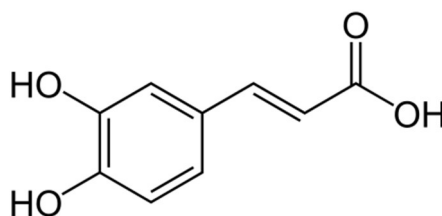
Figure 18. Chemical structure of caffeic acid.

Since the skin represents the largest and outermost organ of human body, it is exposed to many hazards, such as extreme temperatures, UV radiations, mechanical trauma, as well as biological and chemical agents present in pollution and cigarette smoke (CS). CS is considered responsible for multiple, highly diverse effects on human health, including cancer, noncancerous lung diseases, atherosclerotic diseases of the heart and blood vessels, and toxicity to the human reproductive system (Furrukh, 2013; Macacu et al., 2015; Onor et

al., 2017). In addition, CS can affect the skin both directly on the epidermis and indirectly via the bloodstream, causing mucocutaneous signs, precocious skin aging, chronic dermatoses and skin cancer (Ortiz and Grando, 2012; Prieux et al., 2020). Indeed CS components affect cellular redox hemostasis and induce skin inflammation (Chang et al., 2018). For instance, some chemicals, such as polycyclic aromatic hydrocarbons, are able to pass through the epidermis and reach the dermis, leading to systemic effects (Soeur et al., 2017). The skin can counteract the CS toxic effect by natural mechanisms of defense, acting as antioxidants or oxidant-degrading systems. On the other hand, this homeostatic protection can unsuccessfully increase cutaneous ROS, finally leading to the onset of dermatological diseases (Prieux et al., 2020). In this respect, the cutaneous administration of antioxidants represents an approach to restore homeostasis, thus preventing ROS-mediated disorders.

The idea at the basis of the present investigation is the possibility to apply CA on the skin in order to counteract pathologies and disorders induced by CS. Since CA is poorly soluble in water, a nanotechnological formulation has been studied suitable for CA solubilization and able to control CA delivery, prolonging its antioxidant action. Particularly, SLN have been proposed, being biocompatible non-toxic delivery systems, suitable for the inclusion of drugs with different physico-chemical properties in an aqueous physiological environment (Esposito et al., 2008, 2019b; Pink et al., 2019). Since SLN dispersions don't possess adequate viscosity for skin permanence, they need to be thickened, resulting in a final nanoparticulate semi-solid form (Esposito et al., 2013). Thus, a preformulatory study has been conducted aimed at selecting a polymer for SLN thickening. Namely, poloxamer 407 and hyaluronic acid (HA) have been considered (Figure 19). The former is a copolymer constituted of polyoxyethylene- polyoxypropilene units characterized by thermogelling properties, while the latter is a natural polymer known for wound healing properties and investigated in this study to modulate the formulation strength (Artzner et al., 2007; Li et al., 2019; Mayol et al., 2008; Pereira et al., 2013).
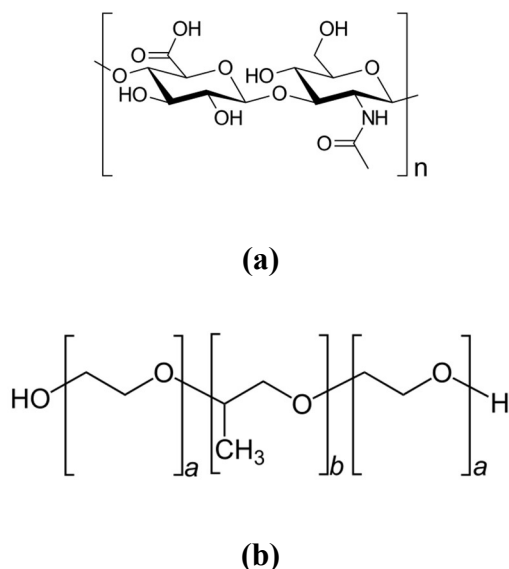
(a)

(b)

Figure 19. Chemical structure of (a) hyaluronic acid and (b) poloxamer 407.

The mechanical properties of the nanoparticulate gel have been characterized by rheological studies, while CA diffusion has been evaluated by Franz cell. Finally, CA antioxidant effect has been evaluated ex-vivo on human skin explants exposed to CS.

6.2   RESULTS AND DISCUSSION

6.2.1   SLN production and characterization

In order to find a vehicle suitable for CA administration on the skin, the drug has been encapsulated in SLN. SLN dispersions were produced by a method based on emulsification of a fused lipid phase constituted of tristearin with an aqueous solution constituted of p188, by hot homogenization and ultrasonication. During the emulsification, tristearin droplets were stabilized by p188, afterward under cooling, the droplets solidified into solid nanoparticles. The final aspect of SLN dispersions was milky and homogeneous. Table 16 reports the composition of SLN produced in the absence and the presence of CA.

Table 16. Composition (% w/w) of the indicated formulations.

Nanoparticulate system	tristearin	p188[1]	water	CA[2]
SLN	5	2.38	92.62	-
CA-SLN	5	2.38	92.52	0.1

[1]poloxamer 188; [2]caffeic acid

6.2.1.1 Morphological analysis

SLN morphology has been studied by cryo-TEM and X-ray diffraction. As shown in Figure 20 (a), CA-SLN were characterized by flat irregular elongated particles.
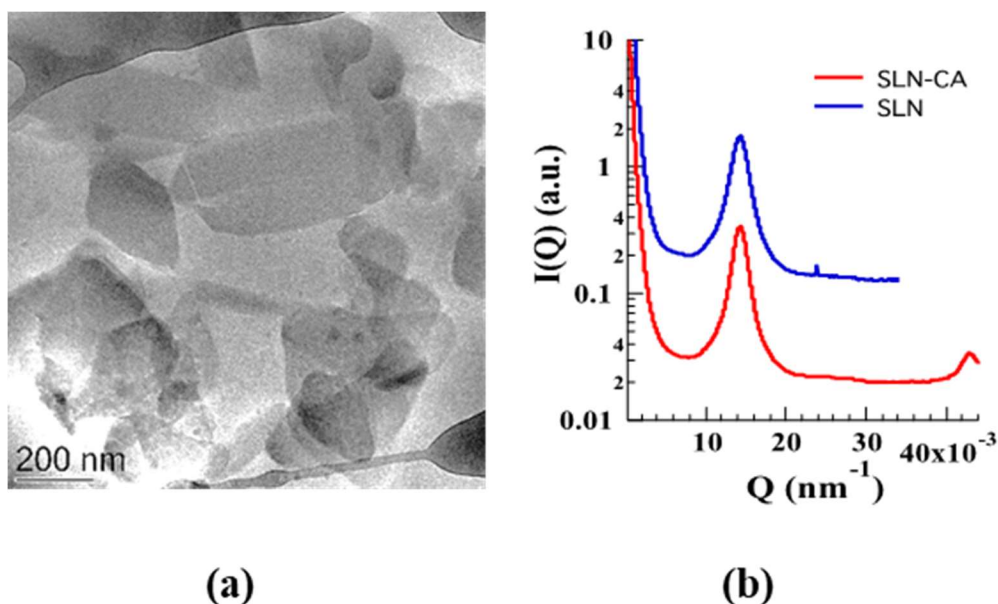
Figure 20. (a) Cryo-TEM images of CA-SLN. (b) X-ray scattering profile for SLN (blue) and CA-SLN (red) samples. SLN sample has been measured only up to $Q = 0.35$ nm^{-1}. Experiments were performed at Diamond Light Source (UK).

With regard to inner structure of SLN, X-ray diffraction evidenced the presence of a lamellar organization. Figure 20(b) shows the X-ray profiles corresponding to CA loaded and unloaded SLN: in both cases Bragg peaks are observed, the position of which scales as 1:2:3

(note that the second order has very low intensity and that SLN sample has been measured in a narrow Q-range), as expected for a 1D lamellar organization of the lipid matrix. The unit cell, which corresponds to the lamellae repeat distance, is 43.9 Å. Since peak intensity, width and position are independent on the presence or absence of CA, it can be concluded that the drug does not alter the inner structural organization of the SLN.

6.2.1.2 Dimensional distribution

SLN and CA-SLN have been analyzed by PCS, in order to have information on their dimensional distribution (Table 17). The mean dimensions of SLN, expressed as equivalent spherical diameters, considering spheres with the same nanoparticle volume, were around 200 nm, with dispersity indexes below 0.3. The presence of CA slightly affected dimensional distribution.

Table 17. Dimensional characteristics and encapsulation parameters of the indicated nanoparticulate systems.

Nanoparticulate system	Z-Average[1] (nm) ± s.d.	Dispersity[1] index ± s.d.	Encapsulation efficiency[2] (%)	Loading capacity[3] (%)
SLN	216 ± 12	0.28 ± 0.02	-	-
CA-SLN	201 ± 11	0.29 ± 0.03	88.2 ± 8.3	1.8 ± 0.03
SLN-P	225 ± 10	0.23 ± 0.04	-	-
SLN-P-CA	230 ± 14	0.26 ± 0.03	88.2 ± 8.3	1.8 ± 0.03

[1]as determined by PCS; [2]Percentage (w/w) of drug encapsulated, with respect to the total amount used for the preparation. [3]Percentage (w/w) of drug within nanoparticles, as compared to the amount of lipid used for the preparation. Data represent the mean ± S.D. of 6 independent experiment

6.2.1.3 Evaluation of CA encapsulation efficiency in SLN

CA was successfully encapsulated within SLN, as determined by analyzing drug content after ultracentrifugation. Indeed CA concentration in SLN was 0.88 mg/ml, namely 88% w/w of the drug employed was associated to the nanoparticulate lipid phase (1.7% with respect to the lipid phase), while 12 % was in the dispersing aqueous phase (Table 17). This result is related to the physicochemical behavior of CA, being partially soluble in water (log P 1.53). It is interesting to note that SLN enabled to 1.76-fold increase CA solubility with respect to water, where CA is soluble up to 0.5 mg/ml.

6.2.2 Preparation and characterization of gels

Since nanoparticulate dispersions do not possess an adequate viscosity for cutaneous administration, a preformulatory study has been conducted in order to find a vehicle suitable for SLN thickening. Particularly different polymers have been considered, namely the copolymer PEO_{98}-POP_{67}-PEO_{98} poloxamer 407 (p407) and HA. P407 is characterized by thermogelling properties, while HA can confer plastic behavior, increasing strength of the final gel (Li et al., 2019; Pereira et al., 2013). Table 18 reports the composition of the gels produced using the polymers alone or in combination. P-HA and P gels were obtained by addition of polymer powder to cold water.

Table 18. Composition (% w/w) of the indicated formulations.

Gel system	tristearin	p188[1]	p407[2]	HA[3]	water	CA[4]
P	-	-	15.0	-	85.0	-
P-HA	-	-	15.0	2.0	83.0	-
P-CA	-	-	15.0	-	84.9	0.1
P-HA-CA	-	-	15.0	2.0	82.9	0.1
SLN-P	4.25	2.02	15.0	-	78.52	-
SLN-P-CA	4.25	2.02	15.0	-	78.42	0.1
P-P188-CA	-	2.02	15.0	-	82.88	0.1

[1]poloxamer 188; [2]poloxamer 407; [3]hyaluronic acid; [4]caffeic acid

Notably CA solubility in P-CA was 1 mg/ml, thus 2-fold higher with respect to CA-SOL; indeed p407 in water self-aggregates forming micelles that increase drug solubility. In the case of P-HA-CA, a preformulatory study has been conducted to find the best way to combine the two polymers. Direct addition of HA powder to p407 solution resulted in clumps difficult to disperse, thus a method was selected based on 1:1 (v/v) dilution of a p407 30 % (w/w) solution with a HA 4 % (w/v) solution, finally leading to the composition of P-HA-CA reported in Table 18.

6.2.2.1 X-ray scattering analysis

In order to investigate the supramolecular structure of the gels, SAXS experiments have been conducted on P, P-CA, P-HA and P-HA-CA at different temperatures (e.g. 20, 30 and 37 °C). Results are reported in Figure 21. Curves are particularly noisy, because of the low polymer concentration and of the low contrast. In the case of P (a), a low-angle, narrow

Bragg peak and a broader peak at higher Q are detected at all temperatures. The two peaks are in the order 1:√3, according to the occurrence of a of a pseudo-hexagonal packing order with a lattice constant of ≈ 220 Å. Quite surprisingly, the peak intensity of the low-angle peak increases on heating, suggesting that the sample ordering increases as a function of temperature. Indeed, even though it is well know that by elevating the temperature, the dehydration of the hydrophobic p407 blocks combined with the hydration of the hydrophilic ones leads to the formation of spherical micelles; it is noteworthy that on heating, the subsequent packing of the micellar structures results in a 3D cubic lattice, which constitutes the main structure of p407 gels. Similar profiles, together with the same thermal effect, have been found for the P-CA sample (b), indicating that the gel supramolecular structure is conserved after the addition of CA.
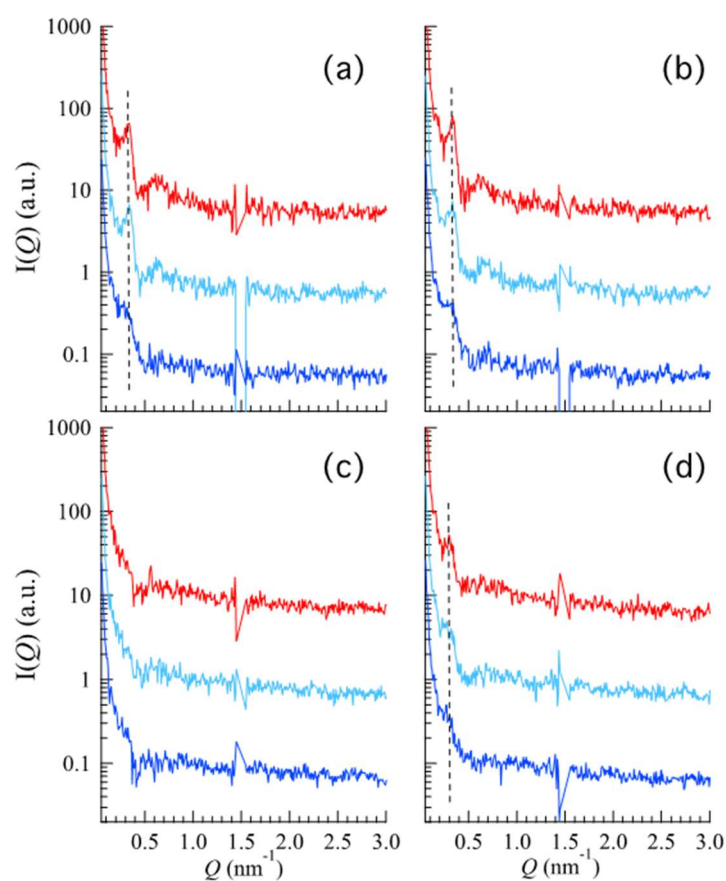

Figure 21. SAXS diffraction profiles of P (a); P-CA (b); P-HA (c) and P-HA-CA (d) at 20 (blue), 30 (light blue) and 37 (red) °C. The dashed line indicates the position of the first correlation peak. Experiments were performed in Graz (AT) laboratory.

A different behavior is detected in the presence of HA: at one side, P-HA SAXS curves (c) are characterized by the absence of peaks at any of the investigated temperatures, while the P-HA-CA sample (d) shows the same profile already observed for P and P-CA gels with two differences: (i) at 25 °C no peaks occur; (ii) the peaks observed at 30 and 37 °C correspond to a larger pseudo-hexagonal packing correlation distance (242 Å). As a first conclusion, SAXS data indicate that the p407 based gels have a well-structured organization both in the absence and the presence of CA, with an increasing internal order induced by temperature, as expected considering the temperature-responsive nature of the gel (Wei et al., 2002) and the sol-gel transition below reported in Table 20. On the contrary, data confirm that HA disorganizes the ordered structure, resulting in the absence of peaks.

In order to better define the gel ordered structure, model fitting of the SAXS data has been performed. According to the accepted structural model, a body-centered cubic lattice of micelle structures with paracrystalline distortion has been considered. The micelles were monodispersed and the size of the paracrystal infinitely large. Paracrystalline distortions were assumed to be isotropic and characterized by a Gaussian distribution. The model scattering intensity I(Q)* was calculated using equation 13:

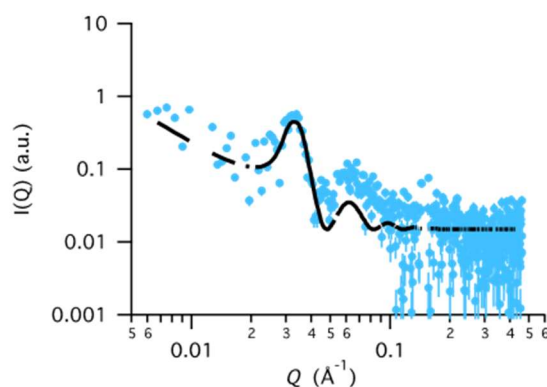$$I(Q)^* = k/V_p \ V_{\text{lattice}} \ P(Q) \ Z(Q) \qquad (13)$$

Figure 22. Data fitting for P-CA SAXS curve at 30°C.

where k is the volume fraction of spheres, V_p is the volume of the micelles, $V_{lattice}$ is a volume correction for the crystal structure, P(Q) is the form factor of the sphere and Z(Q) is the paracrystalline structure factor for a body-centered cubic structure (Matsuoka et al., 1990). Fitting parameters were the nearest neighbor distance (D), the lattice distortion γ, the micelle radius R and the electron densities of the micelle and the solvent. As an example, fitting results are reported in Figure 22, while the most relevant fitting parameters are reported in Table 19.

Table 19. Fitting parameters of SAXS data of gels obtained at 37°C.

Fitting parameter	P (20 °C)	P (37 °C)	P-CA (37 °C)	P-HA-CA (37 °C)
D (Å)	247.7	246.6	250.2	262.6
lattice distortion	0.18	0.14	0.11	0.12
micelle radius (Å)	79.2	93.6	104.8	120.5

Errors are in the order of 5% for D and micellar radius and of 10% for the lattice distortion.

Even if the SAXS curves are very noisy, the fit is remarkably good. Fitted parameters show that poloxamer molecules, self-assembled into spherical micelles of about 90 to 120 Å radii, form a gel in which the spherical micelles are packed into a 3D cubic lattice. Thermo-sensitivity of p407 explains the lattice distortion decrease (e.g., the increase of the gel ordering) observed in P as a function of temperature. On the other side, the presence of CA appears to induce a further increase of order, while HA increases the lattice distortion. This observation is also confirmed by the absence of Bragg peaks which characterizes the P-HA gel.

6.2.2.2 Rheological study

When p407 gels are used for topical applications, the transition temperature at which the fluid aqueous polymer solution turns to a semi-solid material, Tsol-gel, is recognized as one of the most important parameters (Baloglu et al., 2011). Rheology represents a precious way to study the behavior of thermosensitive formulations since in these systems viscoelastic properties (e.g. elastic G' and viscous G'' moduli) depend on their physical state. Therefore, the Tsol-gel can be easily determined by performing rheology experiments as a function of the temperature. Figure 23 reports the G' and G'' profiles for P, P-CA, P-HA and P-HA-CA.

In all cases, the thermal behavior is very similar, thus indicating that on heating all formulations became more elastic than viscous, as expected, due to the transition from liquid to structured gel (Baloglu et al., 2011) The maximum elastic modulus, which is an indication of the strength of the formed gel, is also very similar.

The sol-gel transition temperature was evaluated considering the temperature at which the elastic modulus (G') and the viscous modulus (G") are equal (Dumortier et al., 2006). The resulting Tsol-gel values are shown in Table 20. A few points should be evidence: first, the comparison between P and P-CA profiles (in the case of P-CA the gel forms at a lower temperature with respect to P, with a Tsol-gel difference of 4.2 °C) suggests that the presence of CA increases the system order, as indicated by SAXS results. Second, P-HA-CA displays a Tsol-gel value higher than P-HA (the difference is 2.4 °C), indicating a less ordered structure, in agreement with X-ray scattering findings. Indeed SAXS and rheology are complementary, because the former characterizes the supramolecular structure of samples, while the latter defines the macroscopic behavior (Bodratti and Alexandridis, 2018).
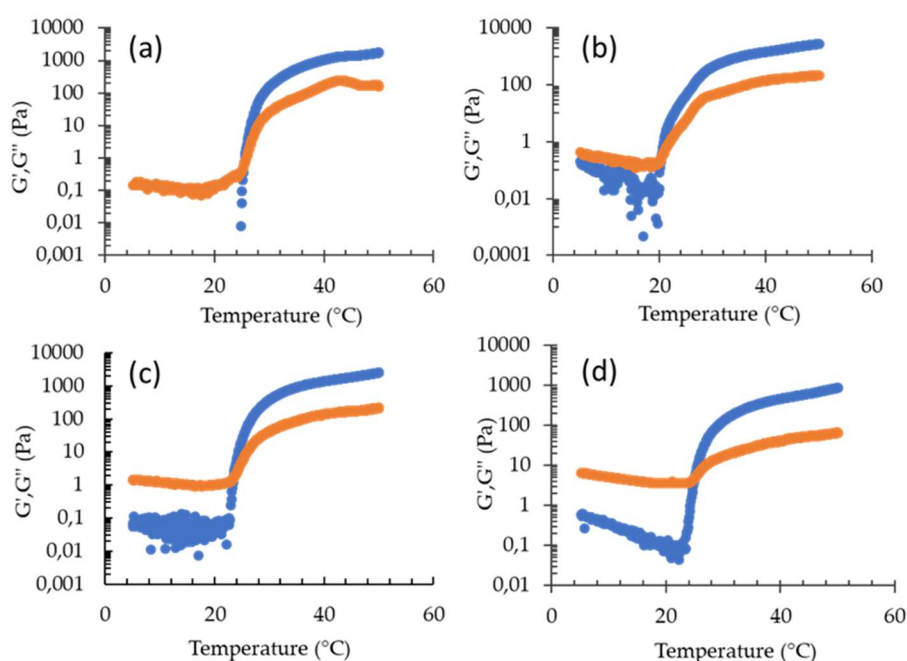

Figure 23. Effect of the temperature on elastic (G', blue) and viscous (G'', orange) moduli for P (a), P-CA (b), P-HA (c) and P-HA-CA (d).

Table 20. $T_{sol-gel}$ and spreadability parameters of the indicated gels.

Gel	$T_{Sol-gel}$	Spreadability (g × cm/sec)
P	26.11 ± 3.1	11.41 ± 1.88
P-CA	21.87 ± 2.1	11.40 ± 1.75
P-HA	22.40 ± 2.2	12.50 ± 1.30
P-HA-CA	24.80 ± 5.2	12.45 ± 1.20
P-P188-CA	28.1 ± 1.2	-
SLN-P	-	10.02 ± 1.68
SLN-P-CA	-	10.00 ± 1.81

6.2.2.3 Gel spreadability study

Spreadability represents a technological parameter affecting the extrudability of semisolid forms from the package, their capability to cover skin area, the patient compliance and definitely the therapeutic efficacy of drugs (Sguizzato et al., 2020a). At this regard, to gain information on their application on skin, the gel spreadability values have been evaluated (Table 20). All the gels possess a suitable spreadability for cutaneous administration. Nonetheless, P and P-CA were less spreadable with respect to HA containing gels, suggesting that the presence of HA reduced gel consistence. CA did not affect spreadability of both gels.

6.2.2.4 In vitro CA diffusion kinetics from gels

In order to investigate the efficiency of gels designed as topical vehicles and to select the polymer to employ for SLN thickening, the in vitro CA diffusion was studied by Franz cell associated to nylon membranes. Particularly P-CA and P-HA-CA have been considered and compared to the plain CA-SOL as reported in Figure 24 (a).
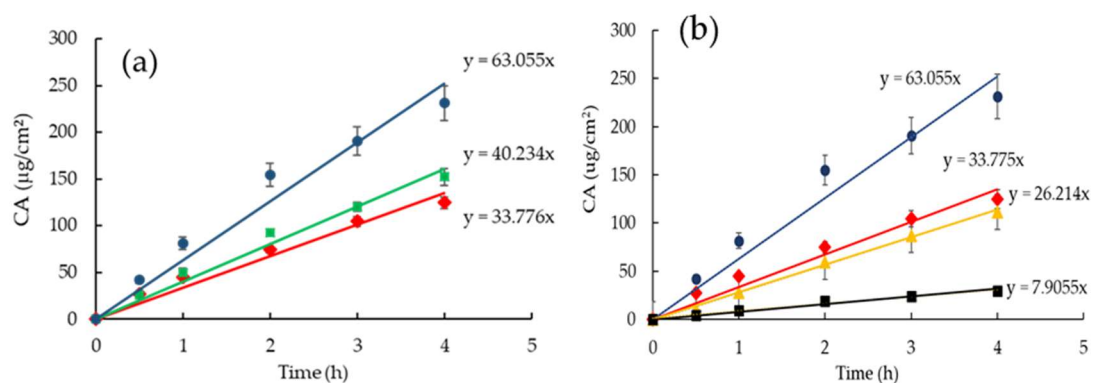
Figure 24. CA diffusion kinetics from CA-SOL (blue), P-HA-CA (green) and P-CA (red), CA-SLN (yellow) and SLN-P-CA (black), as determined by Franz cell. Data are the mean of 6 independent experiments.

Diffusion profiles fitted well with zero-order kinetics. It should be considered that in the case of CA-SOL, CA concentration was 0.5 mg/ml, thus the D, obtained dividing flux by CA concentration within the formulation, was double with respect to the flux (Table 21). CA fluxes from both gels were slower with respect to CA-SOL, particularly in the case of P-CA. Indeed the D of CA from P-HA-CA was 3.13-fold lower than CA-SOL, while in the case of P-CA, D was 3.73-fold lower.

Table 21. Fluxes and diffusion coefficients of the indicated formulations.

Formulation	F^1 (mg/cm^2/h)	D^2 (cm/h)
CA-SOL	63.05 ± 4.41	126.11 ± 8.82
P-HA-CA	40.23 ± 2.81	40.23 ± 2.81
P-CA	33.77 ± 2.36	33.77 ± 2.36
CA-SLN	26.21 ± 1.83	26.21 ± 1.83
SLN-P-CA	7.90 ± 0.55	7.90 ± 0.55

[1]Flux; [2]Diffusion coefficient; Data are the mean of 6 independent Franz cell experiments.

On the basis of the obtained results, since P-CA (a) displayed the lowest $T_{sol-gel}$ and spreadability values and (b) was able to better control CA diffusion, p407 was selected for SLN thickening.

6.2.3   Preparation and characterization of nanoparticulate gels

SLN thickening has been achieved by direct addition of p407 to nanoparticle dispersions. The compositions of the obtained nanoparticulate gels are reported in Table 18. The addition of p407 increased consistency but did not affect the macroscopic aspect of nanoparticulate forms, being milky and homogeneous. Cryo-TEM images, reported in Figure. 25 (a) and Figure 25 (b) show the presence of elongated irregular flat particles that appear more thin and electron dense when observed on side view.
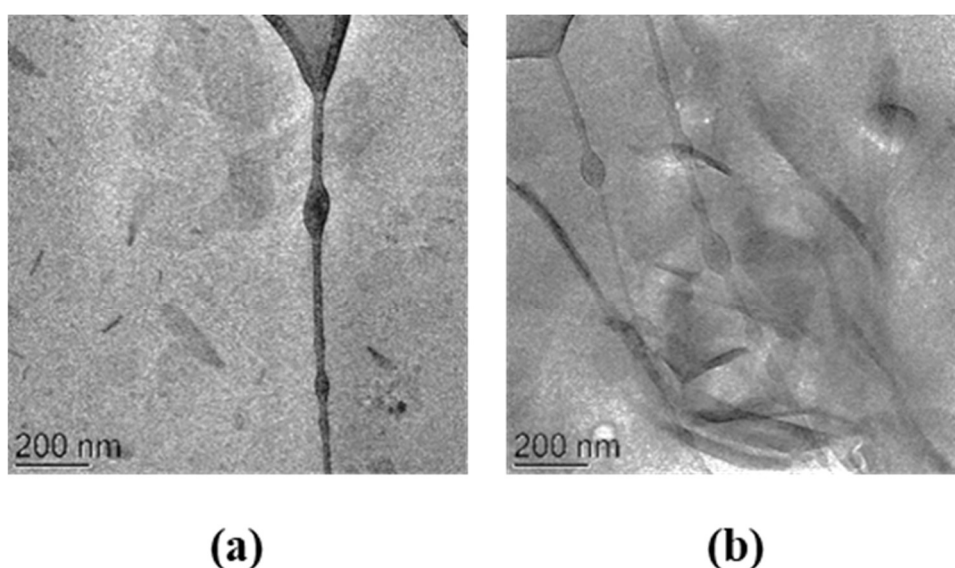

(a)   **(b)**

Figure 25. Cryo-TEM images of SLN-P-CA (a) and (b).

Mean dimensions of SLN-P and SLN-P-CA were almost unvaried, being 10 or 20 mm-higher with respect to plain SLN and CA-SLN, as measured by PCS. As expected, EE values were not affected by p407 addition. The presence of p407 in the aqueous dispersing phase of CA-SLN resulted in the formation of micelles, probably embodying an amount of CA present in the aqueous phase.

6.2.3.1   X-ray scattering analysis

X-ray diffraction experiments on the nanoparticulate gels confirmed that both the nanoparticle inner structure and the whole gel structure were conserved. Indeed, Figure 26 clearly shows that the scattering profile of SLN-P-CA combines the characteristics of the CA-SLN profile (Figure 20b) plus the ones of the profile observed for P-CA (Figures 21b and 26, the second referred to a P-CA sample measured at the same beam-line). Notably, peak positions were very similar: the spacing of the Bragg peaks assigned to SLN scales as 1:2:3 (the second-order peak has a very low intensity also in this case, see Figure 20b), confirming the 1D lamellar organization of the lipid matrix. As a further confirmation of the absence of effects on the structural properties of nanoparticles, the lamellae repeat distance resulted in 43.8 Å (43.9Å in CA-SLN). The position of the low angle peaks corresponding to the gel structural organization (the first narrow and the second rather large, according to the low-degree of order previously discussed) were in the order 1:√3, indicating the preservation of the paracrystalline micellar packing with a lattice constant of ≈ 214 Å (Matsuoka et al., 1990). Accordingly, in the case of P-CA the lattice constant was confirmed to be ca. 220 Å.
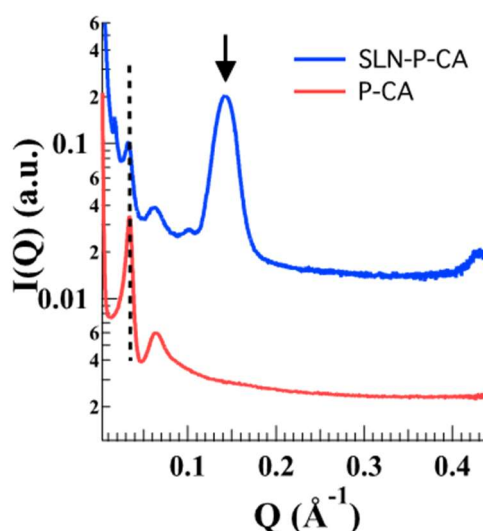

Figure 26. X-ray scattering profiles for P-CA (red) and SLN-P-CA (light blu) samples measured at 37 °C. The dashed line indicates the position of the gel first correlation peak; the arrow points the position of the first Bragg peak related to the inner organization of the SLN. Experiments were performed at Diamond Light Source (UK).

6.2.3.2   Rheological and spreadability studies

The effect of p407 addition has been evaluated on rheological behavior and spreadability of nanoparticulate gel. Particularly the thermosensitive behavior of SLN-P-CA has been compared to plain CA-SLN and to a mixture of p407/ p188 containing CA (P-P188-CA) at the same concentration used for SLN production. Figure 27 shows the effect of the temperature on G' and G'' moduli.

In the case of P-P188-CA (Figure 27a) the G'/G'' profile was similar to P-CA (Figure 23a), even though the presence of p188 delayed significantly the gelation temperature, up to 6 °C concerning P-CA. This behavior could be attributed to the formation of mixed p188/p407 micelles that organized themselves differently concerning the compact paracrystalline structure found in P-CA gel (Artzner et al., 2007; Matsuoka et al., 1990) Conversely, the rheological profile of CA-SLN (Figure 27b) was characterized by the absence of crossover, with G' higher than G'', indicating a more elastic than viscous behavior for the whole temperature range. The differences between P-P188-CA and CA-SLN profiles suggest that p407 governed the copolymer mixture profile, while p188 did not affect CA-SLN rheological behavior. In the case of SLN-P-CA the addition of p407 to SLN did not modify this trend, but a sudden increase of the moduli could be noticed at ≈ 20 ° C. Thus, both SLN and p407 had a major effect on the rheological behavior of the gel. The differences between SLN-P-CA and P-P188-CA profiles should be attributed to the presence of lipid nanoparticles that disorganized the micellar system formed in the case of the mixture of copolymers.

Even though it was not possible to precisely define the $T_{sol-gel}$ of SLN-P-CA, the system was characterized by a soft gel consistency, as confirmed by the spreadability values reported in Table 20. It should be underlined that the spreadability of SLN and CA-SLN was not measurable because of their liquid state. On the other hand, the addition of p407 to SLN and CA-SLN enabled to obtain systems whose spreadability values were closed to those of P and P-CA.
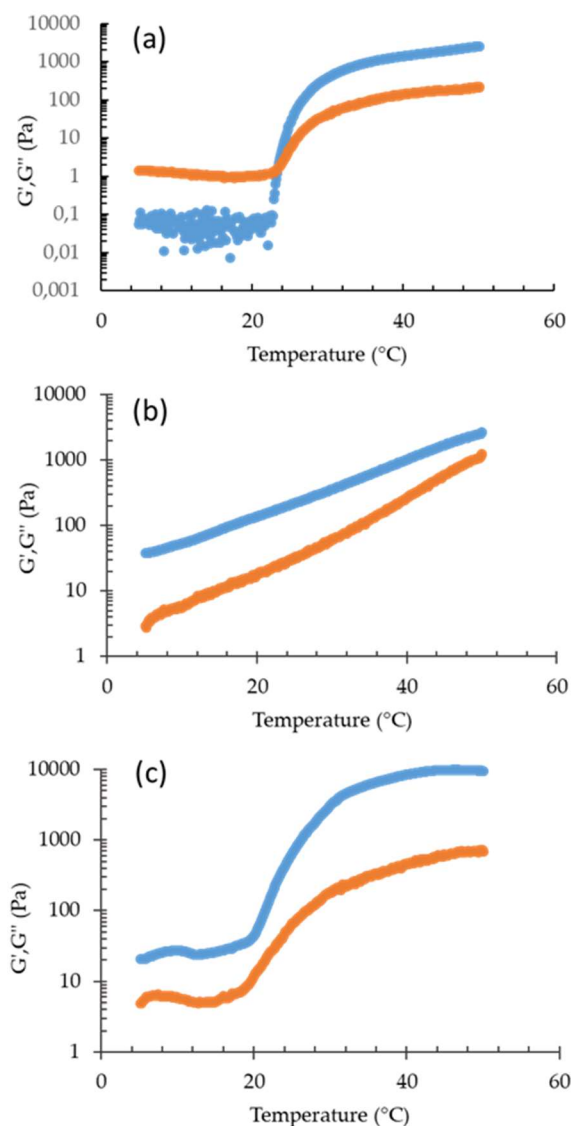
Figure 27. Effect of the temperature on elastic (G', blue) and viscous (G'', orange) for P-P188-CA (a), CA-SLN (a) and SLN-P-CA (b).

6.2.3.3 In vitro CA diffusion kinetics

CA diffusion from SLN-P-CA has been investigated by Franz cell. As shown in Figure 24b, the diffusion profile of CA from the nanoparticulate gel was the slowest, indeed D was 8-fold lower than CA-SOL and 4-fold lower with respect to P-CA. This result suggests that the association between nanoparticles and the entanglement of p407 copolymer chains enabled to slow down CA diffusion.

6.2.4 Ex vivo evaluation of SLN-P-CA in protecting human skin against oxidative damage

6.2.4.1 Immunofluorescence staining

The skin is the main barrier of our body against environmental insults and several studies have investigated the effects of outdoor stressors on cutaneous tissues (McDaniel et al., 2018). For instance, CS, a well-known environmental stressor, is able to interact with lipids present within the SC of the skin, leading to the generation of free radical species and lipid peroxidation products, such as 4-hydroxynonenal (4-HNE) (Pecorelli et al., 2019; Sticozzi et al., 2014). Therefore, in order to investigate the effect of CA delivered by SLN-P in protecting skin against oxidative insults, immunohistochemical analysis for 4HNE protein adducts levels has been performed on HSE with or without SLN-P-CA exposed to CS for 30 min, as reported in the method section, at different time points (0' and 6 hours).

As shown in Figure 28, the HSE exposed to CS displays a significant increase in 4HNE protein adduct levels compared to the not exposed skin explants (Air), both at 0 and 6 hours. Moreover, the pre-treatment with SLN-P-CA was able to counteract the oxidative damage induced by CS exposure, as indicated by the decrease in 4HNE fluorescence intensity level in the SLN-P-CA treated HSE compared to untreated ones.
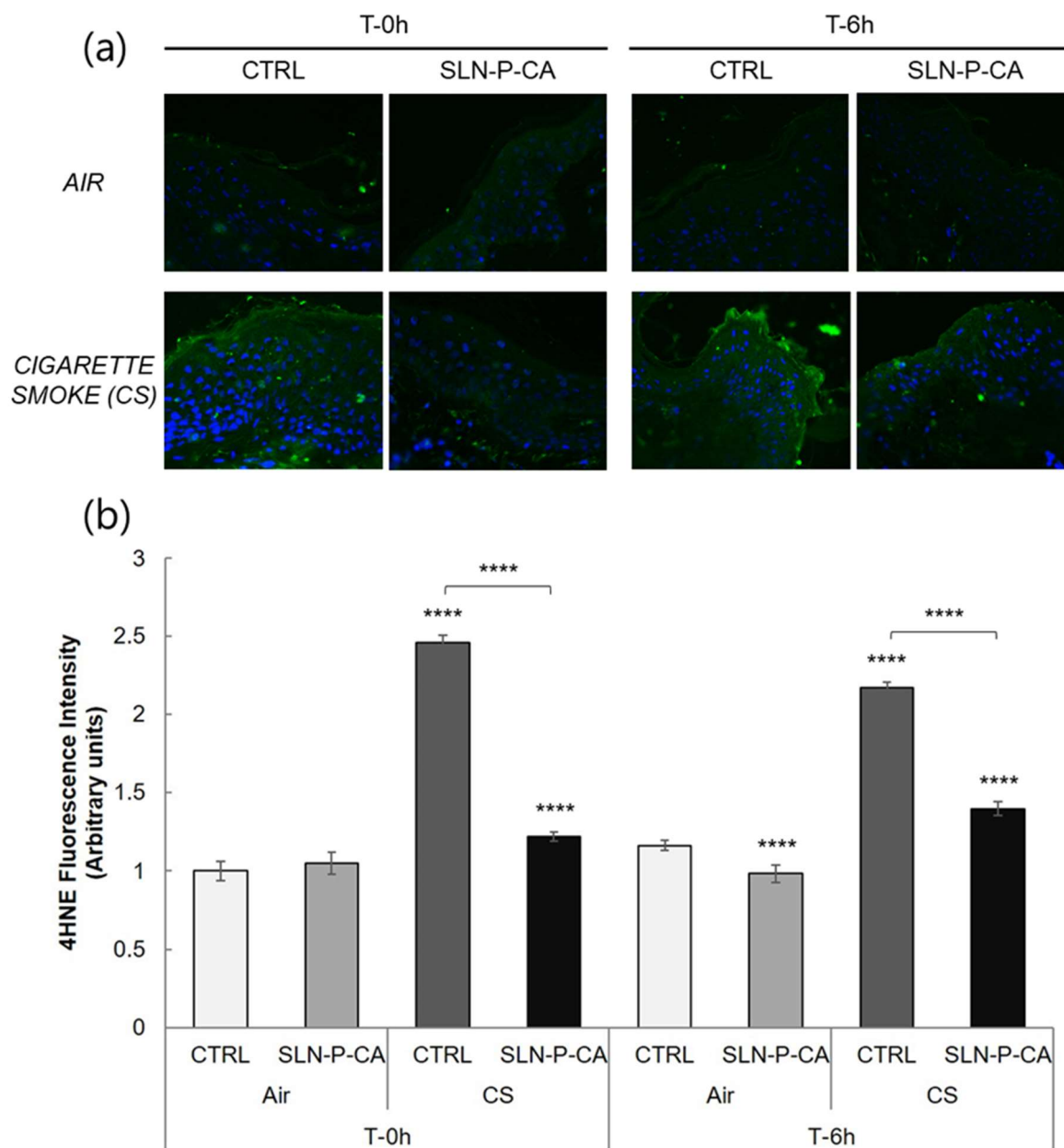
Figure 28: Immunofluorescence (IF) staining for 4HNE (green) and DAPI (blue) in ex vivo human skin biopsies exposed to CS for 30 min directly after exposure and 6 h post-exposure at 40x magnification (panel a). Immunofluorescent signal was semi quantified by using ImageJ software (National Institutes of Health, Bethesda, MD) (panel b). The results are shown as the mean of three experiments. **** $p \leq 0.0001$ with respect to CTRL Air at the same timepoint.

6.2.4.2 Western blot analysis

In order to investigate the effect of CA involved in the cutaneous antioxidant response, Heme oxygenase-1 (HO-1) protein levels (stress-response enzyme (Kubo et al., 2019; Rajagopalan et al., 2016)) were also evaluated in the different samples. HO-1 has been determined by Western blot analysis 24 hours after CS exposure, quantified by densitometry and normalized by the beta-actin level for each sample, as depicted in Figure 29. Our results demonstrate that the pre-treatment with SLN-P-CA was able to counteract the significant increase in HO-1 protein levels induced by CS after 24 hours, confirming the result obtained with immunohistochemical analysis and underlying the ability of the CA containing nanoparticulate gel in preventing skin oxidative stress damage.
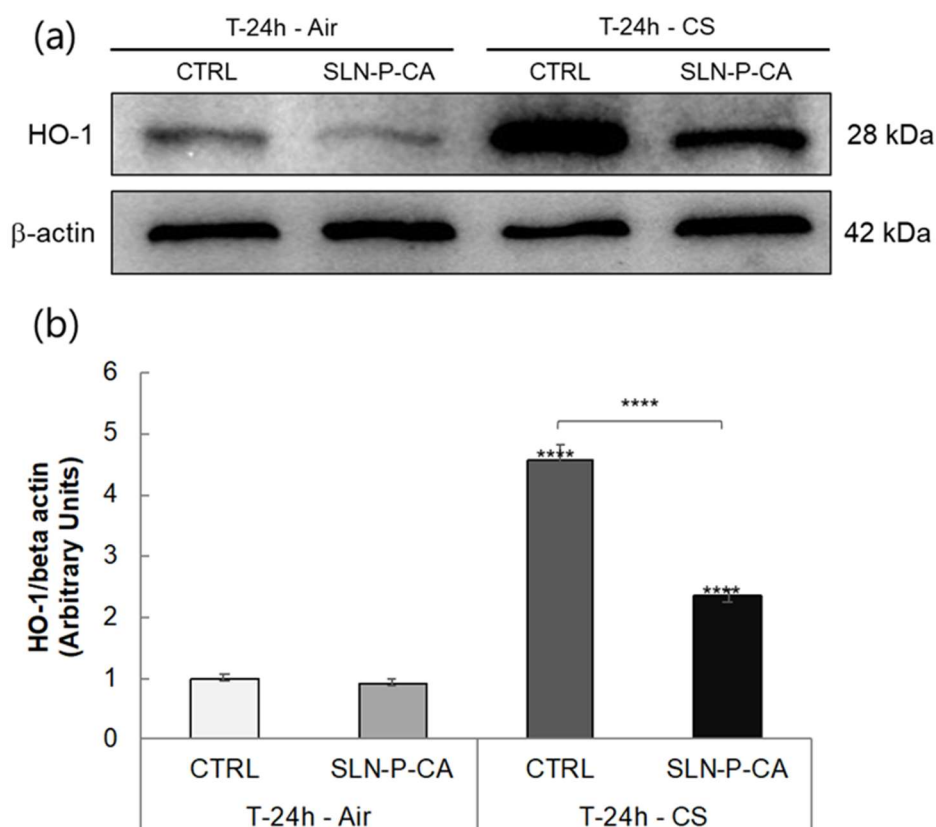
Figure 29: Effect of cigarette smoke (CS) on heme-oxygenase (HO-1) protein expression levels evaluated on human skin explants (HSE) treated with SLN-P-CA, exposed to air or CS for 30 min and harvested after 24 h. (a) Representative Western blot analyses of HO-1 protein expression (with the respective β-actin controls). (b) Mean expression of HO-1 as a ratio of β-actin. The results are shown as the mean of three experiments. **** $p \leq 0.0001$ with respect to CTRL Air.

7 DESIGN AND CHARACTERIZATION OF ETHOSOMES FOR THE TRANSDERMAL DELIVERY OF CAFFEIC ACID

7.1 INTRODUCTION

A broad range of disorders, spanning from inflammatory diseases to skin cancer, many of which did not find yet an efficacious therapy, can affect human skin. Thus, there is an unmet need for effective strategies to treat dermatological pathologies (Boehncke and Schön, 2015; Eyerich and Eyerich, 2018; Leonardi et al., 2018; Wu and Cohen, 2019). Many antioxidant compounds possess therapeutic activities, for instance, CA is a naturally occurring hydroxycinnamic acid with remarkable antioxidant, anti-inflammatory and antiproliferative properties (Esposito et al., 2019a; Gulcin, 2006; Khan et al., 2016; Valko et al., 2007). Notably, some studies have demonstrated CA potential in the treatment of skin inflammatory pathologies, such as psoriasis. Moreover, thanks to its antioxidative power, CA can exert photoprotective action towards DNA damage, protecting skin against aging and preventing melanoma (Działo et al., 2016; Kang et al., 2008; Nichols and Katiyar, 2010; Prasad et al., 2009). Despite the pharmaceutical potential of antioxidant molecules, some of them are prone to degradation, being sensitive to oxygen, light and high temperature (Pinho et al., 2015). Besides, it should be noticed that the barrier effect of the SC often represents an obstacle to active molecules permeation, hampering their final pharmacological effect. In this respect, antioxidant encapsulation could represent an appropriate strategy to control chemical instability and to improve their performances under skin application (Munin and Edwards-Lévy, 2011). Among the different micro and nano-systems provided for drug encapsulation and transdermal delivery, ETHO represent a smart strategy. Indeed, ETHO are vesicular systems constituted of phospholipids, such as phosphatidylcholine (PC), ethanol (20-45%) and water (Godin and Touitou, 2003; Gollavilli et al., 2020; M. Abdulbaqi et al., 2016; Natsheh et al., 2019; Touitou et al., 2000). The multilamellar vesicles of ETHO allow improving the loading of poor soluble molecules with respect to the well-known liposomes. Indeed, the presence of ethanol stabilizes the vesicles and controls their entrapment efficacy (M. Abdulbaqi et al., 2016; Touitou et al., 2000). Moreover, many studies have demonstrated the ETHO capability to achieve transdermal delivery of drugs, due to a synergy between ethanol and phospholipids. In fact, on one hand ethanol renders

vesicles softer with respect to liposome ones, on the other ethanol and phospholipids enhance drug penetration. Indeed, ethanol is able to disorganize the SC barrier, opening spaces for ETHO crossing, while the peculiar structure of phospholipids, similar to skin lipids, promotes ETHO permeation (Godin and Touitou, 2003; M. Abdulbaqi et al., 2016; Natsheh et al., 2019). On this matter some authors have demonstrated the presence of intact vesicles in the skin strata, suggesting that ETHO can overcome the SC, allowing deep drug permeation (Shen et al., 2014; Zhang et al., 2018; Sguizzato et al., 2020b). In this context, the object of the present investigation is a pre-formulative study aimed at the development of ETHO for CA solubilization and delivery through the skin. Particularly, the ETHO capability to control CA degradation has been investigated. Moreover, since low viscous vehicles need a thickening agent to obtain the appropriate residence time when applied on the skin, the copolymer P407 has been added to ETHO. This copolymer, constituted of polyoxyethylene-polyoxypropilene units, possesses thermogelling properties when dispersed in water, passing from fluid to semi-solid materials over a transition temperature $T_{sol-gel}$ a(Artzner et al., 2007; Sguizzato et al., 2020a). The structural organization and mechanical properties of ETHO formulations have been investigated by SAXS and rheometric analyses. Franz cell has been employed to detect the influence of ETHO entrapment on CA diffusion kinetics. Finally, an amperometric study has been conducted in order to evaluate CA permeation through the skin. Particularly, an in vitro tool based on SCOE has been exploited to assess the kinetics of CA penetration through SC and its involvement in antioxidative reactions in skin at the presence of H_2O_2 (Eskandari et al., 2019). In SCOE apparatus, an electrode allows registration of O_2 concentration changes in the membrane due to reactions of H_2O_2 and polyphenols in the skin (Nocchi et al., 2017). This electrochemical monitoring enables to obtain a reliable prediction of in-vivo cutaneous antioxidant administration (Hernández et al., 2019).

7.2 RESULTS AND DISCUSSION

7.2.1 Caffeic acid solubility and stability

To determine the CA stability in water, its content has been evaluated in an aqueous solution of the drug stored in different conditions. Mass spectrometry analyses revealed that CA was soluble in water up to 0.5 mg/ml. CA-SOL underwent complete degradation within one month (Figure 30a). As expected, the degradation was influenced by the temperature, being more rapid in the case of the CA solution stored at 40 °C with respect to 22 and 4 °C.

The mathematical modeling of CA residual content, obtained by fitting profiles with equation 9 and 10 in chapter 3 -methods, section 3.3.3. , revealed that CA stability followed a zero-order kinetic model, as indicated by the high coefficient correlation values reported in Table 22, suggesting that CA stability was independent of its concentration (Permana et al., 2020). In order to control CA stability, the possibility to entrap the drug within a nanotechnological formulation has been investigated.
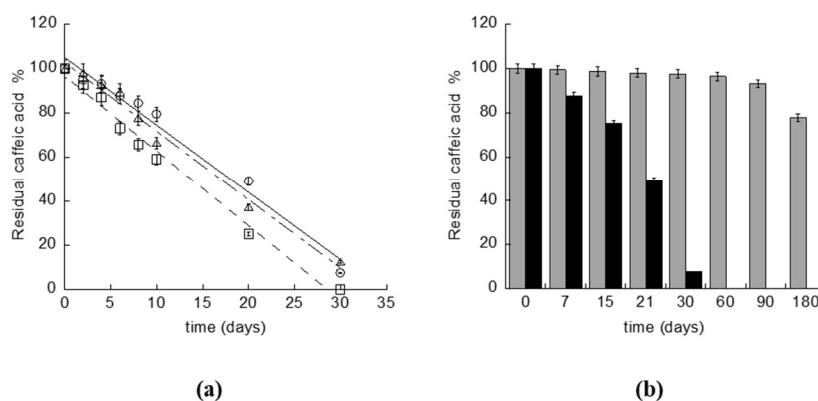

(a)   (b)

Figure 30. (a) Caffeic acid content in aqueous solution stored at 22 (open circle), 4 (triangle) or 40 (square) °C for 30 days. (b) Caffeic acid content in aqueous solution (black) or in ETHO (grey) stored at 22 °C.

Table 22. Kinetic modeling of stability profile of CA-SOL stored for 30 days at different temperatures.

Kinetic parameters	4 °C R^2 / K^1	22 °C R^2 / K	40°C R^2 / K
Zero-order	0.991 / 3.442	0.968 / 3.256	0.986 / 3.382
First order	0.760 / 0.197	0.716 / 0.207	0.869 / 0.142

Where K is the coefficient corresponding to zero or first-order kinetic models and R^2 is the coefficient of determination. data were the mean of 3 independent experiments, S.D. were within ± 5%

86

7.2.2 Preparation of ethosomes

Since CA is soluble in ethanol (up to 50 mg/ml) as per the data from (https://www.chemicalbook.com/ChemicalProductProperty_EN_CB6281061.htm). ETHO were selected for CA delivery, being biocompatible transdermal nano-systems, containing high amounts of ethanol. Particularly, ETHO were constituted of PC ethanol solution and water (30:70 v/v), as reported in Table 23. ETHO were spontaneously and rapidly obtained by a cold method, dropping water into a PC ethanol solution under magnetic stirring, finally leading to milky dispersions. Water addition occurred within 20 sec, afterward the vials have been sealed, preventing ethanol evaporation, indeed ethanol concentration, determined by gas chromatography with thermal conductivity detection (Weatherly et al., 2014) was actually 30 ± 1 % v/v (n = 3). CA-ETHO were obtained after CA solubilization in the PC ethanol solution, followed by the addition of water. ETHO and CA-ETHO compositions are reported in Table 23.

Table 23. Composition of the indicated formulations.

Formulation code	PC[1] % w/w	ethanol % w/w	P407[2] % w/w	water % w/w	CA[3] % w/w
ETHO	0.9	29.1	-	70.0	-
CA-ETHO	0.9	29.1	-	70.0	0.1
pol	-	-	15.0	85.0	-
P-CA	-	-	15.0	84.95	0.05
ETHO-pol	0.76	24.74	15.0	59.5	-
CA-ETHO-pol	0.76	24.74	15.0	59.41	0.085

[1]soy phosphatidylcholine; [2]poloxamer 407; [3]caffeic acid

The EE of CA in ETHO, evaluated by ultracentrifugation and HPLC analysis, indicated that CA was completely associated to vesicles (EE = 98% $\pm$ 2). The high EE achieved by CA-ETHO should be attributed both to the presence of ethanol and to the simple production method, avoiding high energy input, such as heating and mechanical stresses, preserving CA from possible degradation (Munin and Edwards-Lévy, 2011; Sguizzato et al., 2020b). In this respect CA encapsulation in ETHO appears more advantageous with respect to another PC based nanovesicle system recently described by Permana et al. Indeed, the authors reported a more complex preparation procedure, based on rotary evaporation followed by

homogenization and sonication, leading to a 45% EE of CA at the latest (Permana et al., 2020).

The capability of ETHO to solubilize CA has been further investigated, revealing that the upper limit was 5 mg/ml, thus 10-fold higher with respect to CA solubility in water. This result is ascribable to the CA solubility value in ethanol/water (30:70 v/v), being 5.5 mg/ml.

7.2.3 Characterization of ethosomes

To shed light on the structure and dimensions of ETHO, cryo-TEM, PCS and SAXS have been employed. Figure 31 (a) reports a cryo-TEM image of CA-ETHO, showing the typical fingerprint structure, ascribable to the double layer organization of PC, resulting in multilamellar vesicles with spherical, as well as elongated shape. On the other hand, CA-ETHO dispersed within poloxamer gel (CA-ETHO-pol (Figure 31 (b) and (c))maintained similar aspects.

Regarding size distribution as reported in Table 24, mean diameters expressed as Z-Average were around 200 nm, with very slight differences between ETHO and CA-ETHO. PCS analyses evidenced a monomodal size distribution, as indicated by dispersity index values below 0.2 (Table 21).

Table 24. Dimensional distribution parameters of ETHO and ETHO gels, as determined by PCS.

Formulation Code	Time (days)	Z-average (nm) ± s.d.	Dispersity index± s.d.
ETHO	0	212.25 ± 14.10	0.12 ± 0.01
	90	230.52 ± 25.30	0.14 ± 0.03
CA-ETHO	0	218.65 ± 21.0	0.20 ± 0.02
	90	235.45 ± 20.01	0.22 ± 0.03
ETHO-pol	0	279.9 ± 24.30	0.16 ± 0.02
	90	352.15 ± 42.01	0.23 ± 0.03
CA-ETHO-pol	0	288.8 ± 35.50	0.24 ± 0.01
	90	383.25 ± 47.12	0.26 ± 0.03

s.d.: standard deviation; data are the mean of 3 independent determinations on different batches
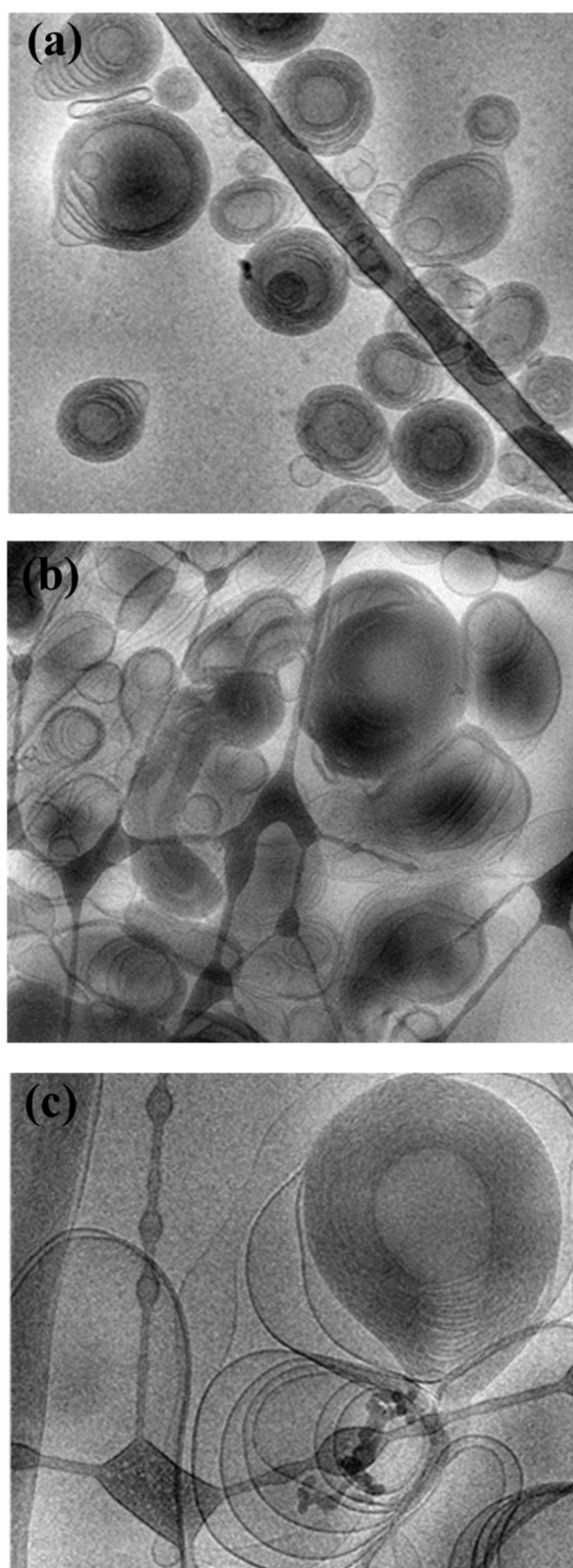
Figure 31. Cryo- TEM images (Cryo-TEM) of CA-ETHO (a) and CA- ETHO-pol (b, c). Bar corresponds to 200 nm (a and b) or 100 nm (c).

SAXS experiments were performed to confirm the structural properties of ETHO. Figure 32a reports water (1), ETHO (2) and CA-ETHO (3) scattering profiles. In the case of ETHO, a typical bilayer form factor scattering pattern (e.g. the broadband centered at about 1.5 nm^{-1}) is observed. Such a profile denotes the presence of PC unilamellar vesicles or, more probably, PC multilamellar vesicles characterized by a very disordered positional correlation between adjacent bilayers and/or by a very limited number of stacked bilayers (Sguizzato et al., 2020b). On the other hand, the X-ray scattering pattern of CA-ETHO is characterized by low-intensity Bragg peaks superposed to the bilayer form factor, as a clear indication of the formation of PC multilamellar vesicles. Therefore, CA presence appears to induce a small but clear increment of the positional correlations between adjacent bilayers (Andreozzi et al., 2010). The bilayer-to-bilayer repeat distance, derived from the peak positions and corresponding to the sum of the bilayer thickness plus the thickness of the water layer separating two adjacent bilayers, was 6.90 nm. In this regard it should be noticed that other authors have found that the incorporation of hydrophobic phenolics into lipid vesicular systems bilayers could thoroughly affect the bilayer organization (Malekar et al., 2016).
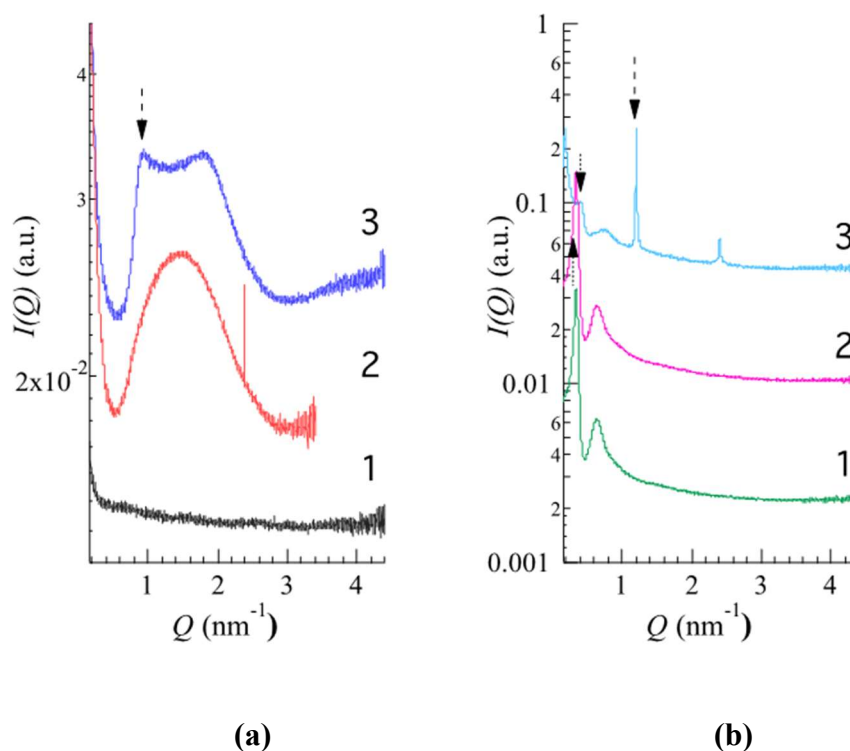

(a)   (b)

Figure 32. SAXS profiles observed at 35 °C. (a): water (1), ETHO (2), CA-ETHO (3); (b): pol (1), P-CA (2), CA-ETHO-pol (3). Arrows indicate the main diffraction peaks.

7.2.4   Evaluation of CA antioxidant activity

The antioxidant activity of the CA-ETHO was evaluated using the DPPH radical scavenging activity and photochemiluminescence methods (Dhavamani et al., 2014; Marinova and Batchvarov, 2011; Singh Hallan et al., 2020). Note worthily, both methods demonstrated that CA encapsulation within ETHO did not affect its antioxidant capacity. Indeed, IC50 values measured by DPPH were 10 μg/ml and 7 μg/ml respectively for CA-ETHO and CA in ethanol solution, while photochemiluminescence revealed an antioxidant capacity of 49.0 ± 0 .9 and 46.4 ± 0.7 μmol TE/ml for CA-ETHO and CA ethanol solution respectively.

7.2.5   Evaluation of CA-ETHO stability

In order to check the size stability of ETHO, size distribution of samples stored in the light at 22 °C has been evaluated by PCS periodically for 3 months. As reported in Figure 33(a) and Table 24, vesicle size remained quite stable, indeed mean diameter slightly increased (≈ 20 nm) after 90 days from ETHO and CA-ETHO production.

CA content in ETHO has been evaluated within 6 months from CA-ETHO preparation, to detect the effectiveness of ETHO in controlling CA degradation. Noteworthily, some authors have investigated the possibility to entrap CA in vesicular or nanoparticulate system, however, to the best of our knowledge, the capability to control CA degradation has not been yet underlined (Dikmen et al., 2015; Permana et al., 2020; Saija et al., 1999; Scheller et al., 2011). Remarkably, after 3 months CA content in ETHO was almost unvaried, being 93% of the initial content, while, after 6 months 77 % of CA was still present in CA-ETHO (Figure 30b). Conversely, a CA ethanol/water solution (30/70, v/v) taken as control, stored at 22 °C, underwent a CA 15 % loss after just 3 days, confirming the role of ETHO in maintaining CA stability.

7.2.6   Ethosome gel preparation and characterization

ETHO dispersions need to be thickened to be applied on the skin (Bendas and Tadros, 2007; Tanrıverdi and Özer, 2013). For this purpose, the copolymer p407 has been directly added into the ETHO dispersions under stirring, up to a final 15 % w/w concentration. The addition of p407 slightly diluted both ETHO and CA-ETHO (Table 23). However, ETHO-pol and CA-ETHO-pol maintained the milky homogeneous aspect of ETHO, while gaining a semi-

solid consistency. It is well known that p407 in water self-aggregates, giving rise to spherical polymeric micelles with a PPO hydrophobic core and a hydrophilic PEO screen (Sguizzato et al., 2020b, 2020a). Upon addition of p407 into ETHO dispersions, reasonably an interaction occurred between the polymer and the multilamellar PC structure constituting the membrane of ETHO vesicles. Moreover, the formation of polymeric micelles, as well as mixed PC-p407 micelles, is conceivable.

In order to detect the influence of p407 on the architecture of CA-ETHO dispersions, their morphology has been visualized by cryo-TEM. Figure 31(b) and 31(c) refer to CA-ETHO-pol, showing irregularly shaped oligo lamellar vesicles with multiple lipid sheets. Particularly, in Figure 31(c) a big multilamellar fingerprint vesicle is detectable, as in the case of CA-ETHO. Cryo-TEM analysis suggests that even if the addition of p407 affected the regular spherical shape of CA-ETHO, the typical supramolecular organization of PC was preserved.

Further insights on the structure of thickened vesicles, especially on the ETHO structural changes due to p407 addition, have been obtained by SAXS. Namely, CA-ETHO-pol has been compared to p407 gel (pol) and to p407 gel loaded with CA (P-CA), whose compositions are reported in Table 23. SAXS results are reported in Figure 32(b), showing very similar curves in the case of pol (1) and P-CA (2), being characterized by two low angle peaks, indicating that no effects were induced by CA addition on p407 aggregation properties. Notably, the recent model-fitting has demonstrated that the two peaks are related to the disordered organization of the polymer micelles in a 3D cubic structure, with a lattice constant of about 20 nm (Sguizzato et al., 2020a). In this respect P-CA profile indicates that 3D organization was not altered by the presence of CA. Conversely, in the case of CA-ETHO-pol (Figure 32(b), 3) the two low angle peaks are further detectable, although in a shifted position, together with strong and narrow Bragg peaks, evidencing that the addition of p407 in CA-ETHO led to a very ordered multilamellar structure. Consequently, three points should be stressed: (i) the diffraction peaks of CA-ETHO-pol were narrower and more intense with respect to CA-ETHO (Figure 32(a), profile 3), suggesting that the diffuse background between the Bragg peaks was no longer modulated by the bilayer form factor. Therefore, the addition of p407 strongly increased the positional correlations between adjacent PC bilayers; (ii) the repeat distance for CA-ETHO-pol appeared 5.20 nm, that is 1.7 nm minor than CA-ETHO, suggesting a diminished hydration of the bilayers; (iii) the 3D

disordered cubic packing observed in P-CA was maintained in the presence of ETHO, though the lattice constant was ≈ 15 nm, hence decreased of roughly 5 nm.

Regarding size distribution, PCS data reported in Table 24 evidenced that mean diameters of ETHO and CA-ETHO underwent roughly a 70 nm increase under p407 thickening, but still maintained a narrow size distribution, as indicated by dispersity indexes. As reported in Figure 33(b)and Table 24, Z-average mean diameters of ETHO-pol and CA-ETHO-pol were almost stable up to 30 days, afterwards they sustained respectively an 80 and 100 nm increase. Anyway, after 3 months from CA-ETHO-pol preparation, Z-Average mean diameter was 383 nm and PI 0.26, indicating that the vesicle size distribution was not particularly affected by aging.
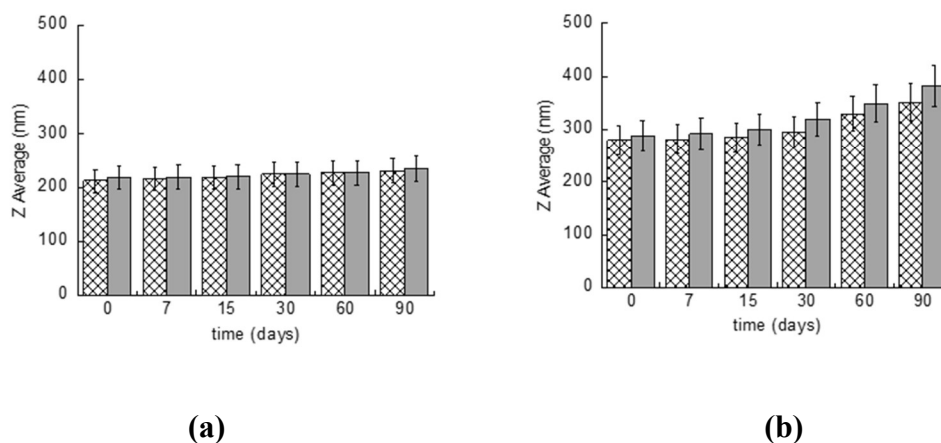

(a) **(b)**

Figure 33. Mean diameter variation for ETHO (a) and ETHO-POL (a) unloaded (criss-cross pattern) or CA loaded (grey pattern). Diameters have been measured by PCS during time, up to 3 months from production and expressed as Z-average. Data are the mean of 3 determinations on different samples.

7.2.7 Rheological study

To straighten out the impact of p407 presence on CA-ETHO and to have information on the thermal response of ETHO formulations, their rheological behaviour has been studied. Particularly the viscoelastic properties have been investigated, evaluating the storage G' and loss G'' moduli. The storage modulus represents the energy stored in the elastic structure of the formulation, while the loss modulus reflects the viscous part or the dissipated energy (Xu

et al., 2014) . Figure 34 reports the G' and G'' profiles for ETHO, ETHO-pol, P-CA and CA-ETHO-pol. In the case of the liquid vehicle ETHO, G' and G'' profiles were roughly constant with low values and overlapped up to 35 °C; afterward they slightly increased, up to 50 °C. On the other hand, in the case of thickened forms, the thermal behavior was very different. Indeed, profiles were characterized by an initial phase where G'' overcame G' at low temperature, followed by a second phase with an inverse trend, with G' higher than G'' at higher temperature. This rheological behavior is characteristic of the thermogelling properties of p407. The inflection points correspond to the $T_{sol-gel}$ temperature, indicating the transition from liquid to structured gel (Dumortier et al., 2006). Since the storage modulus profile overcame the loss modulus, ETHO-pol, P-CA, and CA-ETHO-pol can be considered as mainly elastic above $T_{sol-gel}$. It is interesting to note that the $T_{sol-gel}$ in the case of P-CA was roughly 22 °C (Table 25), while the presence of ETHO substantially reduced $T_{sol-gel}$ by 10 °C. Indeed, the presence of vesicles in ETHO-pol creates a more structured gel network with respect to the pol gel. Moreover, CA presence further increased the gel organization, decreasing the sol-gel transition temperature.
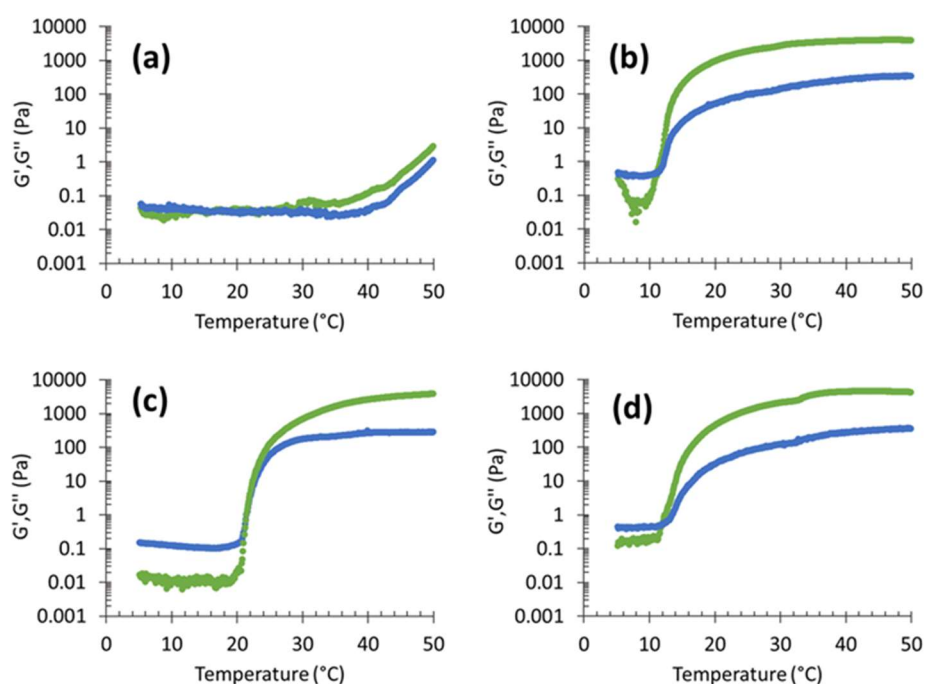

Figure 34. Effect of the temperature on storage (G', green) and loss (G", blue) moduli for ETHO (a), ETHO-pol (b), P-CA (c) and CA-ETHO-pol (d).

7.2.8 Deformability study

One of the peculiar features of ETHO is related to their deformability, enabling them to pass intact through natural membranes, such as the skin (Elsayed et al., 2006). To study the effect of CA and p407 on the deformability of ETHO, the variation of mean diameter has been evaluated under vesicle extrusion. The extrusion was conducted at 25 °C since at higher temperatures CA-ETHO-pol viscosity prevented their passage through the extruder. The results are summarized in Table 25. CA-ETHO were rather more elastic than unloaded ETHO. Notably, ETHO and CA-ETHO were characterized by deformability values 10-and 20-fold higher with respect to the thickened forms. Thus, the presence of p407 decreased the vesicle deformability, indeed as demonstrated by SAXS measurements, in the case of CA-ETHO-pol, the polymer promotes the formation of packed multilamellar structures.

Table 25. Deformability parameters and transition temperatures of the indicated formulations.

Formulation Code	Vesicle size[1] (nm)	Def[2] (ml/min)	$T_{sol-gel}$ (° C)
ETHO	109.13 ± 1.07	6.21 ± 0.52	-
CA-ETHO	116.80 ± 1.60	8.06 ± 0.46	-
P-CA	-	-	21.87 ± 0.99
ETHO-pol	186.93 ± 17.66	0.61 ± 0.04	11.43 ± 0.47
CA-ETHO-pol	194.13 ± 9.71	0.40 ± 0.16	13.60 ± 2.13

[1]Z-Average, as measured by PCS after extrusion; [2] vesicle deformability; data are the mean of 3 independent determinations on different batches

7.2.9 In vitro CA diffusion kinetics

To gain information on the efficiency of ETHO as cutaneous vehicles for CA, its diffusion kinetics have been studied in vitro by Franz cell-associated to nylon membranes (Dhavamani et al., 2014). We chose to employ a synthetic membrane to perform an initial comparative screening between the different formulations, while porcine skin membrane has been further employed for ex-vivo evaluation. Namely, CA-ETHO-pol has been investigated and compared to P-CA and the CA-SOL (Figure 35). From the slopes of the linear profiles, F values have been obtained, D values have been calculated and reported in Table 26. As expected, the fastest diffusion has been obtained in the case of CA-water, followed by P-CA, from which CA diffusion was almost 4-fold slower. CA diffusion from CA-ETHO was

dramatically slower, indeed D values were 137-fold lower with respect to CA-water, suggesting that the multilamellar organization of the vesicles firmly held CA and controlled its diffusion. In this regard other authors described multilamellar vesicles as more suitable to control drug release with respect to unilamellar ones (Joo et al., 2013). The vesicle role in controlling CA diffusion was confirmed also in the case of the thickened vehicle CA-ETHO-pol, indeed the drug diffusion was 8.6-fold lower with respect to P-CA. On the other hand, CA diffusion from CA-ETHO was 4-fold slower than from CA-ETHO-pol. This behavior was unpredictable, indeed the viscous structure of the ETHO gel was expected to restrain CA diffusion. Anyway, it can be hypothesized that, in the case of CA-ETHO-pol, the addition of p407 affected the strong CA association to the PC bilayers, as indicated by the diminished hydration of the bilayers and increased order found by SAXS (Figure 32b). Thus, CA could be more tightly associated to the PC bilayer of ETHO vesicles with respect to ETHO-pol structure, from which CA can diffuse faster.
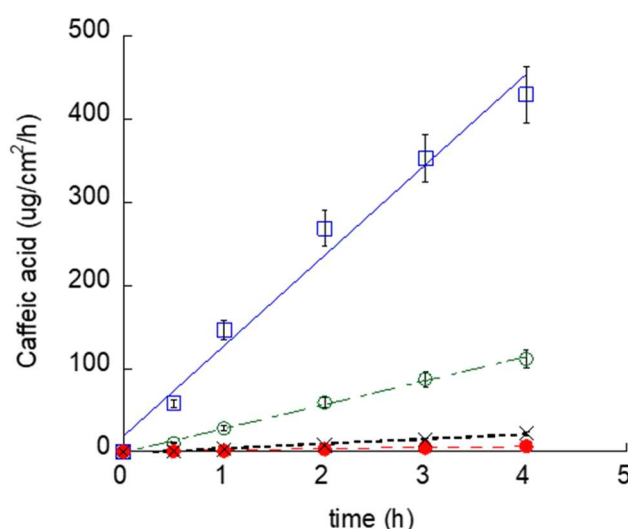

Figure 35. CA diffusion kinetics from CA-water (blue square), P-CA (green open circle), CA-ETHO (black crosses) and CA-ETHO-pol (red closed circle), as determined by Franz cell. Data are the mean of 6 independent experiments.

Table 26. Fluxes and diffusion coefficients of the indicated formulations.

| Formulation code	$F^1 \pm$ s.d. (mg/cm^2/h)	CA (mg/ml)	$D^2 \pm$ s.d. (cm/h)*10^{-3}
CA-water	108.77 ± 13.4	0.5	217.54 ± 26.8
P-CA	28.70 ± 3.4	0.5	57.40 ± 6.8
CA-ETHO	1.59 ± 1.1	1.0	1.59 ± 1.1
CA-ETHO-pol	5.64 ± 2.4	0.85	6.63 ± 2.82

[1]Flux; [2]Diffusion coefficient; data are the mean of 6 independent Franz cell experiments

7.2.10 Ex-vivo evaluation of permeation and role of CA in antioxidant reactions in skin

Amperometric measurements have been conducted to detect the CA permeation through the skin. Particularly SCOE has been prepared by placing skin membrane on the tip of the oxygen electrode. The electrode allows registration of O_2 concentration changes in the membrane due to reactions of H_2O_2 and polyphenols in the skin. In brief, when SCOE is immersed into a buffer solution, the electrode current (baseline current) corresponds to 0.26 mM of dissolved O_2 in the solution. To model inflammatory conditions with elevated ROS in skin, H_2O_2 is added into the solution. The H_2O_2 permeates through the SC and gives rise to additional O_2 (Equation 14), thus increasing electrode current, due to CAT enzyme abundantly present in the epidermis:

$$2H_2O_2 \xrightarrow{Cat} 2H_2O + O_2 \tag{14}$$

The possible polyphenol penetration and its engagement in the antioxidative reactions are indicated by the SCOE, showing the reduction of the electrode current. To understand this amperometric response, it should be considered that several antioxidative enzymes in the skin possess PER type activity (equation 15), which in the presence of polyphenols consume H_2O_2, leaving less of it for CAT reaction (equation 14). The PER type reaction, in the case of the polyphenol CA as a hydrogen donor, for reduction of H_2O_2 to water is specified below.

$$2H_2O_2 + CA \xrightarrow{Peroxidase\ like\ enzymes\ in\ skin} 2H_2O + CA_{ox} \tag{15}$$
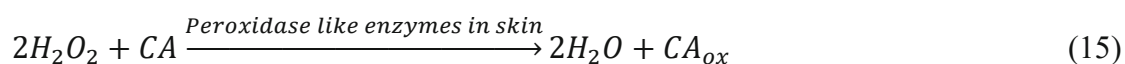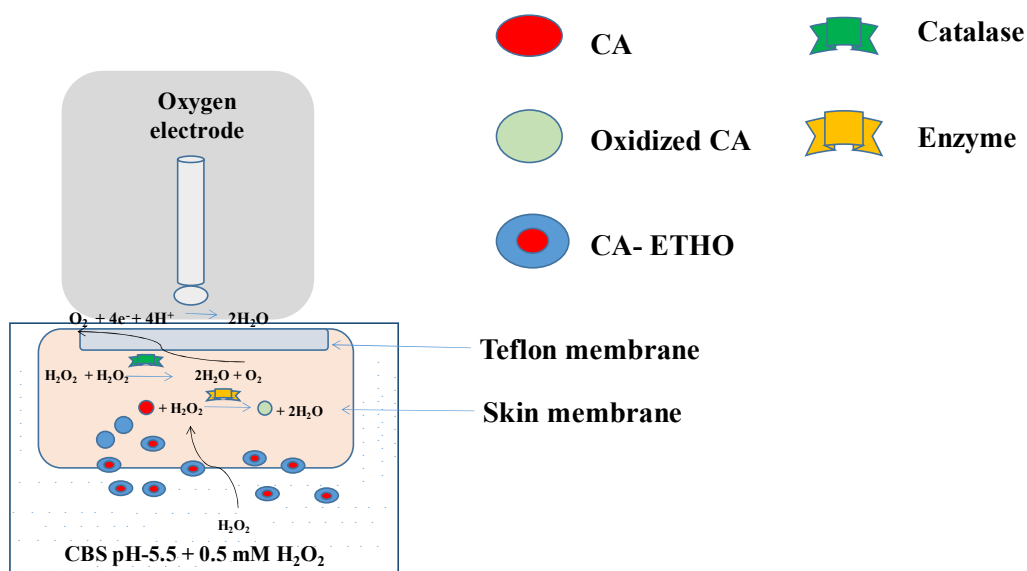
Figure 36. Schematic representation of mechanism of skin covered oxygen electrode.

In a previous study, the possibility of SCOE to monitor the kinetics of polyphenol penetration through SC and its engagement in antioxidative reactions in the presence of H_2O_2 in skin has been demonstrated in Figure 36(Eskandari et al., 2019). SCOE allowed assessing permeability and engagement of CA in antioxidant reactions, which are catalysed by PER like enzymes present in skin. The results of the measurement with this electrode are presented in Figure 37 and can be explained by the following. After the SCOE is immersed in CBS, approximately 30 min are needed to get steady-state current, indicating that skin, O_2 distribution in the skin as well as O_2 diffusion profiles in the skin have equilibrated after immersion of SCOE into CBS. As can be seen from Figure 37, when 0.5 mM of H_2O_2 is injected into the measurement cell filled with CBS, a gradual increase in reduction current (reduction current is regarded as negative by definition) has been observed, due to H_2O_2 penetration into the skin and production of O_2 by CAT reaction (equation 14). Due to biological variability of skin, the SCOE response to H_2O_2 is presented as an average response (Figure 37).
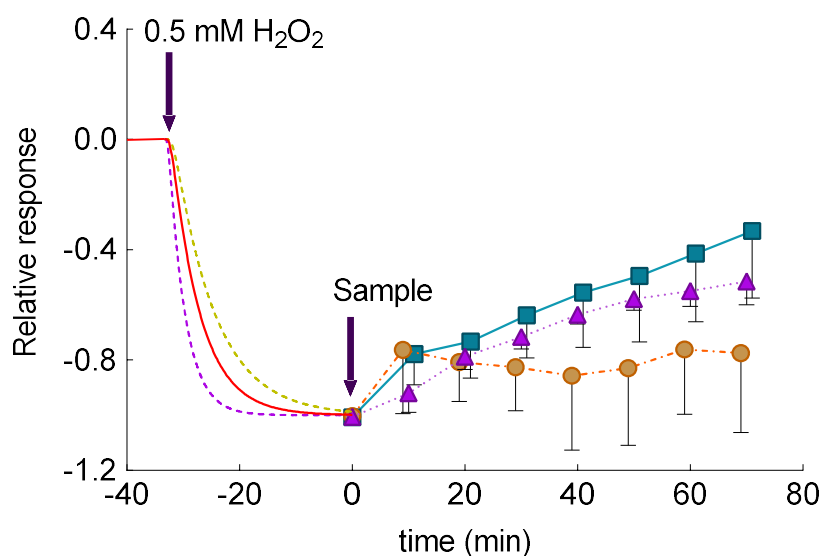
Figure 37. Relative, average amperometric current response of SCOE immersed in CBS, pH 5.5, to addition of H_2O_2 (0.5 mM, red dotted and solid lines, n = 13) CA sol (CA 0.5 mM, triangle, n = 3); CA-ETHO (CA 0.5 mM, square, n = 6) and unloaded ETHO (circles, n = 4).

As can be seen from Figure 37, a steady-state current is reached after approximately 30 min, indicating that equilibrium between H_2O_2 penetration/diffusion in skin and CAT driven O_2 production has been reached. This current response is considered as 100% response to H_2O_2. Since H_2O_2 is, currently, present in the skin, the experiment setup models inflammatory conditions in skin with respect to elevated ROS. The time moment at which this model situation is reached is considered as "time zero" for studies of polyphenols antioxidant effect in the skin. At this time, the CA has been introduced into the measurement cell in form of CA solution (CA-SOL or CA-ETHO. Upon addition of CA-ETHO and CA-SOL, the antioxidant effect of CA has been revealed by SCOE response to lower current (Figure 37), indicating that an amount of H_2O_2 was reduced to water by CA, due to a PER -like reaction in the skin. Noticeably, unloaded ETHO introduced into the cell at time zero, exerted an initial response within 10 min. afterward, unloaded ETHO did not produce a significant change, returning to base line, whereas CA-ETHO kept increasing the SCOE response in the following 60 min. The initial response could be probably ascribed to the antioxidant and barrier enforcing properties of PC (Nwosu et al., 1997; Saito and Ishihara, 1997), conferring antioxidant activity also to unloaded ETHO. On the other hand, in the case of ETHO loaded

with an antioxidant molecule such as CA, a synergistic effect was exploited. In the case of CA-SOL, SCOE response was appreciable, although more delayed and less intense with respect to CA-ETHO. These results suggested that both CA-SOL and CA-ETHO have been engaged in the reduction of H_2O_2. Anyway, the antioxidant effect exerted by CA-ETHO, as well as CA penetration, were more intense with respect to the drug in solution, demonstrating that CA delivery through the skin should be ascribed to the ETHO supramolecular structure and not merely to the ethanol presence. The integrity of skin membranes has been assessed by electrical impedance measurements of their resistance [25]. The measured values were higher than 3 kΩ, demonstrating that skin membranes have good integrity, i.e., intact SC. SCOE findings agree well with those obtained by diffusion experiments in terms of effective delivery of CA through membranes. Noteworthily, CA diffusion through synthetic nylon membrane was retarded by ETHO (lower apparent diffusion coefficient, Table 26) while experiments with SCOE clearly showed that ETHO formulation promoted CA delivery into skin. Therefore, it can be concluded that the present data corroborated previous findings indicating the transdermal potential of ETHO (Godin and Touitou, 2003; M. Abdulbaqi et al., 2016; Natsheh et al., 2019; Touitou et al., 2000).

8 THE POTENTIAL OF CAFFEIC ACID LIPID NANOSYSTEMS FOR SKIN APPLICATION: IN VITRO ASSAYS TO ASSESS DELIVERY AND ANTIOXIDANT EFFECT

8.1 INTRODUCTION

The human skin acts as an environmental barrier, protecting the organism from external insults (Wu and Cohen, 2019). Nonetheless, it should be considered that the skin is exposed to many physical and chemical factors, spanning from UV radiation to xenobiotics (Oliveira et al., 2018), that trigger the dramatic production of ROS (Valko et al., 2007). The skin oxidative stress induced by ROS generation leads to many skin disorders, such as aging, or serious pathologies, such as melanoma (Leonardi et al., 2018). It is well known that natural and synthetic antioxidant molecule*s* are able to counteract the free radical's production, preventing the occurrence of many diseases and boosting the organism with detoxifying mechanisms (Bickers and Athar, 2006; Holst and Williamson, 2008). Particularly, phenolic compounds deriving from vegetable sources possess remarkable antioxidant properties, offering the potential for many medicinal applications (Abdel-Mottaleb et al., 2014; Działo et al., 2016; Nichols and Katiyar, 2010). Among them, CA, naturally found in coffee, fruits, plants, oils, grapes, and tea, is a hydroxycinnamic acid characterized by strong antioxidant power, due to radical scavenging activity and inhibition of lipid peroxidation (Gulcin, 2006; Kang et al., 2008; Prasad et al., 2009). Thanks to this potential, CA can be employed in the treatment of UVB-induced photoaging and in the chemoprevention of malignant melanoma (Jeon et al., 2019; Khan et al., 2016; Pelinson et al., 2019). However, the poor water solubility and chemical stability of CA makes necessary the use of specialized delivery systems suitable for its solubilization, protection from degradation and maintenance of antioxidative power (Fathi et al., 2013; Hallan et al., 2020; Pinho et al., 2015; Sguizzato et al., 2020a). Recently, researchers have proposed nanosystems for antioxidant molecules encapsulation in order to preserve them from degradation and to ensure a prolonged action (Borges et al., 2020; Munin and Edwards-Lévy, 2011). Among the others, nanosystems based on natural lipids have gained particular attention due to their biocompatibility, the capability to encapsulate lipophilic molecules and easy way of production, avoiding the use of organic solvents, thus ensuring a low toxicity profile. Additionally, lipid based

nanosystems are suitable for cutaneous application, due to the affinity of their matrix with the SC intercellular lipids (Esposito et al., 2019b). Upon dispersion in water, lipids give raise to a variety of supramolecular structures, organized in different crystalline phases (Kulkarni, 2012). Among the various colloidal systems that can be obtained depending on composition and production method, SLN and ETHO deserve particular interest. Concerning SLN, their matrix is usually constituted of solid lipids, such as glycerides, sterols, fatty acids or waxes (Mehnert, 2001). Many studies have demonstrated the capability of SLN to encapsulate active molecules in an aqueous physiological environment, modulating their release and prolonging the therapeutic potential (Esposito et al., 2012; Paliwal et al., 2020; Scioli Montoto et al., 2020). Notably, SLN have been recently proposed for oral and cutaneous administration of phenolic compounds, protecting them against chemical degradation (Borges et al., 2020; Han et al., 2014). On the other hand, ETHO are thermodynamically stable vesicular systems constituted of phospholipids, ethanol and water (M. Abdulbaqi et al., 2016). The ETHO vesicles are organized as lipid bilayers connecting two hydrophilic regions, typified by an inner core and a dispersing phase, offering the possibility to solubilize molecules with different physical-chemical properties (M. Abdulbaqi et al., 2016; Sguizzato et al., 2020b). Unlike the well-known liposomes, having some drawbacks, such as poor physical stability and high manufacturing costs, ETHO are striking delivery systems due to long stability and simple production processes (Sguizzato et al., 2020b). Furthermore, the ethanol presence (30-45 % v/v) confers to ETHO vesicles a soft consistency, enabling their interaction with physiological membranes. Due to their potential, ETHO have been investigated as cutaneous delivery systems of many drugs, including phenolic compounds (Godin and Touitou, 2003; Natsheh et al., 2019). The cutaneous application of lipid nanosystems allows treating many dermatological disorders and pathologies. Indeed, the close interaction between the lipid matrix and the SC lipids promotes the passage of the active molecules through the skin (Zeb et al., 2019). In this regard, some authors have reported that SLN matrix applied on the skin can fuse, thus forming a lipid film that exerts an occlusive effect, enabling the permeation of the encapsulated drugs (Han et al., 2014; Zeb et al., 2019). Others suggest the formation of a drug reservoir in skin, depositing the drug in the SC (Jensen et al., 2011). Conversely, many studies have evidenced the transdermal effect of ETHO, allowing deep penetration of drugs through the skin strata (Sguizzato et al., 2020b; Shen et al., 2014; Zhou et al., 2010). In line with this, ethanol is supposed to disorganize the SC barrier, opening spaces through which

the soft and malleable ETHO vesicles can pass, as indicated by the presence of intact ETHO in the epidermis (Niu et al., 2019; Sguizzato et al., 2020b). Different nanosystems have been investigated as carriers for phenolic compounds, demonstrating their interaction with the skin, resulting in permeation of their encapsulated drugs and improvement of their effectiveness (Borges et al., 2020; Esposito et al., 2019a; Fathi et al., 2013). To the best of our knowledge, the influence of the nanosystem type on antioxidant behavior and transdermal potential of the phenolic compound, has not been yet investigated. On this matter, the present study describes a comparison between SLN and ETHO for the cutaneous administration of CA. The effect of CA encapsulation has been evaluated, comparing size, morphology, and EE. Furthermore, the physical-chemical stability of the two nano-systems, as well as in vitro CA diffusion kinetics have been studied. Noteworthily, in order to compare the in vivo antioxidant potential of CA encapsulated in SLN and in ETHO, an amperometry-based approach has been employed. This recently developed electrochemical technique, based on the use of a pig SCOE, allows to predict the kinetics of antioxidant molecules penetration across the SC and its further engagement in anti-oxidative reactions, occurring in the skin in the presence of H_2O_2(Hernández et al., 2019; Nocchi et al., 2017). The SCOE method enables to measure the alterations in O_2 concentration within the skin due to the reactions of H_2O_2 with antioxidants, mimicking in this way their cutaneous administration (Nocchi et al., 2017). In this study, the SCOE approach was employed to compare the penetration enhancer properties of SLN and ETHO upon cutaneous application, as well as the antioxidant power exerted by CA encapsulated in the two nanosystems.

8.2   RESULTS AND DISCUSSIONS

8.2.1   Preparation of nanosystems

The encapsulation of CA in nano-systems suitable for its administration on the skin has been investigated. Particularly the performances of two lipid-based biocompatible vehicles, i.e. SLN and ETHO have been considered and compared. SLN dispersions were produced by emulsification of molten tristearin (representing the lipid phase) with a solution of poloxamer 188 (representing the aqueous phase) by hot homogenization followed by ultrasonication (Sguizzato et al., 2020a). ETHO were produced by a cold method, adding water into a PC ethanol solution under magnetic stirring (Hallan et al., 2020). To encapsulate CA, in the case of CA-SLN the drug was added to fused tristearin before emulsification, while in the case CA-ETHO, the drug was solubilized in the PC ethanol solution before

water addition. Both SLN and ETHO were milky and homogeneous dispersions, devoid of agglomerates, whose aspect was not affected by CA presence. Table 27 reports the composition of unloaded or CA loaded SLN and ETHO.

Table 27. Composition (% w/w) of the produced nanosystems.

Nanosystem	PC[1]	tristearin	poloxamer[2]	ethanol	water
SLN	-	5	2.38	-	92.62
[3]CA-SLN	-	5	2.38	-	92.52
ETHO	0.9	-	-	70	29.1
[3]CA-ETHO	0.9	-	-	69.9	29.1

[1]phosphatidylcholine; [2]poloxamer 188; [3]caffeic acid 0.1 % w/w.

8.2.2 Morphological analysis

The morphology of CA containing nanosystems was investigated by TEM and cryo-TEM, being suitable techniques to get information on the shape of colloidal systems. In the case of TEM, the stained technique allows to obtain a "negatively" colored preparation in which it is possible to view the details of the treated particles under the TEM, appearing transparent on a dark background when crossed by the electron beam. On the other hand, by cryo-TEM higher resolution analysis of colloidal dispersions can be obtained, using unstained vitrified specimens by the "thin-film" technique (Almgren et al., 2000). This latest method enables to detect the inner structure of nanoparticles and to get information on their supramolecular organization. Figure 38 shows microphotographs of CA-SLN (a, b) and CA-ETHO (c, d) obtained by TEM (a, c) and cryo-TEM (b, d). The use of the different microscopic methods enabled to appreciate the differences between SLN and ETHO nanostructures. Indeed, the shape of CA-SLN nanoparticles appears irregular and flat, both in the case of TEM and cryo-TEM images. Instead, CA-ETHO visualized by TEM analysis showed an evanescent and fluffy aspect, typical of nanovesicles, confirmed by cryo-TEM, revealing the PC double layers of multilamellar vesicles with spherical and ovoidal shape. ETHO are typically characterized by a finger-print multilamellar pattern. This structure characterizing the membrane of ETHO makes them suitable for transdermal penetration (Hallan et al., 2020).

The inner structure of SLN and ETHO has been investigated by X-ray diffraction. The SAXS profiles reported in Figure 39 (a) confirm the lamellar organization already detected both in the case of SLN and CA-SLN (Sguizzato et al., 2020a). From the Bragg peaks, a bilayer-to-

bilayer repeat distance (i.e. the sum of the bilayer thickness plus the thickness of the water layer separating two adjacent bilayers) of 4.39 nm has been derived, independently from the presence or the absence of CA. Such a result confirms that the presence of CA did not affect the structural organization of SLN (Sguizzato et al., 2020a).
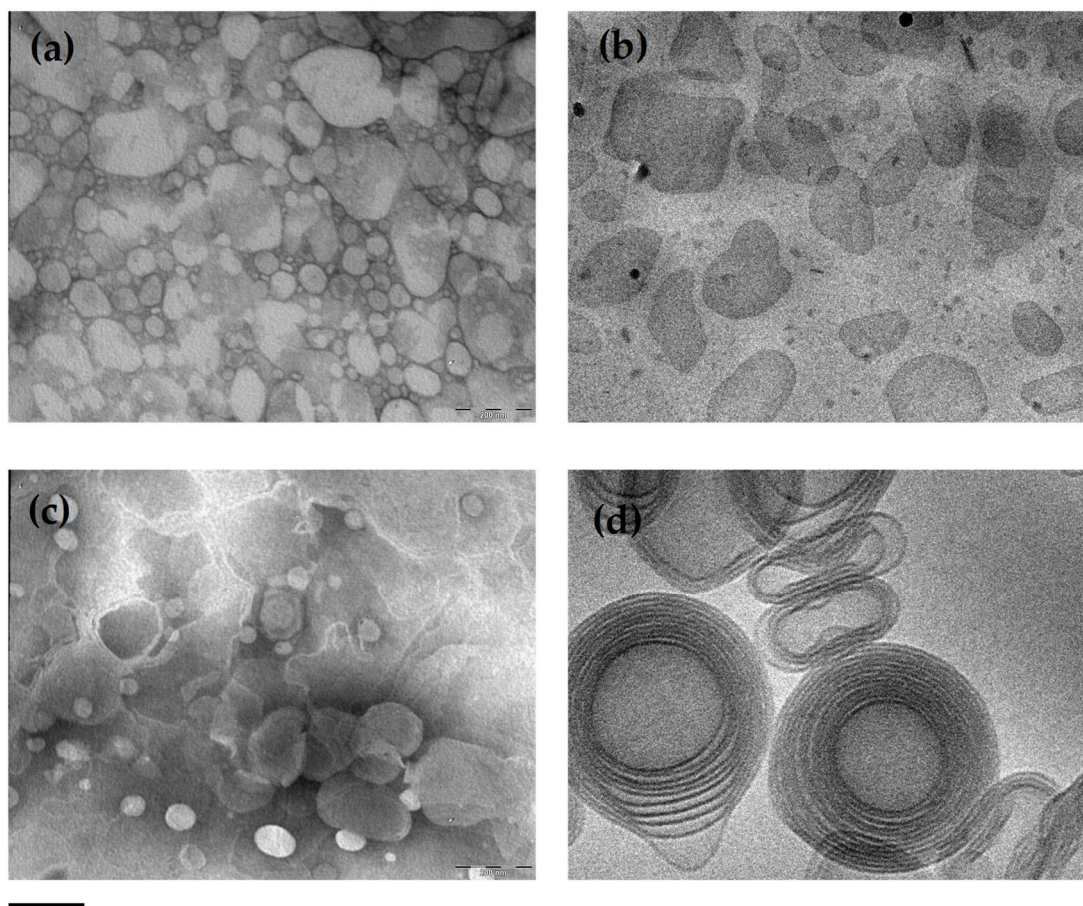

Figure 38. CA-SLN (a, b) and CA-ETHO (c, d) obtained by transmission (a, c) or cryogenic transmission (b, d) electron microscopy. The bar corresponds to 150 nm in panels (a), (b) and (c) and 50 nm in panel (d).

Completely different profiles were observed in the case of ETHO. As shown in Figure 39, panel (b), the scattering pattern for ETHO is characterized by a broad band, approximately centered at 1.5 nm^{-1} and typically associated to the bilayer form factor (Hallan et al., 2020). As observed by cryo-TEM, this profile confirms the presence of PC multilamellar vesicles characterized by a very disordered positional correlation between adjacent bilayers and/or by only a few stacked bilayers (Sguizzato et al., 2020b). After the addition of CA, low

intensity Bragg peaks superposed to the bilayer form factor band become visible, endorsing the presence of PC multilamellar vesicles with an increased positional correlation between adjacent bilayers. Indeed, the observed ordering of the lamellae stacking can be explained by considering that CA insertion modifies the surface charge density of the ETHO bilayers and then the balance between attractive and repulsive forces between adjacent membranes (Andreozzi et al., 2010). The peak position indicates a bilayer-to-bilayer repeat distance of 6.90 nm. As found by other authors, the association of phenolic compounds to vesicular systems organized in bilayers can positively influence the bilayer organization (Malekar et al., 2016).
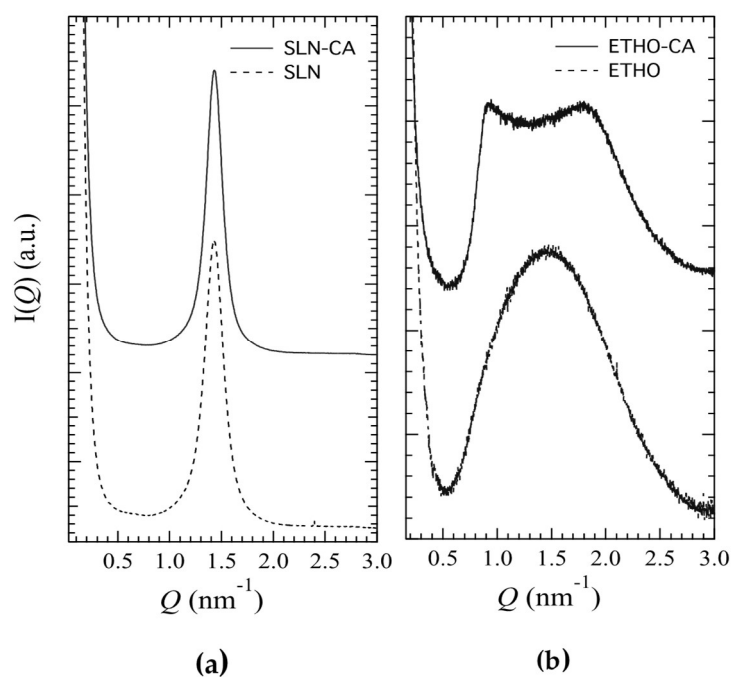

Figure 39. X-ray scattering profile of SLN (a) and ETHO (b) produced either in the absence (dotted lines) or in the presence (solid lines) of CA.

Therefore, based on cryo-TEM and SAXS analysis results, SLN are characterized by a lipid tristearin matrix organized in lamellar structures dispersed in a poloxamer aqueous phase, while the dispersed phase of ETHO is constituted of PC organized in multilamellar vesicles embedding water and ethanol. Surface charge density changes produced by CA addition are probably responsible for the observed bilayer ordering observed in CA-ETHO samples.

8.2.3 Size distribution

The size distribution of nanosystems was evaluated by PCS (Table 28). SLN and ETHO mean diameters ranged between 200 and 220 nm, expressed as Z-average, i.e. the intensity weighted mean hydrodynamic size of nanoparticles, with dispersity indexes 0.28-0.29, indicating a quite homogeneous size distribution as evidenced in the TEM images reported in Figure 38. The typical intensity distribution, reported in Table 28, revealed the presence of two populations, the more represented of which has a diameter of approximately 200 nm. CA did not affect the mean size of the dispersed nanoparticles.

Table 28. Dimensional characteristics, zeta potential, pH and encapsulation parameters of SLN and ETHO.

Parameter	SLN	CA-SLN	ETHO	CA-ETHO
Z-Average[1] (nm) ± s.d.	216 ± 12	201 ± 11	212 ± 14	219 ± 21
Dispersity index[1] ± s.d.	0.28 ± 0.02	0.29 ± 0.03	0.28 ± 0.02	0.29 ± 0.03
Intensity[2] (nm) ± s.d.	180 (88%); 1250 (12%)	175 (90%); 1400 (12%)	210 (94%); 800 (6%)	215 (90%); 850 (10%)
Zeta potential	-13.8 ± 0.1	4.9 ± 0.1	-16.2 ± 4.5	+1.99 ± 2.48
pH	5.46 ± 0.01	3.66 ± 0.02	5.64 ± 0.02	3.75 ± 0.01
Encapsulation efficiency (%)[3]	-	82.2 ± 8.3	-	100 ± 2.0
Loading capacity (%)[4]	-	1.6 ± 0.03	-	11 ± 0.10

[1]as determined by PCS; [2] typical intensity distribution obtained by PCS, referring to the percentage of each population; [3]percentage (w/w) of drug encapsulated, with respect to the total amount used for the preparation; [4]percentage (w/w) of drug within nanosystems, as compared to the amount of lipid used for the preparation. Data represent the mean ± s.d. of 6 independent experiments.

8.2.4 Zeta potential

Zeta potential indicates the electric potential of the nanosystems, including their ionic environment (Zhou et al., 2010). Electrophoretic light scattering enabled to measure the surface charge of nanoparticles. SLN and ETHO produced in the absence of CA displayed negative and similar zeta potential values (Table 28). In the presence of CA, zeta potential values of both nanosystems became less negative, showing an absolute value reduction of 8.91 in the case of CA-SLN and 18.2 in the case of CA-ETHO. Notably, CA-ETHO are characterized by an almost neutral zeta potential value, indicating the presence of roughly the same positive and negative electron charges over ETHO surface, in agreement with

SAXS results, advising surface charge density changes in the case of CA-ETHO. As previously found by other authors, negatively charged nanoparticles can be suitable for incorporating positively charged drugs due to electrostatic attraction(Zhou et al., 2010), suggesting that CA positive charges neutralize the negative charges on the nanoparticle surface. The pH values of SLN and ETHO corroborated this hypothesis. Indeed, while SLN and ETHO showed pH values around 5.5, the values were lower in the presence of CA (Table 28). In this respect, the SLN and ETHO opposite charges with respect to CA could be considered as an important factor, affecting the EE.

8.2.5 CA encapsulation efficiency

The EE of CA within SLN and ETHO, was compared, evaluating the drug content by HPLC after nanosystems ultracentrifugation. As reported in Table 28, both CA-SLN and CA-ETHO displayed very high EE values, being able to increase CA solubility with respect to water (0.5 mg/ml), up to double in the case of CA-ETHO. However, the nanosystems displayed different performances. Indeed, in the case of CA-SLN, 82% w/w of the drug weighed for preparation was associated to the disperse lipid phase, while 18% of CA was found in the dispersing aqueous phase (Table 28). Conversely, in the case of CA-ETHO, EE was total, with 100% of CA associated to the vesicles, representing the lipid disperse phase. The reduction of zeta potential value of ETHO in the presence of CA could account for the higher EE of CA with respect to SLN. Notably, the LC of the vesicles, representing the CA-ETHO disperse phase, was 7-fold higher with respect to the solid particles, i.e. the disperse phase of CA-SLN. At this regard, some consideration should be done: (a) CA is partially soluble in water (logP 1.53), therefore it is assumed to be partly associated with the interface between the nanoparticles and the external aqueous phase; (b) ETHO are based on ethanol/water mixture (30:70 v/v) where CA is slightly soluble (5.5 mg/ml) (Hallan et al., 2020); (c) the bilayer organization of PC vesicles improves CA association. In addition, the differences in nanosystems production method should be considered, indeed in the case of SLN, the melting, ultrasonication and cooling of tristearin could lead to partial degradation of CA (Sguizzato et al., 2020a). Conversely, ETHO production is devoid from heating and mechanical stresses, preserving CA from possible degradation. Thus, ETHO can be considered as more suitable for CA solubilization and encapsulation.

8.2.6 Stability of nanosystems

In order to compare the physical-chemical stability of SLN, ETHO, CA-SLN and CA-ETHO, size distribution, zeta potential and EE of samples stored in the light at 22 °C for 6 months were evaluated. Noteworthily all nanosystems were macroscopically stable, indeed no phase separation or sedimentation phenomena were detected, despite the low zeta potential values evaluated by electrophoresis measurements. Variation of mean diameters of nanosystems, measured by PCS is reported in Figure 40. As clearly shown, nanoparticle and nanovesicle size remained quite stable, indeed SLN and CA-SLN mean size was unvaried after 6 months, while ETHO and CA-ETHO mean diameters underwent a 10% increase after 3 months. CA presence scarcely affected the stability of both type of nanosystems, indeed the size profile of CA-SLN was the lowest, with a mean diameter slightly smaller with respect to SLN (15 nm), while ETHO size profiles with or without CA were completely superposable.
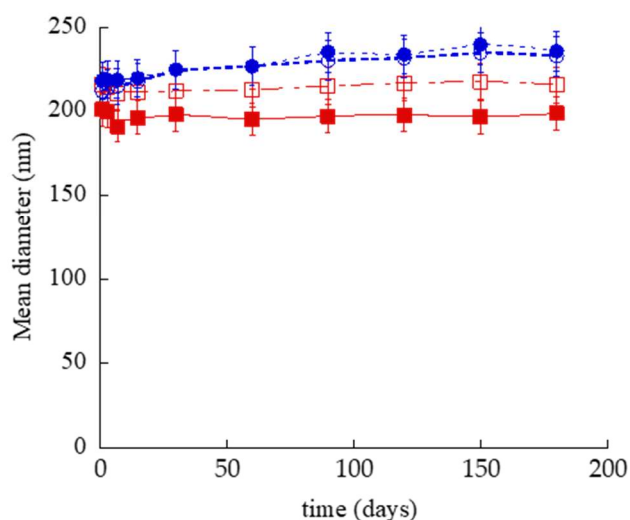

Figure 40. Effect of aging on SLN (open squares), CA-SLN (closed squares), ETHO (open circles) and CA-ETHO (closed circles) mean diameters measured by PCS and expressed as Z-average. Data are the mean ± s.d. on 3 different batch samples stored at 22°C for 6 months.

Regarding dispersity indexes, in all cases the values remained quite stable after 6 months from production, being 0.27, 0.14, 0.25 and 0.22 for SLN, ETHO, CA-SLN CA-SLN and

CA-ETHO respectively, corroborating the size stability trend. Zeta potential of nanosystems measured 6 months after their production decreased. Namely, zeta potential values were 18.3 ± 0.2 and -20.4 ± 0.3 in the case of SLN and ETHO respectively. Conversely, CA-SLN and CA-ETHO zeta potential was -12.6 ± 0.1 and -2.5 ± 0.4 respectively. Thus, in the presence of the drug, after 6 months, zeta potential became more negative with respect to the initial values (see Table 28).

The chemical stability of CA-SLN and CA-ETHO was investigated, evaluating the residual CA content in nanosystems by disaggregation and HPLC analyses. Figure 41 shows CA content variation for CA-SLN, CA-ETHO and CA-water, taken as control. It is straightforward that both nanosystems were able to control CA content with respect to the simple aqueous solution, indeed in this latest case CA complete degradation occurred within 30 days. Notably, CA-ETHO were able to better control CA stability with respect to CA-SLN. Particularly, after 6 months of storage, CA content in CA-SLN was dramatically lower (almost 6-fold) as compared to CA-ETHO, being 13.6 and 77 % for CA-SLN and CA-ETHO respectively.
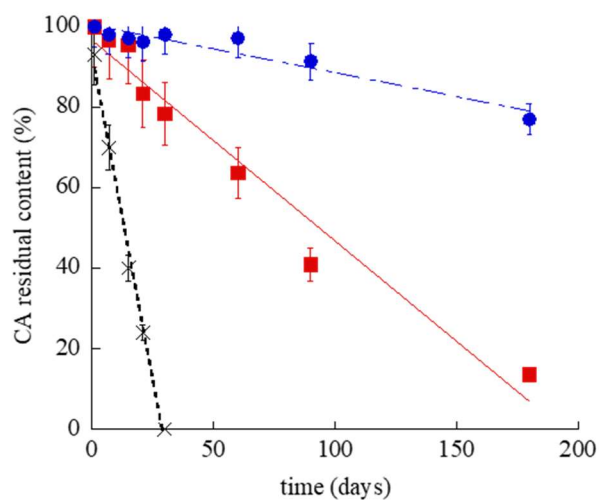

Figure 41. CA residual content during the time for CA-SLN (squares), CA-ETHO (circles) and CA-water (crosses), as evaluated by HPLC. Data are the mean of 3 determinations ± s.d. on samples stored at 22°C for 6 months.

The different efficacy of nanosystems to control CA stability should be attributed to their supramolecular organization. Indeed, in the case of CA-SLN, drug protection was less efficacious with respect to CA-ETHO, since an amount of CA (18 %, w/w) was not encapsulated, thus prone to degradation, being present in the dispersing aqueous phase. The encapsulated drug is supposed to be associated to the surface of SLN and thus partly exposed to degradation during storage. In addition, some authors have demonstrated that during SLN storage, some modification of the crystal lattice may occur, resulting in more stable configuration, leading to the expulsion of drug molecules (Bayón-Cordero et al., 2019). This trend is corroborated by the decrease of CA-SLN zeta potential value, suggesting a less intense electrostatic attraction between CA and the surface of SLN matrix, finally leading to a decrease of CA association. Conversely, in the case of CA-ETHO, the firm and complete association of the drug to the vesicles better preserved CA from degradation (Hallan et al., 2020). At this regard, it should be also considered that some authors have attributed to the multilamellar organization of ETHO the capability to better control drug release with respect to unilamellar vesicles (Joo et al., 2013).

8.2.7   In vitro CA diffusion kinetics

In order to compare the diffusion kinetics of CA alternatively encapsulated in SLN or ETHO or as a solution in CA-water, Franz cells associated to nylon membranes were employed. The amount of CA diffused per unit area was plotted against the square root of time, yielding straight lines, as reported in Figure 42. CA diffusion from CA-water was dramatically faster with respect to CA-SLN and CA-ETHO, indicating that both types of nanoparticles were able to control the drug diffusion. Nonetheless, the gap between CA diffusion profiles from CA-SLN and CA-ETHO highlights the different performances of these nanosystems.
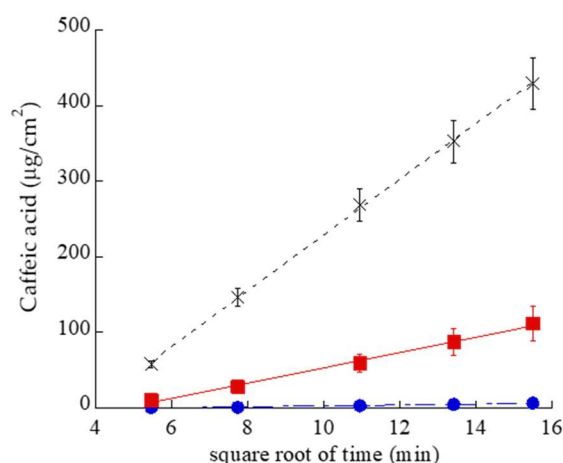
Figure 42. CA diffusion kinetics from CA-water (crosses), CA-SLN (squares) and CA-ETHO (circles), as determined by Franz cell experiments. Data are the mean of 6 independent experiments ± s.d.

Table 29 reports F values, corresponding to the slopes of the diffusion profiles, and D values, obtained by dividing F by CA concentration (mg/ml) in the different forms. In the case of CA-SLN, CA diffusion was 7-fold slower than in the case of CA-water and 18-fold faster than the diffusion from CA-ETHO.

Table 29. Fluxes, diffusion coefficients, antioxidant capacity and irritation indexes of the indicated formulations.

Formulation code	$F^1 \pm$ s.d. ($\mu g/cm^2/h$)	CA (mg/ml)	$D^2 \pm$ s.d. $(cm/h)*10^{-3}$	Irritation index (mean	
				0.25 h	24 h
CA-water	36.93 ± 9.2	0.5	73.86 ± 18.4	-	-
SLN	-	-	-	0.15	0.15
CA-SLN	10.16 ± 2.5	1.0	10.16 ± 2.5	0.25	0.25
ETHO	-	-	-	0.1	0.05
CA-ETHO	0.57 ± 0.09	1.0	0.57 ± 0.09	0.05	0.05

[1]Flux; [2]Diffusion coefficient; data are the mean of 6 independent Franz cell experiments;

These discrepancies evidence that in CA-ETHO the multilamellar vesicle organization and the high ethanol concentration are able to firmly retain CA, while in the case of CA-SLN the drug is probably partly associated on the nanoparticle surface and partly in the poloxamer

dispersing phase, from which it can diffuse in a controlled fashion with respect to the simple aqueous solution, but more quickly if compared to CA-ETHO. It should be underlined that the use of Franz cell associated to synthetic membranes cannot provide information about drug permeability through the skin. However, this model is valuable in pre-formulation studies, to investigate the effect of different compositions on drug diffusion (Salamanca et al., 2018).

8.2.8 CA antioxidant activity evaluation

The DPPH radical scavenging method enabled to compare the antioxidant activity of CA encapsulated within SLN or ETHO. The IC50 values of CA-water, CA-SLN and CA-ETHO were 7µg/ml, 9 µg/ml and 10 µg/ml respectively, indicating that CA antioxidant capacity was maintained, either under encapsulation in SLN or ETHO.

8.2.9 Evaluation of skin membrane resistance upon nanosystems application

To understand the interaction of each type of nanosystems with skin, skin impedance has been measured (Franz diffusion cell with four electrodes in Figure 43). In brief, an electrical current that passes the skin membrane is generated between the counter and the working electrodes. The reference and sensing electrodes measure the potential drop over the membrane and the solution enclosed between these electrodes. By using Ohms law, the impedance of the skin membrane and the enclosed solution is calculated as a ratio of the potential drop to the passing electrical current. The measurements and the calculations are done automatically by connecting the electrodes to Ivium potentiostate (Ivium Technologies, Eindhoven, Netherlands) and exploiting Ivium software, respectively (Björklund et al., 2013).
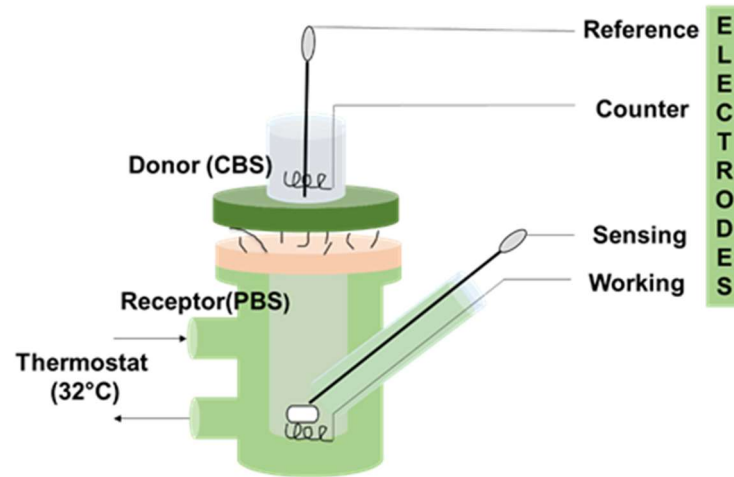
Figure 43. Franz diffusion cell equipped with 4 electrodes for skin membrane resistance measurements using electrical impedance spectroscopy.
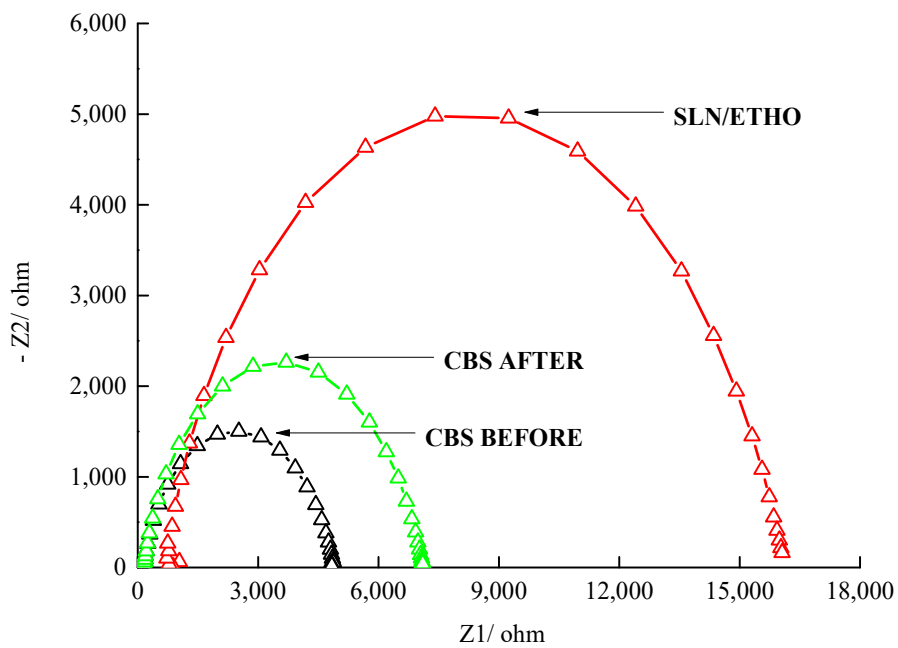

Figure 44. A typical example of impedance vs frequency plot. Data were fitted according to the impedance of an equivalent circuit.

An example of impedance data in Nyquist coordinates obtained for skin membrane in CBS in the absence and in the presence of nanoparticle formulation. The data were recorded using

the Franz cell equipped with four electrodes. Skin resistance values were determined by fitting the of data to the impedance of the equivalent circuit and fitting impedance vs frequency data (Figure 44).
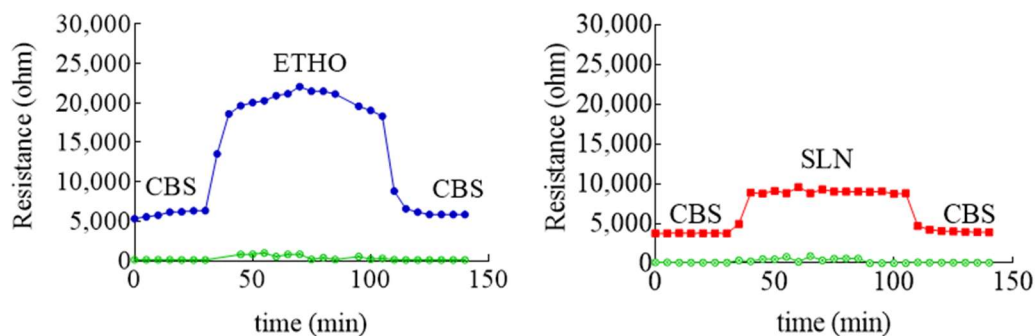

Figure 45. Variation of skin membrane resistance upon addition of SLN (red), ETHO (blue). The green profile refers to receiving phase solution. The skin membrane was assembled in a Franz cell equipped with four electrodes.

The method allows to determine the skin resistance, a parameter directly related to the skin barrier integrity. Indeed, a low skin resistance could indicate a damaged SC (Hernández et al., 2019), possibly leading to permeability increase, especially in the case of hydrophilic solutes (Björklund et al., 2013). Impedance measurements of skin membrane in the presence of ETHO and SLN indicated a strong interaction with skin, as appreciable in Figure 45, showing a 5000 or 16000 ohm increase in the case of SLN and ETHO respectively.

The interaction of SLN and ETHO with skin was reversible since skin resistance decreased to the same initial value upon changing SLN or ETHO back with CBS. Noteworthily, the more pronounced increase of skin resistance occurring in the case of ETHO suggests that PC vesicles established a sort of close contact and blending with skin lipids, sealing the permeability pathways for ions and hydrophilic solutes in the stratum corneum.

8.2.10 In vitro assessment of CA antioxidant activity and permeability in the skin

The SCOE has been used to monitor permeability and involvement of polyphenols in antioxidant reactions, which are catalyzed by PER -like enzymes present in skin. It is worth

underlining that polyphenols can donate hydrogen for the reduction of H_2O_2 in the presence of PER type enzymes available in skin membrane (Furue et al., 2017; Lopez-Torres et al., 1994).In the SCOE model, to mimic the inflammatory condition with respect to ROS production in the skin, H_2O_2 is added into the buffer solution. The H_2O_2 permeation through the SC generates O_2 (equation 14 in chapter 7, section 7.2.10), thus increasing the electrode current due to the abundant presence of CAT enzyme in the epidermis.

The possible polyphenol penetration and its involvement in the antioxidative reactions is indicated by the SCOE, showing a reduction of the electrode current. It is important to underline that many antioxidative enzymes in the skin have PER type activity (equation 15 in chapter 7, section 7.2.10), which in the presence of polyphenols consume H_2O_2, subtracting it from the CAT reaction (equation 14 in chapter 7, section 7.2.10).

The polyphenol CA, being a hydrogen donor, induces a PER type reaction, reducing H_2O_2 to water. Thus, upon permeation through the skin, the electrode SCOE measures the current increase due to the O_2 production promoted by the CAT enzyme activity in the presence of H_2O_2. Before starting SCOE experiments, the integrity of skin membranes has been assessed by electrical impedance measurements of their resistance. The measured values were higher than 3 kΩ, indicating the skin membranes integrity, i.e. intact stratum corneum. The plot, reported in Figure 46, indicates the relative, average amperometric current response of SCOE immersed in CBS (pH 5.5) upon addition of CA-SOL or CA encapsulated in different nanosystems.
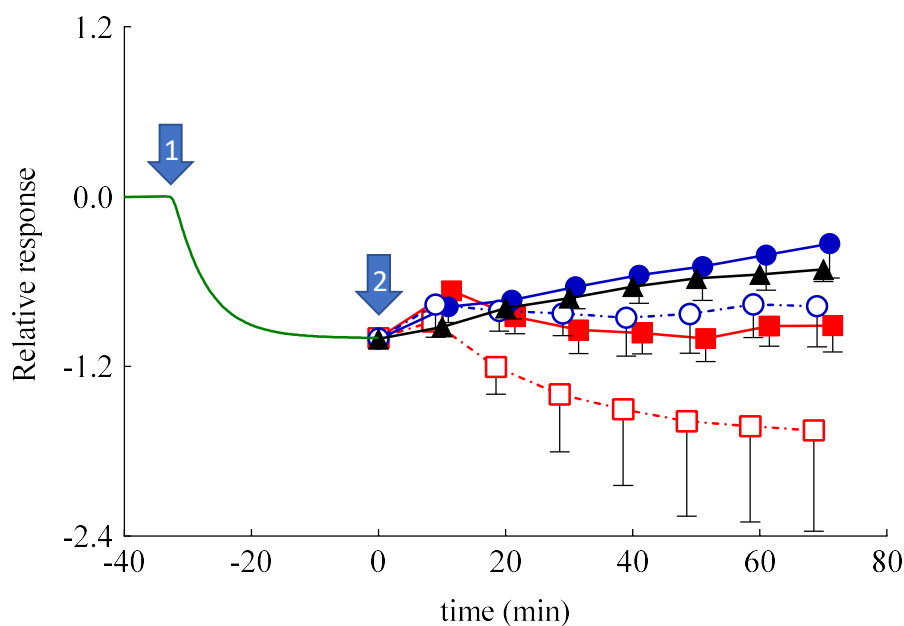
Figure 46. Relative, average amperometric current response of SCOE immersed in CBS (pH 5.5) upon addition of CA in different forms. Arrow #1 marks the addition of H_2O_2 (0.5 mM; n = 19), arrow #2 marks the addition of CA-SOL (CA 0.5 mM, black triangles, n = 3); CA-ETHO (CA 0.5 mM, blue closed circles, n = 6), unloaded ETHO (blue open circles, n = 4), CA-SLN (CA 0.5 mM, red closed squares, n=3), and unloaded SLN (red open squares, n=3). The time scale is adjusted by assigning t = 0 min to the moment when the formulations have been introduced to the measurement cell. Relative response is calculated assigning a baseline current of the SCOE in CBS to zero and the current response to 0.5 mM H_2O_2 equal to 1.

In Figure 46, the response set to zero indicates the steady-state current, usually achieved in 30 min after the SCOE immersion in CBS. Afterward, the addition of H_2O_2 (0.5 mM) (marked by arrow #1) gradually increased the current response (recorded as more negative current), due to O_2 generation by CAT reaction, confirming the H_2O_2 penetration into the skin. At time 0 (arrow #2), CA-SOL, SLN, CA-SLN, ETHO or CA-ETHO were added into the measurement cell. In the case of CA-SOL and CA-ETHO, the current response (the reduction current) of the SCOE decreased, indicating the antioxidant effect of CA that hampered the H_2O_2 effect, due to PER -like reactions in the skin. Noteworthily, CA-ETHO showed a more intense antioxidant activity than CA-SOL, suggesting that CA-ETHO promoted CA permeation with respect to the simple solution of the drug. This result suggests that the transdermal delivery of CA exerted by ETHO was not merely due to the ethanol presence, but instead should be attributed to the CA-ETHO supramolecular structure.

Moreover, in vitro permeation parameters, such as t_{lag} and D_{app}, were calculated (equation 12 in chapter 3- methods, section 3.6.4) and reported in Table 30.
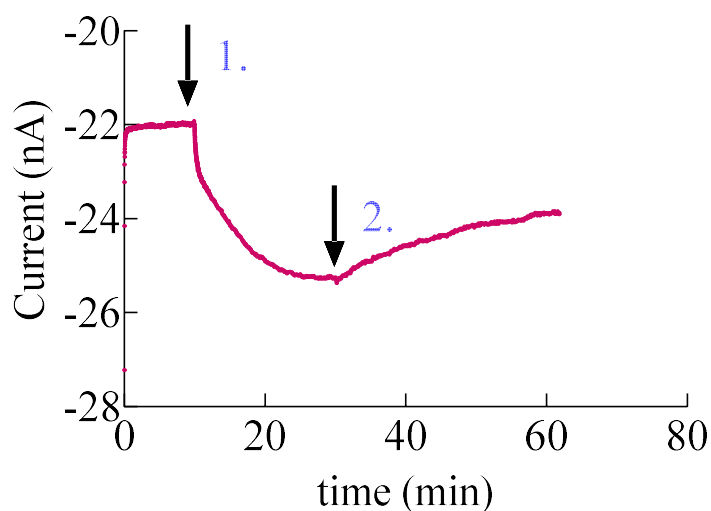

Figure 47. A typical current response of skin membrane covered oxygen electrode (SCOE) to (1) 0.5 mM H_2O_2 and (2) 0.5 mM of CA.

The t_{lag} and Dapp can be calculated by considering the current response recorded as Figure 47 (from injection of H_2O_2 and CA as arrow 1 and arrow 2 respectively. Further, a plot of integral of current response of SCOE vs time reconstructed from an original current response measurement with SCOE as shown in Figure 48. These types of plots were used to estimate a t_{lag} for calculation of apparent diffusion coefficients. Time zero in these plots is assigned to the moment when an appropriate compound or a formulation of interest was added into the measurement cell. The line in this plot represents a fitting of a part of the data where the linear dependence of the current integral vs time is observed (Eskandari et al., 2019).
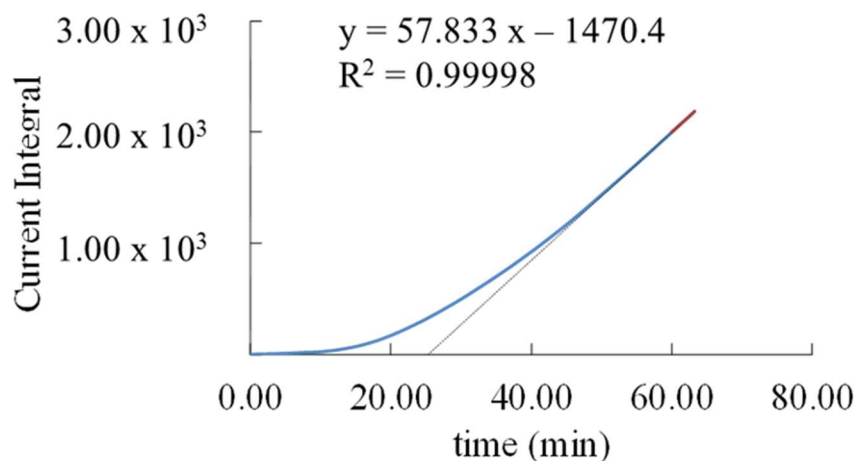
Figure 48. A plot of integral of current response of SCOE vs time.

In case of relative current response of SCOE immersed in CBS after addition of H_2O_2, due to the biological variability of skin membranes the experimental responses have been used to calculate average Dapp (n = 19) and then the average response was generated (Figure 49). In the case of CA-ETHO, t_{lag} was longer with respect to CA-SOL, indicating a more complicated mechanism of CA delivery. This result suggests that PC vesicles require more time to interact with SC lipids with respect to CA-SOL, in which case ethanol simply acts as penetration enhancer, opening pores within stratum corneum.
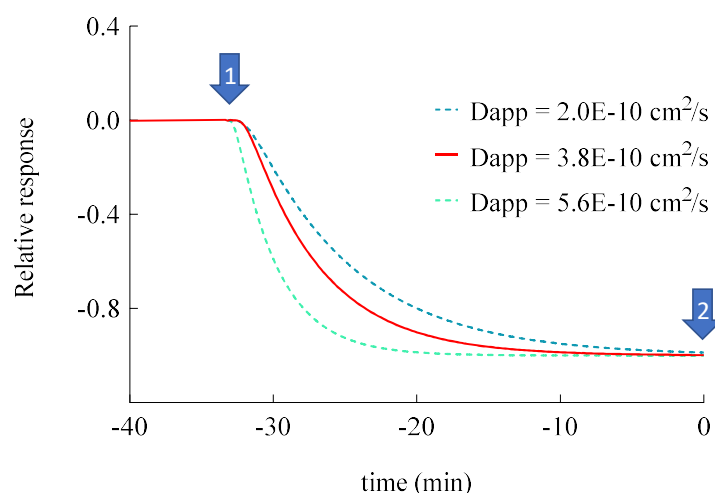
Figure 49. An average response of SCOE to H_2O_2 obtained within different skin membranes (n = 19). Dotted line represent responses generated with Dapp + SD and Dapp - SD. SD – standard deviation.

Table 30. Lag time (t_{lag}) and apparent diffusion coefficient (D_{app}) values of the indicated forms calculated from SCOE and enzyme modified OE responses.

Formulation	SCOE		Enzyme Modified OE	
	t_{lag} (s)	D_{app} (cm²/s)	t_{lag} (s)	D_{app} (cm²/s)
H_2O_2	500 ± 210	$3.8\ (\pm1.80) \times 10^{-10}$	8.4 ± 1.22	$0.05\ (\pm0.0) \times 10^{-5}$
Sol-CA	1462 ± 53	$0.01\ (\pm0.00) \times 10^{-10}$	126 ± 18.32	$7.00\ (\pm0.1) \times 10^{-5}$
SLN-CA	-	-	454 ± 51.61	$2.50\ (\pm4.3) \times 10^{-5}$
ETHO-CA	5400 ± 3000	$0.42\ (\pm0.30) \times 10^{-10}$	-	-

Surprisingly, CA-SLN, SLN, and ETHO exerted an initial response in approximately 10 min, followed by a return to baseline values, or lower in the case of CA-SLN. This behavior in the case of SLN and ETHO could be attributed to an increased skin resistance in the presence of the nanosystems, as demonstrated by impedance measurements (Figure 45). It is known that increased resistance of skin usually slows down permeation of hydrophilic solutes such as H_2O_2 (Jankovskaja et al., 2020).

In order to better understand the amperometric response of CA-SLN more intense with respect to CA-ETHO, the diffusion limiting barrier have been reduced by 10-tape stripping. This step has been performed to damage (thinner and more defective skin barrier) SC to enhance its permeability. The number of tape stripping required to remove the SC barrier

have been optimized (Nocchi et al., 2017). From the data shown (Figure 50), a comparison of intact vs tape stripped (TS) skin has been considered. It can be seen clearly that the gluing of SLN have been disappeared with tape stripping because skin has lost integrity. However, the sensitivity of SCOE toward SLN remained unchanged.
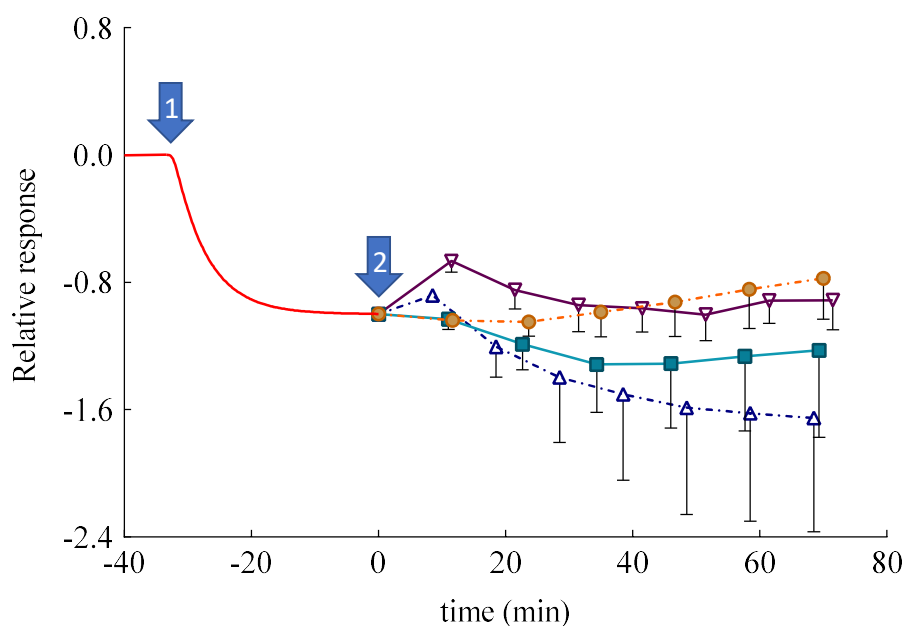

Figure 50. Relative, average amperometric current response of intact and damaged (TS) skin covered oxygen electrode immersed in CBS, pH 5.5, to addition of H_2O_2 (0.5 mM, arrow #1), CA-SLN (CA 0.5 mM, inverted triangles, $n = 3$), unloaded SLN (triangles, $n = 3$), TS CA-SLN (CA 0.5 mM, square, n=3), and unloaded TS SLN (circle, n=3).

An enzyme-modified oxygen electrode model has been employed. Namely, the OE was covered with a dialysis membrane, instead of skin membrane, entrapping CAT/PER enzyme system, employed in order to reproduce the CAT - PER activity exerted within the skin. After reaching the steady-state response in the presence of H_2O_2, at time assigned to zero, CA-SOL, CA-SLN, ETOH:CBS (30:70 v/v) or SLN were added to the measurement cell containing the enzyme-modified OE. As shown in Figure 51, very quick and appreciable amperometric responses have been recorded in the case of CA-SOL and CA-SLN, with higher profile and D_{app} value in the case of CA-SOL (Table 30). The control vehicles did not give appreciable responses, as expected. The amperometric responses, quicker with respect

121

to those obtained by SCOE model, can be attributed to the absence of the pig skin, acting as a diffusional or permeation barrier. The CA-SLN response was less intense with respect to CA-SOL (D_{app} 2.8-fold lower), while the control vehicles responses were practically undetectable. Thus, the OE experiment evidenced the CA-SLN capability of antioxidant delivery with respect to the solution of the drug. The results also remarkably confirmed that the skin represented a barrier to CA permeation in the case of its administration by CA-SLN. On the contrary, when skin was present, in the case of SCOE, the CA-ETHO response, more intense with respect to CA-SOL, confirmed the permeability enhancing effect of ETHO vesicles, promoting the CA antioxidant activity due to its passage through the skin.
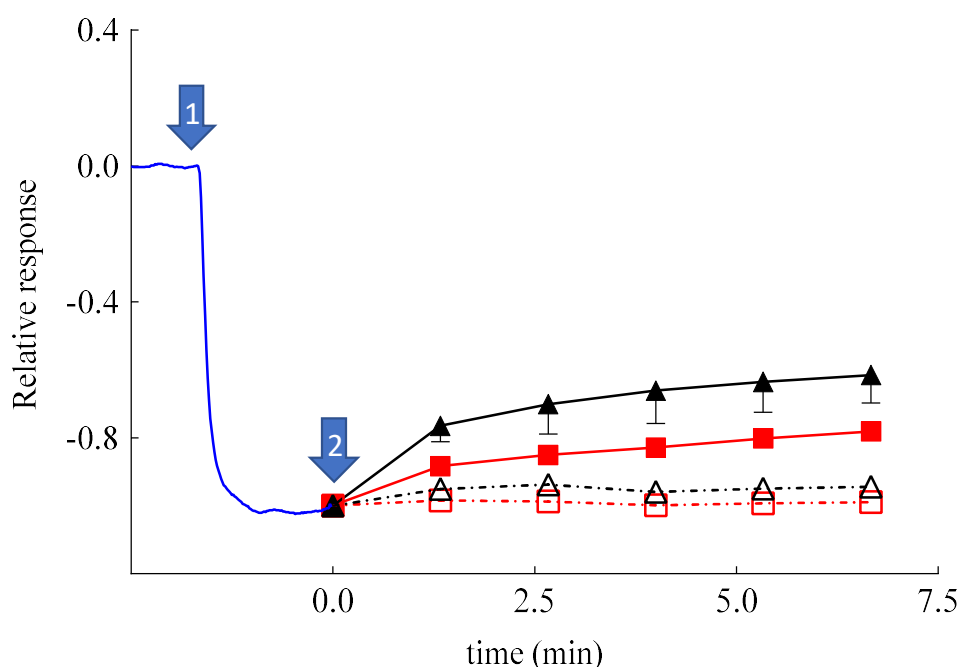

Figure 51. Relative, average amperometric current response on addition of H_2O_2 (0.1 mM) (marked by arrow #1; n = 13) recorded by using CAT / PER enzyme modified oxygen electrode. Arrow #2 marks the addition of CA-SOL (CA 0.03 mM, closed triangles, n=3), CA-SLN (0.03 mM CA, closed squares, n=3), SLN (open squares, n= 3) and EtOH: CBS (30/70 v/v, open triangles, n=3).

Therefore, the amperometric experiments have underlined the different performances of SLN and ETHO applied on the skin. As suggested by other authors, SLN appear less efficient

to promote drug permeation as compared to ETHO. Indeed, many studies have suggested that SLN can exert an occlusive effect (Tanrıverdi and Özer, 2013; Wissing and Müller, 2003), promoting the formation of a drug depot *in* or *on* the SC, while other studies have demonstrated that elastic ETHO can penetrate the SC through the intercellular spaces and release the loaded drug (Zhou et al., 2010; Shen et al., 2014; Niu et al., 2019; Sguizzato et al., 2020b). In this respect, the transdermal effect of CA-ETHO promotes a more intense and prolonged antioxidant activity of CA with respect to CA-SLN.

8.2.11 In vivo comparative irritation test

Despite the matrix of SLN and ETHO is based on lipids generally recognized as safe, accepted by FDA and thoroughly compatible for cutaneous administration, it should be considered that some plant-derived compounds can cause adverse local reactions when applied on the skin(Esposito et al., 2019a; Nohynek et al., 2010). At this regard, to in vivo evaluate the possible irritant reactions induced by cutaneous application of nanosystems unloaded or loaded with CA, a patch test was performed on 20 health volunteers. The number of irritant reactions encountered at 15 min and at 24 h after the removal of the Finn Chamber was recorded, expressed as irritation indexes, and summarized in Table 29. The results indicate that SLN, ETHO, CA-SLN and CA-ETHO can be classified as not irritating if applied to human skin, confirming the suitability of these nanosystems for the treatment of skin disorders (Tanrıverdi and Özer, 2013; Yu et al., 2015).

9 DESIGN OF NANOSYSTEMS FOR THE DELIVERY OF QUORUM SENSING INHIBITORS: A PRELIMINARY STUDY

9.1 INTRODUCTION

Biofilms can be described as a dispersion of immobilized microbial colonies within a self-produced matrix of hydrophilic extracellular polymers such as polysaccharides, proteins, nucleic acids known as extracellular polysaccharide matrix (EPS). Many factors such as surface properties, nutrient availability and the presence of microbial constituents are able to influence the structure and composition of biofilms (Flemming and Wingender, 2010). Indeed, biofilm-forming bacteria initially grow reversibly attached to a surface then create an irreversible attachment facilitating their survival and leading to a more aggressive and resistant host infection (Penesyan et al., 2015). However, biofilm formation is a very complex process in which some cells, when reaching maturity, begin to detach and separate from the aggregates repeatedly, leading to a continuous generation of bacteria able to spread and originate new microcolonies as described in Figure 52. (Hall-Stoodley et al., 2004).
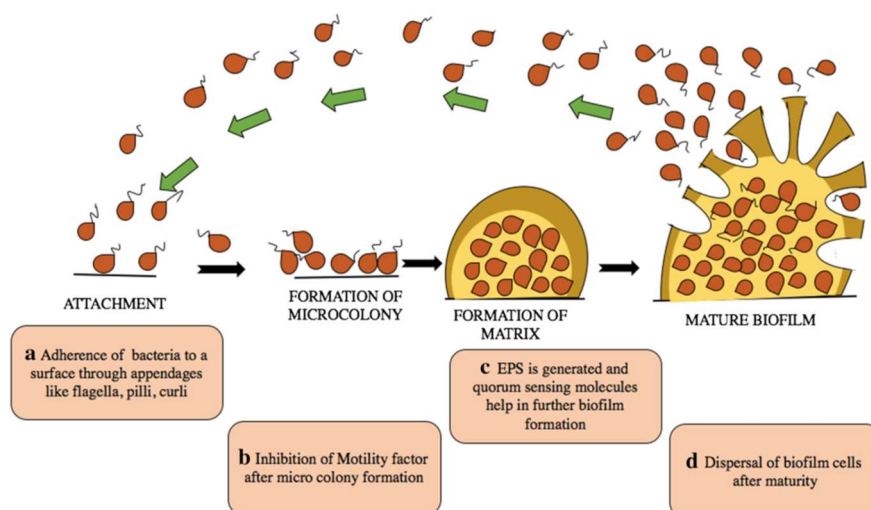

Figure 52. The biofilm formation and dispersal cycle. (Banerjee et al., 2020)

For this reason, bacterial biofilm represents a challenge in counteracting different typologies of infection, including chronic and nosocomial infections. The huge and inappropriate use

of antibiotics during last four decades have reduced the efficacy of traditional antibiotics rising of new bacterial defense mechanisms, together with the spread of antimicrobial resistance. To date in the European Union the infections associated with biofilms and antimicrobial resistance (AMR) are a leading cause of morbidity and of increased healthcare costs (https://www.ecdc.europa.eu/en). Hence, the inhibition of biofilm formation can be considered as a suitable target to design new antibacterial therapies.

Biofilm formation is finely regulated by the Quorum Sensing (QS) system acting intercellular communication through molecular chemical signals that are able to control the production of virulence factors and other biofilm cellular functions (Greenberg, 2003; Hentzer and Givskov, 2003; Li and Tian, 2012). Therefore, compounds able to interfere with communication systems could be able to reduce the production of virulence factors and affect biofilm formation in order to control the development of resistant mutants. In this view, QS inhibitors (QSi) have gained substantial attention to counteract bacterial infection (Rasko and Sperandio, 2010), in order to increase the susceptibility to antibiotics and the clearance of the pathogen by the host immune system (Bjarnsholt and Givskov, 2007). One of the most studied QS system is that belonging to Pseudomonas aeruginosa (P. aeruginosa), a gram-negative bacterium often associated with chronic lung diseases (e.g. cystic fibrosis) and nosocomial infections, that takes advantage of biofilm formation to avoid both the host immune system and antibiotics effect (Bortolotti et al., 2019; Rizzo et al., 2016). P. aeruginosa possesses two QS systems, Las and Rhl characterized by a hierarchical structure (with Las as the main QS system) and include intracellular receptors that bind specific soluble lactones and function as transcriptional factors (Gorgani et al., 2009; Lee and Zhang, 2015). The Las system is controlled by the transcriptional activator LasR and the autoinducer synthase enzyme LasI (Malik et al., 2011). Recently, in our department two novels synthetic QS inhibitor (QSi) have been synthesized, namely CDC and PF based on a cyclopentilamine ring (i.e. homoserine lactone analogues) in order to mimic the N-(3-oxododecanoyl)-L-homoserine lactone (3OC12-HSL) scaffold involved in the synthesis of virulence factors and biofilm formation (Malik et al., 2011).

A critical point in the treatment of biofilm-based bacterial infections is the ability of QSi to efficiently overcome the mucous biofilm layer. In order to bypass this drawback both allowing the transport of effective concentration of drug through biofilm and a controlled release, the possibility to use liposomes was investigated. Particularly, this preformulatory

study focuses on the selection of a liposome composition suitable for new inhibitors of P. aeruginosa biofilm formation to be tested in vitro.

Among the different drug delivery technologies developed for treatment of the biofilm-related infections, nanotechnology plays an important role. Notably, a variety of nano-scaled drug delivery systems have been designed and employed, including polymeric nanoparticles, dendrimers, metal nanoparticles, SLN and liposomes (Drulis-Kawa and Dorotkiewicz-Jach, 2010; Guzman et al., 2012; Ma et al., 2013; Xie et al., 2018; Zhang et al., 2010). Notably, the use of drug delivery systems such as liposomes is a pharmaceutical composition considered to manage effective to achieve a therapeutic effect in humans. As reported in literature, liposomes can be considered one among different nanoparticle platforms, used to facilitate the delivery of antimicrobials to the infection site (Zhang et al., 2010). For instance, the use of liposomes as drug carriers seems to be advantageous over other delivery platforms used to prevent biofilm formation on biomedical surfaces as demonstrated by the number of liposomal formulations approved for clinical use for this purpose at the end of the first decade of this century (Sousa et al., 2011). Therefore, these systems already suitable for conventional antibiotic delivery should be useful for delivery of QSI formulations too.

Liposomes are the most used vesicles to control drug delivery, due to their composition similar to the eukaryotic and prokaryotic cell membrane. Liposomes are nano-sized to microsized spherical structures consisting of two layers of naturally or synthetic phospholipids, such as phosphatidylcholine, phosphatidylethanolamine, phosphatidylserine or phosphatidyl-glycerol surrounding an aqueous core. The liposome-forming lipid bilayer identifies two different sections: a lipophilic compartment and an inner hydrophilic core. Due to its characteristics, the core encapsulates water-soluble molecules while the hydrophobic domain of the bilayer is responsible for entrapping lipophilic agents. Liposomes characteristics, including size, lamellarity and encapsulation efficacy and positive or negative charge, are influenced either by the lipid composition and the preparation method used (Pattni et al., 2015). Cationic liposomes can be prepared by incorporating cationic surfactant in the bilayers. Therefore allowing a high-yield interaction with negatively charged molecules.

Summarizing, in the present paper the synthesis of two new QSi followed by the design and production by direct hydration and extrusion of five different liposomes formulations
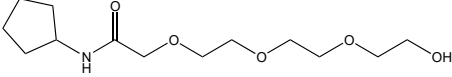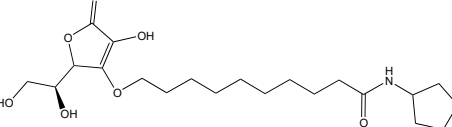
composed of phosphatidyl choline (PC), cholesterol (CH) and charged surfactant is described. Liposomes have been then characterized in terms of size, charge, morphology and in vitro activity to select the more suitable composition for the loading of the two novel biofilm inhibitors. The selected liposome composition has been then studied in terms of morphology, size, entrapment capacity and activity in vitro on biofilm and compared to the activity of the corresponding free compound.

9.2 RESULTS AND DISCUSSION
9.2.1 Synthesis and activity of LasR antagonist

On the basis of our results obtained by Dr. Bortolotti (2019), two compounds with molecular features characterized by high probability to act efficiently as QSi were synthetized, namely CDC and PF (Table 31, Figure 53).

Table 31. Structure and some physico-chemical characteristics of the newly synthesized QSi.

biofilm inhibitor	chemical structure	MW	λmax	LogP
CDC		275	220	0.24
PF		413	220	2.51

QSi are based on the 3-oxoacyl-beta-keto-amide structure containing a polyoxyethylene chain and a cyclopentylamine to increase both stability and solubility in aqueous medium. In addition, PF compound also has ascorbic acid (Vitamin C) in order to take advantage by its natural antimicrobic function to enhance the inhibitory effect on the biofilm. Since these compounds are designed to antagonize LasR receptor which functions as a transcriptional factor, they act at cytoplasmic levels. Moreover, as above underlined, liposomes can be used to facilitate the delivery of antimicrobials to the infection site differently from other nanoparticle platforms (Li et al., 2020; Zhang et al., 2010)
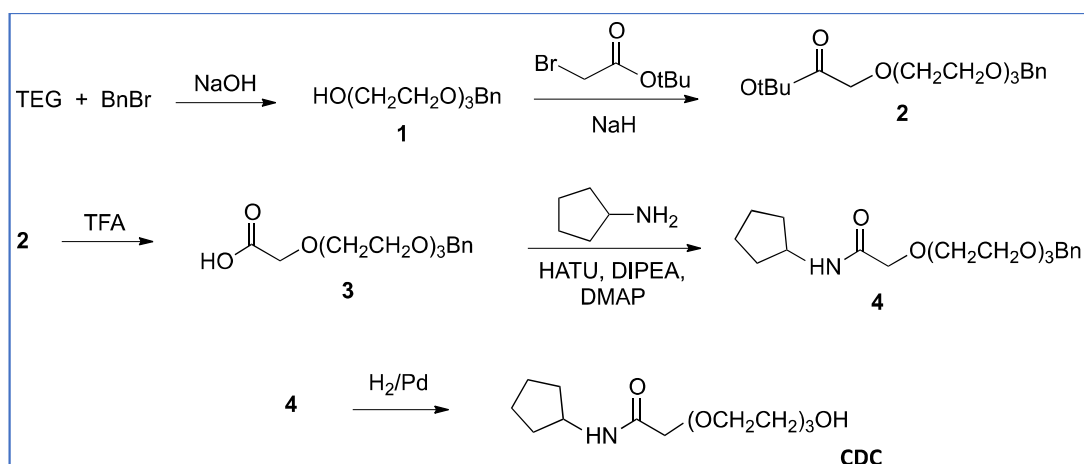
(a)
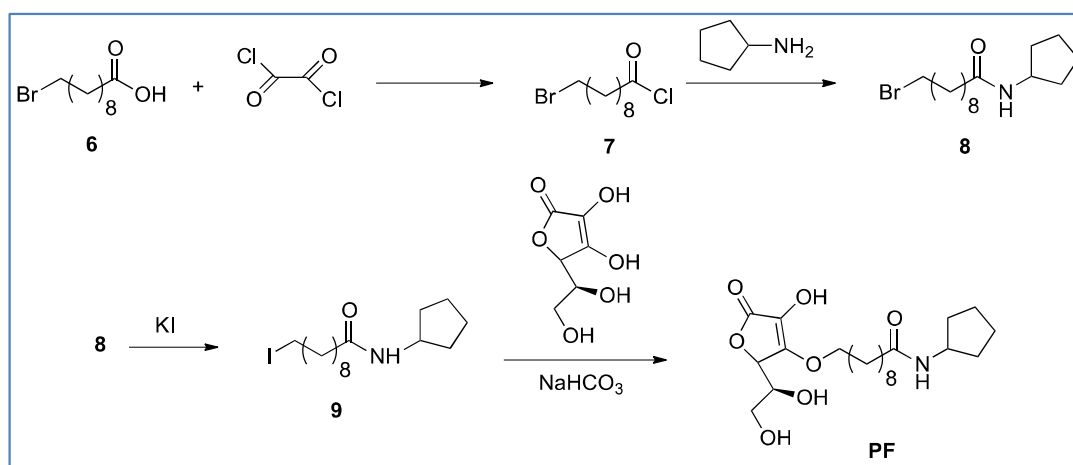
(b)

CDC
^{1}H NMR: (400 MHz, CDCl$_3$): 1.40-1.46 (m, 2H), 1.56-1.70 (m, 4H), 2.01-1.95 (m, 2H), 3.55-3.60 (m, 12H), 4.0 (s, 2H), 4.25-4.27 (m, 1H), 7.2 (br. s, 1H).
^{13}C NMR: (100 MHz, CDCl$_3$): 23.5, 32.6, 50.1, 61.3, 69.4, 69.7, 70.3, 70.4, 72.6, 169.3.

PF
^{1}H NMR: (400 MHz, CD$_3$OD): 1.33 (br. S, 10H), 1.41-1.43 (m, 2H), 1.56-1.61 (m, 4H), 1.69-1.79 (m, 4H), 1.89-1.94 (m, 2H), 2.14 (t, 2H, J = 7.2), 3.64 (d, 2H, J = 6.8), 3.81-3.84 (m, 1H), 4.03-4.08 (m, 1H), 4.46-4.52 (m, 2H), 4.76 (d, 1H, J = 1.6).
^{13}C NMR: (100 MHz, CD$_3$OD): 23.4, 25.7, 28.9, 29.4, 32.1, 35.6, 50.8, 62.0, 69.2, 71.3, 75.2, 119.0, 150.8, 174.5.

(c)

Figure 53. Synthetic flow-charts for CDC (a) and PF (b). ^{1}H and ^{13}C NMR spectra values of final products (c).

QSi are not antibiotics, but molecules able to reduce biofilm formation, therefore CDC and PF were assessed for their ability to inhibit biofilm formation. Both molecules were tested

in the concentration range between 0.5 and 25 µM for 24h and 48h on bacterial growth by measuring the bacterial OD at 600 nm (Bortolotti et al., 2019) and the obtained results indicated that they did not affect the growth of P. aeruginosa (data not shown). Afterwards, the effect of both QSi was tested on biofilm formation by colorimetric biofilm assay. As described in Figure 54, it was observed that after 24h of treatment CDC showed significant biofilm inhibition at 0.5 and 1 µM (p<0.01) (Figure 54a), while all the concentrations tested for PF are able to significantly inhibit P. aeruginosa biofilm formation in a range comprised between 20-40% (p< 0,01) (Figure 54b). On the other hand, after 48h of treatment both CDC (Figure 54c) and PF (Figure 54d) decreased their inhibitory effect on biofilm. These data suggest that the amount of QSi added to bacteria cultures was enough to counteract the quantity of QS molecules produced during a 24 hours culture, not of the following 48 hours.

9.2.2   Preformulatory study: liposome preparation and characterization

In order to find a formulation able to allow the efficient passage of QSi through the mucous biofilm layer, the use of liposomes was investigated by conducting a preformulatory study to select the more suitable liposome composition for in vitro tests. Particularly, liposomes composed of PC, CH and charged surfactant in mixture 2:1:1 (molar ratio), respectively, have been prepared by direct hydration. Charged liposomes were prepared alternatively by adding to the PC/CH mixture the following charged surfactant, namely dicetyl phosphate (LP-DCP), didecyldimethylammonium chloride (LP-DDAC), di isobutyl phenoxy ethyl dimethyl benzyl ammonium chloride (LP-DEBDA) and stearylamine (LP-SA). As a comparison, plain liposomes constituted by PC/CH (LP-P) were also prepared. After preparation, extrusion (using extruder Figure 55) was performed to obtain unilamellar vesicles with a homogeneous size distribution (Cortesi et al., 2007). This strategy allowed the reduction of vesicles mean diameters up to 3-fold as compared to their size after production and at the meantime decreasing the polydispersity and improving the size distribution (data not shown) (Cortesi et al., 2007).
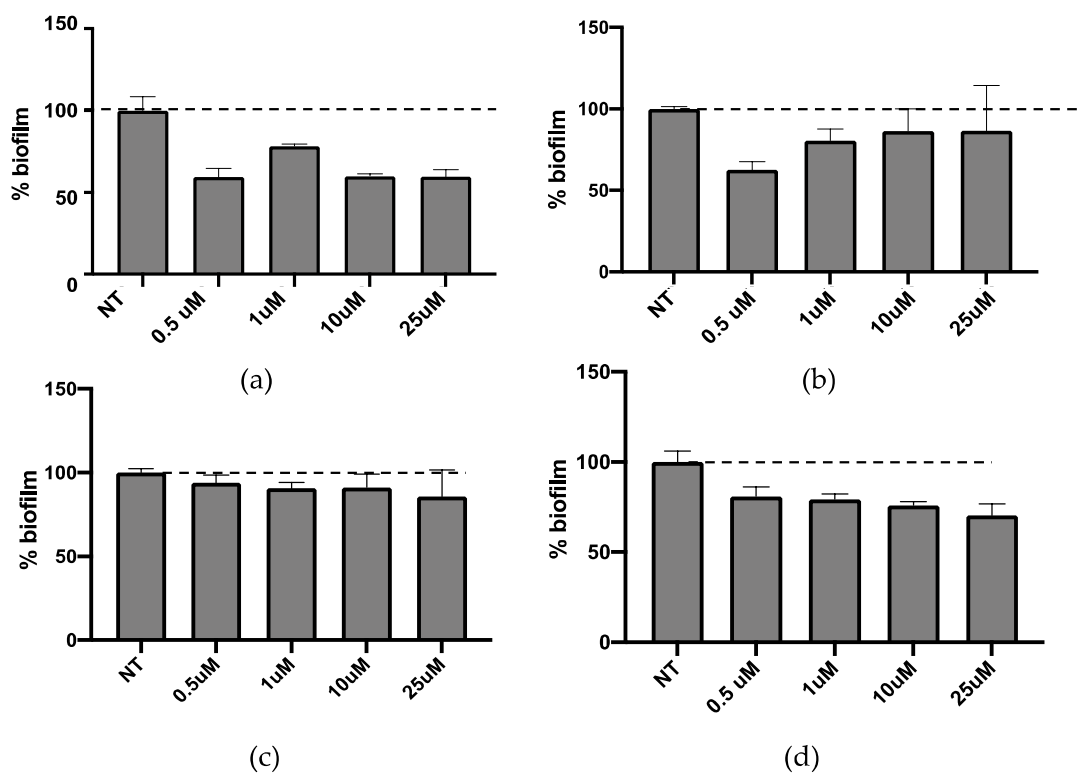
Figure 54. Activity on biofilm of CDC (a, c) or PF (b, d) after 24h (a, b) and 48h (c, d) of treatment.

Figure 55. Filter extruder (Lipex Biomembranes[TM]).

Extruded-liposomes showed similar macroscopic aspects, characterized by homogeneous slightly white dispersions (see Figure 56a.), even if plain LP-P appeared less transparent as compared to charged formulations LP-DCP, LP-DDAC, LP-DEBDA and LP-SA (Figure 56a.), From the morphological point of view, each category of liposomes was visualized by means of freeze-fracture electron microscopy. A representative series of electron microphotographs are reported in Figure 56b, c and d showing plain LP-P, anionic LP-DCP and cationic LP-DDAC liposome formulations, respectively.
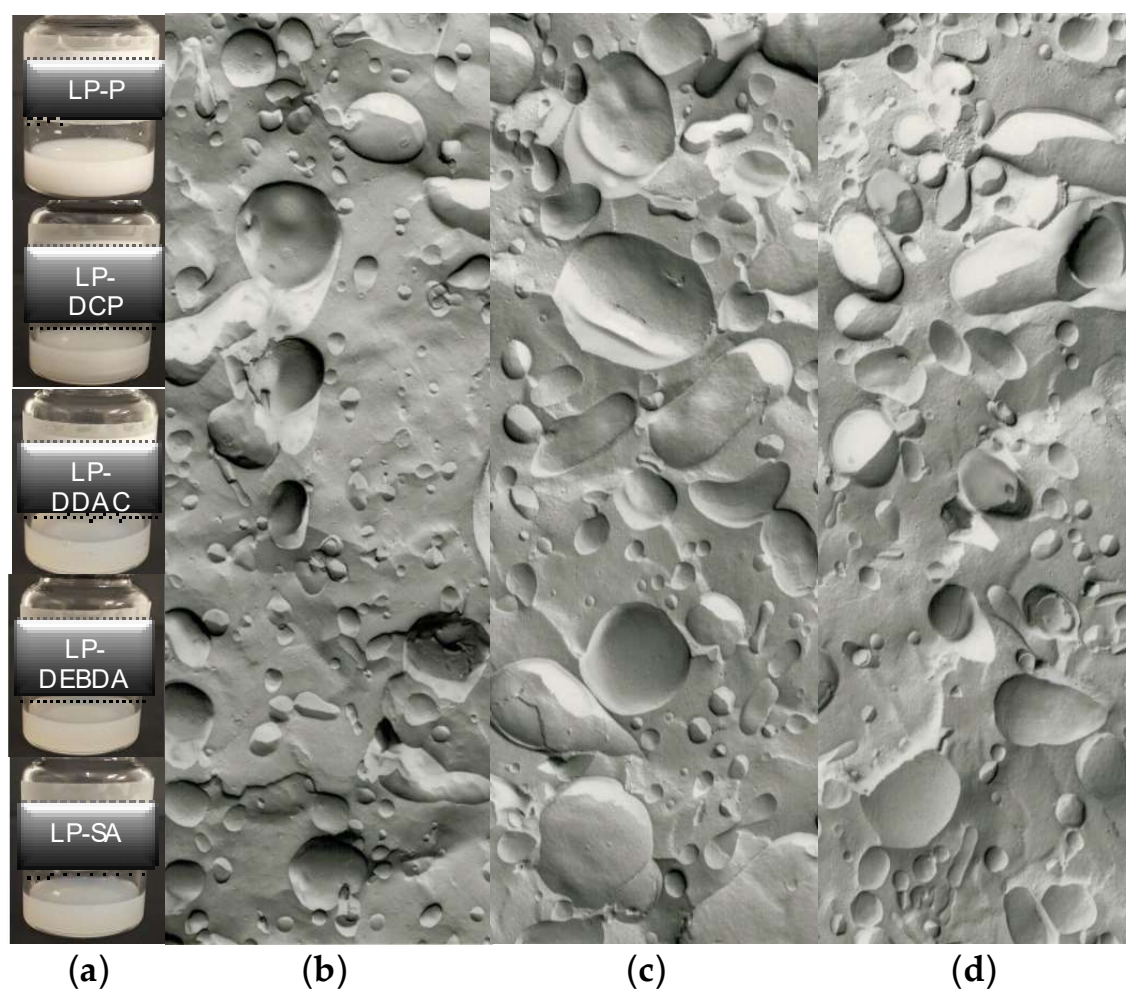

Figure 56. (a) macroscopic aspect of plain liposomes constituted by phosphatidyl choline/cholesterol (LP-P), dicetyl phosphate (LP-DCP), didecyldimethylammonium chloride (LP-DDAC), di isobutyl phenoxy ethyl dimethyl benzyl ammonium chloride (LP-DEBDA) and stearylamine (LP-SA) and representative electron microphotographs of (b) plain (LP-P), (c) anionic (LP-DCP) and (d) cationic (LP-DDAC) liposomes.

The three categories of liposomes displayed unilamellar morphology even if a certain grade of polydispersity was evident. These results corroborated the extruded dimensional data of the five formulations obtained by PCS analyses performed the same day of production and reported in Table 32.

Table 32. Size and zeta potential of liposome formulations after production, as determined by PCS.

	LP-P	LP-DCP	LP-DDAC	LP-DEBDA	LP-SA
Z ave (nm) [1]	191.5 ± 1.7	180.1 ± 3.7	197.0 ± 2.1	180.1 ± 1.0	205.7 ± 1.6
P.I. [2]	0.11 ± 0.07	0.36 ± 0.1	0.20 ± 0.08	0.36 ± 0.06	0.23 ± 0.05
ζ Potential (mV) [3]	-28.4 ± 0.4	-67.4 ± 2.6	$+90.6 \pm 0.3$	$+92.3 \pm 2.0$	$+63.1 \pm 0.9$

[1]Zeta average diameter (mean size). [2]Polydispersity index. [3]Zeta Potential. Data are the mean of 5 independent determinations on different batches of the same dispersion ± standard deviation.

All the formulations showed vesicles mean diameters around 200 nm, ranging from 180 to 205 nm with a slight increase in the case of LP-SA. Concerning the PI, a slight increase was evident in the presence of charged surfactant in the formulation, as compared to plain liposomes. However, a monomodal distribution was appreciable, since P.I. values were below 0.4.

The zeta potential values contributed to good stability of liposome formulations during time, especially significant upon addition of charged surfactant (data not shown). Indeed, thanks to their polar intercalation within the phospholipid bilayer, charged surfactant confer charge to the vesicles, increasing zeta potential values with respect to plain liposomes, therefore promoting their physical stability over time by mean of charge repulsion.

In order to shed light on the structural characteristics of the produced empty liposomes, LP-P, LP-DPC, LP-DDAC, LP-DEBDA and LP-SA were investigated by SAXS. Results related to the effect of cationic and anionic surfactants on unloaded PC liposomes are reported in

Figure 57. In particular, plain liposomes LP-P (Figure 57a) showed the common SAXS diffraction pattern of multilamellar vesicles, characterized by a bilayer repeat distance (which measures the sum of the bilayer thickness and the thickness of the water layer separating two adjacent bilayers) of about 6.72 nm (Cortesi et al., 2007; Hodzic et al., 2012). In contrast, the patterns b-e (Figure 57) demonstrate that the addition of CS to liposome composition leads to a loss of positional correlations between adjacent bilayers, probably due to surface charge density conferred to the bilayers upon surfactant insertion.
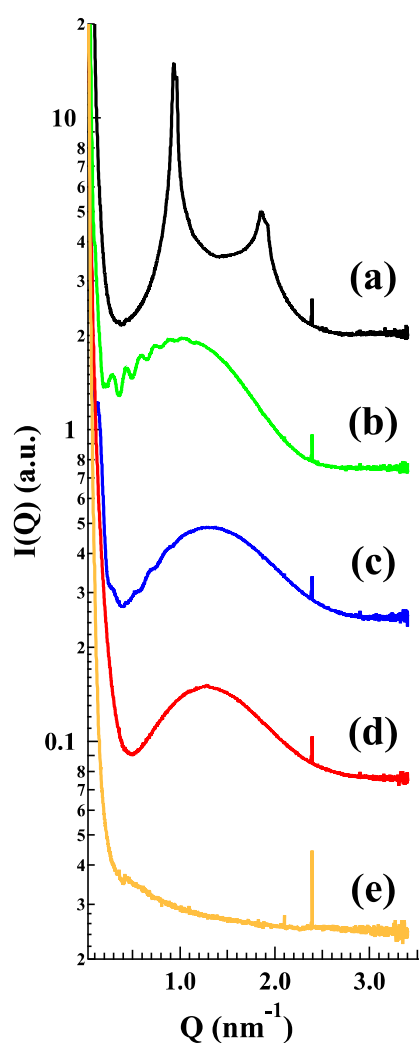

Figure 57. SAXS profiles of the different empty LP-P (a), LP-DDAC (b), LP-DEBDA (c), LP-SA (d) and LP-DCP (e). Experiments were performed at Diamond Light Source (UK).

Indeed, the X-ray diffraction profiles of LP-DDAC, LP-DEBDA and LP-SA display a broad band centered at about 0.14 Å^{-1} without any trace of diffraction peaks, e.g. a typical bilayer form factor scattering pattern indicative of the formation of unilamellar vesicles (Andreozzi et al., 2010; Hodzic et al., 2012). The effect is even greater for anionic surfactants in which the absence of scattering signal observed in the case of LP-DCP suggests a complete loss of structure. The last point should be noticed as the position of the broad band roughly corresponded to the bilayer thickness: the thickness is about 4.7 nm for LP-SA and LP-DEBDA, but increased to about 5.5 nm when liposomes have been prepared in the presence of DDAC. Such an effect could be related to changes induced by DDAC in PC lateral interactions.

9.2.3 Selection of the liposome formulation for LasR antagonist loading

In order to allow the selection of the optimal liposome composition for biofilm inhibitors loading, the five empty liposome formulations were subjected to different in vitro assays, to test their activity on biofilm formation and viability on P. aeruginosa cultures and A594 pulmonary cells, respectively. In view to propose this system as a topic treatment by inhalatory administration, A549 lung cell line was selected to possibly mimic what occurs in vivo. Indeed P. aeruginosa infection often affects the airway system and mainly interacts with epithelial lung cells. In addition, chronicization of P. aeruginosa infection in the lungs is involved in airway diseases (such as BCPO and cystic fibrosis). Particularly P. aeruginosa cultures were treated for 24h with a liposome concentration ranging from 0.5 to 25 μM (Figure 58). None of the liposome formulations affected the bacterial growth at all tested concentrations (data not shown). It was found that LP-P and LP-DCP liposomes induced biofilm formation (Figure 58 a, b). On the other hand LP-DDAC and LP-DEBDA slightly reduced biofilm formation (Figure 58c, d), while LP-SA liposome significantly inhibited biofilm formation at concentrations of 10 and 25 μM (Figure 58e, $p<0.01$). We obtained similar results with a 48 hours treatment (data not shown). Concerning the pulmonary A594 viability performed using MTT test, the obtained results are reported in Figure 59. It was found that plain LP-P (Figure 59a) and anionic LP-DCP (Figure 59b) showed a slight or no cytotoxicity on pulmonary cells.
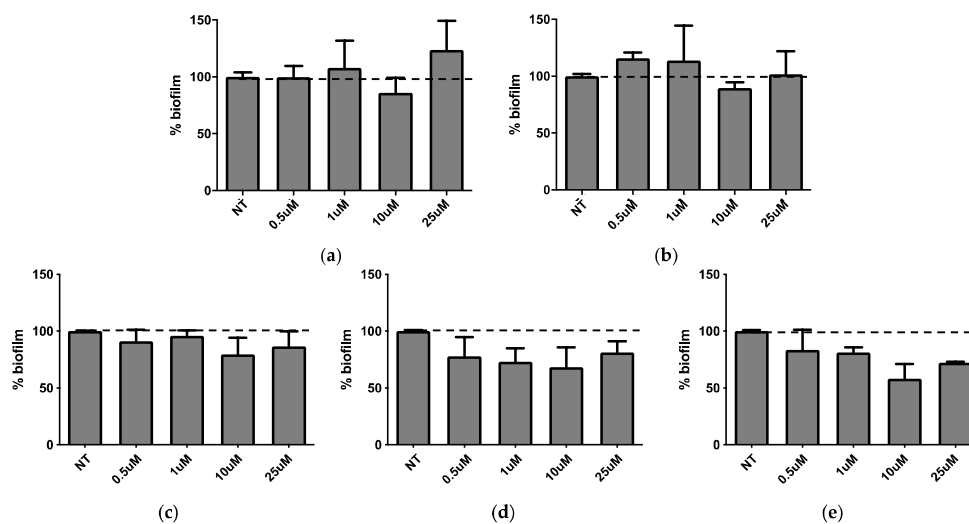
Figure 58. Activity of empty liposomes on biofilm after 24h of treatment. (a) LP-P, (b) LP-DCP, (c) LP-DDAC, (d) LP-DEBDA and (e) LP-SA.

On the other hand, cationic liposome formulations demonstrated a different behavior, depending on the type of cationic surfactant used. Notably, LP-DDAC (Figure 59c) and LP-DEBDA (Figure 59d) showed a strong cytotoxic effect, whilst LP-SA (Figure 59e) displayed no cytotoxicity.
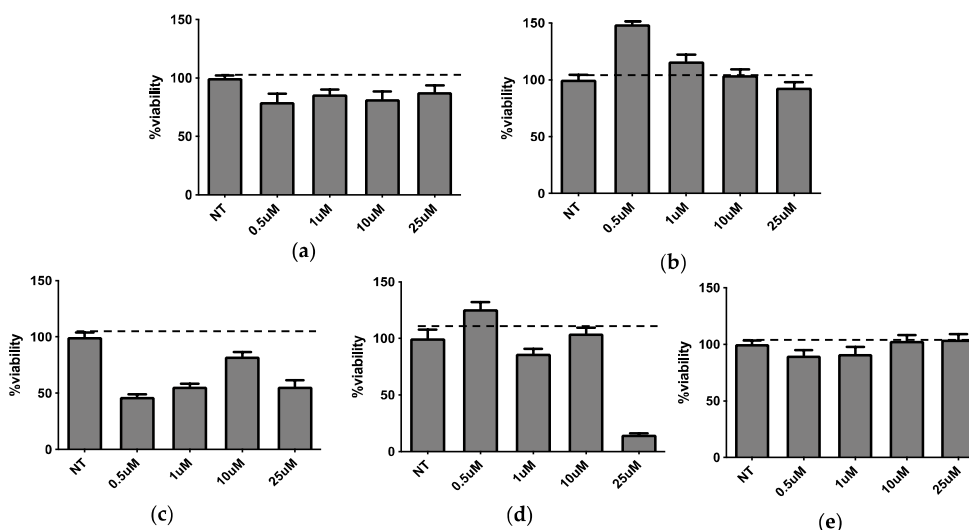

Figure 59. Effect on A549 pulmonary cells viability (MTT assay) after 24h of treatment with LP-P (a), LP-DCP (b), LP-DDAC (c), LP-DEBDA (d) and LP-SA (e).

Taking together the effect of empty liposomes on cell viability, the bacterial growth and biofilm formation with the results obtained by preformulatory study concerning the characterization of empty liposomes (i.e. homogeneous aspect, monodisperse distribution and unilamellar morphology), LP-SA has been selected as composition suitable for the loading of the new synthesized biofilm inhibitors CDC and PF.

9.2.4 Loading of biofilm inhibitors on LP-SA liposomes

LP-SA containing biofilm inhibitors CDC (LP-SA/CDC) and PF (LP-SA/PF) were prepared by direct hydration and extrusion using the same scheme procedure as described for unloaded formulations. However, QSi were dissolved in the aforementioned organic solvents along with other components to achieve the final concentration 10 mM in the dispersion. The macroscopic aspects of both extruded and non-extruded liposomes loaded with inhibitors have been shown in Figure 60.

The entrapment capacity (EC) of each compound within LP-SA was determined after 1 day from liposome production, as described in the Materials and Methods section. Namely, loaded LP-SA dispersion was separated with filter centrifugation and an amount of supernatant with loaded liposomes was disaggregated and quantified by HPLC for drug content (Pattni et al., 2015).

The obtained results summarized in Table 33, show that both compounds were quantitatively loaded within the vesicles. Concerning the effect of the loading onto the vesicle size, it was found that both QSi displayed an increase of the mean size of liposomes, being around 11% for CDC and 20% for PF, but maintained a quite homogeneous size distribution, as indicated by PI values (Table 33).

Table 33. Characteristics of LP-SA unloaded or loaded with biofilm inhibitors.

LP-SA	Z-ave[1] (nm)	PI[1]	ZP[2] (mV)	EC%[1]
unloaded	205.7 ± 1.6	0.229 ± 0.02	+ 63.1 ± 0.9	/
[3]CDC-loaded	223.6 ± 1.9	0.252 ± 0.01	+ 67.8 ± 0.4	98.8 ± 0.5
[3]PF-loaded	239.6 ± 1.4	0.326 ± 0.06	+ 43.1 ± 1.7	99.4 ± 1.3

[1]Values are the mean of determinations on different batches of the same type of dispersion. [2]Zeta potential and [3] Inhibitor concentration 10 mM.
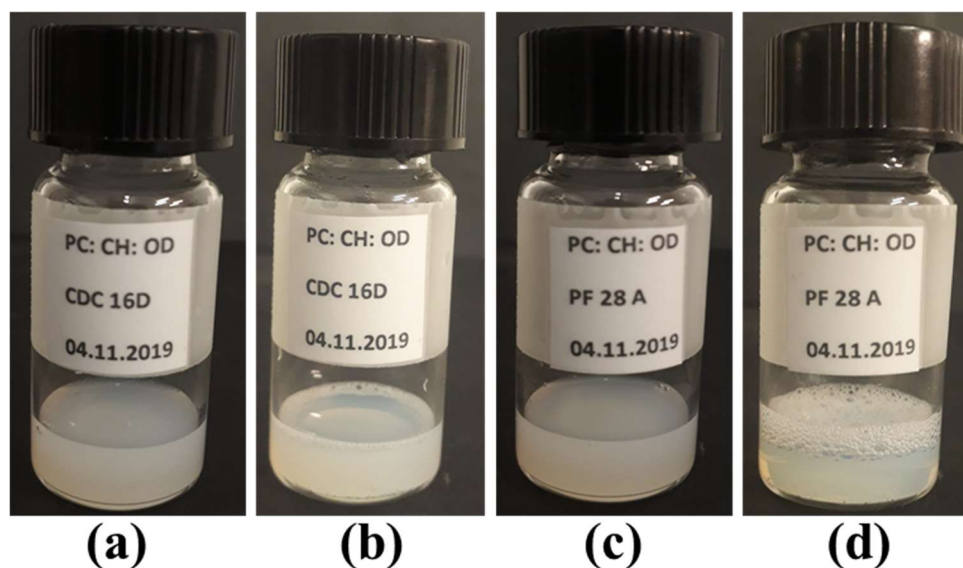
Figure 60. Macroscopic aspect of CDC and PF loaded liposomes non- extruded (a and c) and extruded (b and d) respectively.

Regarding influences of QSi on deep liposome morphology, Figure 61. reports the freeze-fracture electron microphotographs (left) and the SAXS profiles (right) obtained from unloaded and CDC and PF loaded LP-SA. The scattering pattern is essentially characterized by the bilayer form factor, but the drug presence induced a low-intensity diffraction pattern, which possibly corresponded to a multilamellar structure characterized by a low positional correlation between adjacent bilayers and/or by a very low number of stacked bilayers (Andreozzi et al., 2010). The measured repeat distances (10.05 and 9.20 nm for CDC and PF, respectively) displayed a larger value as compared to that observed in plain PC/CH liposomes (6.72 nm), therefore confirming strong repulsive bilayer-bilayer interactions induced by the charged surfactants on the PC bilayers.
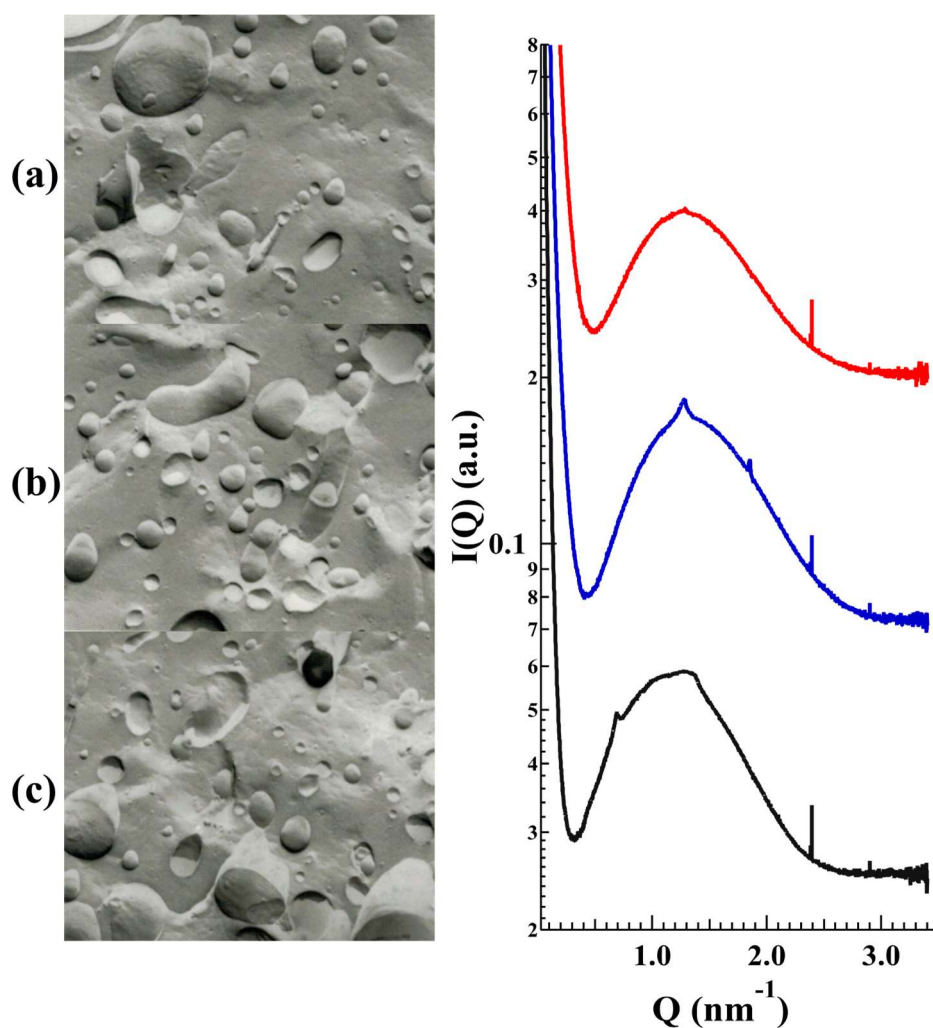
Figure 61. Freeze-fracture electron microphotographs (left) and SAXS profiles (right) of LP-SA formulations either unloaded (a, red) or CDC (b, blue) and PF (c, black) loaded. SAXS experiments were performed at Diamond Light Source (UK).

9.2.5   In vitro release studies

In vitro release studies were performed by dialysis using dialysis membranes (Merck Millipore, Milan, Italy) with 15000 Da cut-off. Sink conditions and QSi solubilization were established adding 30% methanol by volume to the aqueous receiving phase (Siewert et al., 2003). 20 ml of receiving phase were poured in the external compartment and continuously stirred at 500 rpm with a magnetic bar. 2 ml of each QSi-loaded LP-SA were placed in the dialysis bag then at predetermined time intervals 0.15 ml of receiving phase were withdrawn and QSi content was evaluated by HPLC as above reported. Each removed sample volume

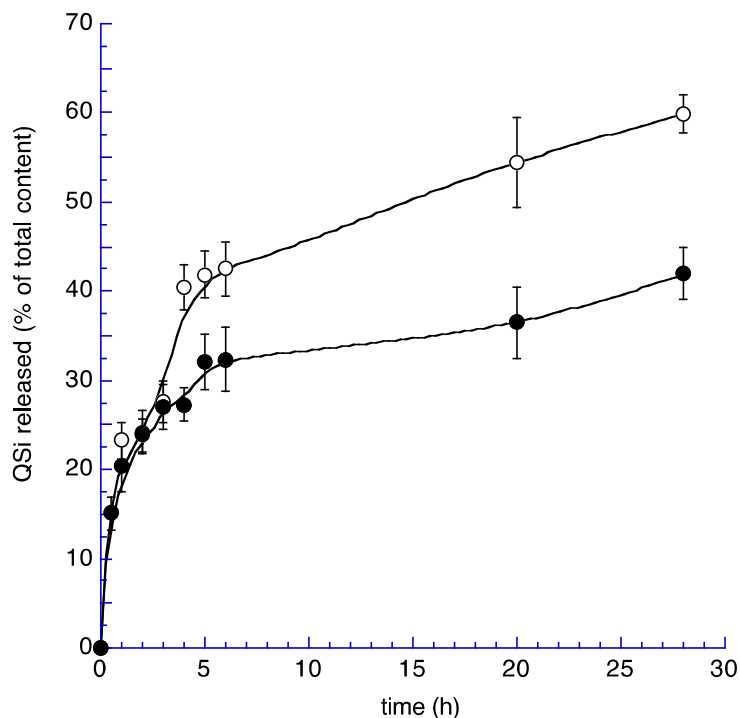was replaced with the same amount of fresh receiving phase. The obtained results are reported in Figure 62.

Figure 62. Release kinetics of CDC (○) and PF (●) from LP-SA, as determined by dialysis. Data are the mean of three experiments ± s.d.

The release obtained indicated that both CDC and PF are released in a controlled manner reaching after 28h at least the 60% and 40% of total amount of QSi, respectively for CDC and PF.

9.2.6   In vitro experiments of LP-SA loaded biofilm inhibitors

QSi-loaded LP-SA were then assessed for biofilm inhibitory activity. The liposome formulation did not affect bacterial growth after 24h of treatment at the concentration range between 0.5-25 μM (data not showed). The biofilm assay performed at the same experimental conditions showed the inhibition of biofilm formation for both compounds in a dose-dependent manner (Figure 63a and b), that was significant for concentrations above

10 µM and 1 µM for liposomes carrying CDC and PF, respectively (p<0.01). The liposome formulation of both compounds led to a dose-dependent effect on biofilm formation.

When we compared the results obtained on biofilm inhibition with the QSi alone (Figure 54) or liposome-loaded (Figure 63), we observed an effectively increased biofilm inhibition for LP-SA/CDC 10 and 25 µM as compared to the same concentration of sole CDC. It was hypothesized that the loading of QSi compounds into LP-SA might reduce the release of the active compounds and needed a longer treatment. Therefore, biofilm inhibition experiments in the presence of sole or LP-SA loaded QSi, have been repeated extending the treatment to 48h. Particularly, after 48h of treatment both CDC (Figure 63c) and PF (Figure 63d) decreased their inhibitory effect on biofilm when used alone as compared to the 24h treatment (Figure 63a, b). On the contrary, when both QSi were administered as liposomal formulation, they maintained and increased their effect on biofilm formation (Figure 63c and d), showing their activity already at low concentrations (LP-SA/CDC: 0.5 µM, p=0.0005; LP-SA/PF: 1 µM, p<0.0001). Therefore, it can be evidenced that QSi-loaded liposomes enhanced their ability to interfere with biofilm formation supporting a longer activity as compared to the free form of each QSi up to 48 hours from the treatment. These data confirm the hypothesis of a gradual release of QSi from the liposomes, therefore enabling to maintain and to enhance the treatment efficacy for a longer period. This effect is particularly evident for CDC compound, which presented an increased effect already at the concentrations of 0.5 and 1 µM, as compared to the administration of CDC alone (0.5 µM: 81% vs 94%; 1 µM: 75% vs 90%; p<0.01). The enhancement of this effect should be possibly ascribed to a better distribution of lipophilic molecules in an aqueous environment due to the distribution within vesicle bilayer, therefore influencing its bioavailability (Fahr et al., 2005).
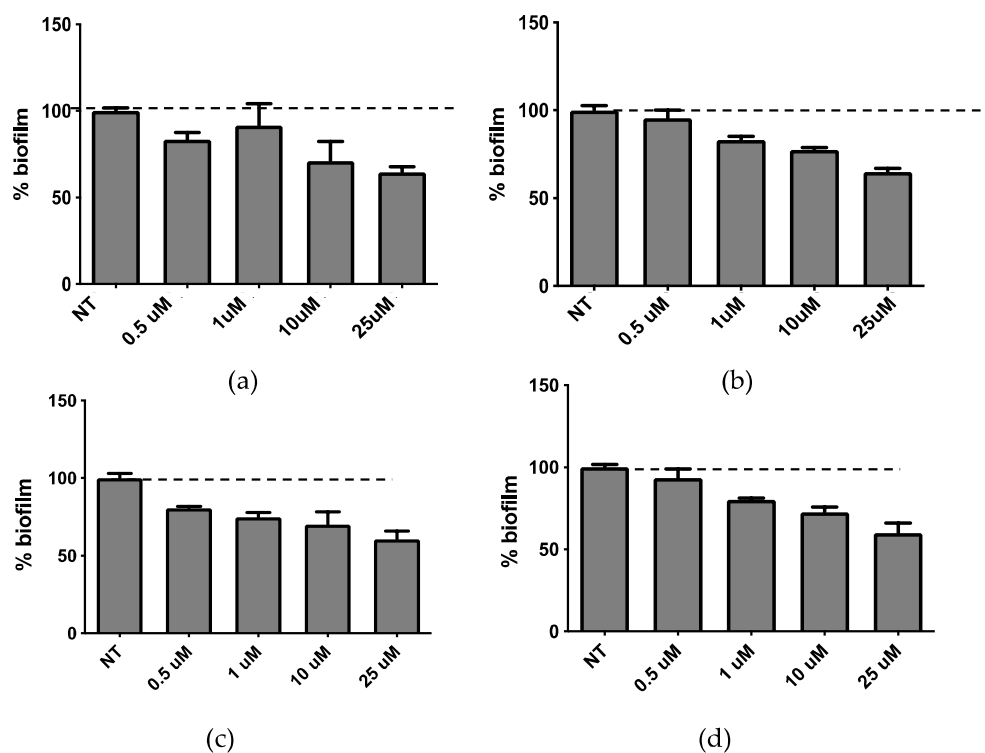
Figure 63. Activity on biofilm of LP-SA loaded CDC (a, c) or PF (b, d) after 24h (a, b) and 48h (c, d) of treatment.

This preliminary study was finalized to evaluate the possible employment of liposomes as carriers for QSi. By combining the results obtained from the preformulatory study on the choice of liposomes lipid composition with those on the cytotoxic effect and the inhibitory activity on the formation of the biofilm, it was possible to select LP-SA as a liposomal formulation to proceed with the loading of two QSi synthesized in our laboratories

10 DESIGN AND CHARACTERIZATION OF ETHOSOMES FOR THE TRANSDERMAL DELIVERY OF MANGIFERIN: A PRELIMINARY STUDY

10.1 INTRODUCTION

The skin is the foremost barrier and the largest organ in the human body. Throughout the natural process of aging, the skin is the most crucial barrier due to the influence of internal as well as external aging. Natural (e.g. stratum cornea, melanin) and cosmetic barriers are not sufficient to the skin. The UV radiation passes through the skin and generates oxidative stress and free radicals. As a result, many ECM (Extracellular Matrix Enzymes) responsible for the degradation of skin macromolecules are activated (Lahmann et al., 2001; Quan et al., 2009).

There are many chemicals used to fight the free oxygen species generated by internal and external factors. Among them are many photo protectors with different mechanisms of action, mainly on the skin's surface (Wang et al., 2010). Mangiferin (MG), a C-glucosyl xanthone with the formula 1, 3, 6, 7-tetrahydroxyxanthone-C2-β-D-glucoside (Figure 64), has been widely investigated in terms of both in vivo and in vitro studies. It has been proven to possess abundant pharmacological actions, including antioxidative, antiaging, antitumor, antibacterial, antiviral, immunomodulatory, antidiabetic, hepatoprotective, and analgesic effects (Ajila et al., 2010; Guha et al., 1996). MG has been identified in many plant classes and maybe abundantly isolated from various parts of Mangifera indica (mango), including the leaves, stem bark, fruit peels and root (Iseda, 1957).
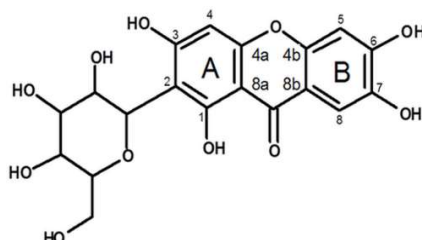

Figure 64. Chemical structure of mangiferin.

It is known that MG is slightly soluble in ethanol, sparingly soluble in water and practically insoluble in some nonpolar solvents (e.g. n-hexane, diethyl ether) (Acosta et al., 2016). The MG permeation into the skin and through the skin, as an influence on the skin's condition, have not been analyzed so far. In the xenobiotic passage process to the skin and through the skin, the SC is the most important barrier. It has been found that the greatest ability to overcome the SC is related to compounds whose log P is between 1 and 3, a molecular weight of less than 500 Da (Lipinski et al., 1997). However, MG has very low solubility in aqueous media (0.111 mg/ml/ logP value -0.631) and poor lipophilicity, and its efficacy in vivo is hampered by low absorption and high speed of clearance. The bioavailability at skin level is low and, when applied as a cream or gel, it hardly crosses the SC and remains on the skin surface (Khurana et al., 2018). Therefore, suitable cargo for transdermal delivery of MG is much needed.

The ultra deformable vesicles of ETHO allow improving loading of poorly soluble molecules with respect to the well-known liposomes. Indeed, the presence of ethanol stabilizes the vesicles and controls their entrapment efficacy (M. Abdulbaqi et al., 2016; Touitou et al., 2000). In addition, transethosomes are the combination of transferosomes (liposomes with certain edge activators) and ETHO (Figure 65) Elasticity of the lipid bilayers is a very important aspect of the enhancement in permeation of deformable lipid vesicles. It has been reported that surfactants in vesicle systems can change the packing characteristics of the lipids in the liposomal bilayer, which modify a liposomal system with high flexibility and elasticity (El Maghraby et al., 2004).

The skin is composed of negatively charged membranes, the reason is negatively charged lipids present in lipid layers in SC. The charge on the vesicle surface is a very crucial factor for transcutaneous diffusion of antioxidants. For instance, positively charged liposomes can pass deeper and disrupt the tight junctions of lower epidermis layers (Van Tran et al., 2019). transethosomes have shown an irregular spherical shape and higher vesicle elasticity and skin permeation/penetration (Song et al., 2012). This fact may be due to the combination of ethanol and edge activators that causes a rearrangement in the lipid bilayer of these vesicles. Therefore, the surfactant (softening agents) acts as an edge activator that destabilizes the lipid bilayers and increases the deformability of the vesicle. Due to the combination of vesicle systems with surfactant, they can easily penetrate the pores in SC which are 5 times less in diameter than their size (Cevc et al., 1995). The ETHO give the possibility to use

edge activators like sodium cholate, sodium deoxycholate, Span 60, Span 65, Span 80, Tween 20, Tween 60, Tween 80, and dipotassium glycyrrhizinate (Kumar Mishra et al., 2019; Loan Honeywell-Nguyen et al., 2004). The employment of surfactant can also extend the durability of ETHO and prevent drug leakage. (Chen et al., 2014).
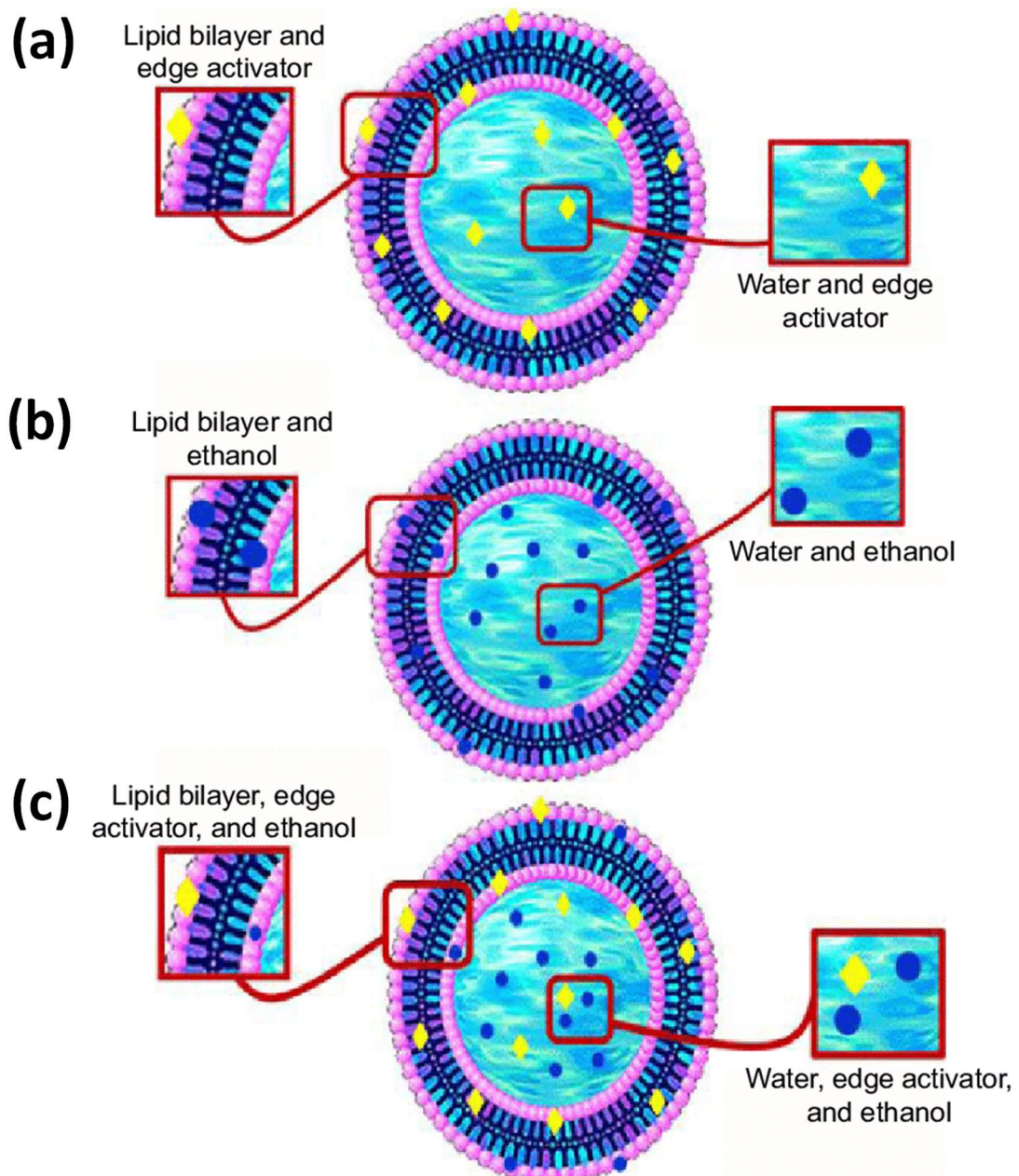

Figure 65. Schematic illustration of evolution of transethosomes displaying various components and structural morphology (Ascenso et al., 2015) .

In this study, ETHO and transethosomes with tween 80 and DDAB have been developed to select the best possible carrier for transdermal delivery of MG across the skin membrane. For this, developed formulations have been characterised for physical evaluation, chemical evaluation, and antioxidant activity by modified OE. Further, the anti-proliferative activity of MG-SOL (MG in ethanol/water, 30/70 v/v) with respect to MG-ETHO and transethosomes (namely, MG-ETHO T80 and MG-ETHO DDAB) have been evaluated

10.2 RESULTS AND DISCUSSIONS

This preliminary study focused on the use of ETHO containing MG to evaluate their effect on transdermal penetration. Indeed, ETHO being mainly composed of phospholipids, ethanol and water are very easy to be prepared. Moreover, the addition of surfactant molecules (such as DDAB and T80) as edge activator could improve their permeation through the skin.

10.2.1 Preparation and characterization of Ethosomes

Plain and edge activator ETHO along with the compositions as reported in Table 34 have been prepared successfully via the cold method. The dispersions were stable and homogenous, completely without aggregates.

Table 34. Composition of ethosome formulations considered in this study.

Formulation code	MG % w/w	PC[1] % w/w	Ethanol % w/w	Surfactant	Water % w/w
ETHO	-	0.9	29.1	-	70
ETHO-MG	0.1	0.9	29.1	-	69.9
ETHO T80	-	0.89	28.81	0.3[2]	70
ETHO T80- MG	0.1	0.9	29.1	0.3[2]	69.6
ETHO DDAB	-	0.9	29.1	0.2[3]	69.8
ETHO DDAB-MG	0.1	0.9	29.1	0.2[3]	69.7

[1]soy phosphatidylcholine; [2]Polysorbate 80; [3] Dimethyldioctadecylammonium bromide

Figure 66 reports the dimensions, and zeta potential values obtained on the first and 30th day after production. From the analysis of these data, the diameter remained almost unvaried either with loaded and unloaded ETHO and ETHO T80 with size below 200 nm. However,

the presence of DDAB induced a reduction of size as compared to plain ETHO or ETHO T80 . The PI was always below 0.3 indicating a monodisperse distribution. The strong positive values for zeta potential in the case of ETHO DDAB indicates the successful association of DDAB to ETHO and improved physical stability.
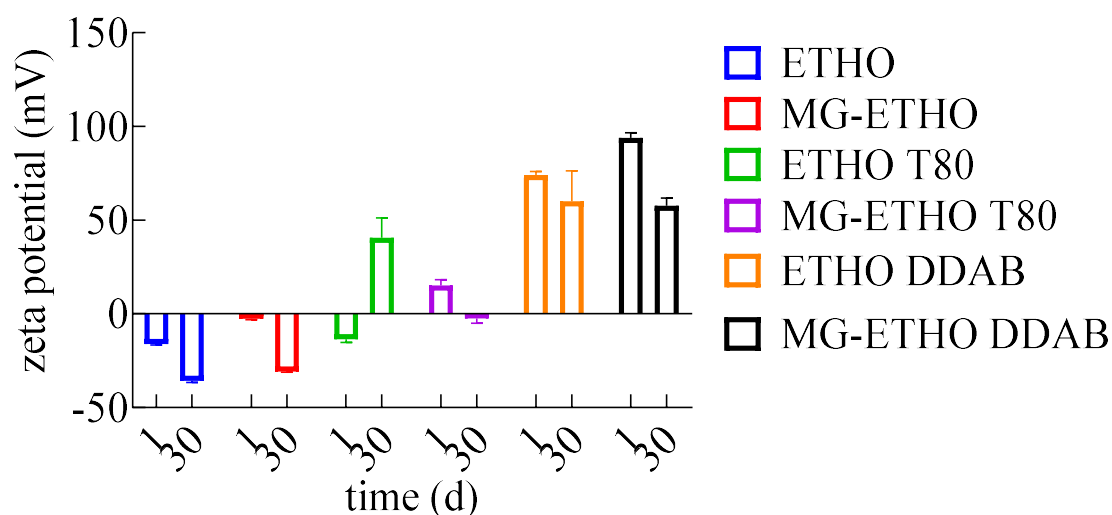
(a)
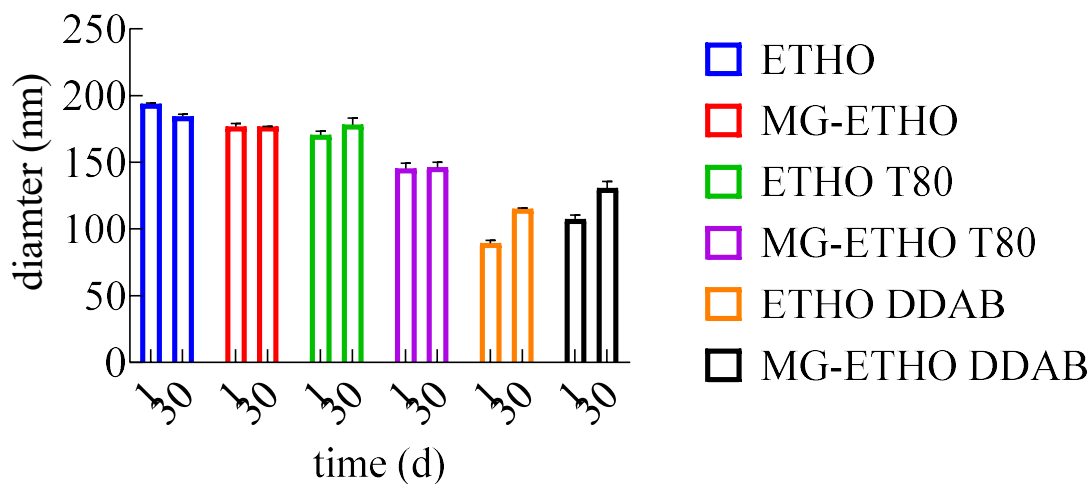
(b)

Figure 66. (a) The diameter of vesicles at day 1 and 30 by PCS. (b) The zeta potential values at day 1 and 30.

The MG content in loaded ETHO have been evaluated by UV spectroscopy. Namely, MG-ETHO undergone ultracentrifugation at 4000 rpm for 15 min and the further lipid part collected disaggregated in the presence of ethanol and filtered. The MG in the aqueous and disaggregated lipid part was analyzed with UV spectrophotometer at 255 nm reported in Table 35. It is worth underlining that almost 100% of the initial concentration of MG has been recovered in both phases constituting ETHO, but largely found in the core of ETHO (Table 35). The possible reason could be simple approach of production and avoiding any high-energy inputs such as heating and mechanical stress.

Table 35. Percentage of MG recovery.

	vesicles	**Aqueous phase**
MG-ETHO	75.8 ± 2.3 %	24.2 ± 0.9 %
MG-ETHO T80	63.2 ± 3.6 %	36.8 ± 1.2 %
MG-ETHO DDAB	57.1 ± 1.1 %	42.9 ± 0.4%

10.2.2 Enzyme modified OE

The SCOE has been employed to access anti-oxidant activity of MG. However, it was difficult to pass through skin membrane because MG is a very big molecule comprised of a C-glucosylated xanthone (Benard and Chi, 2015). Therefore, the t_{lag} recorded was very high (data are not shown). A slight modification in the OE has been employed to assess the MG against enzymatic reactions mimicking to the enzymatic system within the skin. The skin has been replaced with a dialysis membrane. The possibility to modify OE with two enzymes namely, CAT (CAT / H2O2- H2O2 oxidoreductase) from bovine liver and PER have been explored. The combination of CAT: PER (1:1 v/v, comprised 1 mg/ ml) has been poured onto the tip of OE and covered with a dialysis membrane. Almost 100% response has been obtained (Figure 67a) by adding 0.1mM of MG in ETOH: DMSO, 8:2 v/v (MG-SOL). Further, the three types of vesicles containing 0.1mM MG were injected and the response has been analyzed (Figure 67b).
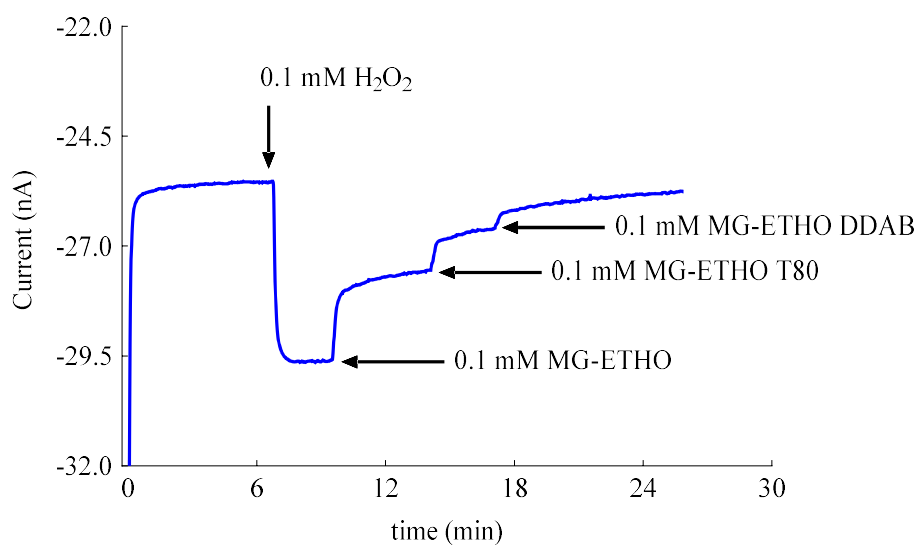
(a)
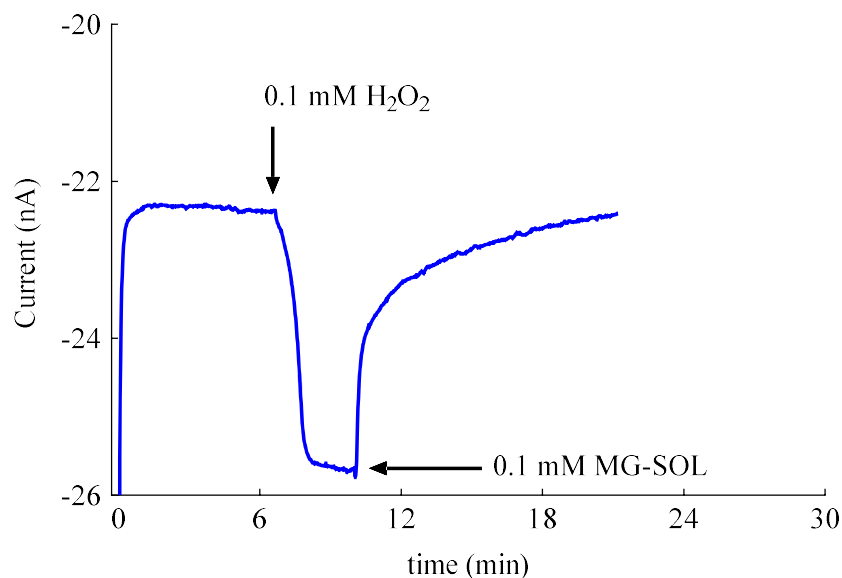
(b)

Figure 67. (a) Response on the addition of 0.1 mM H_2O_2 has been recorded by CAT enzyme, after the steady-state response is reached in the presence of H_2O_2, 0.1 mM MG-SOL.and 0.1 mM MG containing MG-ETHO, MG-ETHO T80 and MG-ETHO DDAB have been injected to buffer solution.

148

Finally, It can be concluded that MG-ETHO, MG-ETHO T80 and MG-ETHO DDAB have released the MG quickly which further was interacted with enzymes resulted in a decrease in reduction current.

10.2.3 Cytotoxicity studies

In order to get information about the cytotoxic effect of the formulations considered in the present study, the MTT test was performed as described in chapter-3, section 3.7.1. This preliminary screening has been conducted in order to choose the suitable carrier for MG.
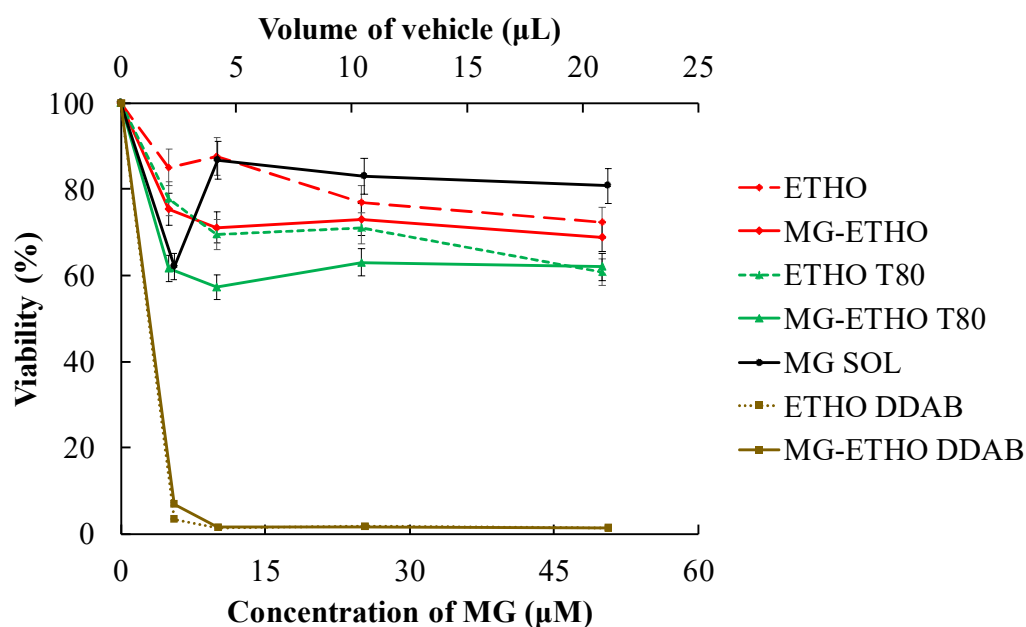
Figure 68. Cytotoxicity of selected formulations evaluated by MTT test on HaCaT cells after 24h of treatment. Data are given as mean ± SD.

From the obtained results (Figure 68), MG-SOL, ETHO, MG-ETHO, ETHO T80 and MG-ETHO T80 showed more than 60% of cell viability up to the highest concentration. Moreover, it should be underlined that the presence of MG did not affect the toxicity of the vehicles, since no significant differences were detected between empty and loaded formulations. However, major toxicity has been found in the case of ETHO DDAB and MG-

ETHO DDAB. At all concentrations tested, both the empty and the loaded formulations showed the almost complete cell death, revealing the toxic effect of DDAB.

Taking together the obtained results, except for loaded and unloaded ETHO DDAB, the 10µM concentration can be selected for further studies.

11 CONCLUSIONS

Taking into account the results obtained during my Ph.D., the conclusions can be summarized as follows.

The investigation reported in chapter 4 was aimed at exploring the possibility of combining the advantages of both SLN and MNP for better drug targeting. MNP and SLN have been fabricated using the co-precipitation method and emulsion followed by the dilution technique respectively. After optimizing blank SLN, successful loading of MNP have been achieved and the presence of MNP inside the core of SLN have been assured by elemental analysis. Separately, schemed SLN also have been optimized for CUR and evaluated for various parameters.

Concerning the study reported in chapter 5, the low solubility of EA in aqueous solution involves to a very difficult administration. To ameliorate it, significant amounts of surfactants have to be used resulting in toxicity in vivo. In this view, the possibility to administrate EA using lipid nanoparticles could be very useful and interesting. It was demonstrated that the inclusion of EA within NLC could improve the water solubility, allowing for a reduction of the dosage. Moreover, the maintaining of high antioxidant effect and low toxicity were evidenced for both types of NLC-EA, even if NLC-EA1 seems to be better than NLC-EA2.

The study described in chapter 6 showed that SLN-P-CA were able to long control CA antioxidant effect, as corroborated by ex-vivo evaluation on HSE, suggesting that the effect of CA is long-lasting. It is possible indeed that CA does not only quench the free radicals present in CS, but stimulates the cellular antioxidant response by activating the NRF2 pathway, as already observed by other authors (Yang et al., 2019). Further studies will be performed in order to better understand the level of penetration of this formulation, based on time and dose in different in vivo models. This would allow to understand whether the topical application could have even a protective effect not only in the upper epidermis but even at the lower cutaneous layers, such as basal epidermis and dermis.

The results of the study described in chapter 7 demonstrated that ETHO can be successfully employed to encapsulate CA with higher EE with respect to other nanosystems previously described and to control CA chemical stability, long maintaining its antioxidant potential.

Experiments with SCOE suggested that ETHO enhanced delivery of CA and its antioxidant action to porcine skin with respect to CA delivery from simple solution. In this respect it could be asserted that the transdermal effect has to be ascribed to ETHO and not to the only presence of ethanol that could act as penetration enhancer. Nonetheless, future studies will be undertaken in order to better investigate the interaction of ETHO with skin and/or mechanism of CA delivery by ETHO.

In chapter 8, the study has evidenced the differences in SLN and ETHO performances as nanosystems for CA cutaneous application. Notwithstanding the capability to encapsulate the phenolic molecule and maintain its antioxidant power, CA-ETHO can better protect CA against degradation, as compared to CA-SLN. Noteworthily, even though the in vitro Franz cell experiment suggests a more intense diffusion of CA in the case of CA-SLN and a very low diffusion in the case of ETHO, a completely different behavior was detected by SCOE experiment based on pig skin. Indeed, this ex-vivo model highlighted the transdermal potential of CA-ETHO that promoted CA antioxidant activity through the skin. The novel approach based on SCOE was effective and helpful to evaluate the transdermal antioxidant effect in the case of CA-ETHO. Furthermore, the CAT/PER modified OE enabled to demonstrate the delivery of antioxidant effect by CA-SLN. Notably, the work and results obtained with skin or enzymes modified OE reveal the limitations and the possibilities for developing novel and versatile strategies to understand the effectiveness of nanosystems as carriers for phenolic compounds.

The preliminary study reported in chapter 9 suggests that LP-SA could be considered a promising delivery system for QSi administration, especially for those compounds showing a lipophilic character, probably in reason of a better dissolution and subsequent bioavailability in aqueous environment. However, studies are underway to confirm these results, to test the stability over time of the vesicle systems produced and to improve the release of QSi in the districts involved in the formation of biofilms.

The preliminary results obtained from chapter 10, the three types of ETHO containing MG have been designed and evaluated for the basic characterization. The systems were found physically stable with almost quantitative EE and also have shown the antioxidant activity assessed by OE. However, the ETHO DDAB and MG-ETHO DDAB has shown remarkable

toxicity in the MTT assay. Finally, the further studies will be conducted by considering the ETHO/ MG-ETHO and ETHO T80/ MG-ETHO T80.

Though nanomedicine is still at an initial phase of development, many therapeutic active agents that exploit nanotechnology have been accepted and commercialized. In this thesis, we tried to develop different types of nanosystems and several evaluation techniques have been employed. However, for significant progress to be made toward this goal, much more effort is needed to establish testing criteria, validate efficacy, and accumulate safety data for various nanotherapeutic agents and materials.

12 BIBLIOGRAPHY

Abdel-Mottaleb, M.M., Try, C., Pellequer, Y., Lamprecht, A., 2014. Nanomedicine strategies for targeting skin inflammation. Nanomedicine 9, 1727–1743. https://doi.org/10.2217/nnm.14.74

Abidi, H., Ghaedi, M., Rafiei, A., Jelowdar, A., Salimi, A., Asfaram, A., Ostovan, A., 2018. Magnetic solid lipid nanoparticles co-loaded with albendazole as an anti-parasitic drug: Sonochemical preparation, characterization, and in vitro drug release. Journal of Molecular Liquids 268, 11–18. https://doi.org/10.1016/j.molliq.2018.06.116

Acosta, J., Sevilla, I., Salomón, S., Nuevas, L., Romero, A., Amaro, D., 2016. Determination of mangiferin solubility in solvents used in the biopharmaceutical industry. Journal of Pharmacy & Pharmacognosy Research 4, 49–53.

Adler, A.F., Leong, K.W., 2010. Emerging links between surface nanotechnology and endocytosis: Impact on nonviral gene delivery. Nano Today 5, 553–569. https://doi.org/10.1016/j.nantod.2010.10.007

Ajila, C.M., Jaganmohan Rao, L., Prasada Rao, U.J.S., 2010. Characterization of bioactive compounds from raw and ripe Mangifera indica L. peel extracts. Food and Chemical Toxicology 48, 3406–3411. https://doi.org/10.1016/j.fct.2010.09.012

Akbaba, H., Karagöz, U., Selamet, Y., Kantarcı, A.G., 2017. Synthesis and characterization of cationic lipid coated magnetic nanoparticles using multiple emulsions as microreactors. Journal of Magnetism and Magnetic Materials 426, 518–524. https://doi.org/10.1016/j.jmmm.2016.11.126

Akbarzadeh, A., Rezaei-Sadabady, R., Davaran, S., Joo, S.W., Zarghami, N., Hanifehpour, Y., Samiei, M., Kouhi, M., Nejati-Koshki, K., 2013. Liposome: classification, preparation, and applications. Nanoscale Res Lett 8, 102. https://doi.org/10.1186/1556-276X-8-102

Akula, P., P.K., L., 2018. Effect of pH on weakly acidic and basic model drugs and determination of their ex vivo transdermal permeation routes. Braz. J. Pharm. Sci. 54. https://doi.org/10.1590/s2175-97902018000200070

Allen, T.M., Cullis, P.R., 2013. Liposomal drug delivery systems: From concept to clinical applications. Advanced Drug Delivery Reviews 65, 36–48. https://doi.org/10.1016/j.addr.2012.09.037

Almgren, M., Edwards, K., Karlsson, G., 2000. Cryo transmission electron microscopy of liposomes and related structures. Colloids and Surfaces A: Physicochemical and Engineering Aspects 174, 3–21. https://doi.org/10.1016/S0927-7757(00)00516-1

Andreozzi, P., Funari, S.S., La Mesa, C., Mariani, P., Ortore, M.G., Sinibaldi, R., Spinozzi, F., 2010. Multi- to Unilamellar Transitions in Catanionic Vesicles. J. Phys. Chem. B 114, 8056–8060. https://doi.org/10.1021/jp100437v

Arafa, M.G., El-Kased, R.F., Elmazar, M.M., 2018. Thermoresponsive gels containing gold nanoparticles as smart antibacterial and wound healing agents. Sci Rep 8, 13674. https://doi.org/10.1038/s41598-018-31895-4

Artzner, F., Geiger, S., Olivier, A., Allais, C., Finet, S., Agnely, F., 2007. Interactions between Poloxamers in Aqueous Solutions: Micellization and Gelation Studied by Differential Scanning Calorimetry, Small Angle X-ray Scattering, and Rheology. Langmuir 23, 5085–5092. https://doi.org/10.1021/la062622p

Ascenso, A., Batista, C., Cardoso, P., Mendes, T., Praça, F., Bentley, V., Raposo, S., Simões, S., 2015. Development, characterization, and skin delivery studies of related ultradeformable vesicles: transfersomes, ethosomes, and transethosomes. IJN 5837. https://doi.org/10.2147/IJN.S86186

Avval, Z.M., Malekpour, L., Raeisi, F., Babapoor, A., Mousavi, S.M., Hashemi, S.A., Salari, M., 2020. Introduction of magnetic and supermagnetic nanoparticles in new approach of targeting drug delivery and cancer therapy application. Drug Metabolism Reviews 52, 157–184. https://doi.org/10.1080/03602532.2019.1697282

Badhani, B., Sharma, N., Kakkar, R., 2015. Gallic acid: a versatile antioxidant with promising therapeutic and industrial applications. RSC Adv. 5, 27540–27557. https://doi.org/10.1039/C5RA01911G

Bala, I., Bhardwaj, V., Hariharan, S., Kumar, M.N.V.R., 2006. Analytical methods for assay of ellagic acid and its solubility studies. Journal of Pharmaceutical and Biomedical Analysis 40, 206–210. https://doi.org/10.1016/j.jpba.2005.07.006

Baloglu, E., Karavana, S.Y., Senyigit, Z.A., Guneri, T., 2011. Rheological and mechanical properties of poloxamer mixtures as a mucoadhesive gel base. Pharmaceutical Development and Technology 16, 627–636. https://doi.org/10.3109/10837450.2010.508074

Banerjee, D., Shivapriya, P.M., Gautam, P.K., Misra, K., Sahoo, A.K., Samanta, S.K., 2020. A Review on Basic Biology of Bacterial Biofilm Infections and Their Treatments by Nanotechnology-Based Approaches. Proc. Natl. Acad. Sci., India, Sect. B Biol. Sci. 90, 243–259. https://doi.org/10.1007/s40011-018-01065-7

Barbosa, L.R.S., Ortore, M.G., Spinozzi, F., Mariani, P., Bernstorff, S., Itri, R., 2010. The Importance of Protein-Protein Interactions on the pH-Induced Conformational Changes of Bovine Serum Albumin: A Small-Angle X-Ray Scattering Study. Biophysical Journal 98, 147–157. https://doi.org/10.1016/j.bpj.2009.09.056

Bayón-Cordero, L., Alkorta, I., Arana, L., 2019. Application of Solid Lipid Nanoparticles to Improve the Efficiency of Anticancer Drugs. Nanomaterials 9, 474. https://doi.org/10.3390/nano9030474

Bellefroid, C., Lechanteur, A., Evrard, B., Mottet, D., Debacq-Chainiaux, F., Piel, G., 2019. In vitro skin penetration enhancement techniques: A combined approach of ethosomes and microneedles. International Journal of Pharmaceutics 572, 118793. https://doi.org/10.1016/j.ijpharm.2019.118793

Benard, O., Chi, Y., 2015. Medicinal Properties of Mangiferin, Structural Features, Derivative Synthesis, Pharmacokinetics and Biological Activities. MRMC 15, 582–594. https://doi.org/10.2174/1389557515666150401111410

Bendas, E.R., Tadros, M.I., 2007. Enhanced transdermal delivery of salbutamol sulfate via ethosomes. AAPS PharmSciTech 8, 213. https://doi.org/10.1208/pt0804107

Benson, H.A.E., 2016. Vesicles for Transdermal Delivery of Peptides and Proteins, in: Dragicevic, N., Maibach, H.I. (Eds.), Percutaneous Penetration Enhancers Chemical Methods in Penetration Enhancement. Springer Berlin Heidelberg, Berlin, Heidelberg, pp. 297–307. https://doi.org/10.1007/978-3-662-47862-2_19

Benzie, I.F.F., Strain, J.J., 1996. The Ferric Reducing Ability of Plasma (FRAP) as a Measure of "Antioxidant Power": The FRAP Assay. Analytical Biochemistry 239, 70–76. https://doi.org/10.1006/abio.1996.0292

Bergantin, C., Maietti, A., Cavazzini, A., Pasti, L., Tedeschi, P., Brandolini, V., Marchetti, N., 2017. Bioaccessibility and HPLC-MS/MS chemical characterization of phenolic antioxidants in Red Chicory (Cichorium intybus). Journal of Functional Foods 33, 94–102. https://doi.org/10.1016/j.jff.2017.02.037

Bickers, D.R., Athar, M., 2006. Oxidative Stress in the Pathogenesis of Skin Disease. Journal of Investigative Dermatology 126, 2565–2575. https://doi.org/10.1038/sj.jid.5700340

Bjarnsholt, T., Givskov, M., 2007. Quorum-sensing blockade as a strategy for enhancing host defences against bacterial pathogens. Phil. Trans. R. Soc. B 362, 1213–1222. https://doi.org/10.1098/rstb.2007.2046

Björklund, S., Ruzgas, T., Nowacka, A., Dahi, I., Topgaard, D., Sparr, E., Engblom, J., 2013. Skin Membrane Electrical Impedance Properties under the Influence of a Varying Water Gradient. Biophysical Journal 104, 2639–2650. https://doi.org/10.1016/j.bpj.2013.05.008

Blois, M.S., 1958. Antioxidant Determinations by the Use of a Stable Free Radical. Nature 181, 1199–1200. https://doi.org/10.1038/1811199a0

Bodratti, A., Alexandridis, P., 2018. Formulation of Poloxamers for Drug Delivery. JFB 9, 11. https://doi.org/10.3390/jfb9010011

Boehncke, W.-H., Schön, M.P., 2015. Psoriasis. The Lancet 386, 983–994. https://doi.org/10.1016/S0140-6736(14)61909-7

Borges, A., de Freitas, V., Mateus, N., Fernandes, I., Oliveira, J., 2020. Solid Lipid Nanoparticles as Carriers of Natural Phenolic Compounds. Antioxidants 9, 998. https://doi.org/10.3390/antiox9100998

Bortolotti, D., LeMaoult, J., Trapella, C., Di Luca, D., Carosella, E.D., Rizzo, R., 2015. Pseudomonas aeruginosa Quorum Sensing Molecule *N* -(3-Oxododecanoyl)-l-Homoserine-Lactone Induces HLA-G Expression in Human Immune Cells. Infect. Immun. 83, 3918–3925. https://doi.org/10.1128/IAI.00803-15

Bortolotti, D., Trapella, C., Bragonzi, A., Marchetti, P., Zanirato, V., Alogna, A., Gentili, V., Cervellati, C., Valacchi, G., Sicolo, M., Turrin, G., Fantinati, A., Di Luca, D., Rizzo, R., 2019. Conjugation of LasR Quorum-Sensing Inhibitors with Ciprofloxacin Decreases the Antibiotic Tolerance of *P. aeruginosa* Clinical Strains. Journal of Chemistry 2019, 1–13. https://doi.org/10.1155/2019/8143739

Bulbake, U., Doppalapudi, S., Kommineni, N., Khan, W., 2017. Liposomal Formulations in Clinical Use: An Updated Review. Pharmaceutics 9, 12. https://doi.org/10.3390/pharmaceutics9020012

Buwalda, S.J., Boere, K.W.M., Dijkstra, P.J., Feijen, J., Vermonden, T., Hennink, W.E., 2014. Hydrogels in a historical perspective: From simple networks to smart materials. Journal of Controlled Release 190, 254–273. https://doi.org/10.1016/j.jconrel.2014.03.052

Byoun, W., Jang, M., Yoo, H., 2019. Fabrication of highly fluorescent multiple Fe3O4 nanoparticles core-silica shell nanoparticles. J Nanopart Res 21, 1. https://doi.org/10.1007/s11051-018-4445-6

Cao, G., Alessio, H.M., Cutler, R.G., 1993. Oxygen-radical absorbance capacity assay for antioxidants. Free Radical Biology and Medicine 14, 303–311. https://doi.org/10.1016/0891-5849(93)90027-R

Carbone, C., Fuochi, V., Zielińska, A., Musumeci, T., Souto, E.B., Bonaccorso, A., Puglia, C., Petronio Petronio, G., Furneri, P.M., 2020. Dual-drugs delivery in solid lipid nanoparticles for the treatment of Candida albicans mycosis. Colloids and Surfaces B: Biointerfaces 186, 110705. https://doi.org/10.1016/j.colsurfb.2019.110705

Cevc, G., Schätzlein, A., Blume, G., 1995. Transdermal drug carriers: Basic properties, optimization and transfer efficiency in the case of epicutaneously applied peptides. Journal of Controlled Release 36, 3–16. https://doi.org/10.1016/0168-3659(95)00056-E

Chandrawati, R., Caruso, F., 2012. Biomimetic Liposome- and Polymersome-Based Multicompartmentalized Assemblies. Langmuir 28, 13798–13807. https://doi.org/10.1021/la301958v

Chang, C.-H., Han, M.-L., Teng, N.-C., Lee, C.-Y., Huang, W.-T., Lin, C.-T., Huang, Y.-K., 2018. Cigarette Smoking Aggravates the Activity of Periodontal Disease by

Disrupting Redox Homeostasis- An Observational Study. Sci Rep 8, 11055. https://doi.org/10.1038/s41598-018-29163-6

Chaterji, S., Kwon, I.K., Park, K., 2007. Smart polymeric gels: Redefining the limits of biomedical devices. Progress in Polymer Science 32, 1083–1122. https://doi.org/10.1016/j.progpolymsci.2007.05.018

Chavda, H., Patel, C., Anand, I., 2010. Biopharmaceutics classification system. Syst Rev Pharm 1, 62. https://doi.org/10.4103/0975-8453.59514

Chen, M., Gupta, V., Anselmo, A.C., Muraski, J.A., Mitragotri, S., 2014. Topical delivery of hyaluronic acid into skin using SPACE-peptide carriers. Journal of Controlled Release 173, 67–74. https://doi.org/10.1016/j.jconrel.2013.10.007

Chen, P., Song, H., Yao, S., Tu, X., Su, M., Zhou, L., 2017. Magnetic targeted nanoparticles based on β-cyclodextrin and chitosan for hydrophobic drug delivery and a study of their mechanism. RSC Adv. 7, 29025–29034. https://doi.org/10.1039/C7RA02398G

Chugani, S., Kim, B.S., Phattarasukol, S., Brittnacher, M.J., Choi, S.H., Harwood, C.S., Greenberg, E.P., 2012. Strain-dependent diversity in the Pseudomonas aeruginosa quorum-sensing regulon. Proceedings of the National Academy of Sciences 109, E2823–E2831. https://doi.org/10.1073/pnas.1214128109

Cortesi, R., Esposito, E., Cuccu, I., Romagnoli, R., Menegatti, E., Zaid, A.N., Nastruzzi, C., 2007. Liposomes and Micellar Dispersions For Delivery of Benzoheterocyclic Derivatives of Distamycin A. Drug Delivery 14, 1–8. https://doi.org/10.1080/10717540600640211

Cortesi, R., Esposito, E., Menegatti, E., Gambari, R., Nastruzzi, C., 1996. Effect of cationic liposome composition on in vitro cytotoxicity and protective effect on carried DNA. International Journal of Pharmaceutics 139, 69–78. https://doi.org/10.1016/0378-5173(96)04574-7

de Alcântara Sica de Toledo, L., Rosseto, H.C., dos Santos, R.S., Spizzo, F., Del Bianco, L., Montanha, M.C., Esposito, E., Kimura, E., Bonfim-Mendonça, P. de S., Svidzinski, T.I.E., Cortesi, R., Bruschi, M.L., 2018. Thermal Magnetic Field Activated Propolis Release From Liquid Crystalline System Based on Magnetic Nanoparticles. AAPS PharmSciTech 19, 3258–3271. https://doi.org/10.1208/s12249-018-1163-4

de Almeida, R.R., Gallo, J., da Silva, A.C.C., da Silva, A.K.O., Pessoa, O.D.L., Araújo, T.G., Leal, L.K.A.M., Fechine, P.B.A., Bañobre-López, M., Ricardo, N.M.P.S., 2017. Preliminary Evaluation of Novel Triglyceride-Based Nanocomposites for Biomedical Applications. J. Braz. Chem. Soc. https://doi.org/10.21577/0103-5053.20170007

Dhavamani, S., Poorna Chandra Rao, Y., Lokesh, B.R., 2014. Total antioxidant activity of selected vegetable oils and their influence on total antioxidant values in vivo: A photochemiluminescence based analysis. Food Chemistry 164, 551–555. https://doi.org/10.1016/j.foodchem.2014.05.064

Dikmen, G., Guney, G., Genc, L., 2015. Characterization of Solid Lipid Nanoparticles Containing Caffeic Acid and Determination of its Effects on MCF-7 Cells. PRA 10, 224–232. https://doi.org/10.2174/1574892810666150115124413

Drulis-Kawa, Z., Dorotkiewicz-Jach, A., 2010. Liposomes as delivery systems for antibiotics. International Journal of Pharmaceutics 387, 187–198. https://doi.org/10.1016/j.ijpharm.2009.11.033

Dulińska-Litewka, J., Łazarczyk, A., Hałubiec, P., Szafrański, O., Karnas, K., Karewicz, A., 2019. Superparamagnetic Iron Oxide Nanoparticles—Current and Prospective Medical Applications. Materials 12, 617. https://doi.org/10.3390/ma12040617

Dumortier, G., El Kateb, N., Sahli, M., Kedjar, S., Boulliat, A., Chaumeil, J.C., 2006. Development of a Thermogelling Ophthalmic Formulation of Cysteine. Drug Development and Industrial Pharmacy 32, 63–72. https://doi.org/10.1080/03639040500390934

Działo, M., Mierziak, J., Korzun, U., Preisner, M., Szopa, J., Kulma, A., 2016. The Potential of Plant Phenolics in Prevention and Therapy of Skin Disorders. IJMS 17, 160. https://doi.org/10.3390/ijms17020160

Edderkaoui, M., Odinokova, I., Ohno, I., Gukovsky, I., Go, V.L.W., Pandol, S.J., Gukovskaya, A.S., 2008. Ellagic acid induces apoptosis through inhibition of nuclear factor kB in pancreatic cancer cells. WJG 14, 3672. https://doi.org/10.3748/wjg.14.3672

El Maghraby, G.M.M., Williams, A.C., Barry, B.W., 2004. Interactions of surfactants (edge activators) and skin penetration enhancers with liposomes. International Journal of Pharmaceutics 276, 143–161. https://doi.org/10.1016/j.ijpharm.2004.02.024

Elsayed, M.M.A., Abdallah, O.Y., Naggar, V.F., Khalafallah, N.M., 2006. Deformable liposomes and ethosomes: Mechanism of enhanced skin delivery. International Journal of Pharmaceutics 322, 60–66. https://doi.org/10.1016/j.ijpharm.2006.05.027

Eskandari, M., Rembiesa, J., Startaitė, L., Holefors, A., Valančiūtė, A., Faridbod, F., Ganjali, M.R., Engblom, J., Ruzgas, T., 2019. Polyphenol-hydrogen peroxide reactions in skin: In vitro model relevant to study ROS reactions at inflammation. Analytica Chimica Acta 1075, 91–97. https://doi.org/10.1016/j.aca.2019.05.032

Esposito, E., Fantin, M., Marti, M., Drechsler, M., Paccamiccio, L., Mariani, P., Sivieri, E., Lain, F., Menegatti, E., Morari, M., Cortesi, R., 2008. Solid Lipid Nanoparticles as Delivery Systems for Bromocriptine. Pharm Res 25, 1521–1530. https://doi.org/10.1007/s11095-007-9514-y

Esposito, E., Mariani, P., Ravani, L., Contado, C., Volta, M., Bido, S., Drechsler, M., Mazzoni, S., Menegatti, E., Morari, M., Cortesi, R., 2012. Nanoparticulate lipid dispersions for bromocriptine delivery: Characterization and in vivo study. European Journal of Pharmaceutics and Biopharmaceutics 80, 306–314. https://doi.org/10.1016/j.ejpb.2011.10.015

Esposito, E., Nastruzzi, C., Sguizzato, M., Cortesi, R., 2019a. Nanomedicines to Treat Skin Pathologies with Natural Molecules. CPD 25, 2323–2337. https://doi.org/10.2174/1381612825666190709210703

Esposito, E., Ravani, L., Contado, C., Costenaro, A., Drechsler, M., Rossi, D., Menegatti, E., Grandini, A., Cortesi, R., 2013. Clotrimazole nanoparticle gel for mucosal administration. Materials Science and Engineering: C 33, 411–418. https://doi.org/10.1016/j.msec.2012.09.007

Esposito, E., Sguizzato, M., Bories, C., Nastruzzi, C., Cortesi, R., 2018. Production and Characterization of a Clotrimazole Liposphere Gel for Candidiasis Treatment. Polymers 10, 160. https://doi.org/10.3390/polym10020160

Esposito, E., Sguizzato, M., Drechsler, M., Mariani, P., Carducci, F., Nastruzzi, C., Cortesi, R., 2017. Progesterone lipid nanoparticles: Scaling up and in vivo human study. European Journal of Pharmaceutics and Biopharmaceutics 119, 437–446. https://doi.org/10.1016/j.ejpb.2017.07.015

Esposito, E., Sguizzato, M., Drechsler, M., Mariani, P., Carducci, F., Nastruzzi, C., Valacchi, G., Cortesi, R., 2019b. Lipid nanostructures for antioxidant delivery: a comparative preformulation study. Beilstein J. Nanotechnol. 10, 1789–1801. https://doi.org/10.3762/bjnano.10.174

Esposito, E., Sticozzi, C., Ravani, L., Drechsler, M., Muresan, X.M., Cervellati, F., Cortesi, R., Valacchi, G., 2015. Effect of new curcumin-containing nanostructured lipid dispersions on human keratinocytes proliferative responses. Exp Dermatol 24, 449–454. https://doi.org/10.1111/exd.12696

Eyerich, K., Eyerich, S., 2018. Immune response patterns in non-communicable inflammatory skin diseases. J Eur Acad Dermatol Venereol 32, 692–703. https://doi.org/10.1111/jdv.14673

Fahr, A., Hoogevest, P. van, May, S., Bergstrand, N., S. Leigh, M.L., 2005. Transfer of lipophilic drugs between liposomal membranes and biological interfaces: Consequences for drug delivery. European Journal of Pharmaceutical Sciences 26, 251–265. https://doi.org/10.1016/j.ejps.2005.05.012

Fang, C.-L., A. Al-Suwayeh, S., Fang, J.-Y., 2013. Nanostructured Lipid Carriers (NLCs) for Drug Delivery and Targeting. Recent Patents on Nanotechnology 7, 41–55. https://doi.org/10.2174/187221013804484827

Fathi, M., Mirlohi, M., Varshosaz, J., Madani, G., 2013. Novel Caffeic Acid Nanocarrier: Production, Characterization, and Release Modeling. Journal of Nanomaterials 2013, 1–9. https://doi.org/10.1155/2013/434632

Fjaeraa, C., Nånberg, E., 2009. Effect of ellagic acid on proliferation, cell adhesion and apoptosis in SH-SY5Y human neuroblastoma cells. Biomedicine & Pharmacotherapy 63, 254–261. https://doi.org/10.1016/j.biopha.2008.07.093

Flemming, H.-C., Wingender, J., 2010. The biofilm matrix. Nat Rev Microbiol 8, 623–633. https://doi.org/10.1038/nrmicro2415

Furrukh, M., 2013. Tobacco Smoking and Lung Cancer : Perception Changing Facts = تدخين التبغ و سرطان الرئة : إدراك تغير الحقائق. SQUMJ 13, 345–358. https://doi.org/10.12816/0003255

Furue, M., Uchi, H., Mitoma, C., Hashimoto-Hachiya, A., Chiba, T., Ito, T., Nakahara, T., Tsuji, G., 2017. Antioxidants for Healthy Skin: The Emerging Role of Aryl Hydrocarbon Receptors and Nuclear Factor-Erythroid 2-Related Factor-2. Nutrients 9, 223. https://doi.org/10.3390/nu9030223

Gabizon, A.A., de Rosales, R.T.M., La-Beck, N.M., 2020. Translational considerations in nanomedicine: The oncology perspective. Advanced Drug Delivery Reviews S0169409X20300454. https://doi.org/10.1016/j.addr.2020.05.012

Garcês, A., Amaral, M.H., Sousa Lobo, J.M., Silva, A.C., 2018. Formulations based on solid lipid nanoparticles (SLN) and nanostructured lipid carriers (NLC) for cutaneous use: A review. European Journal of Pharmaceutical Sciences 112, 159–167. https://doi.org/10.1016/j.ejps.2017.11.023

Ghadiri, M., Vasheghani-Farahani, E., Atyabi, F., Kobarfard, F., Mohamadyar-Toupkanlou, F., Hosseinkhani, H., 2017. Transferrin-conjugated magnetic dextran-spermine nanoparticles for targeted drug transport across blood-brain barrier: TRANSFERRIN-CONJUGATED MAGNETIC DEXTRAN-SPERMINE NANOPARTICLES. J. Biomed. Mater. Res. 105, 2851–2864. https://doi.org/10.1002/jbm.a.36145

Godin, B., Touitou, E., 2003. Ethosomes: New Prospects in Transdermal Delivery. Crit Rev Ther Drug Carrier Syst 20, 63–102. https://doi.org/10.1615/CritRevTherDrugCarrierSyst.v20.i1.20

Gollavilli, H., Hegde, A.R., Managuli, R.S., Bhaskar, K.V., Dengale, S.J., Reddy, M.S., Kalthur, G., Mutalik, S., 2020. Naringin nano-ethosomal novel sunscreen creams: Development and performance evaluation. Colloids and Surfaces B: Biointerfaces 193, 111122. https://doi.org/10.1016/j.colsurfb.2020.111122

Gorgani, N., Ahlbrand, S., Patterson, A., Pourmand, N., 2009. Detection of point mutations associated with antibiotic resistance in Pseudomonas aeruginosa. International Journal of Antimicrobial Agents 34, 414–418. https://doi.org/10.1016/j.ijantimicag.2009.05.013

Greenberg, E.P., 2003. Bacterial communication and group behavior. J. Clin. Invest. 112, 1288–1290. https://doi.org/10.1172/JCI200320099

Grillone, A., Riva, E.R., Mondini, A., Forte, C., Calucci, L., Innocenti, C., de Julian Fernandez, C., Cappello, V., Gemmi, M., Moscato, S., Ronca, F., Sacco, R., Mattoli, V., Ciofani, G., 2015. Active Targeting of Sorafenib: Preparation, Characterization,

and In Vitro Testing of Drug-Loaded Magnetic Solid Lipid Nanoparticles. Adv. Healthcare Mater. 4, 1681–1690. https://doi.org/10.1002/adhm.201500235

Guha, S., Ghosal, S., Chattopadhyay, U., 1996. Antitumor, Immunomodulatory and Anti-HIV Effect of Mangiferin, a Naturally Occurring Glucosylxanthone. Chemotherapy 42, 443–451. https://doi.org/10.1159/000239478

Gulcin, I., 2006. Antioxidant activity of caffeic acid (3,4-dihydroxycinnamic acid). Toxicology 217, 213–220. https://doi.org/10.1016/j.tox.2005.09.011

Guzman, M., Dille, J., Godet, S., 2012. Synthesis and antibacterial activity of silver nanoparticles against gram-positive and gram-negative bacteria. Nanomedicine: Nanotechnology, Biology and Medicine 8, 37–45. https://doi.org/10.1016/j.nano.2011.05.007

Hallan, S.S., Kaur, P., Kaur, V., Mishra, N., Vaidya, B., 2016. Lipid polymer hybrid as emerging tool in nanocarriers for oral drug delivery. Artificial Cells, Nanomedicine, and Biotechnology 44, 334–349. https://doi.org/10.3109/21691401.2014.951721

Hallan, S.S., Sguizzato, M., Mariani, P., Cortesi, R., Huang, N., Simelière, F., Marchetti, N., Drechsler, M., Ruzgas, T., Esposito, E., 2020. Design and Characterization of Ethosomes for Transdermal Delivery of Caffeic Acid. Pharmaceutics 12, 740. https://doi.org/10.3390/pharmaceutics12080740

Hall-Stoodley, L., Costerton, J.W., Stoodley, P., 2004. Bacterial biofilms: from the Natural environment to infectious diseases. Nat Rev Microbiol 2, 95–108. https://doi.org/10.1038/nrmicro821

Han, S.B., Kwon, S.S., Jeong, Y.M., Yu, E.R., Park, S.N., 2014. Physical characterization and *in vitro* skin permeation of solid lipid nanoparticles for transdermal delivery of quercetin. Int J Cosmet Sci 36, 588–597. https://doi.org/10.1111/ics.12160

Han, Y.-G., Aoyagi, M., Kogiso, M., Asakawa, M., Shimizu, T., 2012. Preparation of pH-sensitive lipid-modified magnetite nanoparticle dispersion. Colloids and Surfaces A: Physicochemical and Engineering Aspects 395, 63–69. https://doi.org/10.1016/j.colsurfa.2011.12.004

Hentzer, M., Givskov, M., 2003. Pharmacological inhibition of quorum sensing for the treatment of chronic bacterial infections. J. Clin. Invest. 112, 1300–1307. https://doi.org/10.1172/JCI20074

Hernández, A.R., Vallejo, B., Ruzgas, T., Björklund, S., 2019. The Effect of UVB Irradiation and Oxidative Stress on the Skin Barrier—A New Method to Evaluate Sun Protection Factor Based on Electrical Impedance Spectroscopy. Sensors 19, 2376. https://doi.org/10.3390/s19102376

Hervault, A., Thanh, N.T.K., 2014. Magnetic nanoparticle-based therapeutic agents for thermo-chemotherapy treatment of cancer. Nanoscale 6, 11553–11573. https://doi.org/10.1039/C4NR03482A

Hodzic, A., Zoumpoulakis, P., Pabst, G., Mavromoustakos, T., Rappolt, M., 2012. Losartan's affinity to fluid bilayers modulates lipid–cholesterol interactions. Phys. Chem. Chem. Phys. 14, 4780. https://doi.org/10.1039/c2cp40134g

Holst, B., Williamson, G., 2008. Nutrients and phytochemicals: from bioavailability to bioefficacy beyond antioxidants. Current Opinion in Biotechnology 19, 73–82. https://doi.org/10.1016/j.copbio.2008.03.003

Hristo Svilenov,, Christo Tzachev, 2014. Solid Lipid Nanoparticles – A Promising Drug Delivery System [WWW Document]. URL https://scholar.google.com/scholar_lookup?title=Solid%20lipid%20nanoparticles%E2%80%94a%20promising%20drug%20delivery%20system&author=H.%20Svilenov%20&author=C.%20Tzachev&publication_year=2014 (accessed 10.2.20).

Igartua, M., Saulnier, P., Heurtault, B., Pech, B., Proust, J.E., Pedraz, J.L., Benoit, J.P., 2002. Development and characterization of solid lipid nanoparticles loaded with magnetite. International Journal of Pharmaceutics 233, 149–157. https://doi.org/10.1016/S0378-5173(01)00936-X

Iseda, S., 1957. On Mangiferin, the Coloring Matter of Mango (Mangifera indica Linn.). V. Identification of Sugar Component and the Structure of Mangiferin. BCSJ 30, 629–633. https://doi.org/10.1246/bcsj.30.629

Jagur-Grodzinski, J., 2010. Polymeric gels and hydrogels for biomedical and pharmaceutical applications: POLYMERIC GELS AND HYDROGELS. Polym. Adv. Technol. 21, 27–47. https://doi.org/10.1002/pat.1504

Jain, S., Tiwary, A.K., Sapra, B., Jain, N.K., 2007. Formulation and evaluation of ethosomes for transdermal delivery of lamivudine. AAPS PharmSciTech 8, 249. https://doi.org/10.1208/pt0804111

Janbaz, K.H., Saeed, S.A., Gilani, A.H., 2004. Studies on the protective effects of caffeic acid and quercetin on chemical-induced hepatotoxicity in rodents. Phytomedicine 11, 424–430. https://doi.org/10.1016/j.phymed.2003.05.002

Jankovskaja, S., Labrousse, A., Prévaud, L., Holmqvist, B., Brinte, A., Engblom, J., Rezeli, M., Marko-Varga, G., Ruzgas, T., 2020. Visualisation of H2O2 penetration through skin indicates importance to develop pathway-specific epidermal sensing. Microchim Acta 187, 656. https://doi.org/10.1007/s00604-020-04633-9

Jensen, L.B., Petersson, K., Nielsen, H.M., 2011. In vitro penetration properties of solid lipid nanoparticles in intact and barrier-impaired skin. European Journal of Pharmaceutics and Biopharmaceutics 79, 68–75. https://doi.org/10.1016/j.ejpb.2011.05.012

Jeon, J., Sung, J., Lee, H., Kim, Y., Jeong, H.S., Lee, J., 2019. Protective activity of caffeic acid and sinapic acid against UVB-induced photoaging in human fibroblasts: XXXX. J Food Biochem 43, e12701. https://doi.org/10.1111/jfbc.12701

Johnston, T.P., Palmer, W.K., 1993. Mechanism of poloxamer 407-induced hypertriglyceridemia in the rat. Biochemical Pharmacology 46, 1037–1042. https://doi.org/10.1016/0006-2952(93)90668-M

Joo, K.-I., Xiao, L., Liu, S., Liu, Y., Lee, C.-L., Conti, P.S., Wong, M.K., Li, Z., Wang, P., 2013. Crosslinked multilamellar liposomes for controlled delivery of anticancer drugs. Biomaterials 34, 3098–3109. https://doi.org/10.1016/j.biomaterials.2013.01.039

Kang, N.J., Lee, K.W., Shin, B.J., Jung, S.K., Hwang, M.K., Bode, A.M., Heo, Y.-S., Lee, H.J., Dong, Z., 2008. Caffeic acid, a phenolic phytochemical in coffee, directly inhibits Fyn kinase activity and UVB-induced COX-2 expression. Carcinogenesis 30, 321–330. https://doi.org/10.1093/carcin/bgn282

Kesharwani, R., Patel, D.K., Sachan, A., Kumar, V., Mazumdar, B., 2015. Ethosomes: A Novel Approach for Transdermal and Topical Drug Delivery. Res. Jour. Topi. and Cosmet. Scie. 6, 15. https://doi.org/10.5958/2321-5844.2015.00003.5

Khan, F.A., Maalik, A., Murtaza, G., 2016. Inhibitory mechanism against oxidative stress of caffeic acid. Journal of Food and Drug Analysis 24, 695–702. https://doi.org/10.1016/j.jfda.2016.05.003

Khanduja, K.L., Gandhi, R.K., Pathania, V., Syal, N., 1999. Prevention of N-nitrosodiethylamine-induced lung tumorigenesis by ellagic acid and quercetin in mice. Food and Chemical Toxicology 37, 313–318. https://doi.org/10.1016/S0278-6915(99)00021-6

Khurana, R.K., Gaspar, B.L., Welsby, G., Katare, O.P., Singh, K.K., Singh, B., 2018. Improving the biopharmaceutical attributes of mangiferin using vitamin E-TPGS co-loaded self-assembled phosholipidic nano-mixed micellar systems. Drug Deliv. and Transl. Res. 8, 617–632. https://doi.org/10.1007/s13346-018-0498-4

Kubo, H., Asai, K., Kojima, K., Sugitani, A., Kyomoto, Y., Okamoto, A., Yamada, K., Ijiri, N., Watanabe, T., Hirata, K., Kawaguchi, T., 2019. Astaxanthin Suppresses Cigarette Smoke-Induced Emphysema through Nrf2 Activation in Mice. Marine Drugs 17, 673. https://doi.org/10.3390/md17120673

Kulkarni, C.V., 2012. Lipid crystallization: from self-assembly to hierarchical and biological ordering. Nanoscale 4, 5779. https://doi.org/10.1039/c2nr31465g

Kumar, L., Verma, S., Singh, K., Prasad, D.N., Jain, A.K., 2016. Ethanol Based Vesicular Carriers in Transdermal Drug Delivery: Nanoethosomes and Transethosomes in Focus. NanoWorld J 2. https://doi.org/10.17756/nwj.2016-030

Kumar Mishra, K., Deep Kaur, C., Verma, S., Kumar Sahu, A., Kumar Dash, D., Kashyap, P., Prasad Mishra, S., 2019. Transethosomes and Nanoethosomes: Recent Approach on Transdermal Drug Delivery System, in: Akhyar Farrukh, M. (Ed.), Nanomedicines. IntechOpen. https://doi.org/10.5772/intechopen.81152

Lademann, J., Richter, H., Teichmann, A., Otberg, N., Blume-Peytavi, U., Luengo, J., Weiß, B., Schaefer, U.F., Lehr, C.-M., Wepf, R., 2007. Nanoparticles – An efficient carrier for drug delivery into the hair follicles. European Journal of Pharmaceutics and Biopharmaceutics 66, 159–164. https://doi.org/10.1016/j.ejpb.2006.10.019

Lahmann, C., Bergemann, J., Harrison, G., Young, A.R., 2001. Matrix metalloproteinase-1 and skin ageing in smokers. The Lancet 357, 935–936. https://doi.org/10.1016/S0140-6736(00)04220-3

Lai, F., Caddeo, C., Manca, M.L., Manconi, M., Sinico, C., Fadda, A.M., 2020. What's new in the field of phospholipid vesicular nanocarriers for skin drug delivery. International Journal of Pharmaceutics 583, 119398. https://doi.org/10.1016/j.ijpharm.2020.119398

Lambers, H., Piessens, S., Bloem, A., Pronk, H., Finkel, P., 2006. Natural skin surface pH is on average below 5, which is beneficial for its resident flora. Int J Cosmet Sci 28, 359–370. https://doi.org/10.1111/j.1467-2494.2006.00344.x

Lamichhane, N., Udayakumar, T., D'Souza, W., Simone II, C., Raghavan, S., Polf, J., Mahmood, J., 2018. Liposomes: Clinical Applications and Potential for Image-Guided Drug Delivery. Molecules 23, 288. https://doi.org/10.3390/molecules23020288

Landete, J.M., 2011. Ellagitannins, ellagic acid and their derived metabolites: A review about source, metabolism, functions and health. Food Research International 44, 1150–1160. https://doi.org/10.1016/j.foodres.2011.04.027

Larrosa, M., García-Conesa, M.T., Espín, J.C., Tomás-Barberán, F.A., 2010. Ellagitannins, ellagic acid and vascular health. Molecular Aspects of Medicine 31, 513–539. https://doi.org/10.1016/j.mam.2010.09.005

Lee, J., Zhang, L., 2015. The hierarchy quorum sensing network in Pseudomonas aeruginosa. Protein Cell 6, 26–41. https://doi.org/10.1007/s13238-014-0100-x

Lee, J.-H., Huh, Y.-M., Jun, Y., Seo, J., Jang, J., Song, H.-T., Kim, S., Cho, E.-J., Yoon, H.-G., Suh, J.-S., Cheon, J., 2007. Artificially engineered magnetic nanoparticles for ultra-sensitive molecular imaging. Nat Med 13, 95–99. https://doi.org/10.1038/nm1467

Leonardi, G., Falzone, L., Salemi, R., Zanghï¿½, A., Spandidos, D., Mccubrey, J., Candido, S., Libra, M., 2018. Cutaneous melanoma: From pathogenesis to therapy (Review). Int J Oncol. https://doi.org/10.3892/ijo.2018.4287

Li, J., Anraku, Y., Kataoka, K., 2020. Self-Boosting Catalytic Nanoreactors Integrated with Triggerable Crosslinking Membrane Networks for Initiation of Immunogenic Cell Death by Pyroptosis. Angew. Chem. Int. Ed. 59, 13526–13530. https://doi.org/10.1002/anie.202004180

Li, X., Li, A., Feng, F., Jiang, Q., Sun, H., Chai, Y., Yang, R., Wang, Z., Hou, J., Li, R., 2019. Effect of the hyaluronic acid-poloxamer hydrogel on skin-wound healing: in vitro and in vivo studies. Anim Models Exp Med ame2.12067. https://doi.org/10.1002/ame2.12067

Li, X., Wei, J., Aifantis, K.E., Fan, Y., Feng, Q., Cui, F.-Z., Watari, F., 2016. Current investigations into magnetic nanoparticles for biomedical applications: Magnetic Nanoparticles for Biomedical Applications. J. Biomed. Mater. Res. 104, 1285–1296. https://doi.org/10.1002/jbm.a.35654

Li, Y.-H., Tian, X., 2012. Quorum Sensing and Bacterial Social Interactions in Biofilms. Sensors 12, 2519–2538. https://doi.org/10.3390/s120302519

Lim, S.-J., Lee, M.-K., Kim, C.-K., 2004. Altered chemical and biological activities of all-trans retinoic acid incorporated in solid lipid nanoparticle powders. Journal of Controlled Release 100, 53–61. https://doi.org/10.1016/j.jconrel.2004.07.032

Ling, W., Wang, M., Xiong, C., Xie, D., Chen, Q., Chu, X., Qiu, X., Li, Y., Xiao, X., 2019. Synthesis, surface modification, and applications of magnetic iron oxide nanoparticles. J. Mater. Res. 34, 1828–1844. https://doi.org/10.1557/jmr.2019.129

Lipinski, C.A., Lombardo, F., Dominy, B.W., Feeney, P.J., 1997. Experimental and computational approaches to estimate solubility and permeability in drug discovery and development settings. Advanced Drug Delivery Reviews 23, 3–25. https://doi.org/10.1016/S0169-409X(96)00423-1

Lo, C., Lai, T.-Y., Yang, J.-S., Yang, J.-H., Ma, Y.-S., Weng, S.-W., Lin, H.-Y., Chen, H.-Y., Lin, J.-G., Chung, J.-G., 2011. Gallic acid inhibits the migration and invasion of A375.S2 human melanoma cells through the inhibition of matrix metalloproteinase-2 and Ras: Melanoma Research 21, 267–273. https://doi.org/10.1097/CMR.0b013e3283414444

Loan Honeywell-Nguyen, P., Gooris, G.S., Bouwstra, J.A., 2004. Quantitative Assessment of the Transport of Elastic and Rigid Vesicle Components and a Model Drug from these Vesicle Formulations into Human Skin In Vivo. Journal of Investigative Dermatology 123, 902–910. https://doi.org/10.1111/j.0022-202X.2004.23441.x

Loarca-Piña, G., Kuzmicky, P.A., González de Mejía, E., Kado, N.Y., 1998. Inhibitory effects of ellagic acid on the direct-acting mutagenicity of aflatoxin B1 in the Salmonella microsuspension assay. Mutation Research/Fundamental and Molecular Mechanisms of Mutagenesis 398, 183–187. https://doi.org/10.1016/S0027-5107(97)00245-5

Løkling, K.-E., Fossheim, S.L., Klaveness, J., Skurtveit, R., 2004. Biodistribution of pH-responsive liposomes for MRI and a novel approach to improve the pH-responsiveness. Journal of Controlled Release 98, 87–95. https://doi.org/10.1016/j.jconrel.2004.04.015

Lombardo, D., Kiselev, M.A., Caccamo, M.T., 2019. Smart Nanoparticles for Drug Delivery Application: Development of Versatile Nanocarrier Platforms in Biotechnology and Nanomedicine. Journal of Nanomaterials 2019, 1–26. https://doi.org/10.1155/2019/3702518

Lopez-Torres, M., Shindo, Y., Packer, L., 1994. Effect of Age on Antioxidants and Molecular Markers of Oxidative Damage in Murine Epidermis and Dermis. Journal of Investigative Dermatology 102, 476–480. https://doi.org/10.1111/1523-1747.ep12373032

Luchini, A., Vitiello, G., 2019. Understanding the Nano-bio Interfaces: Lipid-Coatings for Inorganic Nanoparticles as Promising Strategy for Biomedical Applications. Front. Chem. 7, 343. https://doi.org/10.3389/fchem.2019.00343

M. Abdulbaqi, I., Darwis, Y., Abdul Karim Khan, N., Abou Assi, R., Ali Khan, A., 2016. Ethosomal nanocarriers: the impact of constituents and formulation techniques on ethosomal properties, in vivo studies, and clinical trials. IJN 2279. https://doi.org/10.2147/IJN.S105016

Ma, H., Williams, P.L., Diamond, S.A., 2013. Ecotoxicity of manufactured ZnO nanoparticles – A review. Environmental Pollution 172, 76–85. https://doi.org/10.1016/j.envpol.2012.08.011

Macacu, A., Autier, P., Boniol, M., Boyle, P., 2015. Active and passive smoking and risk of breast cancer: a meta-analysis. Breast Cancer Res Treat 154, 213–224. https://doi.org/10.1007/s10549-015-3628-4

Malekar, S.A., Sarode, A.L., Bach, A.C., Worthen, D.R., 2016. The Localization of Phenolic Compounds in Liposomal Bilayers and Their Effects on Surface Characteristics and Colloidal Stability. AAPS PharmSciTech 17, 1468–1476. https://doi.org/10.1208/s12249-016-0483-5

Malik, A., Afaq, S., Shahid, M., Akhtar, K., Assiri, A., 2011. Influence of ellagic acid on prostate cancer cell proliferation: A caspase–dependent pathway. Asian Pacific Journal of Tropical Medicine 4, 550–555. https://doi.org/10.1016/S1995-7645(11)60144-2

Marinova, G., Batchvarov, V., 2011. Evaluation of the methods for determination of the free radical scavenging activity by DPPH. Bulgarian Journal of Agricultural Science 17, 11–24.

Matsuoka, H., Tanaka, H., Iizuka, N., Hashimoto, T., Ise, N., 1990. Elastic scattering from cubic lattice systems with paracrystalline distortion. II. Phys. Rev. B 41, 3854–3856. https://doi.org/10.1103/PhysRevB.41.3854

Mayol, L., Quaglia, F., Borzacchiello, A., Ambrosio, L., Rotonda, M., 2008. A novel poloxamers/hyaluronic acid in situ forming hydrogel for drug delivery: Rheological, mucoadhesive and in vitro release properties. European Journal of Pharmaceutics and Biopharmaceutics 70, 199–206. https://doi.org/10.1016/j.ejpb.2008.04.025

McDaniel, D., Farris, P., Valacchi, G., 2018. Atmospheric skin aging-Contributors and inhibitors. J Cosmet Dermatol 17, 124–137. https://doi.org/10.1111/jocd.12518

Mehnert, W., 2001. Solid lipid nanoparticles Production, characterization and applications. Advanced Drug Delivery Reviews 47, 165–196. https://doi.org/10.1016/S0169-409X(01)00105-3

Mishra, D., Mishra, P.K., Dabadghao, S., Dubey, V., Nahar, M., Jain, N.K., 2010. Comparative evaluation of hepatitis B surface antigen–loaded elastic liposomes and ethosomes for human dendritic cell uptake and immune response. Nanomedicine: Nanotechnology, Biology and Medicine 6, 110–118. https://doi.org/10.1016/j.nano.2009.04.003

Mishra, V., Bansal, K., Verma, A., Yadav, N., Thakur, S., Sudhakar, K., Rosenholm, J., 2018. Solid Lipid Nanoparticles: Emerging Colloidal Nano Drug Delivery Systems. Pharmaceutics 10, 191. https://doi.org/10.3390/pharmaceutics10040191

Montiel Schneider, M.G., Lassalle, V.L., 2017. Magnetic iron oxide nanoparticles as novel and efficient tools for atherosclerosis diagnosis. Biomedicine & Pharmacotherapy 93, 1098–1115. https://doi.org/10.1016/j.biopha.2017.07.012

Mukherjee, S., Ray, S., Thakur, R., 2009. Solid lipid nanoparticles: A modern formulation approach in drug delivery system. Indian J Pharm Sci 71, 349. https://doi.org/10.4103/0250-474X.57282

Müller, R.H., 2000. Solid lipid nanoparticles (SLN) for controlled drug delivery – a review of the state of the art. European Journal of Pharmaceutics and Biopharmaceutics 50, 161–177. https://doi.org/10.1016/S0939-6411(00)00087-4

Müller, R.H., Radtke, M., Wissing, S.A., 2002. Solid lipid nanoparticles (SLN) and nanostructured lipid carriers (NLC) in cosmetic and dermatological preparations. Advanced Drug Delivery Reviews 54, S131–S155. https://doi.org/10.1016/S0169-409X(02)00118-7

Munin, A., Edwards-Lévy, F., 2011. Encapsulation of Natural Polyphenolic Compounds; a Review. Pharmaceutics 3, 793–829. https://doi.org/10.3390/pharmaceutics3040793

Muresan, Ximena M., Sticozzi, C., Belmonte, G., Cervellati, F., Ferrara, F., Lila, M.A., Valacchi, G., 2018. SR-B1 involvement in keratinocytes in vitro wound closure. Archives of Biochemistry and Biophysics 658, 1–6. https://doi.org/10.1016/j.abb.2018.09.014

Muresan, Ximena Maria, Sticozzi, C., Belmonte, G., Savelli, V., Evelson, P., Valacchi, G., 2018. Modulation of cutaneous scavenger receptor B1 levels by exogenous stressors impairs "in vitro" wound closure. Mechanisms of Ageing and Development 172, 78–85. https://doi.org/10.1016/j.mad.2017.11.006

Natsheh, H., Vettorato, E., Touitou, E., 2019. Ethosomes for Dermal Administration of Natural Active Molecules. CPD 25, 2338–2348. https://doi.org/10.2174/1381612825666190716095826

Nichols, J.A., Katiyar, S.K., 2010. Skin photoprotection by natural polyphenols: anti-inflammatory, antioxidant and DNA repair mechanisms. Arch Dermatol Res 302, 71–83. https://doi.org/10.1007/s00403-009-1001-3

Niu, X.-Q., Zhang, D.-P., Bian, Q., Feng, X.-F., Li, H., Rao, Y.-F., Shen, Y.-M., Geng, F.-N., Yuan, A.-R., Ying, X.-Y., Gao, J.-Q., 2019. Mechanism investigation of ethosomes transdermal permeation. International Journal of Pharmaceutics: X 1, 100027. https://doi.org/10.1016/j.ijpx.2019.100027

Nocchi, S., Björklund, S., Svensson, B., Engblom, J., Ruzgas, T., 2017. Electrochemical monitoring of native catalase activity in skin using skin covered oxygen electrode. Biosensors and Bioelectronics 93, 9–13. https://doi.org/10.1016/j.bios.2017.01.001

Noh, S., Moon, S.H., Shin, T.-H., Lim, Y., Cheon, J., 2017. Recent advances of magneto-thermal capabilities of nanoparticles: From design principles to biomedical applications. Nano Today 13, 61–76. https://doi.org/10.1016/j.nantod.2017.02.006

Nohynek, G.J., Antignac, E., Re, T., Toutain, H., 2010. Safety assessment of personal care products/cosmetics and their ingredients. Toxicology and Applied Pharmacology 243, 239–259. https://doi.org/10.1016/j.taap.2009.12.001

Nwosu, C.V., Boyd, L.C., Sheldon, B., 1997. Effect of fatty acid composition of phospholipids on their antioxidant properties and activity index. J Amer Oil Chem Soc 74, 293–297. https://doi.org/10.1007/s11746-997-0139-4

Oliveira, R.R., Carrião, M.S., Pacheco, M.T., Branquinho, L.C., de Souza, A.L.R., Bakuzis, A.F., Lima, E.M., 2018. Triggered release of paclitaxel from magnetic solid lipid nanoparticles by magnetic hyperthermia. Materials Science and Engineering: C 92, 547–553. https://doi.org/10.1016/j.msec.2018.07.011

Onor, I.O., Stirling, D.L., Williams, S.R., Bediako, D., Borghol, A., Harris, M.B., Darensburg, T.B., Clay, S.D., Okpechi, S.C., Sarpong, D.F., 2017. Clinical Effects of Cigarette Smoking: Epidemiologic Impact and Review of Pharmacotherapy Options. IJERPH 14, 1147. https://doi.org/10.3390/ijerph14101147

Ortiz, A., Grando, S.A., 2012. Smoking and the skin: Tobacco effects on skin. International Journal of Dermatology 51, 250–262. https://doi.org/10.1111/j.1365-4632.2011.05205.x

Paliwal, R., Paliwal, S.R., Kenwat, R., Kurmi, B.D., Sahu, M.K., 2020. Solid lipid nanoparticles: a review on recent perspectives and patents. Expert Opinion on Therapeutic Patents 30, 179–194. https://doi.org/10.1080/13543776.2020.1720649

Pang, X., Cui, F., Tian, J., Chen, J., Zhou, J., Zhou, W., 2009. Preparation and characterization of magnetic solid lipid nanoparticles loaded with ibuprofen. Asian Journal of Pharmaceutical Science 4, 132–137.

Pankhurst, Q., Jones, S., Dobson, J., 2016. Applications of magnetic nanoparticles in biomedicine: the story so far. J. Phys. D: Appl. Phys. 49, 501002. https://doi.org/10.1088/0022-3727/49/50/501002

Pardeike, J., Hommoss, A., Müller, R.H., 2009. Lipid nanoparticles (SLN, NLC) in cosmetic and pharmaceutical dermal products. International Journal of Pharmaceutics 366, 170–184. https://doi.org/10.1016/j.ijpharm.2008.10.003

Pardeshi, C., Rajput, P., Belgamwar, V., Tekade, A., Patil, G., Chaudhary, K., Sonje, A., 2012. Solid lipid based nanocarriers: An overview / Nanonosači na bazi čvrstih lipida: Pregled. Acta Pharmaceutica 62, 433–472. https://doi.org/10.2478/v10007-012-0040-z

Patitsa, M., Karathanou, K., Kanaki, Z., Tzioga, L., Pippa, N., Demetzos, C., Verganelakis, D.A., Cournia, Z., Klinakis, A., 2017. Magnetic nanoparticles coated with polyarabic acid demonstrate enhanced drug delivery and imaging properties for cancer theranostic applications. Sci Rep 7, 775. https://doi.org/10.1038/s41598-017-00836-y

Pattni, B.S., Chupin, V.V., Torchilin, V.P., 2015. New Developments in Liposomal Drug Delivery. Chem. Rev. 115, 10938–10966. https://doi.org/10.1021/acs.chemrev.5b00046

Paul, S.D., Sharma, H., Jeswani, G., Jha, A.K., 2017. Novel gels: implications for drug delivery, in: Nanostructures for Drug Delivery. Elsevier, pp. 379–412. https://doi.org/10.1016/B978-0-323-46143-6.00012-9

Pecora, R., 2000. Dynamic light scattering measurement of nanometer particles in liquids. Journal of Nanoparticle Research 2, 123–131. https://doi.org/10.1023/A:1010067107182

Pecorelli, A., Ciccoli, L., Signorini, C., Leoncini, S., Giardini, A., D'Esposito, M., Filosa, S., Hayek, J., De Felice, C., Valacchi, G., 2011. Increased levels of 4HNE-protein plasma adducts in Rett syndrome. Clinical Biochemistry 44, 368–371. https://doi.org/10.1016/j.clinbiochem.2011.01.007

Pecorelli, A., Woodby, B., Prieux, R., Valacchi, G., 2019. Involvement of 4-hydroxy-2-nonenal in pollution-induced skin damage. BioFactors biof.1513. https://doi.org/10.1002/biof.1513

Pedersen, P.J., Adolph, S.K., Subramanian, A.K., Arouri, A., Andresen, T.L., Mouritsen, O.G., Madsen, R., Madsen, M.W., Peters, G.H., Clausen, M.H., 2010. Liposomal Formulation of Retinoids Designed for Enzyme Triggered Release. J. Med. Chem. 53, 3782–3792. https://doi.org/10.1021/jm100190c

Peira, E., Marzola, P., Podio, V., Aime, S., Sbarbati, A., Gasco, M.R., 2003. *In Vitro* and *In Vivo* Study of Solid Lipid Nanoparticles Loaded with Superparamagnetic Iron Oxide. Journal of Drug Targeting 11, 19–24. https://doi.org/10.1080/1061186031000086108

Pelinson, L.P., Assmann, C.E., Palma, T.V., da Cruz, I.B.M., Pillat, M.M., Mânica, A., Stefanello, N., Weis, G.C.C., de Oliveira Alves, A., de Andrade, C.M., Ulrich, H., Morsch, V.M.M., Schetinger, M.R.C., Bagatini, M.D., 2019. Antiproliferative and apoptotic effects of caffeic acid on SK-Mel-28 human melanoma cancer cells. Mol Biol Rep 46, 2085–2092. https://doi.org/10.1007/s11033-019-04658-1

Penesyan, A., Gillings, M., Paulsen, I., 2015. Antibiotic Discovery: Combatting Bacterial Resistance in Cells and in Biofilm Communities. Molecules 20, 5286–5298. https://doi.org/10.3390/molecules20045286

Pereira, G.G., Dimer, F.A., Guterres, S.S., Kechinski, C.P., Granada, J.E., Cardozo, N.S.M., 2013. Formulation and characterization of poloxamer 407®: thermoreversible gel containing polymeric microparticles and hyaluronic acid. Quím. Nova 36, 1121–1125. https://doi.org/10.1590/S0100-40422013000800008

Permana, A.D., Utami, R.N., Courtenay, A.J., Manggau, M.A., Donnelly, R.F., Rahman, L., 2020. Phytosomal nanocarriers as platforms for improved delivery of natural antioxidant and photoprotective compounds in propolis: An approach for enhanced both dissolution behaviour in biorelevant media and skin retention profiles. Journal of Photochemistry and Photobiology B: Biology 205, 111846. https://doi.org/10.1016/j.jphotobiol.2020.111846

Pinho, E., Soares, G., Henriques, M., 2015. Evaluation of antibacterial activity of caffeic acid encapsulated by β -cyclodextrins. Journal of Microencapsulation 32, 804–810. https://doi.org/10.3109/02652048.2015.1094531

Pink, D.L., Loruthai, O., Ziolek, R.M., Wasutrasawat, P., Terry, A.E., Lawrence, M.J., Lorenz, C.D., 2019. On the Structure of Solid Lipid Nanoparticles. Small 15, 1903156. https://doi.org/10.1002/smll.201903156

Pollock, S., Antrobus, R., Newton, L., Kampa, B., Rossa, J., Latham, S., Nichita, N.B., Dwek, R.A., Zitzmann, N., 2010. Uptake and trafficking of liposomes to the endoplasmic reticulum. FASEB j. 24, 1866–1878. https://doi.org/10.1096/fj.09-145755

Prabu, S.L., Suriyaprakash, T.N.K., Thirumurugan, R., 2017. Medicated Nanoparticle for Gene Delivery, in: Maiti, S., Sen, K.K. (Eds.), Advanced Technology for Delivering Therapeutics. InTech. https://doi.org/10.5772/65709

Prasad, N.R., Jeyanthimala, K., Ramachandran, S., 2009. Caffeic acid modulates ultraviolet radiation-B induced oxidative damage in human blood lymphocytes. Journal of Photochemistry and Photobiology B: Biology 95, 196–203. https://doi.org/10.1016/j.jphotobiol.2009.03.007

Prieux, R., Eeman, M., Rothen-Rutishauser, B., Valacchi, G., 2020. Mimicking cigarette smoke exposure to assess cutaneous toxicity. Toxicology in Vitro 62, 104664. https://doi.org/10.1016/j.tiv.2019.104664

Puglia, C., Bonina, F., Rizza, L., Cortesi, R., Merlotti, E., Drechsler, M., Mariani, P., Contado, C., Ravani, L., Esposito, E., 2010. Evaluation of Percutaneous Absorption of Naproxen from Different Liposomal Formulations. Journal of Pharmaceutical Sciences 99, 2819–2829. https://doi.org/10.1002/jps.22028

Quan, T., Qin, Z., Xia, W., Shao, Y., Voorhees, J.J., Fisher, G.J., 2009. Matrix-Degrading Metalloproteinases in Photoaging. Journal of Investigative Dermatology Symposium Proceedings 14, 20–24. https://doi.org/10.1038/jidsymp.2009.8

Rai, R., Alwani, S., Badea, I., 2019. Polymeric Nanoparticles in Gene Therapy: New Avenues of Design and Optimization for Delivery Applications. Polymers 11, 745. https://doi.org/10.3390/polym11040745

Rajagopalan, P., Nanjappa, V., Raja, R., Jain, A.P., Mangalaparthi, K.K., Sathe, G.J., Babu, N., Patel, K., Cavusoglu, N., Soeur, J., Pandey, A., Roy, N., Breton, L., Chatterjee, A., Misra, N., Gowda, H., 2016. How Does Chronic Cigarette Smoke Exposure Affect Human Skin? A Global Proteomics Study in Primary Human Keratinocytes. OMICS: A Journal of Integrative Biology 20, 615–626. https://doi.org/10.1089/omi.2016.0123

Rasekh, M., Ahmad, Z., Cross, R., Hernández-Gil, J., Wilton-Ely, J.D.E.T., Miller, P.W., 2017. Facile Preparation of Drug-Loaded Tristearin Encapsulated Superparamagnetic Iron Oxide Nanoparticles Using Coaxial Electrospray Processing. Mol. Pharmaceutics 14, 2010–2023. https://doi.org/10.1021/acs.molpharmaceut.7b00109

Rasko, D.A., Sperandio, V., 2010. Anti-virulence strategies to combat bacteria-mediated disease. Nat Rev Drug Discov 9, 117–128. https://doi.org/10.1038/nrd3013

Reichel, D., Tripathi, M., Perez, J.M., 2019. Biological Effects of Nanoparticles on Macrophage Polarization in the Tumor Microenvironment. Nanotheranostics 3, 66–88. https://doi.org/10.7150/ntno.30052

Rizzo, R., Bergamini, G., Bortolotti, D., Leal, T., D'Orazio, C., Pintani, E., Melchiorri, L., Zavatti, E., Assael, B.M., Sorio, C., Melotti, P., 2016. HLA-G expression and regulation during *Pseudomonas aeruginosa* infection in cystic fibrosis patients. Future Microbiology 11, 363–373. https://doi.org/10.2217/fmb.15.143

Robinson, M.K., Cohen, C., de Fraissinette, A. de B., Ponec, M., Whittle, E., Fentem, J.H., 2002. Non-animal testing strategies for assessment of the skin corrosion and skin irritation potential of ingredients and finished products. Food and Chemical Toxicology 40, 573–592. https://doi.org/10.1016/S0278-6915(02)00005-4

Rosillo, M.A., Sanchez-Hidalgo, M., Cárdeno, A., Alarcón de la Lastra, C., 2011. Protective effect of ellagic acid, a natural polyphenolic compound, in a murine model of

Crohn's disease. Biochemical Pharmacology 82, 737–745. https://doi.org/10.1016/j.bcp.2011.06.043

Saija, A., Tomaino, A., Cascio, R.L., Trombetta, D., Proteggente, A., De Pasquale, A., Uccella, N., Bonina, F., 1999. Ferulic and caffeic acids as potential protective agents against photooxidative skin damage. Journal of the Science of Food and Agriculture 79, 476–480. https://doi.org/10.1002/(sici)1097-0010(19990301)79:3<476::aid-jsfa270>3.0.co;2-l

Saito, H., Ishihara, K., 1997. Antioxidant activity and active sites of phospholipids as antioxidants. J Amer Oil Chem Soc 74, 1531–1536. https://doi.org/10.1007/s11746-997-0072-6

Salamanca, C., Barrera-Ocampo, A., Lasso, J., Camacho, N., Yarce, C., 2018. Franz Diffusion Cell Approach for Pre-Formulation Characterisation of Ketoprofen Semi-Solid Dosage Forms. Pharmaceutics 10, 148. https://doi.org/10.3390/pharmaceutics10030148

Salvi, V.R., Pawar, P., 2019. Nanostructured lipid carriers (NLC) system: A novel drug targeting carrier. Journal of Drug Delivery Science and Technology 51, 255–267. https://doi.org/10.1016/j.jddst.2019.02.017

Santos, I.S., Ponte, B.M., Boonme, P., Silva, A.M., Souto, E.B., 2013. Nanoencapsulation of polyphenols for protective effect against colon–rectal cancer. Biotechnology Advances 31, 514–523. https://doi.org/10.1016/j.biotechadv.2012.08.005

Scheller, S., Dworniczak, S., Pogorzelska, T., Rajca, M., Shani, J., 2011. Effect of Quercetin, Caffeic Acid and Caffeic Acid Phenylethyl Ester, Solubilized in Non-ionic Surfactants, on Histamine Release in vivo and in vitro. Arzneimittelforschung 50, 72–76. https://doi.org/10.1055/s-0031-1300166

Scioli Montoto, S., Muraca, G., Ruiz, M.E., 2020. Solid Lipid Nanoparticles for Drug Delivery: Pharmacological and Biopharmaceutical Aspects. Front. Mol. Biosci. 7, 587997. https://doi.org/10.3389/fmolb.2020.587997

Seeram, N., Adams, L., Henning, S., Niu, Y., Zhang, Y., Nair, M., Heber, D., 2005. In vitro antiproliferative, apoptotic and antioxidant activities of punicalagin, ellagic acid and a total pomegranate tannin extract are enhanced in combination with other polyphenols as found in pomegranate juice. The Journal of Nutritional Biochemistry 16, 360–367. https://doi.org/10.1016/j.jnutbio.2005.01.006

Seeram, N.P., Lee, R., Heber, D., 2004. Bioavailability of ellagic acid in human plasma after consumption of ellagitannins from pomegranate (Punica granatum L.) juice. Clinica Chimica Acta 348, 63–68. https://doi.org/10.1016/j.cccn.2004.04.029

Sguizzato, M., Cortesi, R., Gallerani, E., Drechsler, M., Marvelli, L., Mariani, P., Carducci, F., Gavioli, R., Esposito, E., Bergamini, P., 2017. Solid lipid nanoparticles for the delivery of 1,3,5-triaza-7-phosphaadamantane (PTA) platinum (II) carboxylates.

Materials Science and Engineering: C 74, 357–364. https://doi.org/10.1016/j.msec.2016.12.020

Sguizzato, M., Mariani, P., Ferrara, F., Drechsler, M., Hallan, S.S., Huang, N., Simelière, F., Khunti, N., Cortesi, R., Marchetti, N., Valacchi, G., Esposito, E., 2020a. Nanoparticulate Gels for Cutaneous Administration of Caffeic Acid. Nanomaterials 10, 961. https://doi.org/10.3390/nano10050961

Sguizzato, M., Mariani, P., Spinozzi, F., Benedusi, M., Cervellati, F., Cortesi, R., Drechsler, M., Prieux, R., Valacchi, G., Esposito, E., 2020b. Ethosomes for Coenzyme Q10 Cutaneous Administration: From Design to 3D Skin Tissue Evaluation. Antioxidants 9, 485. https://doi.org/10.3390/antiox9060485

Sguizzato, M., Valacchi, G., Pecorelli, A., Boldrini, P., Simelière, F., Huang, N., Cortesi, R., Esposito, E., 2020c. Gallic acid loaded poloxamer gel as new adjuvant strategy for melanoma: A preliminary study. Colloids and Surfaces B: Biointerfaces 185, 110613. https://doi.org/10.1016/j.colsurfb.2019.110613

Shanavas, A., Sasidharan, S., Bahadur, D., Srivastava, R., 2017. Magnetic core-shell hybrid nanoparticles for receptor targeted anti-cancer therapy and magnetic resonance imaging. Journal of Colloid and Interface Science 486, 112–120. https://doi.org/10.1016/j.jcis.2016.09.060

Shen, L.-N., Zhang, Y.-T., Wang, Q., Xu, L., Feng, N.-P., 2014. Enhanced in vitro and in vivo skin deposition of apigenin delivered using ethosomes. International Journal of Pharmaceutics 460, 280–288. https://doi.org/10.1016/j.ijpharm.2013.11.017

Siewert, M., Dressman, J., Brown, C.K., Shah, V.P., Aiache, J.-M., Aoyagi, N., Bashaw, D., Brown, C., Brown, W., Burgess, D., Crison, J., DeLuca, P., Djerki, R., Dressman, J., Foster, T., Gjellan, K., Gray, V., Hussain, A., Ingallinera, T., Klancke, J., Kraemer, J., Kristensen, H., Kumi, K., Leuner, C., Limberg, J., Loos, P., Margulis, L., Marroum, P., Moeller, H., Mueller, B., Mueller-Zsigmondy, M., Okafo, N., Ouderkirk, L., Parsi, S., Qureshi, S., Robinson, J., Shah, V., Siewert, M., Uppoor, R., Williams, R., 2003. FIP/AAPS guidelines to dissolution/in vitro release testing of novel/special dosage forms. AAPS PharmSciTech 4, 43–52. https://doi.org/10.1208/pt040107

Singh Hallan, S., Sguizzato, M., Pavoni, G., Baldisserotto, A., Drechsler, M., Mariani, P., Esposito, E., Cortesi, R., 2020. Ellagic Acid Containing Nanostructured Lipid Carriers for Topical Application: A Preliminary Study. Molecules 25, 1449. https://doi.org/10.3390/molecules25061449

Soare, J.R., Dinis, T.C.P., Cunha, A.P., Almeida, L., 1997. Antioxidant Activities of Some Extracts of *Thymus zygis*. Free Radical Research 26, 469–478. https://doi.org/10.3109/10715769709084484

Soeur, J., Belaïdi, J.-P., Chollet, C., Denat, L., Dimitrov, A., Jones, C., Perez, P., Zanini, M., Zobiri, O., Mezzache, S., Erdmann, D., Lereaux, G., Eilstein, J., Marrot, L., 2017. Photo-pollution stress in skin: Traces of pollutants (PAH and particulate matter)

impair redox homeostasis in keratinocytes exposed to UVA1. Journal of Dermatological Science 86, 162–169. https://doi.org/10.1016/j.jdermsci.2017.01.007

Song, C.K., Balakrishnan, P., Shim, C.-K., Chung, S.-J., Chong, S., Kim, D.-D., 2012. A novel vesicular carrier, transethosome, for enhanced skin delivery of voriconazole: Characterization and in vitro/in vivo evaluation. Colloids and Surfaces B: Biointerfaces 92, 299–304. https://doi.org/10.1016/j.colsurfb.2011.12.004

Sousa, C., Botelho, C.M., Oliveira, R., 2011. Nanotechnology applied to medical biofilms control.

Spagnol, C.M., Zaera, A.M., Isaac, V.L.B., Corrêa, M.A., Salgado, H.R.N., 2018. Release and permeation profiles of spray-dried chitosan microparticles containing caffeic acid. Saudi Pharmaceutical Journal 26, 410–415. https://doi.org/10.1016/j.jsps.2017.12.021

Sticozzi, C., Cervellati, F., Muresan, X.M., Cervellati, C., Valacchi, G., 2014. Resveratrol prevents cigarette smoke-induced keratinocytes damage. Food Funct. 5, 2348. https://doi.org/10.1039/C4FO00407H

Ta, T., Porter, T.M., 2013. Thermosensitive liposomes for localized delivery and triggered release of chemotherapy. Journal of Controlled Release 169, 112–125. https://doi.org/10.1016/j.jconrel.2013.03.036

Tanrıverdi, S.T., Özer, Ö., 2013. Novel topical formulations of Terbinafine-HCl for treatment of onychomycosis. European Journal of Pharmaceutical Sciences 48, 628–636. https://doi.org/10.1016/j.ejps.2012.12.014

Tetyczka, C., Hodzic, A., Kriechbaum, M., Juraić, K., Spirk, C., Hartl, S., Pritz, E., Leitinger, G., Roblegg, E., 2019. Comprehensive characterization of nanostructured lipid carriers using laboratory and synchrotron X-ray scattering and diffraction. European Journal of Pharmaceutics and Biopharmaceutics 139, 153–160. https://doi.org/10.1016/j.ejpb.2019.03.017

Touitou, E., Dayan, N., Bergelson, L., Godin, B., Eliaz, M., 2000. Ethosomes — novel vesicular carriers for enhanced delivery: characterization and skin penetration properties. Journal of Controlled Release 65, 403–418. https://doi.org/10.1016/S0168-3659(99)00222-9

Un Nabi, S.A.A., Sheraz, M.A., Ahmed, S., Mustaan, N., Ahmad, I., 2016. Pharmaceutical Gels: A Review. RADS Journal of Pharmacy and Pharmaceutical Sciences 4, 40–48.

Üner, M., 2016. Characterization and Imaging of Solid Lipid Nanoparticles and Nanostructured Lipid Carriers, in: Aliofkhazraei, M. (Ed.), Handbook of Nanoparticles. Springer International Publishing, Cham, pp. 117–141. https://doi.org/10.1007/978-3-319-15338-4_3

Valacchi, G., Pecorelli, A., Belmonte, G., Pambianchi, E., Cervellati, F., Lynch, S., Krol, Y., Oresajo, C., 2017. Protective Effects of Topical Vitamin C Compound Mixtures against Ozone-Induced Damage in Human Skin. Journal of Investigative Dermatology 137, 1373–1375. https://doi.org/10.1016/j.jid.2017.01.034

Valko, M., Leibfritz, D., Moncol, J., Cronin, M.T.D., Mazur, M., Telser, J., 2007. Free radicals and antioxidants in normal physiological functions and human disease. The International Journal of Biochemistry & Cell Biology 39, 44–84. https://doi.org/10.1016/j.biocel.2006.07.001

Van Tran, V., Moon, J.-Y., Lee, Y.-C., 2019. Liposomes for delivery of antioxidants in cosmeceuticals: Challenges and development strategies. Journal of Controlled Release 300, 114–140. https://doi.org/10.1016/j.jconrel.2019.03.003

Verma, P., Pathak, K., 2010. Therapeutic and cosmeceutical potential of ethosomes: An overview. J Adv Pharm Tech Res 1, 274. https://doi.org/10.4103/0110-5558.72415

Wang, C.Y., Huang, L., 1984. Polyhistidine mediates an acid-dependent fusion of negatively charged liposomes. Biochemistry 23, 4409–4416. https://doi.org/10.1021/bi00314a026

Wang, M., Li, J., Rangarajan, M., Shao, Y., LaVoie, E.J., Huang, T.-C., Ho, C.-T., 1998. Antioxidative Phenolic Compounds from Sage (*Salvia officinalis*). J. Agric. Food Chem. 46, 4869–4873. https://doi.org/10.1021/jf980614b

Wang, S.Q., Balagula, Y., Osterwalder, U., 2010. Photoprotection: a Review of the Current and Future Technologies. Dermatologic Therapy 23, 31–47. https://doi.org/10.1111/j.1529-8019.2009.01289.x

Weatherly, C.A., Woods, R.M., Armstrong, D.W., 2014. Rapid Analysis of Ethanol and Water in Commercial Products Using Ionic Liquid Capillary Gas Chromatography with Thermal Conductivity Detection and/or Barrier Discharge Ionization Detection. J. Agric. Food Chem. 62, 1832–1838. https://doi.org/10.1021/jf4050167

Wei, G., Xu, H., Ding, P.T., Li, S.M., Zheng, J.M., 2002. Thermosetting gels with modulated gelation temperature for ophthalmic use: the rheological and gamma scintigraphic studies. Journal of Controlled Release 83, 65–74. https://doi.org/10.1016/S0168-3659(02)00175-X

Wissing, S.A., Müller, R.H., 2003. The influence of solid lipid nanoparticles on skin hydration and viscoelasticity – in vivo study. European Journal of Pharmaceutics and Biopharmaceutics 56, 67–72. https://doi.org/10.1016/S0939-6411(03)00040-7

Wu, J.H., Cohen, B.A., 2019. The stigma of skin disease: Current Opinion in Pediatrics 31, 509–514. https://doi.org/10.1097/MOP.0000000000000792

Xie, J., Ji, Y., Xue, W., Ma, D., Hu, Y., 2018. Hyaluronic acid-containing ethosomes as a potential carrier for transdermal drug delivery. Colloids and Surfaces B: Biointerfaces 172, 323–329. https://doi.org/10.1016/j.colsurfb.2018.08.061

Xu, X., Shen, Y., Wang, W., Sun, C., Li, C., Xiong, Y., Tu, J., 2014. Preparation and in vitro characterization of thermosensitive and mucoadhesive hydrogels for nasal delivery of phenylephrine hydrochloride. European Journal of Pharmaceutics and Biopharmaceutics 88, 998–1004. https://doi.org/10.1016/j.ejpb.2014.08.015

Yang, D., Moh, S., Son, D., You, S., Kinyua, A., Ko, C., Song, M., Yeo, J., Choi, Y.-H., Kim, K., 2016. Gallic Acid Promotes Wound Healing in Normal and Hyperglucidic Conditions. Molecules 21, 899. https://doi.org/10.3390/molecules21070899

Yang, S.-Y., Pyo, M.C., Nam, M.-H., Lee, K.-W., 2019. ERK/Nrf2 pathway activation by caffeic acid in HepG2 cells alleviates its hepatocellular damage caused by t-butylhydroperoxide-induced oxidative stress. BMC Complement Altern Med 19, 139. https://doi.org/10.1186/s12906-019-2551-3

Ying, X.-Y., Du, Y.-Z., Hong, L.-H., Yuan, H., Hu, F.-Q., 2011. Magnetic lipid nanoparticles loading doxorubicin for intracellular delivery: Preparation and characteristics. Journal of Magnetism and Magnetic Materials 323, 1088–1093. https://doi.org/10.1016/j.jmmm.2010.12.019

Yu, X., Du, L., Li, Y., Fu, G., Jin, Y., 2015. Improved anti-melanoma effect of a transdermal mitoxantrone ethosome gel. Biomedicine & Pharmacotherapy 73, 6–11. https://doi.org/10.1016/j.biopha.2015.05.002

Zeb, A., Arif, S.T., Malik, M., Shah, F.A., Din, F.U., Qureshi, O.S., Lee, E.-S., Lee, G.-Y., Kim, J.-K., 2019. Potential of nanoparticulate carriers for improved drug delivery via skin. J. Pharm. Investig. 49, 485–517. https://doi.org/10.1007/s40005-018-00418-8

Zhang, L., Pornpattananangkul, D., Hu, C.-M., Huang, C.-M., 2010. Development of Nanoparticles for Antimicrobial Drug Delivery. CMC 17, 585–594. https://doi.org/10.2174/092986710790416290

Zhang, Y., Ng, W., Hu, J., Mussa, S.S., Ge, Y., Xu, H., 2018. Formulation and in vitro stability evaluation of ethosomal carbomer hydrogel for transdermal vaccine delivery. Colloids and Surfaces B: Biointerfaces 163, 184–191. https://doi.org/10.1016/j.colsurfb.2017.12.031

Zhou, Y., Wei, Y.-H., Zhang, G.-Q., Wu, X.-A., 2010. Synergistic penetration of ethosomes and lipophilic prodrug on the transdermal delivery of acyclovir. Arch. Pharm. Res. 33, 567–574. https://doi.org/10.1007/s12272-010-0411-2

Zhu, N., Ji, H., Yu, P., Niu, J., Farooq, M., Akram, M., Udego, I., Li, H., Niu, X., 2018. Surface Modification of Magnetic Iron Oxide Nanoparticles. Nanomaterials 8, 810. https://doi.org/10.3390/nano8100810

13 APPENDICES

13.1 SYNTHESIS AND CHARACTERIZATION OF LAS QS INHIBITORS

Synthetic flow schemes and physicochemical properties of CDC and PF are reported in chapter 9 (section, 9.2.1, Table 28, Figure 51). Commercially available reagents were used without further purification. NMR spectra were recorded on a Varian Mercury Plus 400 spectrometer at 400 MHz (^{1}H) and 100 MHz (^{13}C). Peak positions are given in parts per million (δ) down-field from tetramethylsilane used as an internal standard. J values are expressed in hertz. Electrospray mass spectra were recorded on a Waters Micromass ZQ-20000 instrument. All reactions were monitored by thin-layer chromatography and/or reversed-phase high-performance liquid chromatography (HPLC). Analytical TLC was carried out using Merck precoated silica gel F-254 plates. Preparative flash chromatography was done using Merck silica gel 60 (0.063-0.200 mm) using the indicated eluent. Solvents were dried according to standard procedures and reactions requiring anhydrous conditions were performed under argon atmosphere. Solutions containing the final product were dried with Na_2SO_4, filtered, and concentrated under reduced pressure using a rotatory evaporator. Analytical RP-HPLC was performed on a Beckman System Gold 168 using C18 columns, namely a Phenomex Luna (4.6 mm x 10 cm, 3μ) for CDC and a Waters XBridge (4.6 mm x 15 cm, 5μ) for PF, the flow was 0.5 mL/min with detection at 220 nm and with a binary eluents system (eluent A: H_2O + 0.1% TFA, eluent B: CH_3CN + 0.1% TFA), using a linear gradient (t = 0 min: 0% B, t = 25 min: 100% B). Final compounds were purified by preparative HPLC Water Delta Prep 4000 with detection at 220 nm using an XTerra C18 column (30 x 50 mm, 5μ) with the binary system (eluent A: H_2O + 0.1%TFA, eluent B: 60% CH_3CN and 40% H_2O + 0.1% TFA) using a linear gradient (t = 0 min: 15% B, t = 30 min: 100% B, t = 40 min: 100% B). Melting points were measured with a hot plate Reichert-Kofler microscope and are uncorrected.

The above mentioned QSI were synthesized by Prof. Paolo Marchetti and Prof. Claudio Trapella. Erika Marzola, Department of Chemical and Pharmaceutical Sciences, University of Ferrara (Italy), performed HPLC measurements.